CONSTRUCTION OF BALLISTIC LUNAR TRANSFERS IN THE EARTH-MOON-SUN SYSTEM

by
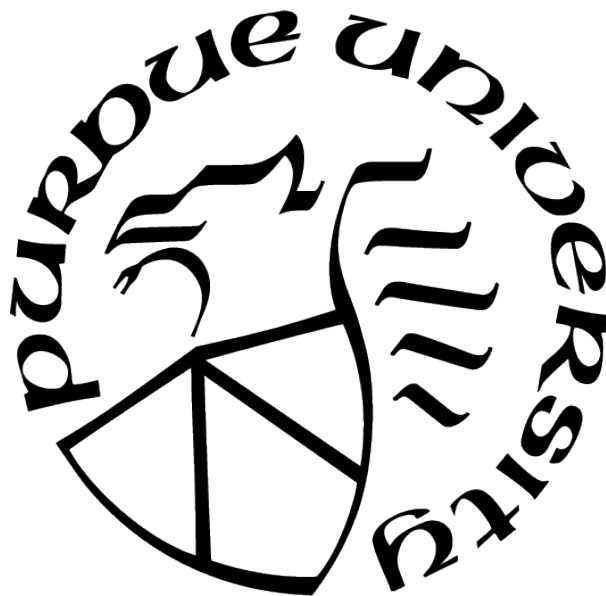
Stephen T. Scheuerle

A Thesis

Submitted to the Faculty of Purdue University

In Partial Fulfillment of the Requirements for the degree of

Master of Science in Aeronautics and Astronautics

School of Aeronautics and Astronautics

West Lafayette, Indiana

May 2021

THE PURDUE UNIVERSITY GRADUATE SCHOOL
STATEMENT OF COMMITTEE APPROVAL

Dr. Kathleen Howell, Chair

School of Aeronautics and Astronautics

Dr. Carolin Frueh

School of Aeronautics and Astronautics

Dr. James Longuski

School of Aeronautics and Astronautics

Approved by:

Dr. Gregory A. Blaisdell

To my parents, Nancy & Steve, and my sister Katie

ACKNOWLEDGMENTS

I'm extremely grateful to my family. You have supported me through each challenge. You have encouraged me to persevere, be creative, and approach every problem from a constructive and positive viewpoint. Mom, you have shown me how to be imaginative and believe that with the right mindset, anything is possible. Dad, you have taught me that with persistence, every obstacle becomes an opportunity. To my sister, Katie, you have guided me to pursue my dreams, no matter how ambitious they may seem. And to my Grandfather, who inspired me to explore space, and stay curious. Thank you all for encouraging the pursuit of my passions. I am fortunate to have an incredible family that helps me attain my endeavors.

I would like to express my gratitude to my advisor, Professor Kathleen C. Howell. Your exceptional guidance and mentorship has helped shape this research. Thank you for offering opportunities for me to grow in both an academic and professional setting. This work would not have been feasible without your assistance, insight, and knowledge. As I continue in my studies, I look forward to learning more from your expertise. I would also like to recognize the support from my committee members, Professors Carolin Frueh and James Longuski. Thank you for the feedback and time that you have provided me.

I would also like to show my appreciation to my friends. To the past and current members of the Multi-body dynamics research group, your feedback and inquiries have been instrumental to this research. I am privileged to be surrounded by a community of compassionate individuals, who are eager to learn and explore. Thank you for your friendship and support throughout this experience. I look forward to working with you all over the coming years. To my friends from NC State, your unwavering confidence towards my aspirations has encouraged my passions even further. I am extremely grateful for your guidance and advice over the last few years. I cannot express how much you all have helped me attain this goal.

TABLE OF CONTENTS

LIST OF TABLES

LIST OF FIGURES

14

ABSTRACT

An increasing interest in lunar exploration calls for low-cost techniques of reaching the Moon. Ballistic lunar transfers are long duration trajectories that leverage solar perturbations to reduce the multi-body energy of a spacecraft upon arrival into cislunar space. An investigation is conducted to explore methods of constructing ballistic lunar transfers. The techniques employ dynamical systems theory to leverage the underlying dynamical flow of the multi-body regime. Ballistic lunar transfers are governed by the gravitational influence of the Earth-Moon-Sun system; thus, multi-body gravity models are employed, i.e., the circular restricted three-body problem (CR3BP) and the bicircular restricted four-body problem (BCR4BP). The Sun-Earth CR3BP provides insight into the Sun's effect on transfers near the Earth. The BCR4BP offers a coherent model for constructing end-to-end ballistic lunar transfers. Multiple techniques are employed to uncover ballistic transfers to conic and multi-body orbits in cislunar space. Initial conditions to deliver the spacecraft into various orbits emerge from Periapse Poincaré maps. From a chosen geometry, families of transfers from the Earth to conic orbits about the Moon are developed. Instantaneous equilibrium solutions in the BCR4BP provide an approximate for the theoretical minimum lunar orbit insertion costs, and are leveraged to create low-cost solutions. Trajectories to the L_2 2:1 synodic resonant Lyapunov orbit, L_2 2:1 synodic resonant Halo orbit, and the 3:1 synodic resonant Distant Retrograde Orbit (DRO) are investigated.

1. INTRODUCTION

The Moon offers scientific insight into the formation of the Solar System and a proving ground for the future of humanity in space. NASA's Artemis and Gateway programs provide an infrastructure for a sustainable human presence in lunar orbit [1]. Alongside the public sector, private entities offer a framework for lunar exploration through robotic missions and human landing systems. These missions range from impulsive, crewed space capsules to low-thrust CubeSats [2]. One factor that is necessary for each architecture is a viable path from the Earth to the Moon. The mission design process balances different components of the trajectory to meet set criteria. A trade-off between the flight duration and propellant cost is most frequently considered. Historically, direct transfers are employed to produce short transfer solutions that reach the Moon in a matter of days. More recently, low-energy transfers have offered novel techniques of accessing cislunar space. These low-energy transfers, known as ballistic lunar transfers, are able to reduce mission propellant costs by leveraging solar perturbations. For the Sun to have a definitive impact on the mission architecture, transfers must spend multiple months traversing beyond the orbit of the Moon. Therefore, ballistic lunar transfers present an alternative approach to reaching cislunar space that lowers the insertion maneuver cost in exchange for a longer time of flight.

1.1 Problem Statement

With an increasing demand to fly ballistic lunar transfers, an understanding of these trajectories is essential. Techniques within dynamical systems theory and numerical methods are exploited to gain insight into the dynamical structures that permit these low-energy transfers. This investigation aims to: (1) analyze the evolution in energy within the bicircular restricted four-body problem, (2) construct families of ballistic lunar transfers, and (3) leverage techniques within dynamical systems theory to assess efficient solutions.

1.2 Previous Contributions

Ballistic lunar transfers have been flown previously for missions with limited propellant capabilities. In 1991, the trajectory for the Hiten spacecraft leveraged a low-energy transfer as a part of its extended mission. Hiten became the first spacecraft to fly a ballistic arc that temporarily captured the spacecraft around the Moon. Later in the mission, a maneuver was performed to enter lunar orbit [3]. In 2011, NASA launched the Gravity Recovery and Interior Laboratory (GRAIL) mission. The mission included two spacecraft, Ebb and Flow, that incorporated ballistic lunar transfers into the mission architecture. The path to the Moon took three months for the two GRAIL spacecraft and ultimately resided in a low-altitude, near-circular lunar orbit [4]. The lunar orbit insertion cost for the GRAIL spacecraft were approximately 670 m/sec. A direct transfer to an equivalent conic orbit costs roughly 940 m/sec. Thus, low-energy transfers reduced the lunar orbit insertion maneuver cost by approximately 270 m/sec [5]. Previous missions have displayed some of the advantages of ballistic lunar transfer mission scenarios.

Upcoming lunar missions are incorporating ballistic lunar transfers into the trajectory design. NASA's Cislunar Autonomous Positioning System Technology Operations and Navigation Experiment (CAPSTONE) mission is a CubeSat scheduled to launch in 2021. CAPSTONE aims to use a ballistic lunar transfer to enter into a near rectilinear halo orbit, lowering the insertion maneuver cost to below 16 m/sec [6]. Additionally, JAXA's Equilibrium Lunar-Earth point 6U Spacecraft (EQUULEUS) [7] and NASA's Lunar IceCube [8] are both CubeSats that are secondary payloads on the Artemis 1 launch. To some extent, both missions will leverage solar perturbations in their recovery efforts to enter orbit about the Moon. Ballistic lunar transfers enable small spacecraft to reach the lunar vicinity.

Dynamical systems theory and numerical methods have aided in the exploration of viable transfer scenarios. Parker et al. employ numerical techniques in an ephemeris model to characterize ballistic lunar transfers to conic orbits about the Moon [5], [9]. Additionally, ballistic lunar transfers are constructed using dynamical systems theory in a coupled circular restricted three-body problem (CR3BP) as exhibited by Parker et al.[10]. Transfers to near rectilinear halo orbits (NRHO) are investigated by Parrish et al. [11]. Tselousova et al.

apply dynamical systems theory techniques in the bicircular restricted four-body problem (BCR4BP) and the CR3BP produce ballistic lunar transfers [12]. A transcription method alongside a grid search in the BCR4BP produces a technique to construct ballistic lunar transfers as demonstrated by Oshima et al.[13]. Using the CR3BP, Sweetser determines an approach to compute the theoretical minimum maneuver cost for a ballistic lunar transfer departing from a circular low Earth orbit, to a circular low lunar orbit [14]. Analysis into departing flow near the cislunar vicinity within the BCR4BP is offered by Boudad [15],[16]. Clearly, previous investigations offer insight into the behavior of ballistic lunar transfers, and their presiding dynamical models.

1.3 Document Overview

The main goal of this research is to investigate techniques in constructing ballistic lunar transfers and understanding the dynamical structures that govern these paths. An overview of the document is written out below:

- **Chapter 2:** In this chapter, the dynamical models employed in this document are introduced. The N-body problem offers a foundation to derive simplified gravity models. The N-body problem is versatile in its implementation and suitable to model complex dynamical systems. This investigation employs two gravity models: the circular restricted three-body problem (CR3BP), and the bicircular restricted four-body problem (BCR4BP). The equations of motion for both the CR3BP and the BCR4BP are derived through the adoption of the N-body problem. The equations of motion for the CR3BP describe the path of a small body, i.e., a spacecraft, due to the net gravitational forces by two primary bodies. The equations of motion for the BCR4BP determine the trajectory of a small body due to the gravitational influence of three primary bodies, such that the orbits of the primary bodies are bicircular, i.e, a planet-moon-star system. One example of the CR3BP is the Earth-Moon system, and one example of the BCR4BP is the Earth-Moon-Sun system. The CR3BP is a time-independent system and includes an integral of the motion. The BCR4BP is a periodic, time-dependent system, which does not contain a constant of integration. Therefore, disadvantages to

the four-body problem are the added complexity of the system and the accessible tools within the model. Additional properties of each model such as equilibrium solutions, zero velocity surfaces, and symmetry are explored.

- **Chapter 3:** Techniques within dynamical systems theory and numerical methods are presented in this chapter. The lack of an analytical solution to the CR3BP or the BCR4BP requires an infrastructure in numerical methods. The linear variational equations and state transition matrices are derived. Single-shooting and multiple-shooting targeting strategies are prefaced through the application of multi-dimensional Newton-Raphson schemes. Targeting methods offer a numeric approach to accomplish a set of constraints. Natural parameter and pseudo-arclength continuation are implemented to extend a single solution into a family. Families of solutions provide insight into the accessible solution-space. Dynamical systems techniques such as periodic orbits, Poincaré maps, and invariant manifolds are introduced as applicable concepts to this investigation. Poincaré maps aid in visualizing the solution-space, and invariant manifolds present near-ballistic transfers into unstable multi-body orbits. An analysis of the evolution in energy for the BCR4BP is conducted to assess the impact perturbations have on the spacecraft.

- **Chapter 4:** Given the foundation devised by the previous chapters, methods of constructing ballistic lunar transfers are explored. Ballistic lunar transfers leverage solar perturbations to reduce the energy upon arriving into cislunar space. First, the Sun-Earth CR3BP is exploited to characterize the Sun's impact on trajectories near the Earth. Families of transfers are produced in the CR3BP to assess the dynamical behavior of the transfers in a simplified model and offer initial conditions to transition into the BCR4BP. Multiple techniques of constructing families of ballistic lunar transfers to conic orbits in the BCR4BP are investigated. The categories of families include fixed period, fixed arrival epoch, and fixed maneuver. Each type of family contributes different insights into the feasible transfer geometries. By employing energy properties of the BCR4BP, an approximation for the theoretical minimum insertion maneuver is contrived, and arcs along the instantaneous equilibrium solutions offer transfers near the

theoretical minimum. Invariant manifold theory is applied to identify nearly-ballistic transfers into unstable multi-body orbits. Fixed arrival location and tangential velocity constraints are incorporated to create transfers to stable periodic orbits.

- **Chapter 5:** The concluding remarks offer an overview of the results from this investigation. Considering the problem statement, the knowledge gained from each key point is expressed: the evolution in energy, constructing ballistic lunar transfers, and incorporating dynamical systems theory to uncover efficient solutions. The chapter considers the future development of the investigation. Transitioning solutions to the ephemeris model verifies the transfer geometries examined. Exploring features of the BCR4BP model presents an approach to mission design in the four-body regime. A stochastic stability analysis aids in the classification of low-energy paths. Additional research is necessary to describe the complex nature of ballistic lunar transfers.

2. SYSTEM MODELS

To design and analyze spacecraft trajectories, dynamical models are selected to represent the system. A dynamical model is a mathematical representation of an environment. In the case of spacecraft trajectory design, a model represents the governing dynamics acting on a vehicle and the differential equations that govern its path as it evolves through space. There are many contributing factors to the evolution of a spacecraft trajectory, but the most dominant influence is gravity. Dynamical models incorporating gravity have been examined by mathematicians and scientists for centuries. Various assumptions are included with each model, to either assist in the accuracy of the prediction, or to generalize the results. This section introduces the system models used this analysis and addresses the advantages and disadvantages of each model.

2.1 N-Body Problem

The N-body problem describes the motion of an object due to the gravitational forces exerted by the remaining $N-1$ bodies. An expression for the scalar force exerted by gravity appeared in *Philosophiæ Naturalis Principia Mathematica*[17] by Isaac Newton. This expression, i.e., Newton's Law of Universal Gravitation, is written as,

$$M_1 R_1'' = G \frac{M_1 M_2}{R_{12}^2} \tag{2.1}$$

where the scalar distance between body i and a fixed inertial point O is R_i. The second time derivative of position, or the scalar acceleration experienced by the body, is represented as R_i''. Each body is assumed to be a point mass, possessing a mass of M_i. The gravitational constant is denoted as G, approximately equal to $6.67 \cdot 10^{-11} \ \frac{m^3}{kg \cdot sec^2}$. The scalar distance between two bodies i and j, is R_{ij}, and is written in vector form as,

$$\vec{R}_{ij} = \vec{R}_j - \vec{R}_i \tag{2.2}$$

Quantities with an arrow overbar represent vector notation. The term $\vec{R}_{ij}$ is the position vector from body i to j; the base point of each vector $\vec{R}_k$ is the inertial point O. Equation (2.1) in vector form yields an expression for the acceleration of a single body due to the gravitational forces of the remaining $N-1$ bodies. This equation is written as,

$$M_i \vec{R}_i'' = -G \sum_{j=1, j \neq i}^{N} \frac{M_i M_j}{R_{ji}^3} \vec{R}_{ji} \quad \text{where } i = 1, 2, \ldots, N \tag{2.3}$$

Equation (2.3) serves as the general form for representing the N-body problem, where the acceleration on body i at any instant in time is determined by the position of the remaining $N-1$ bodies. As the bodies move through three-dimensional space, the problem relies on $3N$ second-order, nonlinear scalar differential equations to describe the motion of the system. For each second-order scalar differential equation, two constants of integration are necessary to construct an analytical expression for the motion. Therefore, $6N$ integrals of the motion are required to determine a closed-form solution to the N-body problem. Ten scalar integrals of the motion are known to exist for the N-body problem: one corresponding to the conservation of energy, three that relate to the conservation of angular momentum, and six associated with the conservation of linear momentum. In the simplest case, the two-body problem requires twelve ($6N$ where $N = 2$) integrals of the motion, when only ten exist. However, the problem reformulated in terms of the relative to the motion of the two bodies requires only six constants. Since ten constants are available, the relative two-body problem is solvable analytically. This relative two-body model yields conic orbits represented by Keplerian elements. Beyond two bodies, no closed-form solutions exist for $N \geq 3$; thus, the N-body problem does not possess an analytical solution. To explore the N-body problem when $N \geq 3$, numerous techniques leveraging dynamical systems theory and numerical methods are employed.

The N-body problem is the foundational model for spacecraft trajectory design. The highest-fidelity gravity model incorporates ephemeris information, that is, leveraging the ephemerides of the surrounding bodies to predict the motion of a spacecraft. The advantage of an ephemeris model is its accuracy within the context of the actual physical environment. However, a disadvantage is the complexity added to the dynamical model. To simplify the

problem, additional assumptions are introduced into the N-body problem. This investigation focuses on two of these simplified models, the Circular Restricted Three-Body Problem (CR3BP), and the Bicircular Restricted Four-Body Problem (BCR4BP).

2.2 Circular Restricted Three-Body Problem

The three-body problem considers the motion of three bodies due to their mutual gravitational interactions. The three-body problem is an example of the N-body problem, where $N = 3$. As previously observed, a closed-form analytical solution does not exist for the three-body problem; however, a set of assumptions simplifies the model. The Circular Restricted Three-Body Problem (CR3BP) is one example of a simplified three-body model, one that leverage conditions that offer a reasonable environment for spacecraft trajectory design.

2.2.1 Model Assumptions

A set of assumptions in the N-body problem reduces the model to the CR3BP. The three bodies are assumed to be centrobaric, and are denoted as P_1, P_2, and P_3 (with masses of M_1, M_2, and M_3, respectively). The motion of each body is dependent solely on their mutual gravitational influence. Thus, other forces such as solar radiation pressure, atmospheric drag, and oblate Earth effects are not included in this model. Arbitrarily, the bodies are selected such that $M_1 \geq M_2 > M_3$. In addition, one significant assumption to reduce the model, is denoting the mass of P_3 as much less than the mass of either P_1 or P_2, i.e., $M_3 \ll M_2$, $M_3 \ll M_1$. Thus, P_1 and P_2 are denoted as the primaries. This assumption is reasonable within the context of many applications in the solar system. For example, a focus on the motion of a spacecraft in the vicinity of cislunar space, the mass of the spacecraft is negligible compared to the mass of either the Earth or the Moon. One of the significant outcomes of this assumption, is that P_3 does not influence the motion of the primary bodies (either P_1 or P_2). Thus, the motion of P_1 and P_2 is completely described as a conic in the two-body problem. For the CR3BP, to further reduce complexity it is also assumed that the primary bodies move in circular orbits about their common barycenter (B_1). An inertial reference frame centered at B_1 is produced, where $\hat{X}$ and $\hat{Y}$ are two unit vectors that span

25

the primary orbital plane, and $\hat{Z}$ is the unit vector along the angular momentum vector for the primary bodies circular orbit. Figure 2.1 represents the $\hat{X} - \hat{Y}$ projection of the inertial reference frame.
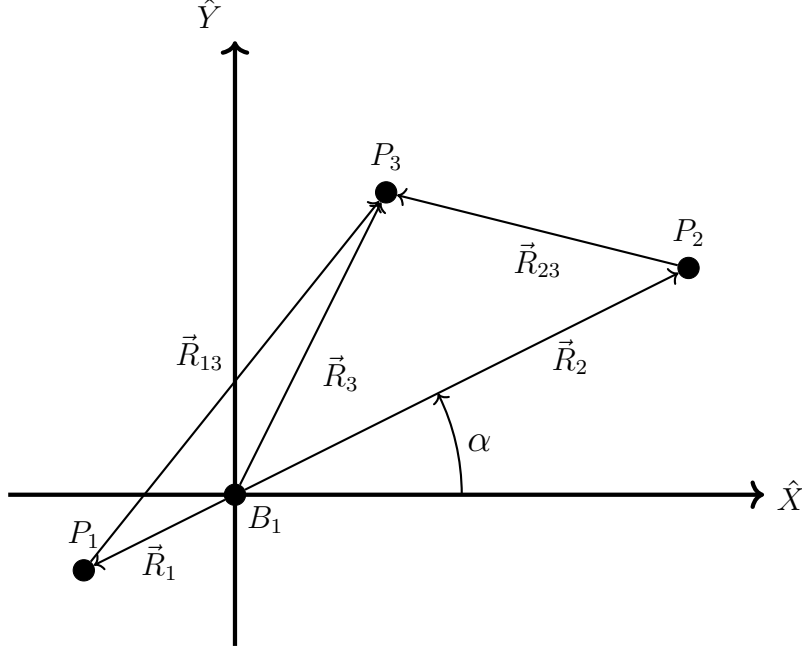
Figure 2.1. CR3BP in an inertial reference frame with B_1 at the origin

2.2.2 Derivation of the Equations of Motion

The equations of motion provide the underlying dynamical structure for the CR3BP. The CR3BP is derived from the N-body problem through Equation (2.3) where $N = 3$. As the two primary bodies (P_1 and P_2) are assumed to be in circular orbits, the N-body formulation governs the behavior of P_3, expressed as,

$$M_3 {}^I \vec{R}_3'' = -G\frac{M_3 M_1}{R_{13}^3}\vec{R}_{13} - G\frac{M_3 M_2}{R_{23}^3}\vec{R}_{23}$$

$$^I \vec{R}_3'' = -G\frac{M_1}{R_{13}^3}\vec{R}_{13} - G\frac{M_2}{R_{23}^3}\vec{R}_{23} \tag{2.4}$$

where the value $^I \vec{R}_3''$ refers to the inertial acceleration vector experienced by P_3 ($\frac{^I d^2 \vec{R}_3}{d\tau^2}$). Equation (2.4) represents the inertial vector equation of motion for the P_3 in the CR3BP.

Figure 2.1 illustrates the $\hat{X} - \hat{Y}$ projection in this model, and offers the definition of each position vector. Even though P_1 and P_2 are not impacted by the motion of P_3, they move relative to the inertial frame. Thus, the position of the primary bodies at a given instant in time (τ) is written as,

$$
\begin{aligned}
\vec{R}_1 &= -R_1(\cos{(\dot{\alpha}\tau)}\hat{X} + \sin{(\dot{\alpha}\tau)}\hat{Y}) \\
\vec{R}_2 &= R_2(\cos{(\dot{\alpha}\tau)}\hat{X} + \sin{(\dot{\alpha}\tau)}\hat{Y})
\end{aligned}
\tag{2.5}
$$

where $\dot{\alpha}$ is the constant mean motion in the circular orbits of the primary bodies. Additionally, the motion of the primary bodies is governed by their distance from B_1. A benefit to using an inertial reference frame is that it provides a clear visualization of the motion of each body, i.e., the view from a fixed observer. However, one challenge to a formulation in the inertial frame is insight into the relative dynamical structure between each body. When all three bodies are moving, the patterns in the motion of P_3 lack clarity. In addition, Equation (2.5) is an explicit function of time; thus, the equations of motion in the inertial frame are time-variant and dependent on the relative orientation of the primary bodies.

A standard formulation of the CR3BP incorporates a rotating reference frame, advantageous for analyzing the motion of P_3. When introducing a rotating reference frame, the angular rate of the frame is selected to match the mean motion of the primary bodies. Under these conditions, both P_1 and P_2 are in fixed positions as viewed in the rotating frame. For simplicity, a set of unit vectors is defined such that the $\hat{x}$-axis is directed from P_1 to P_2. The $\hat{z}$-axis is along the angular momentum vector of the circular orbits for the primary bodies (parallel to $\hat{Z}$), and the $\hat{y}$-axis completes the orthonormal triad. The origin of this reference frame the system barycenter, B_1. Figure 2.2 highlights the difference between the two reference frames, where the rotating frame is denoted in blue, and the inertial frame is rendered in black.

An analytical solution to the 3-body problem does not exist. Even with the simplifying assumptions in the CR3BP, numerical integration is still required. To generalize the

27
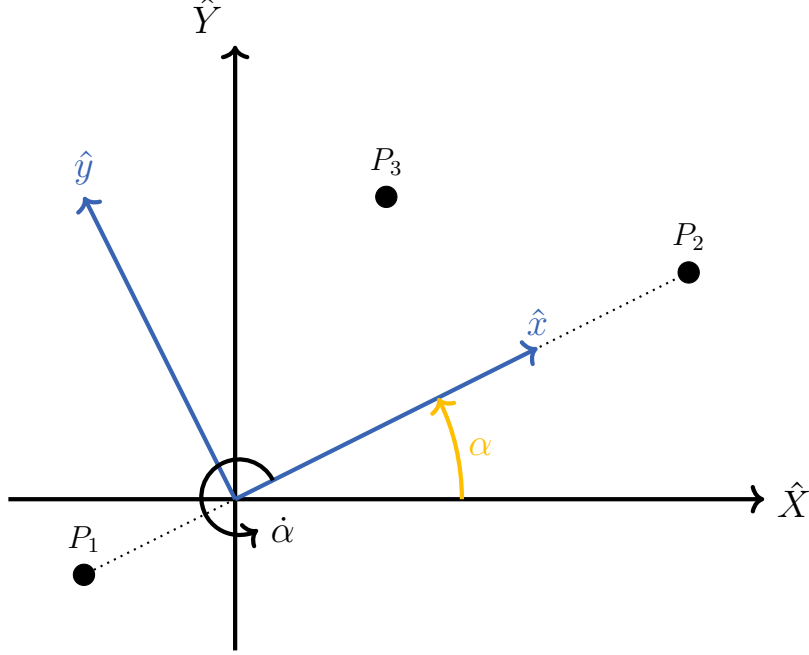
Figure 2.2. Relationship between the Inertial Reference Frame (black) and the Rotating Reference Frame (blue) for the CR3BP

CR3BP, and aid numerical integration, the differential equations are nondimensionalized. To nondimensionalize the problem, characteristic quantities for the model are defined as,

$$l^\star := R_1 + R_2 \tag{2.6}$$

$$m^\star := M_1 + M_2 \tag{2.7}$$

$$\tau^\star := \sqrt{\frac{l^{\star 3}}{Gm^\star}} \tag{2.8}$$

The characteristic length is denoted $l^\star$, defined as the distance between P_1 and P_2. Since the primary bodies are moving in circular orbits about their common barycenter, $l^\star$ remains constant. The characteristic mass is $m^\star$, that is, the total mass of P_1 and P_2. The characteristic time, $\tau^\star$, is the inverse of the mean motion ($\dot{\alpha}$) for the reference frame. A consequence of the definition of characteristic time is a nondimensional gravitational constant that is equal

to one ($G^\star = 1$), removing the quantity from the equations of motion. Given these characteristic quantities, the nondimensional mean motion n for the primary system is evaluated as,

$$n = \dot{\alpha}\tau^\star = \sqrt{\frac{Gm^\star}{l^{\star 3}}}\sqrt{\frac{l^{\star 3}}{Gm^\star}} = 1 \tag{2.9}$$

Utilizing the characteristic quantities, the nondimensional forms for the position vectors, mass, and time are defined as,

$$\vec{r} = \frac{\vec{R}_3}{l^\star} \tag{2.10}$$

$$\vec{r}_{13} = \frac{\vec{R}_{13}}{l^\star} \tag{2.11}$$

$$\vec{r}_{23} = \frac{\vec{R}_{23}}{l^\star} \tag{2.12}$$

$$\mu = \frac{M_2}{m^\star} = 1 - \frac{M_1}{m^\star} \tag{2.13}$$

$$t = \frac{\tau}{\tau^\star} \tag{2.14}$$

Equations (2.10), (2.11), and (2.12) are the nondimensional relative position vectors. The nondimensional location of P_3 relative to the barycenter is expressed as $\vec{r}$ without a subscript for convenience. Equation (2.13) describes the mass parameter of the system, equivalent to the mass ratio of the primary P_2 over the total mass of the primary bodies. The value of μ is always less than or equal to one-half, as the mass of P_2 is arbitrarily defined to be less than or equal to the mass of P_1. Equation (2.14) denotes nondimensional time. The nondimensional time derivative of position, as viewed by an inertial observer, is written as

$^I\dot{\vec{r}}_i$ $\left(\frac{d\vec{r}_i}{dt}\right)$. The nondimensional parameters are introduced into the equations of motion for the CR3BP as follows,

$$\frac{\tau^{\star2}}{l^\star}{}^I\vec{R}''_3 = \left[-G\frac{M_1}{R_{13}^3}\vec{R}_{13} - G\frac{M_2}{R_{23}^3}\vec{R}_{23}\right]\frac{\tau^{\star2}}{l^\star}$$

$$^I\ddot{\vec{r}} = -G\left[\frac{M_1}{R_{13}^3}\vec{R}_{13} + \frac{M_2}{R_{23}^3}\vec{R}_{23}\right]\frac{l^{\star3}}{Gm^\star l^\star}$$

$$^I\ddot{\vec{r}} = -\frac{M_1}{m^\star r_{13}^3}\vec{r}_{13} - \frac{M_2}{m^\star r_{23}^3}\vec{r}_{23}$$

$$^I\ddot{\vec{r}} = -\frac{1-\mu}{r_{13}^3}\vec{r}_{13} - \frac{\mu}{r_{23}^3}\vec{r}_{23} \tag{2.15}$$

Equation (2.15) represents the nondimensional equations of motion as viewed in the inertial reference frame for the CR3BP. The value $^I\ddot{\vec{r}}$ is the acceleration vector for P_3 in the inertial frame. Comparing Equation (2.4) to (2.15), nondimensionalizing the problem simplifies the equations such that the acceleration vector is a function of position of P_3 relative to the primary bodies, and the mass parameter of the system.

A nondimensional rotating frame formulation for the CR3BP further simplifies the problem and offers some useful insights. As the rotating frame view fixes the locations of P_1 and P_2, the position vectors from the primary bodies to P_3 ($\vec{r}_{13}$ and $\vec{r}_{23}$) are dependent on the position of P_3 ($\vec{r}$) and the mass parameter (μ). The position vector describing the location of P_3 is defined in terms of rotating coordinates,

$$\vec{r} = x\hat{x} + y\hat{y} + z\hat{z} \tag{2.16}$$

Since the motion of the primary bodies are described by a closed Keplerian orbit, the distance of P_1 and P_2 from the barycenter is, thus, determined. For circular orbits, the distance of each body from the barycenter, at any given instant, is dependent on the mass ratio and distance between the two bodies. As the problem is nondimensionalized, it becomes a function of the mass parameter μ written as,

$$r_1 = \frac{M_2}{m^\star} = \mu$$

$$r_2 = \frac{M_1}{m^\star} = 1 - \mu \tag{2.17}$$

Equation (2.17) denotes the distances P_1 and P_2 from the barycenter in the nondimension-alized system. From the definition of the rotating reference frame, the primary bodies are fixed along the $\hat{x}$-axis. With this information, the relative position vectors of P_3 with respect to P_1 and P_2 are straightforward as,

$$
\begin{aligned}
\vec{r}_{13} = \vec{r}_3 - \vec{r}_1 = (x + \mu)\hat{x} + y\hat{y} + z\hat{z} \\
\vec{r}_{23} = \vec{r}_3 - \vec{r}_2 = (x - 1 + \mu)\hat{x} + y\hat{y} + z\hat{z}
\end{aligned}
\tag{2.18}
$$

The differential equations that govern motion in the CR3BP are nondimensionalized to aid in alleviating numerical errors and generalize the results, and formulated in a rotating frame to fix the position of the primary bodies. To employ a rotating coordinate frame, the equations of motion are expressed relative to the frame. Although Equation (2.15) represents a nondimensional equation of motion, the observer is fixed in the inertial frame. The basic kinematic equation transitions from the inertial coordinate frame to a rotating coordinate frame,

$$
\begin{aligned}
{}^{I}\dot{\vec{r}} = {}^{R}\dot{\vec{r}} + {}^{I}\vec{\omega}^{R} \times \vec{r} \\
{}^{I}\ddot{\vec{r}} = {}^{R}\ddot{\vec{r}} + 2\,{}^{I}\vec{\omega}^{R} \times {}^{R}\dot{\vec{r}} + {}^{I}\vec{\omega}^{R} \times {}^{I}\vec{\omega}^{R} \times \vec{r}
\end{aligned}
\tag{2.19}
$$

where the term ${}^{R}\ddot{\vec{r}}$ corresponds to the acceleration of P_3 as observed in the rotating reference frame. In Equation (2.19) ${}^{I}\vec{\omega}^{R}$ is the angular velocity of the rotating coordinate frame with respect to the inertial frame. The angular velocity vector is normal to the orbital plane ($\hat{z}$ or $\hat{Z}$); the magnitude of the vector is equal to the nondimensional mean motion, n, thus, ${}^{I}\vec{\omega}^{R} = n\hat{z}$. Using Equations (2.16), (2.17), and (2.19), the acceleration of P_3 as viewed in the rotating frame and expressed in terms of rotating coordinates as derived in terms of its scalar components,

$$
\begin{aligned}
\ddot{x} &= 2n\dot{y} + n^2 x - \frac{(1-\mu)(x+\mu)}{r_{13}^3} - \frac{\mu(x-1+\mu)}{r_{23}^3} \\
\ddot{y} &= -2n\dot{x} + n^2 y - \frac{(1-\mu)y}{r_{13}^3} - \frac{\mu y}{r_{23}^3} \\
\ddot{z} &= -\frac{(1-\mu)z}{r_{13}^3} - \frac{\mu z}{r_{23}^3}
\end{aligned}
\tag{2.20}
$$

Equation (2.20) represents the nondimensional equations of motion for the CR3BP in a rotating coordinate frame. From Equation (2.9), the mean motion is equal to one $(n = 1)$, which further simplifies the equations. By formulating the CR3BP in a rotating coordinate frame, the equations of motion are a function of the mass parameter (μ) and the instantaneous position and velocity of P_3. A pseudo-potential function simplifies the equations of motion to the following,

$$\Omega = \frac{1}{2}(x^2 + y^2) + \frac{1 - \mu}{r_{13}} + \frac{\mu}{r_{23}} \tag{2.21}$$

$$\begin{aligned}
\ddot{x} &= 2\dot{y} + \Omega_x \\
\ddot{y} &= -2\dot{x} + \Omega_y \\
\ddot{z} &= \Omega_z
\end{aligned} \tag{2.22}$$

where Ω is the pseudo-potential function corresponding to the differential equations. The scalar equations of motion are rewritten in Equation (2.22) in terms of the pseudo-potential function. Note that the subscripts on Ω represent the partial derivative with respect to the components of position ($\Omega_x = \frac{\partial \Omega}{\partial x}$). As the equations of motion are expressed in terms of a pseudo-potential function, that is not an explicit function time, the CR3BP is a conservative, time-invariant system.

2.2.3 Integral of the Motion

Integrals of the motion deliver solutions to the differential equations. Even without a complete solution, however, integrals of the motion are advantageous in characterizing and comparing dynamical structures. As the CR3BP is a conservative system, an integral of the motion is sought for the formulation in the rotating coordinate frame. Previous authors demonstrate that a single integral of the motion is associated with the differential equations

in the CR3BP[18]. The value is determined by integrating the dot product between the velocity and acceleration vectors of P_3 as follows,

$$\dot{\vec{r}} \cdot \ddot{\vec{r}} = \dot{x}\ddot{x} + \dot{y}\ddot{y} + \dot{z}\ddot{z}$$

$$\dot{\vec{r}} \cdot \ddot{\vec{r}} = \dot{x}\Omega_x + \dot{y}\Omega_y + \dot{z}\Omega_z \tag{2.23}$$

Because the pseudo-potential expression is not a function of time, the right side of Equation (2.23) represents its total nondimensional time derivative, $\frac{d\Omega}{dt}$. As the pseudo-potential function is time-invariant, Equation (2.23) is equal to zero. Thus, by integrating as a function of t, the following is determined,

$$\int (\dot{x}\ddot{x} + \dot{y}\ddot{y} + \dot{z}\ddot{z})dt = \int (\dot{x}\Omega_x + \dot{y}\Omega_y + \dot{z}\Omega_z)dt$$

$$\frac{\dot{x}^2}{2} + \frac{\dot{y}^2}{2} + \frac{\dot{z}^2}{2} = dx\frac{\partial \Omega}{\partial x} + dy\frac{\partial \Omega}{\partial y} + dz\frac{\partial \Omega}{\partial z} + constant$$

$$\frac{1}{2}(\dot{x}^2 + \dot{y}^2 + \dot{z}^2) = \Omega + constant$$

$$JC = -(\dot{x}^2 + \dot{y}^2 + \dot{z}^2) + 2\Omega \tag{2.24}$$

where JC is the scalar integral of the motion in the CR3BP. This value is representative of the Jacobi integral in Lagrangian mechanics, and is denoted the Jacobi constant for this analysis. Note that for a given value of the pseudo-potential function, i.e, a fixed position, an increase in velocity magnitude results in a lower value of the Jacobi constant. Therefore, the Jacobi constant serves as an "energy-like" value, where a higher energy associated with the motion of P_3 corresponds to a lower value of JC. Even a single integral of the motion offers many benefits to any dynamical systems analysis, including reducing the dimensionality of the problem, comparing transfer energies, and bounding the accessible regions for a given energy level.

2.2.4 Equilibrium Solutions

Equilibrium solutions provide insight into the dynamical structures governing a system behavior. Given a dynamical system represented by a set of differential equations, equilibrium solutions exist for the time derivatives of the state vector equal to zero. In the CR3BP, a fully defined state is a six-dimensional vector consisting of the position and velocity states for P_3. Therefore, the velocity and acceleration of P_3 are zero for an equilibrium solution to exist, i.e., $\dot{x} = \dot{y} = \dot{z} = \ddot{x} = \ddot{y} = \ddot{z} = 0$. By replacing these values into Equation (2.20), the equations of motion for the CR3BP are simplified as,

$$0 = x - \frac{(1-\mu)(x+\mu)}{r_{13}^3} - \frac{\mu(x-1+\mu)}{r_{23}^3} \tag{2.25}$$

$$0 = y - \frac{(1-\mu)y}{r_{13}^3} - \frac{\mu y}{r_{23}^3} \tag{2.26}$$

$$0 = -\frac{(1-\mu)z}{r_{13}^3} - \frac{\mu z}{r_{23}^3} \tag{2.27}$$

As the mass parameter μ is always positive and less than one half, Equation (2.27) demonstrates that $z = 0$ for any equilibrium points. Therefore, all equilibrium solutions in the CR3BP exist in the $\hat{x}\hat{y}$-plane. In 1767, Leonhard Euler identified the first set of equilibrium points in the CR3BP, i.e., the collinear points[19]. Equilibrium locations of the collinear equilibrium solutions along the $\hat{x}$-axis are apparent as $y = z = 0$ satisfies Equations (2.26)-(2.27). Thus, by removing the dependency on y and z, Equation (2.25) becomes,

$$x = \frac{(1-\mu)(x+\mu)}{|x+\mu|^3} + \frac{\mu(x-1+\mu)}{|x-1+\mu|^3} \tag{2.28}$$

The terms in the denominator represent the distance from the primaries to P_3, reduced to the $\hat{x}$-axis. To reduce the equation further, the following property for absolute values, i.e.,

$$\frac{x+\mu}{|x+\mu|^3} = \frac{1}{(x+\mu)^2} \quad \text{or} \quad -\frac{1}{(x+\mu)^2} \tag{2.29}$$

where the negative and positive values refer to an x position to the left or right of P_1 along the x-axis, respectively. By applying the property from Equation (2.29) to Equation (2.28), the absolute value terms are replaced by the following possible equations,

$$
\begin{aligned}
x &= -\frac{(1-\mu)}{(x+\mu)^2} - \frac{\mu}{(x-1+\mu)^2} \\
x &= \frac{(1-\mu)}{(x+\mu)^2} - \frac{\mu}{(x-1+\mu)^2} \\
x &= \frac{(1-\mu)}{(x+\mu)^2} + \frac{\mu}{(x-1+\mu)^2}
\end{aligned}
\tag{2.30}
$$

The solutions to Equation (2.30) are the three collinear equilibrium points and exist along the $\hat{x}$-axis to the left, between, and to the right of the primary bodies. The process of solving Equation (2.30) is non-trivial, therefore, a Newton-Raphson algorithm is employed to compute the locations of the collinear equilibrium points. Note that the equilibrium locations are dependent on the value of μ.

In 1772, Joseph-Louis Lagrange exposed two additional equilibrium solutions in the CR3BP, denoted as the equilateral points [20]. These equilibrium points are off the $\hat{x}$-axis, where the y component is non-zero. The locations of the equilateral points are determined through the simplification of Equation (2.26), written as,

$$
\begin{aligned}
0 &= y - \frac{(1-\mu)y}{r_{13}^3} - \frac{\mu y}{r_{23}^3} \\
0 &= y\left(1 - \frac{1-\mu}{r_{13}^3} - \frac{\mu}{r_{23}^3}\right)
\end{aligned}
\tag{2.31}
$$

where y is not equal to zero. Therefore, the value within the parenthesis in Equation (2.31) must equal zero, which occurs when $r_{13} = r_{23} = 1$. The distance from P_3 to both primaries is equal at only two locations in the CR3BP, such that P_1, P_2, and the equilibrium point form an equilateral triangle. Knowing the characteristics of an equilateral triangle, a geometric expression for the placement of the equilibrium solutions is written as,

$$
\begin{aligned}
x &= \cos\frac{\pi}{3} - \mu = \frac{1}{2} - \mu \\
y &= \sin\frac{\pi}{3} = \pm\frac{\sqrt{3}}{2}
\end{aligned}
\tag{2.32}
$$

35

where the y component has two possible solutions. Together, the collinear and equilateral equilibrium solutions provide five equilibrium points in the CR3BP. The equilibrium solutions are denoted the Lagrange points, L_i where $i = 1,2,...,5$. The Lagrange points are labelled in order of increasing energy (decreasing in terms of the Jacobi constant). The equilateral equilibrium points L_4 and L_5 occur at the same energy level; thus, L_4 is defined to be the equilateral solution with a positive y component. Figure 2.3 illustrates the planar locations of all five Lagrange points in the CR3BP as yellow diamonds. The dashed lines highlight the sides of the equilateral triangles dictating the positions of L_4 and L_5. For the collinear points, L_1 lies between the two primary bodies, and L_2 and L_3 are located to the right and left of both primary bodies, respectively.
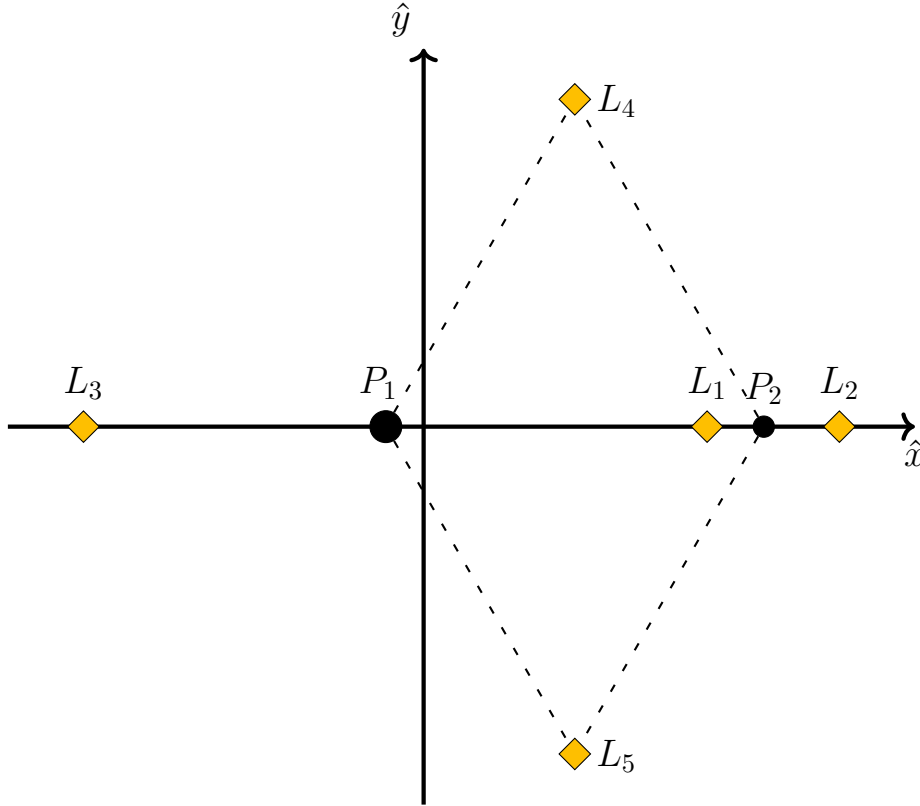
Figure 2.3. Location of the Lagrange Points in the CR3BP for an arbitrary system, displayed in the P_1-P_2 rotating coordinate frame

The position of the Lagrange points varies depending on the mass ratio of the primary bodies. For example, the locations of the Lagrange points in the Sun-Earth and Earth-Moon

systems are summarized in Table 2.1. As the Sun-Earth mass parameter is much smaller than the Earth-Moon mass parameter, the locations of L_1 and L_2 are much closer to Earth (P_2) in the Sun-Earth system. Additionally, the x-coordinate of L_4 and L_5 shifts relative to the rotating reference frame. The Jacobi constant for the Lagrange points are listed in Table 2.2 to the level of accuracy indicated. The Earth-Moon and Sun-Earth systems are the focus of this investigation, however, the Lagrange points are easily constructed for a system defined by any mass ratio. The Lagrange points are employed throughout this investigation, and offer insight into the dynamical structures associated with the CR3BP.

Table 2.1. Lagrange points in the Sun-Earth and Earth-Moon systems, displayed in nondimensional units in the respective rotating coordinate frames

Lagrange Points	Sun-Earth [ndim]	Earth-Moon [ndim]
μ	3.00348×10^{-6}	1.21506×10^{-2}
L_1	[0.99003 0 0]	[0.83692, 0, 0]
L_2	[1.01003 0 0]	[1.15568, 0, 0]
L_3	[-1.00000 0 0]	[-1.00506, 0, 0]
L_4	[.50000 0.86603 0]	[0.48785, 0.86603, 0]
L_5	[.50000 -0.86603 0]	[0.48785, -0.86603, 0]

Table 2.2. Jacobi constant of each Lagrange point in the Sun-Earth (JC_{SE}) and Earth-Moon (JC_{EM}) systems

Lagrange Points	JC_{SE}	JC_{EM}
L_1	3.000891	3.188341
L_2	3.000886	3.172160
L_3	3.000003	3.012147
L_4 and L_5	2.999997	2.988109

2.2.5 Zero Velocity Surfaces

The existence of the Jacobi constant reflects a valuable dynamical property that governs the motion of P_3. Recall Equation (2.24) where the energy level associated with the state

for P_3 relies on the velocity of the body and the pseudo-potential function (Ω). If the Jacobi constant value is known, Equation (2.24) is rearranged to the following,

$$V^2 = -JC + 2\Omega \qquad (2.33)$$

where V is the relative velocity magnitude for P_3. As velocity is a physical property, the right side of the equation must always be greater than or equal to zero, or $JC \leq 2\Omega$. As the pseudo-potential function is dependent on the position of P_3 in the rotating coordinate frame, some regions of space become inaccessible. Therefore, the set of surfaces defined by $JC = 2\Omega$ bounds the motion of P_3, also written as,

$$JC = (x^2 + y^2) + \frac{2(1-\mu)}{r_{13}} + \frac{2\mu}{r_{23}} \qquad (2.34)$$

In the planar case, where $z = \dot{z} = 0$, the surfaces are reduced to curves in the $\hat{x}\hat{y}$-plane, labelled the zero velocity curves (ZVC). The ZVC bound the regions of space denoted as the forbidden regions. Within a forbidden region, the velocity of the P_3 is imaginary. As an imaginary velocity is physically inaccessible, the region is unattainable for that energy level. In Figure 2.4, the ZVC are plotted for the Earth-Moon system when a Jacobi constant possesses a value of 3.19. The blue shaded region is the forbidden region at this energy level, and the yellow dots are the locations of the Lagrange points. The Jacobi constant value in Figure 2.4 is a higher value than that corresponding to all Lagrange points in the Earth-Moon system (see Table 2.2). Figure 2.5 is the same ZVC plot as in Figure 2.4, but zoomed into the lunar vicinity. At this energy level, the ZVC separate the space into three distinct regions, near the Earth, near the Moon, and exterior to the Earth-Moon system. As the Jacobi constant remains fixed along a trajectory, the motion of P_3 at this energy level is restricted to one of these three regions. For example, if P_3 originated near the Earth with a Jacobi constant value of 3.19, it cannot reach the region of space near the Moon, nor can it depart the Earth-Moon system. Similarly, a spacecraft beyond the Earth-Moon system at $JC = 3.19$ cannot approach the Earth nor the Moon in the CR3BP.

Transfers that traverse the region between P_1 and P_2 become accessible as the energy of P_3 increases. By definition, the Lagrange points are fixed in the P_1-P_2 rotating coordinate frame, therefore, each equilibrium point must lie on the ZVC at their respective energy level. In Figure 2.6, the ZVC is constructed using the precise Jacobi constant value for L_1 (JC_{L_1}) and the curve intersects the equilibrium point. The Lagrange point is stationary and serves as a barrier to motion across the two regions, therefore, P_3 cannot traverse through L_1 at this value of the Jacobi constant. By decreasing the Jacobi constant value to 3.175, which lies between JC_{L_1} and JC_{L_2}, Figure 2.7 is constructed. In Figure 2.7, the ZVC recedes from the Lagrange point L_1, which allows P_3 to freely traverse between the regions surrounding P_1 and P_2. The gap in the forbidden region in the vicinity of a Lagrange point is denoted a portal. For values of the Jacobi constant that are less than JC_{L_1}, the L_1 portal is open, such that P_3 freely traverses between P_1 and P_2. The relationship between the ZVCs and the value of the Jacobi constant offers insight into the regions accessible to a spacecraft. As the Jacobi constant decreases past the energy values associated with each Lagrange point, additional portals open.
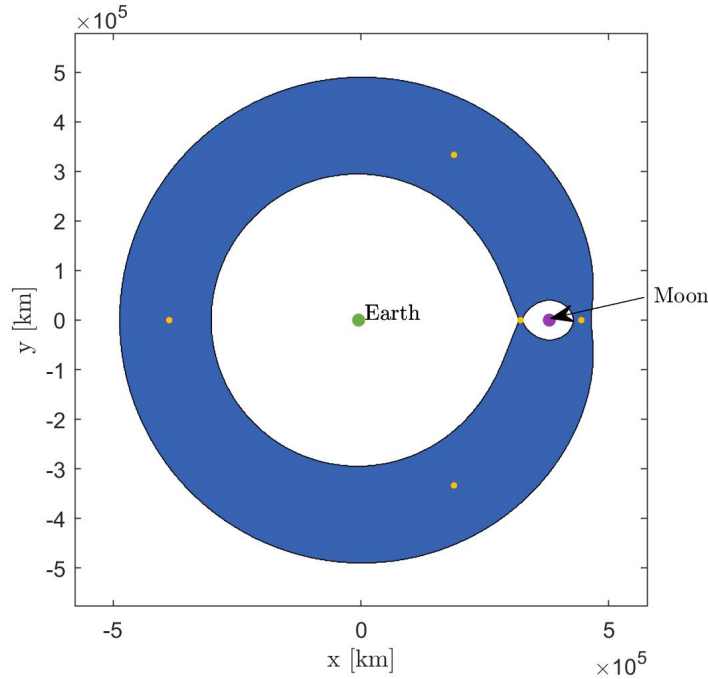
Figure 2.4. ZVC in the Earth-Moon system for a Jacobi constant of 3.19
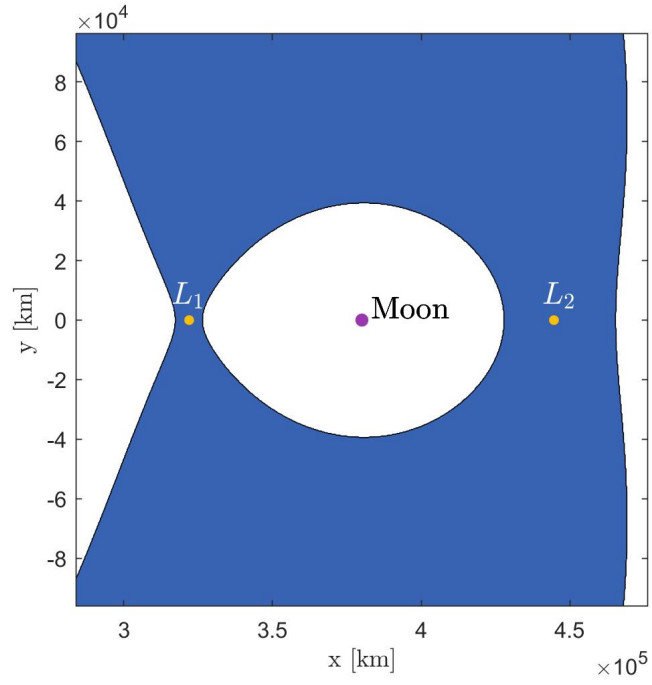
Figure 2.5. ZVC in the Earth-Moon system for a Jacobi constant value of 3.19, centered about the Moon
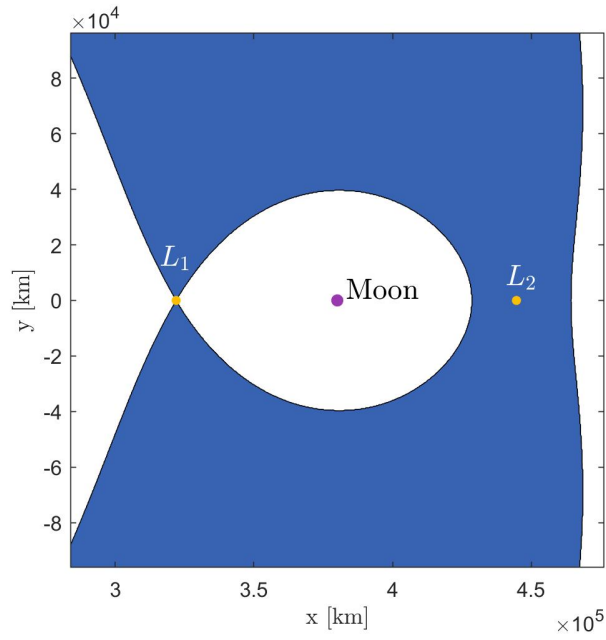
Figure 2.6. ZVC in the Earth-Moon system for a Jacobi constant value of 3.188341 (JC_{L_1}), centered about the Moon
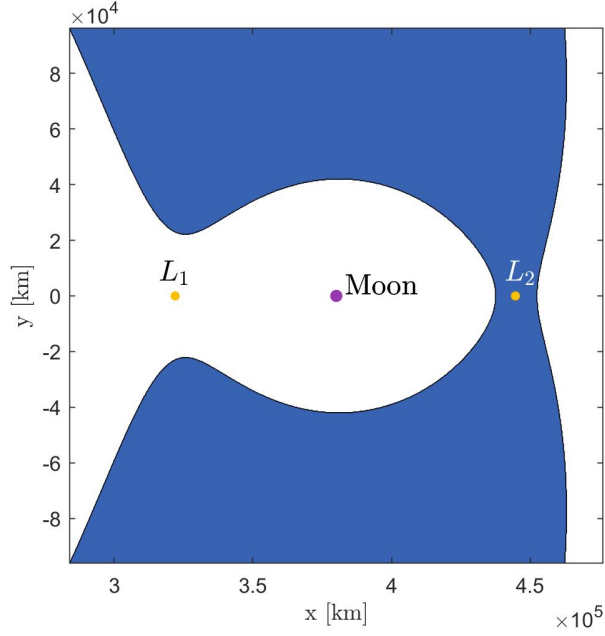
Figure 2.7. ZVC in the Earth-Moon system for a Jacobi constant value of 3.175 ($JC_{L_2} < JC < JC_{L_1}$), centered about the Moon

Similar to L_1, the portals associated with L_2 and L_3 also open as the Jacobi constant value changes as appartent and in Figures 2.8 and 2.9. In Figure 2.8, the Jacobi constant value is below that of JC_{L_2} and above JC_{L_3}, thus, the dynamic behavior allows P_3 to traverse between the interior and exterior regions of the Earth-Moon system through the L_2 portal. Figure 2.9 reflects a Jacobi constant value between JC_{L_3} and $JC_{L_{4,5}}$, where the portal to the left of the Earth, near the Lagrange point L_3, opens. For Figure 2.10, the value of the Jacobi constant is below that of $JC_{L_{4,5}}$, where the ZVC no longer exists in the $\hat{x}\hat{y}$-plane. The correlation between the Jacobi constant value and the transfer designs available for P_3 supplies insight into the potential behavior in the CR3BP. For planar motion, a portal that is open or closed frequently dictates the feasibility of various mission designs.

Spatial transfers are bounded by the zero velocity surfaces. When the motion of P_3 is not restricted to the $\hat{x}\hat{y}$-plane, Equation (2.34) dictates that the accessible regions in the spatial problem that govern the path of P_3. The surfaces are denoted zero velocity surfaces (ZVS) with the same properties as the ZVC, such that the ZVC in configuration space is a slice of the ZVS through the $\hat{x}\hat{y}$-plane. Figure 2.11 is a sample ZVS in the Earth-Moon system when
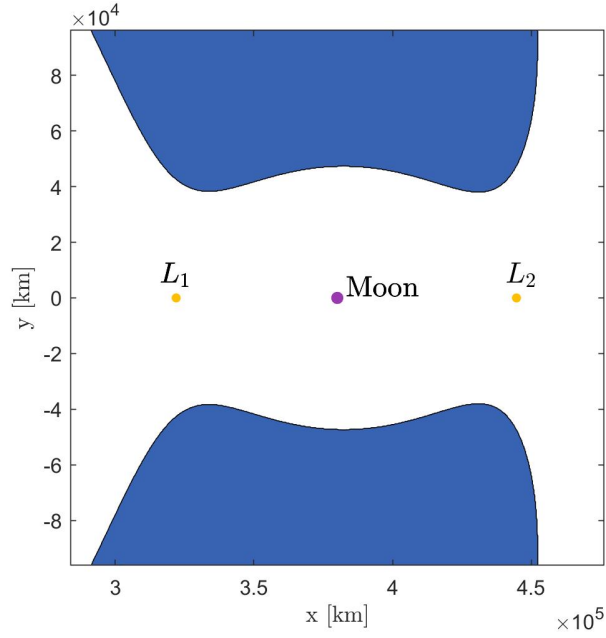
Figure 2.8. ZVC in the Earth-Moon system for a Jacobi constant value of 3.150 ($JC_{L_3} < JC < JC_{L_2}$), centered about the Moon

the Jacobi constant value is equal to 3.150. Figure 2.11**a** is plotted as the planar projection and Figure 2.11**b** is an isometric view of the same ZVS. The blue surfaces represent the ZVS, where P_3 is free to traverse throughout the inner lobe near the Earth, in the vicinity near the Moon, and exterior to the outer surface. For Jacobi constant values lower than $JC_{L_{4,5}}$, although no ZVC lie in the $\hat{x}\hat{y}$-plane, ZVS do exist off the plane.
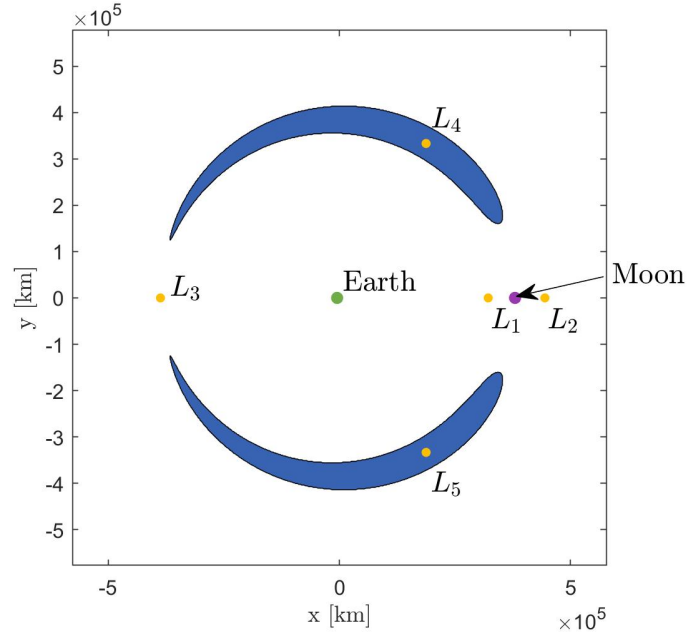
Figure 2.9. ZVC in the Earth-Moon system for a Jacobi constant value of 3.011 ($JC_{L_{4,5}} < JC < JC_{L_3}$)
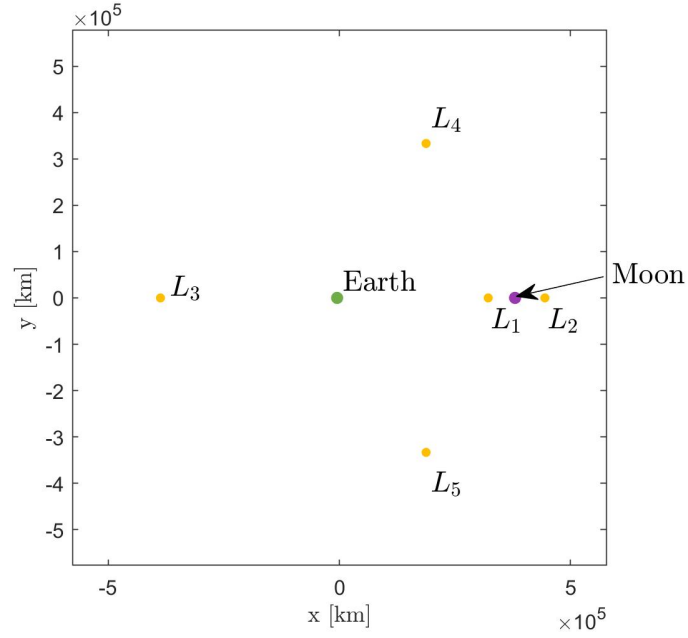
Figure 2.10. ZVC in the Earth-Moon system for a Jacobi constant value of 2.980 ($JC < JC_{L_{4,5}}$)
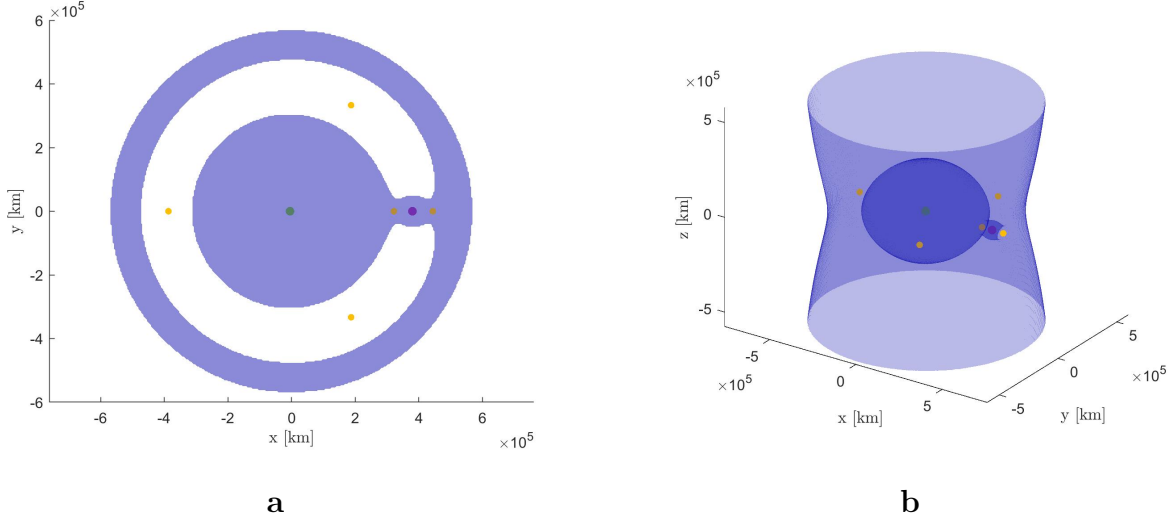
Figure 2.11. Zero velocity surface in the Earth-Moon CR3BP with a Jacobi constant value of 3.150; planar view **a**, isometric view **b**

2.2.6 Symmetry

Leveraging symmetric properties within the CR3BP aids in the construction of dynamical structures. In 1955, Roy et al. summarized the conditions necessary for a continuous trajectory to possess symmetry within the N-body problem [21]. The general Mirror Theorem requires the velocity of each body to be perpendicular to every radial vector from any given body to the center of mass of the system. Thus, the Mirror Theorem offers guidance for defining a state vector such that, once propagated forward in time delivers the mirror image of the same state in reverse time. In the CR3BP, P_1 and P_2 are assumed to traverse circular orbits where the radial vector is always perpendicular to the velocity direction; thus, the circular motion of the primary bodies is symmetric. For the motion of P_3 to meet the criteria for the Mirror Theorem, the velocity of P_3 must be perpendicular to $\vec{r}$, $\vec{r}_1$, and $\vec{r}_2$, that occurs when the velocity vector lies in the $\hat{y}\hat{z}$-plane. As the velocity vector must also be perpendicular to $\vec{r}$, the position of P_3 must be in the $\hat{x}\hat{z}$-plane. If P_3 is off the $\hat{x}$-axis, then the velocity vector is restricted to the $\hat{y}$ direction. An example is represented in Figure 2.12, where the red point represents the initial state on the $\hat{x}$-axis with a velocity in the $\hat{y}$ direction. The blue arc represents the state propagated forward in time, and the yellow arc is the state backwards in time. The arrows represent the motion of P_3 as propagated forward

44

in time. From Figure 2.12, there is a mirror image of the transfer between the forward and backward propagated state.
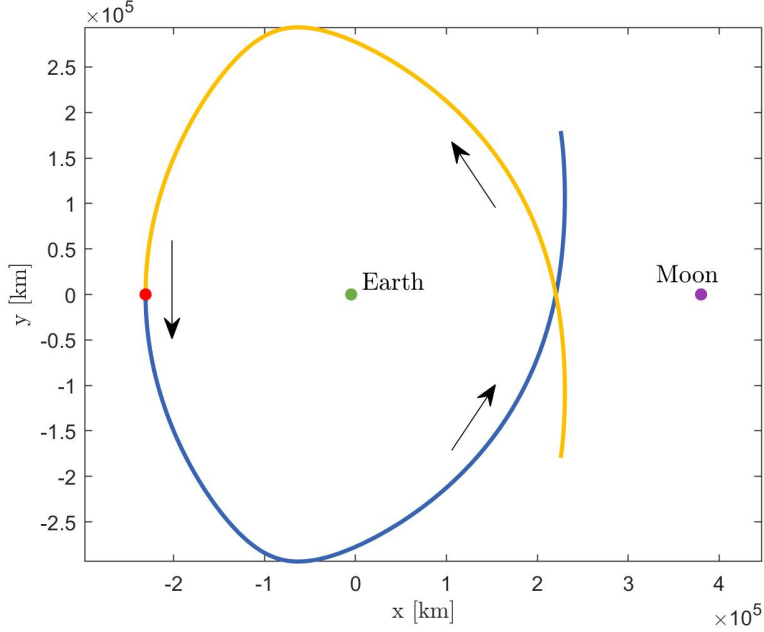
Figure 2.12. Mirror Theorem condition for P_3 in the CR3BP

The Mirror Theorem also applies to two independent solutions, where symmetry exists across the $\hat{x}\hat{z}$-plane when one state is propagated in reverse time. In this case, the state as defined $[x, y, z, \dot{x}, \dot{y}, \dot{z}]^T$ is propagated forward in time and alternatively, $[x, -y, z, -\dot{x}, \dot{y}, -\dot{z}]^T$ is propagated in reverse time to construct mirror image solutions, even though they are not one continuous solution. Symmetry in the CR3BP, as viewed in a rotating coordinate system, is a consequence of the formulation of the differential equations that govern the motion of P_3. The mirror imaged state is computed from the following transformation matrix,

$$
J(-t) = \begin{bmatrix} 1 & 0 & 0 & 0 & 0 & 0 \\ 0 & -1 & 0 & 0 & 0 & 0 \\ 0 & 0 & 1 & 0 & 0 & 0 \\ 0 & 0 & 0 & -1 & 0 & 0 \\ 0 & 0 & 0 & 0 & 1 & 0 \\ 0 & 0 & 0 & 0 & 0 & -1 \end{bmatrix} \tag{2.35}
$$

where J is the transformation matrix from a given state to the mirror image state from a propagation backwards in time. The transformation property produces a symmetric transfer design across the $\hat{x}\hat{z}$-plane.

Understanding symmetric solutions in the CR3BP reduces the required number of numerical computations. The transfers constructed from the states $[x, y, z, \dot{x}, \dot{y}, \dot{z}]^T$ and $[x, y, -z, \dot{x}, \dot{y}, -\dot{z}]^T$ are the same when projected onto the $\hat{x}\hat{y}$-plane, even though the out-of-plane component is mirrored. Symmetric properties in the CR3BP reduce the numerical computations necessary to explore a solution space. Within the spatial problem, understanding the symmetry across the $\hat{x}\hat{z}$-plane reduces the numerical integration by half. Additional advantages of symmetry arise throughout this investigation and offer insight into the transfer designs available.

2.3 Bicircular Restricted Four-Body Problem

The four-body problem models the motion of four bodies due to their mutual gravitational interactions. The bicircular restricted four-body problem (BCR4BP) is a simplified four-body model, expanding the formulation of the CR3BP with an additional body. The BCR4BP depicts the motion of a spacecraft governed by the gravitational forces in a planet-moon-star system. The BCR4BP of interest in this investigation describes the motion of a massless particle, P_3, influenced by the gravitational fields of three massive bodies, i.e., the Earth (P_1), Moon (P_2) and Sun (P_4).

2.3.1 Model Assumptions

Assumptions in the BCR4BP rely on the N-body problem and the properties of the multi-body system being investigated. The formulation of the BCR4BP is similar to that of the CR3BP, where P_1 and P_2 are assumed to follow circular orbits about their common barycenter B_1. The assumed circular orbits of P_1 and P_2 is a simplification to the motion of the Earth and Moon. Additionally, B_1 and P_4 are modeled in circular orbits about the full system barycenter B_2. The motion of B_1 and P_4 in the BCR4BP is an adaption of the true dynamics of the Sun and Earth-Moon system. In this formulation of the BCR4BP model, perturbations induced by P_4 do not influence the motion of P_1 and P_2 [22].

Periodic multi-body models enable repeating dynamical structures. For the BCR4BP model to be periodic, the relative orientation of P_1, P_2, and P_4 must be repeatable. Conditions where the model is periodic exist when the mean motion of the two systems are in resonance, or the inclination between the two orbital planes is equal to zero. In most natural systems, for example, the Earth-Moon-Sun system, neither case is actually true. To leverage the advantages of a periodic model, either of these two conditions enables trajectory design. To represent a system where the orbital planes are nearly coplanar, a simplification yields a periodic model. The coplanar BCR4BP incorporates the assumption that the inclination between the two orbital planes is assumed to be zero. In this investigation, the Earth, Moon, and Sun are restricted to one plane. The motion of the Earth-Moon-Sun system follows a path that resembles Figure 2.13. In Figure 2.13, the primary bodies move in the $\hat{X} - \hat{Y}$

plane. The dotted arcs in Figure 2.13 depict the circular motion of the primary bodies and B_1. As the P_1-P_2 system and the P_4-B_1 systems traverse circular orbits, the magnitude of the vectors $\vec{R}_{12}$ and $\vec{R}_{4B_1}$ remain constant throughout time. It is advantageous to describe the motion of P_3 in two different rotating coordinate frames, the P_1-P_2 rotating frame and the P_4-B_1 rotating frame. The derivation of the differential equations that govern the motion of P_3 relies on the selected rotating coordinate system. Therefore, two formulations of the BCR4BP are employed in this analysis. The angles $\tilde{\alpha}$ and $\underline{\alpha}$ orient the primary bodies relative to the inertial frame. Note that the resultant equations of motion, irregardless of the coordinate frame, describe the same dynamics.
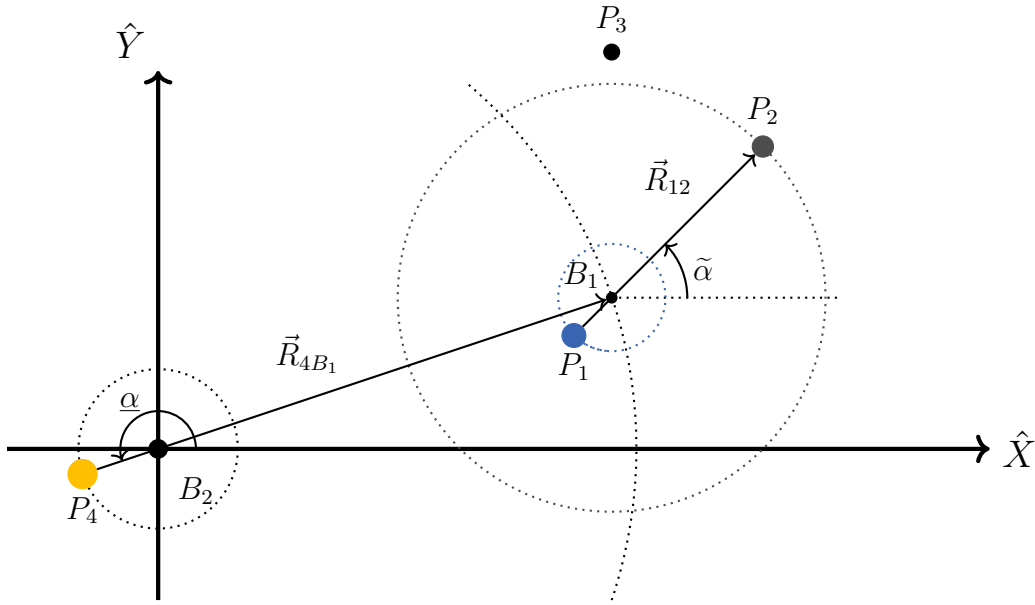
Figure 2.13. BCR4BP in an inertial reference frame with B_2 at the origin

2.3.2 Earth-Moon Rotating Coordinate Frame

The Earth-Moon rotating coordinate frame characterizes accessible dynamical structures in close proximity to the Earth-Moon system. Construction of this rotating coordinate frame relies on the definition of the P_1-P_2 system, where the Earth is P_1 and the Moon is P_2. To differentiate between the rotating frames, quantities with a tilde are related to the Earth-Moon system. Figure 2.14 depicts the P_1-P_2 rotating reference frame centered at the Earth Moon Barycenter (B_1), where the position vector of P_3 is written as $[\tilde{x}, \tilde{y}, \tilde{z}]$. The location

of the Earth and Moon remain fixed in this frame, while the Sun (P_4) traverses the dotted circle clockwise direction. The angle θ_S orients the position of the Sun in the rotating frame, and the scalar distance a_S is constant. For a Sun angle of zero degrees, the Moon is in conjunction with the Sun, where each primary body is aligned along the $\hat{\hat{x}}$-axis, which refers to a new Moon. For the Earth-Moon-Sun system, $\dot{\theta}_S$ is negative. Similarly for a Sun angle of π, the Moon is in opposition to the Sun, i.e., a full Moon.
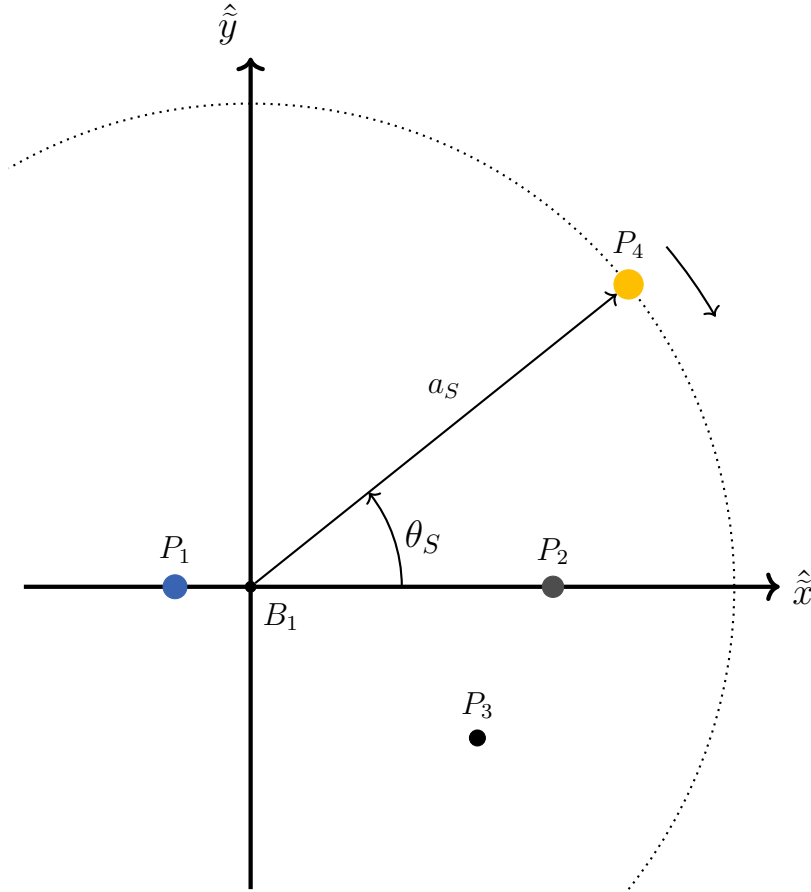
Figure 2.14. The P_1-P_2 rotating coordinate frame

Derivation of the Equations of Motion

A set of differential equations governs the motion of P_3 in the BCR4BP. The dynamical model delivers the equations of motion. Similar to the derivation of the differential equations in the CR3BP, the BCR4BP is based on the N-body problem through Equation (2.3) where

$N = 4$. As the motion of P_1, P_2, and P_4 is simplified, the N-body formulation is necessary to predict the motion of P_3, written as,

$$M_3{}^I\vec{R}''_{B_2 3} = -G\frac{M_3 M_1}{R_{13}^3}\vec{R}_{13} - G\frac{M_3 M_2}{R_{23}^3}\vec{R}_{23} - G\frac{M_3 M_4}{R_{43}^3}\vec{R}_{43}$$

$$^I\vec{R}''_{B_2 3} = -G\frac{M_1}{R_{13}^3}\vec{R}_{13} - G\frac{M_2}{R_{23}^3}\vec{R}_{23} - G\frac{M_4}{R_{43}^3}\vec{R}_{43} \tag{2.36}$$

Recall that the value $^I\vec{R}''_{B_2 3}$ refers to the inertial acceleration experienced by P_3 ($\frac{^I d^2\vec{R}_3}{d\tau^2}$). The position vector $^I\vec{R}_3$ originates from the inertially fixed point B_2; the vectors $\vec{R}_{ij}$ are formulated in Equation (2.2) as the vector from body i to j. Equation (2.36) is the inertial equation of motion for P_3 in vector form in the BCR4BP. In the inertial frame, all four bodies move throughout time. The position of the Earth, Moon, Sun, and Earth-Moon barycenter (B_1) relative to the total system barycenter (B_2) is,

$$\vec{R}_{B_2 1} = \vec{R}_{B_2 B_1} - R_{B_1 1}(\cos{(\tilde{\alpha}'\tau)}\hat{X} + \sin{(\tilde{\alpha}'\tau)}\hat{Y})$$

$$\vec{R}_{B_2 2} = \vec{R}_{B_2 B_1} + R_{B_1 2}(\cos{(\tilde{\alpha}'\tau)}\hat{X} + \sin{(\tilde{\alpha}'\tau)}\hat{Y})$$

$$\vec{R}_{B_2 B_1} = -R_{B_2 B_1}(\cos{(\underline{\alpha}'\tau)}\hat{X} + \sin{(\underline{\alpha}'\tau)}\hat{Y}) \tag{2.37}$$

$$\vec{R}_{B_2 4} = R_{B_2 4}(\cos{(\underline{\alpha}'\tau)}\hat{X} + \sin{(\underline{\alpha}'\tau)}\hat{Y})$$

where $\tilde{\alpha}$ is the angle measured counterclockwise from $\hat{X}$ to $\vec{R}_{B_1 2}$, $\underline{\alpha}$ is the angle measured counterclockwise from $\hat{X}$ to $\vec{R}_{B_2 4}$, and τ is dimensional time. A visual representation of the inertial angles ($\tilde{\alpha}$ and $\underline{\alpha}$) are illustrated in Figure 2.13. For simplicity, assume that the initial orientation of the system is aligned such that $\tilde{\alpha}_0 = \underline{\alpha}_0 = 0$. The mean motion of the P_1-P_2 and P_4-B_1 systems in the inertial frame are $\tilde{\alpha}'$ and $\underline{\alpha}'$, respectively. The location of the primary bodies is a function of the initial orientation and the mean motion of each system. From Equation (2.37), the location of P_1 and P_2 rely on the position of B_1. Due to the bicircular motion of the primary bodies, the scalar distances $R_{B_1 1}$, $R_{B_1 2}$, R_{B_1} and R_4 remain constant through time.

The BCR4BP is nondimensionalized to alleviate numerical errors. The characteristic quantities for the Earth-Moon system are,

$$\tilde{l}^\star := |\vec{R}_{12}| \approx 384748 \text{ km} \tag{2.38}$$

$$\widetilde{m^\star} := M_1 + M_2 \approx 6.0460\text{e}24 \text{ kg} \tag{2.39}$$

$$\widetilde{\tau^\star} := \sqrt{\frac{\tilde{l}^{\star 3}}{G\widetilde{m^\star}}} \approx 375700 \text{ s} \tag{2.40}$$

where $\tilde{l}^\star$ is the distance from the Earth to the Moon, $\widetilde{m^\star}$ is the mass of the Earth-Moon system, and $\widetilde{\tau^\star}$ is the characteristic time of the Earth-Moon system. Consistent with the characteristic quantities for the CR3BP as defined in Equations (2.6), (2.7), and (2.8), the quantities $\tilde{l}^\star$, $\widetilde{m^\star}$ and $\widetilde{\tau^\star}$ are re-evaluated in the BCR4BP. Utilizing the characteristic quantities, the nondimensional forms of the position vectors, mass, and time are constructed as follows

$$\tilde{\vec{r}} = \frac{\vec{R}_3}{\tilde{l}^\star}$$

$$\tilde{\vec{r}}_{13} = \frac{\vec{R}_{13}}{\tilde{l}^\star}$$

$$\tilde{\vec{r}}_{23} = \frac{\vec{R}_{23}}{\tilde{l}^\star}$$

$$\tilde{\vec{r}}_{43} = \frac{\vec{R}_{43}}{\tilde{l}^\star}$$

$$\tilde{\mu} = \frac{M_2}{\widetilde{m^\star}} = 1 - \frac{M_1}{\widetilde{m^\star}}$$

$$\tilde{t} = \frac{\tau}{\widetilde{\tau^\star}}$$

The nondimensional position vectors $\tilde{\vec{r}}$, $\tilde{\vec{r}}_{13}$, $\tilde{\vec{r}}_{23}$, and $\tilde{\vec{r}}_{43}$ describe the position of P_3 from B_1, the Earth, the Moon, and the Sun, respectively. The constant quantity $\tilde{\mu}$ is the mass parameter of the Earth-Moon system, and $\tilde{t}$ is the nondimensional time. Given the mass

parameter ($\widetilde{\mu}$) and the characteristic length ($\widetilde{l}^\star$) for the Earth-Moon system, characteristics of the Sun are described as,

$$\widetilde{m}_S = \frac{M_S}{\widetilde{\mu}} \tag{2.41}$$

$$a_S = \frac{\vec{R}_{4B_1}}{\widetilde{l}^\star} \tag{2.42}$$

where $\widetilde{m}_S$ is the nondimensional mass of the Sun, and a_S represents the nondimensionalized, fixed scalar distance from the Sun to the Earth-Moon barycenter B_1. The quantity a_S is displayed in Figure 2.14. The nondimensional parameters are introduced into the inertial equations of motion from Equation (2.36),

$$\frac{\widetilde{\tau}^{\star 2}}{\widetilde{l}^\star}{}^I\vec{R}''_{B_2 3} = \left[-G\frac{M_1}{R_{13}^3}\vec{R}_{13} - G\frac{M_2}{R_{23}^3}\vec{R}_{23} - G\frac{M_4}{R_{43}^3}\vec{R}_{43} \right]\frac{\widetilde{\tau}^{\star 2}}{\widetilde{l}^\star}$$

$${}^I\ddot{\vec{r}}_{B_2 3} = -G\left[\frac{M_1}{R_{13}^3}\vec{R}_{13} + \frac{M_2}{R_{23}^3}\vec{R}_{23} + \frac{M_4}{R_{43}^3}\vec{R}_{43} \right]\frac{\widetilde{l}^{\star 3}}{G\widetilde{m^\star l^\star}}$$

$${}^I\ddot{\widetilde{\vec{r}}}_{B_2 3} = -\frac{M_1}{\widetilde{m^\star \widetilde{r}_{13}^3}}\widetilde{\vec{r}}_{13} - \frac{M_2}{\widetilde{m^\star \widetilde{r}_{23}^3}}\widetilde{\vec{r}}_{23} - \frac{M_4}{\widetilde{m^\star \widetilde{r}_{43}^3}}\widetilde{\vec{r}}_{43}$$

$${}^I\ddot{\widetilde{\vec{r}}}_{B_2 3} = -\frac{1-\widetilde{\mu}}{\widetilde{r}_{13}^3}\widetilde{\vec{r}}_{13} - \frac{\widetilde{\mu}}{\widetilde{r}_{23}^3}\widetilde{\vec{r}}_{23} - \frac{\widetilde{m}_S}{\widetilde{r}_{43}^3}\widetilde{\vec{r}}_{43} \tag{2.43}$$

where $\widetilde{\vec{r}}_{ij}$ is the position vector from body i to j nondimensionalized to the P_1-P_2 system, and ${}^I\ddot{\widetilde{\vec{r}}}_{B_2 3}$ is the nondimensional acceleration for P_3 with respect to the system barycenter B_2. For simplicity, vectors from B_1 to i will be denoted as $\widetilde{\vec{r}}_i$. Distances from the Earth and Moon to B_1 are constant as displayed in Equation (2.17). The nondimensional distances from B_1 to B_2, and from B_2 and P_4 are,

$$\widetilde{r}_{B_2} = a_S\frac{\widetilde{m}_S}{\widetilde{m}_S + 1} \tag{2.44}$$

$$\widetilde{r}_{B_2 4} = \frac{a_S}{\widetilde{m}_S + 1} \tag{2.45}$$

The mean motion of the Earth-Moon system $(\tilde{n}_{EM})$ equals one as the system is nondimensionalized relative to the Earth and Moon. The mean motion of the Sun-B_1 system nondimensionalized relative to the Earth-Moon system is,

$$\tilde{n}_{SB_1} = \sqrt{\frac{G(M_4 + \widetilde{m^\star})}{R_{4B_1}^3}}\sqrt{\frac{\tilde{l}^{\star^3}}{\widetilde{Gm^\star}}} = \sqrt{\frac{\widetilde{m}_S + 1}{a_S^3}} \tag{2.46}$$

where the quantity $(\tilde{n}_{SB_1})$ is the nondimensional mean motion of the Sun-B_1 system.

There are advantages and disadvantages to viewing the motion of P_3 in the inertial coordinate frame. An advantage to the inertial reference frame for the BCR4BP, similar to the CR3BP, is that the frame illustrates the movement of the entire system as viewed in Figure 2.13. A disadvantage to the inertial frame is the challenge in classifying dynamical structures relative to three moving bodies. To aid in the characterization of the motion of P_3 in the vicinity of the Earth and Moon, the equations of motion are derived relative to the Earth-Moon rotating coordinate frame.

To construct the equations of motion in a rotating reference frame, the origin is shifted to the Earth-Moon barycenter B_1. The total system barycenter, B_2, is the only inertially fixed location. Thus, the motion about B_1 includes rotational components due to the formulation of the reference frame. The position vector $\widetilde{\vec{r}}_{B_2 3}$ is also written as,

$$\widetilde{\vec{r}}_{B_2 3} = \widetilde{\vec{r}}_3 - \widetilde{\vec{r}}_{B_2} \tag{2.47}$$

The nondimensional vector $\widetilde{\vec{r}}_{B_2}$ is constructed from the dimensional vector $\vec{R}_{B_2 B_1}$ from Equation (2.37), and the scalar distance $\tilde{r}_{B2}$ from Equation (2.44),

$$\widetilde{\vec{r}}_{B_2} = \tilde{r}_{B_2}(\cos{(\tilde{n}_{SB_1}\tilde{t})}\hat{X} + \sin{(\tilde{n}_{SB_1}\tilde{t})}\hat{Y})$$
$$\widetilde{\vec{r}}_{B_2} = \frac{a_S\widetilde{m}_S}{\widetilde{m}_S + 1}(\cos{(\tilde{n}_{SB_1}\tilde{t})}\hat{X} + \sin{(\tilde{n}_{SB_1}\tilde{t})}\hat{Y}) \tag{2.48}$$

To determine the accelaration of P_3 with respect to B_1 ($^I\ddot{\vec{\tilde{r}}}_3$), the second derivative of Equation (2.47) is determined to be,

$$^I\ddot{\vec{\tilde{r}}}_{B_23} = {}^I\ddot{\vec{\tilde{r}}}_3 - {}^I\ddot{\vec{\tilde{r}}}_{B2} \tag{2.49}$$

The dimensional quantity for $^I\ddot{\vec{\tilde{r}}}_{B_23}$ is given from Equation (2.36), i.e, $^I\vec{R}''_{B_23}$. The term $^I\ddot{\vec{\tilde{r}}}_{B2}$ is the second time derivative of the vector from B_1 to B_2. An expression for $^I\ddot{\vec{\tilde{r}}}_{B2}$ is evaluated as,

$$^I\ddot{\vec{\tilde{r}}}_{B2} = -\tilde{n}_{SB_1}^2 \vec{\tilde{r}}_{B2}$$

$$^I\ddot{\vec{\tilde{r}}}_{B2} = -\frac{\tilde{n}_{SB_1}^2 \widetilde{m}_S}{\widetilde{m}_S + 1}(\cos{(\tilde{n}_{SB_1}\tilde{t})}\hat{X} + \sin{(\tilde{n}_{SB_1}a_S\tilde{t})}\hat{Y})$$

$$^I\ddot{\vec{\tilde{r}}}_{B2} = -\frac{(\widetilde{m}_S + 1)a_S\widetilde{m}_S}{(\widetilde{m}_S + 1)a_S^3}(\cos{(\tilde{n}_{SB_1}\tilde{t})}\hat{X} + \sin{(\tilde{n}_{SB_1}\tilde{t})}\hat{Y})$$

$$^I\ddot{\vec{\tilde{r}}}_{B2} = -\frac{\widetilde{m}_S}{a_S^2}(\cos{(\tilde{n}_{SB_1}\tilde{t})}\hat{X} + \sin{(\tilde{n}_{SB_1}\tilde{t})}\hat{Y}) \tag{2.50}$$

The trigonometric components of Equation (2.50) are equivalent to the unit vector directed from B_1 to the Sun (P_4), i.e., $\frac{\vec{\tilde{r}}_4}{a_S}$. Through the combination of Equations (2.36), (2.49), and (2.50), the inertial acceleration of P_3 with respect to the Earth-Moon B_1 is constructed as,

$$^I\ddot{\vec{\tilde{r}}}_3 = {}^I\ddot{\vec{\tilde{r}}}_{B_23} + {}^I\ddot{\vec{\tilde{r}}}_{B2}$$

$$^I\ddot{\vec{\tilde{r}}}_3 = -\frac{1-\tilde{\mu}}{\tilde{r}_{13}^3}\vec{\tilde{r}}_{13} - \frac{\tilde{\mu}}{\tilde{r}_{23}^3}\vec{\tilde{r}}_{23} - \frac{\widetilde{m}_S}{\tilde{r}_{43}^3}\vec{\tilde{r}}_{43} - \frac{\widetilde{m}_S}{a_S^2}\left(\frac{\vec{\tilde{r}}_4}{a_S}\right)$$

$$^I\ddot{\vec{\tilde{r}}}_3 = -\frac{1-\tilde{\mu}}{\tilde{r}_{13}^3}\vec{\tilde{r}}_{13} - \frac{\tilde{\mu}}{\tilde{r}_{23}^3}\vec{\tilde{r}}_{23} - \frac{\widetilde{m}_S}{\tilde{r}_{43}^3}\vec{\tilde{r}}_{43} - \frac{\widetilde{m}_S}{a_S^3}\vec{\tilde{r}}_4 \tag{2.51}$$

A rotating coordinate system about the Earth-Moon barycenter (B_1) simplifies the governing equations of motion. The Earth-Moon rotating coordinate frame is centered at the Earth-Moon barycenter B_1. The $\tilde{x}$-axis is directed toward the Moon. The $\tilde{z}$-axis is along the angular momentum vector of the Earth-Moon system, and the $\tilde{y}$-axis completes the orthonormal triad. The positions of Earth and Moon rely on the mass parameter of the system as $\vec{\tilde{r}}_1 = -\tilde{\mu}\,\hat{\tilde{x}}$ and $\vec{\tilde{r}}_2 = (1-\tilde{\mu})\,\hat{\tilde{x}}$, respectively. Figure 2.14 illustrates the Earth-Moon rotating

coordinate frame. The differential equations of motion for P_3 in the rotating frame are derived from Equation (2.19) and Equation (2.51). The angular momentum vector employed in Equation (2.51) is equivalent to the mean motion of the Earth-Moon system, i.e., $({}^I\vec{\omega}^R = n_{EM}\hat{\tilde{z}})$, that is equal to one. The scalar quantities of acceleration for P_3 as viewed in the Earth-Moon rotating coordinate frame and expressed in terms of rotating coordinates are,

$$
\begin{aligned}
\ddot{\tilde{x}} &= 2\dot{\tilde{y}} + \tilde{x} - \frac{(1-\tilde{\mu})(\tilde{x}+\tilde{\mu})}{\tilde{r}_{13}^3} - \frac{\tilde{\mu}(\tilde{x}-1+\tilde{\mu})}{\tilde{r}_{23}^3} - \frac{\widetilde{m}_S(\tilde{x} - a_S\cos(\theta_S))}{\tilde{r}_{43}^3} - \frac{\widetilde{m}_S}{a_S^2}\cos(\theta_S) \\
\ddot{\tilde{y}} &= -2\dot{\tilde{x}} + \tilde{y} - \frac{(1-\tilde{\mu})\tilde{y}}{\tilde{r}_{13}^3} - \frac{\tilde{\mu}\tilde{y}}{\tilde{r}_{23}^3} - \frac{\widetilde{m}_S(\tilde{y} - a_S\sin(\theta_S))}{\tilde{r}_{43}^3} - \frac{\widetilde{m}_S}{a_S^2}\sin(\theta_S) \\
\ddot{\tilde{z}} &= -\frac{(1-\tilde{\mu})\tilde{z}}{\tilde{r}_{13}^3} - \frac{\tilde{\mu}\tilde{z}}{\tilde{r}_{23}^3} - \frac{\widetilde{m}_S\tilde{z}}{\tilde{r}_{43}^3}
\end{aligned}
\tag{2.52}
$$

where θ_S is the angle measured counterclockwise from the $\hat{\tilde{x}}$-axis to $\vec{\tilde{r}}_4$, denoted the Sun angle. The Sun angle describes the relative orientation of the Sun in the Earth-Moon rotating coordinate frame, displayed in Figure 2.14. The angular velocity of the Sun $(\dot{\theta}_S)$ in the Earth-Moon rotating frame is constant, and equals the difference in the mean motion of the Sun-B_1 and Earth-Moon systems,

$$
\dot{\theta}_S = \tilde{n}_{SB_1} - \tilde{n}_{EM} = \tilde{n}_{SB_1} - 1
\tag{2.53}
$$

where the nondimensional mean motion of the Sun-B_1 system is expressed in Equation (2.46). The angular velocity of the Sun in the Earth-Moon rotating frame is negative; thus, the Sun traverses clockwise about B_1. The equations of motion for P_3 are rewritten with a pseudo-potential function $(\widetilde{\Upsilon})$,

$$
\widetilde{\Upsilon} = \frac{1}{2}(\tilde{x}^2 + \tilde{y}^2) + \frac{1-\tilde{\mu}}{\tilde{r}_{13}} + \frac{\tilde{\mu}}{\tilde{r}_{23}} + \frac{\widetilde{m}_S}{\tilde{r}_{43}} - \frac{\widetilde{m}_S}{a_S^2}(\tilde{x}\cos(\theta_S) + \tilde{y}\sin(\theta_S))
\tag{2.54}
$$

$$
\begin{aligned}
\ddot{\tilde{x}} &= 2\dot{\tilde{y}} + \widetilde{\Upsilon}_{\tilde{x}} \\
\ddot{\tilde{y}} &= -2\dot{\tilde{x}} + \widetilde{\Upsilon}_{\tilde{y}} \\
\ddot{\tilde{z}} &= \widetilde{\Upsilon}_{\tilde{z}}
\end{aligned}
\tag{2.55}
$$

55

The pseudo-potential function in Equation (2.54) relies on the relative orientation of the Sun in the Earth-Moon rotating frame, i.e., the Sun angle, θ_S. As the Sun angle is a function of time, the BCR4BP is a time-dependent model. However, as the Sun remains in the Earth-Moon orbital plane, the model is periodic in the Earth-Moon rotating frame.

Hamiltonian

The Hamiltonian values serve as 'energy-like' quantities in the BCR4BP. As in the CR3BP, the Jacobi Constant provides advantages for analyzing and characterizing structures that evolve within a dynamical model. Similar to the CR3BP, an 'energy-like' quantity exists in the BCR4BP [23], defined as the Hamiltonian, with two useful formulations in either rotating frame, although it does not remain constant. The two quantities in the BCR4BP are denoted the Earth-Moon Hamiltonian (H_{EM}) and the Sun-B_1 Hamiltonian (H_{SB_1}). Unlike the CR3BP, the Hamiltonian quantities are not integrals of the motion in the BCR4BP, and vary as P_3 traverses through the system. As the time-varying Hamiltonian adds complexity to analysis of dynamical structures, it supplies insight into the perturbative forces applied in the two formulations of the BCR4BP. The Earth-Moon Hamiltonian describes the energy of P_3 as it traverses through the Earth-Moon rotating coordinate frame. The Earth-Moon Hamiltonian is expressed as,

$$H_{EM} = -(\dot{\tilde{x}}^2 + \dot{\tilde{y}}^2 + \dot{\tilde{z}}^2) + 2\widetilde{\Upsilon} \tag{2.56}$$

where $(\dot{\tilde{x}}, \dot{\tilde{y}}, \dot{\tilde{z}})$ are the velocity components of P_3 in the Earth-Moon rotating frame, and $\widetilde{\Upsilon}$ is the pseudo-potential function expressed in Equation (2.55). The expression for the Earth-Moon Hamiltonian is similar to that for the Jacobi Constant. Comparing Equation (2.56) to Equation (2.24), the sole difference is the pseudo-potential function. The Earth-Moon

CR3BP pseudo-potential function, and the BCR4BP derived in the Earth-Moon rotating coordinate frame are comparable as follows,

$$\Omega = \frac{1}{2}(x^2 + y^2) + \frac{1 - \mu}{r_{13}} + \frac{\mu}{r_{23}}$$

$$\widetilde{\Upsilon} = \frac{1}{2}(\tilde{x}^2 + \tilde{y}^2) + \frac{1 - \tilde{\mu}}{\tilde{r}_{13}} + \frac{\tilde{\mu}}{\tilde{r}_{23}} + \frac{\widetilde{m}_S}{\tilde{r}_{43}} - \frac{\widetilde{m}_S}{a_S^2}(\tilde{x}\cos(\theta_S) + \tilde{y}\sin(\theta_S))$$

By removing the components of $\widetilde{\Upsilon}$ that rely on the gravitational influence of the Sun ($\widetilde{m}_S$ = 0), the two equations are equivalent. Thus, by removing the Sun in the Earth, Moon, Sun BCR4BP, the dynamical model is reduced to the Earth-Moon CR3BP. The pseudo-potential function $\widetilde{\Upsilon}$ varies with the Sun angle, thus, the Earth-Moon Hamiltonian is time-dependent along a transfer. In close proximity to the Earth and Moon, the Hamiltonian remains fairly constant, with minor variations due to solar perturbations. As the spacecraft evolves further from the Earth-Moon system, the Hamiltonian experiences large variations as the Sun's perturbative force increases. A sample transfer in the Earth-Moon BCR4BP is displayed in Figure 2.15. The transfer originates with a Sun angle equal to zero ($\theta_S = 0$), and is propagated for twenty days following the direction of the arrows. The Earth-Moon Hamiltonian is plotted over time in Figure 2.15 for the sample trajectory in Figure 2.15. The maximum deviation in the Earth-Moon Hamiltonian value from the initial starting point occurs at 9.24 days into flight, and the difference is $\Delta H_{EM} = 0.01868$ nondimensional units. The figure illustrates some oscillatory-like behavior, that is generally non-intuitive.
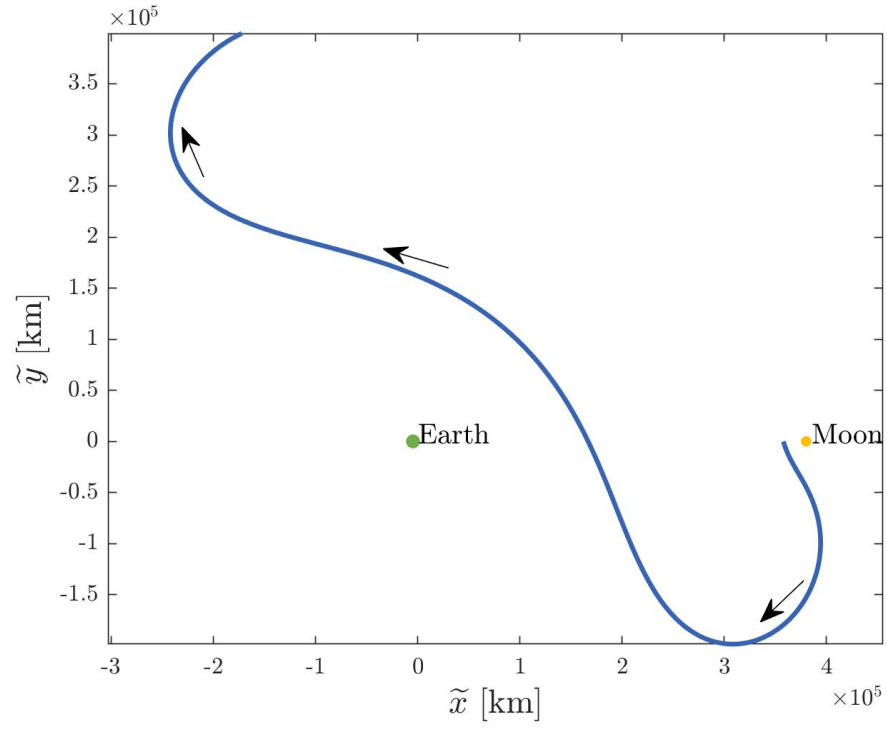
Figure 2.15. Sample trajectory in the BCR4BP, Earth-Moon Rotating Coordinate Frame
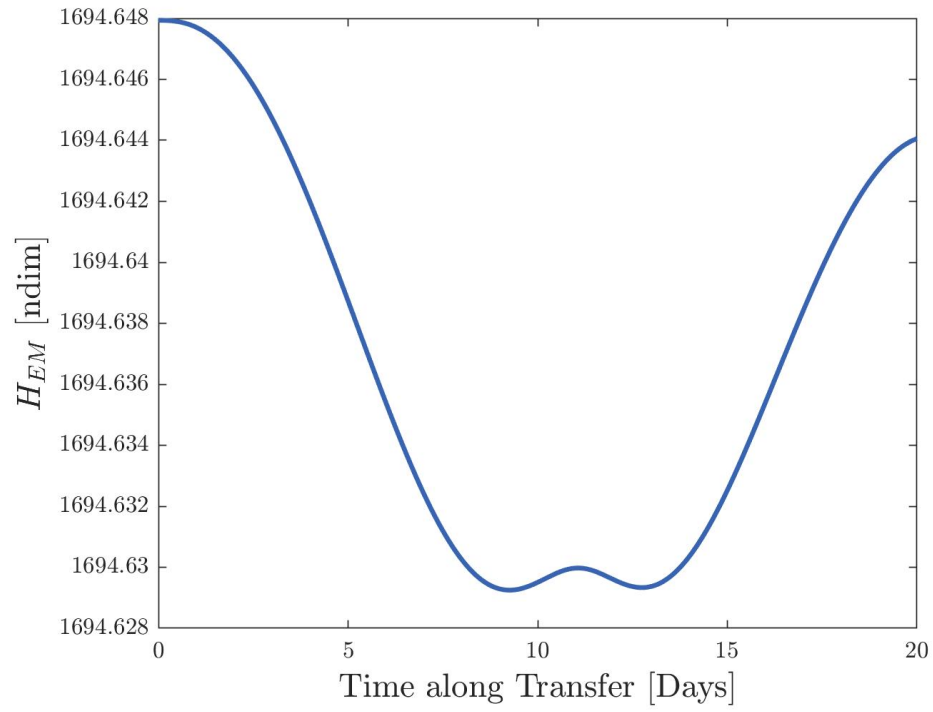
Figure 2.16. The Earth-Moon Hamiltonian along the sample transfer plotted in Figure 2.15

Instantaneous Equilibrium Solutions

Instantaneous equilibrium solutions offer insight into dynamical structures in the BCR4BP. Equilibrium solutions are solutions to a set of differential equations such that the derivations are zero, i.e. an instantaneous location in equilibrium. As the BCR4BP is a time-dependent model in both the Earth-Moon or Sun-B_1 formulation, the models rely on an additional variable to define a state, either the Sun angle or Earth-Moon angle. The corresponding angular rates $\dot{\theta}_S$ and $\dot{\theta}_{EM}$ are included in the set of governing equations for the BCR4BP. Recall, for an equilibrium point to exist, the entire set of differential equations must equal zero. By definition, $\dot{\theta}_S$ and $\dot{\theta}_{EM}$ are constant and never zero. Therefore, there are no equilibrium solutions in the BCR4BP. However, sets of instantaneous equilibrium solutions are relevant. An instantaneous equilibrium solution occurs when the velocity and acceleration of P_3 as viewed by an observer in the appropriate frame equals zero for a fixed orientation of the Earth, Moon, and Sun. By varying the orientation of the primary bodies, sets of instantaneous equilibrium solutions are constructed. If P_3 is placed at an instantaneous equilibrium solution and the model is propagated forward in time, at the initial instant P_3 remains stationary and begins to move as the primary bodies shift into new orientations. Instantaneous equilibrium solutions are constructed in both the Earth-Moon and Sun-B_1 coordinate frames.

Construction of the instantaneous equilibrium solutions relies on an initial condition from the CR3BP. Recall that the location of the Lagrange points in the CR3BP are determined for the Earth-Moon system, as represented in Table 2.1. As in the Earth-Moon formulation of the BCR4BP, the dynamics is similar in nature to the Earth-Moon CR3BP, the Lagrange points act as candidate locations for the sets of instantaneous equilibrium solutions. To determine the positions of the instantaneous equilibrium solutions, the Earth-Moon BCR4BP equations of motion, as in Equation (2.52), are combined with the definition of an equilibrium solution, i.e. $\dot{\tilde{x}} = \dot{\tilde{y}} = \dot{\tilde{z}} = \ddot{\tilde{x}} = \ddot{\tilde{y}} = \ddot{\tilde{z}} = 0$. As the equations of motion include the Sun angle dependent terms, an analytical expansion is nontrivial; thus, the construction of the instantaneous equilibrium points relies on numerical methods. A differential corrections strategy is employed to determine the locations of the sets of instantaneous equilibrium

59

points. A set of instantaneous equilibrium solutions serve as analogs to the Lagrange points L_i and are denoted as $\widetilde{E}_i$. An instantaneous equilibrium solution at a specific Sun angle θ_S is labelled $\widetilde{E}_i(\theta_S)$. Fives sets of instantaneous equilibrium solutions are plotted in Figure 2.17, i.e, $\widetilde{E}_1$-$\widetilde{E}_5$, relative to their corresponding Lagrange point, for all possible Sun angles $(0 \leq \theta_S < 2\pi)$. Note that $\widetilde{E}_1$ and $\widetilde{E}_2$ are indistinguishable from L_1 and L_2 at this scale, $\widetilde{E}_3$ is the magenta curve, $\widetilde{E}_4$ is red, and $\widetilde{E}_5$ is plotted in blue. The coplanar assumption is active for this formulation of the BCR4BP, all instantaneous equilibrium solutions remain in the $\widetilde{x}\widetilde{y}$-plane.
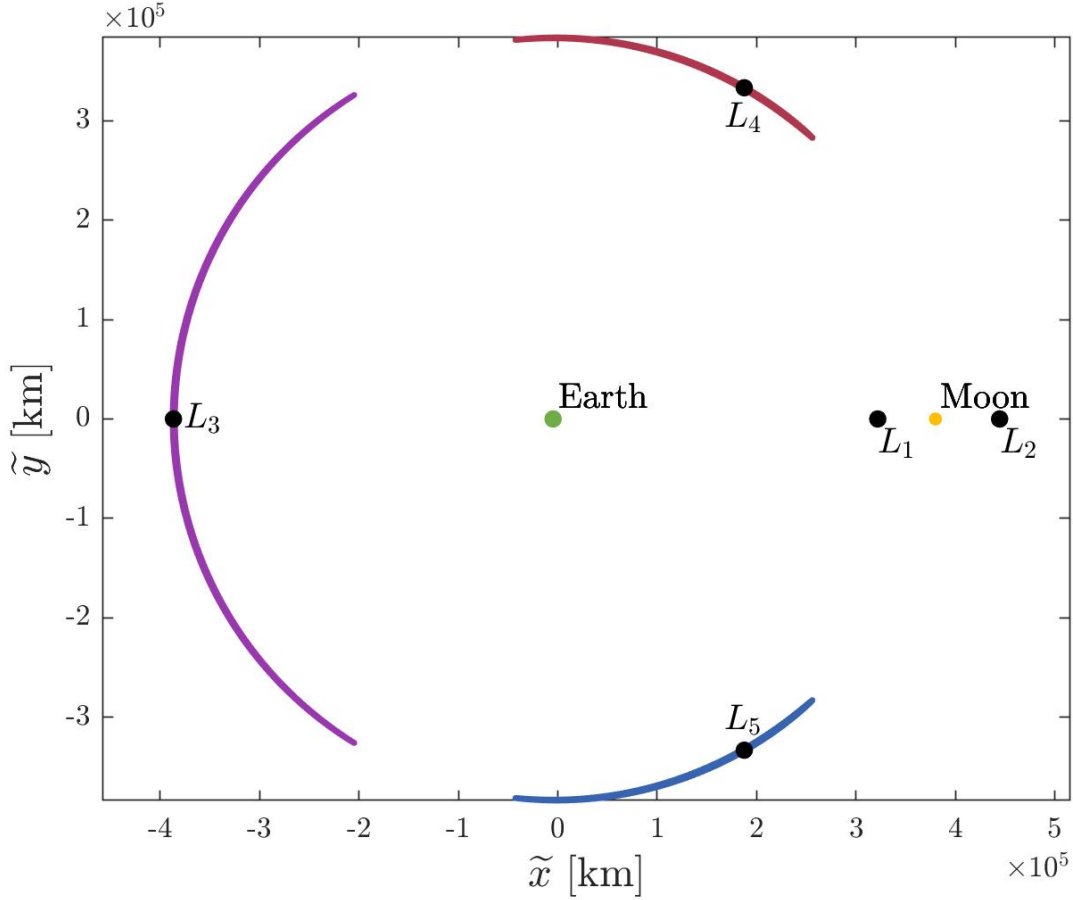
Figure 2.17. Five sets of instantaneous equilibrium solutions in the Earth-Moon rotating coordinate frame

The sets $\widetilde{E}_1$ and $\widetilde{E}_2$ are visualize in Figures 2.18 and 2.19 and differentiate the BCR4BP solutions from the Lagrange points. Note that the curves displayed in Figures 2.17 to 2.19

do not represents paths that P_3 could traverse, rather the curves represent sets of discrete instantaneous equilibrium solutions.
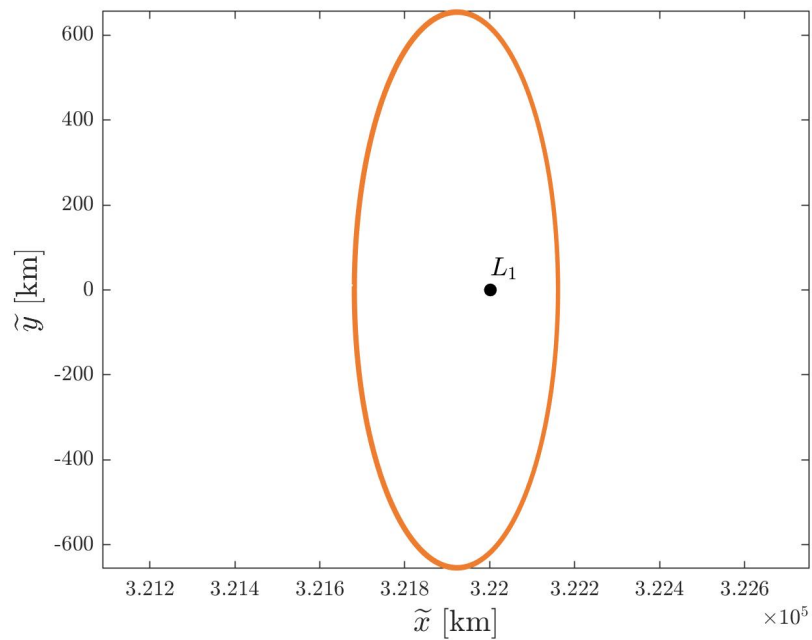
Figure 2.18. $\widetilde{E}_1$ in the Earth-Moon rotating coordinate frame
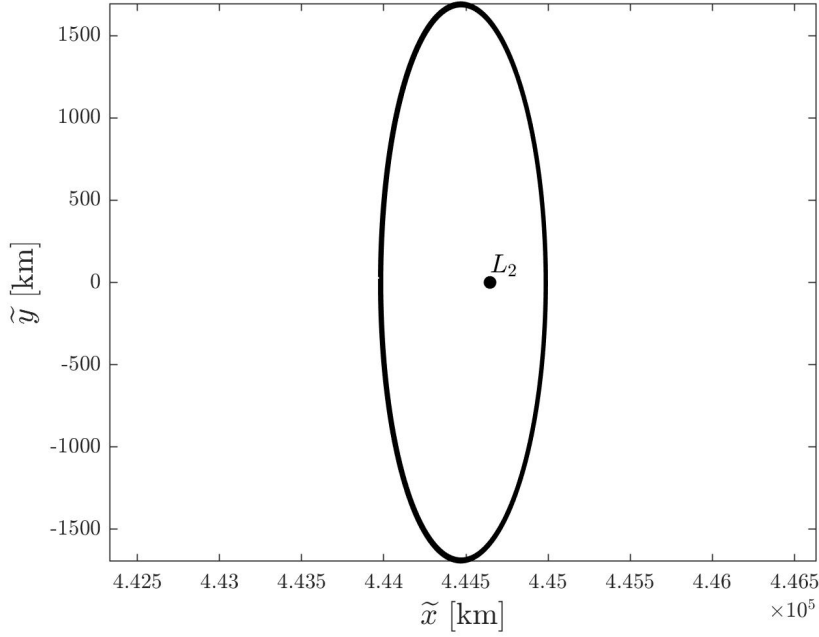
Figure 2.19. $\widetilde{E}_2$ in the Earth-Moon rotating coordinate frame

The instantaneous equilibrium solutions associated with the third Lagrange point (L_3) does not offer a one to one correspondence with the Sun Angle. As viewed in position space, Figure 2.17, the position of $\widetilde{E}_3$ is impacted by solar perturbations as compared to L_3, shifting away from the $\widetilde{x}$-axis. Observe the $\widetilde{x}$ component of the set $\widetilde{E}_3$ as a function of the respective Sun angle in Figure 2.20. Noted in Figure 2.20, for a subset of Sun angles, multiple instantaneous equilibrium solutions within the $\widetilde{E}_3$ set exist. For example, at a Sun angle of 100 degrees, three instantaneous equilibrium solutions are available. Thus, depending on the orientation of the Sun in the Earth-Moon rotating coordinate frame, when combined with the other instantaneous sets ($\widetilde{E}_1$-$\widetilde{E}_5$), five to seven instantaneous equilibrium solutions exist at an instant in time.

The Earth-Moon Hamiltonian describes the energy characteristics of the instantaneous equilibrium solutions. As the Jacobi constant reflects the energy values of the Lagrange points in the CR3BP, the Earth-Moon Hamiltonian indicates the energy level for each instantaneous equilibrium solution. The solutions, by definition, possess zero velocity; thus, the Earth-Moon Hamiltonian value is a function of the position of each point. The Earth-
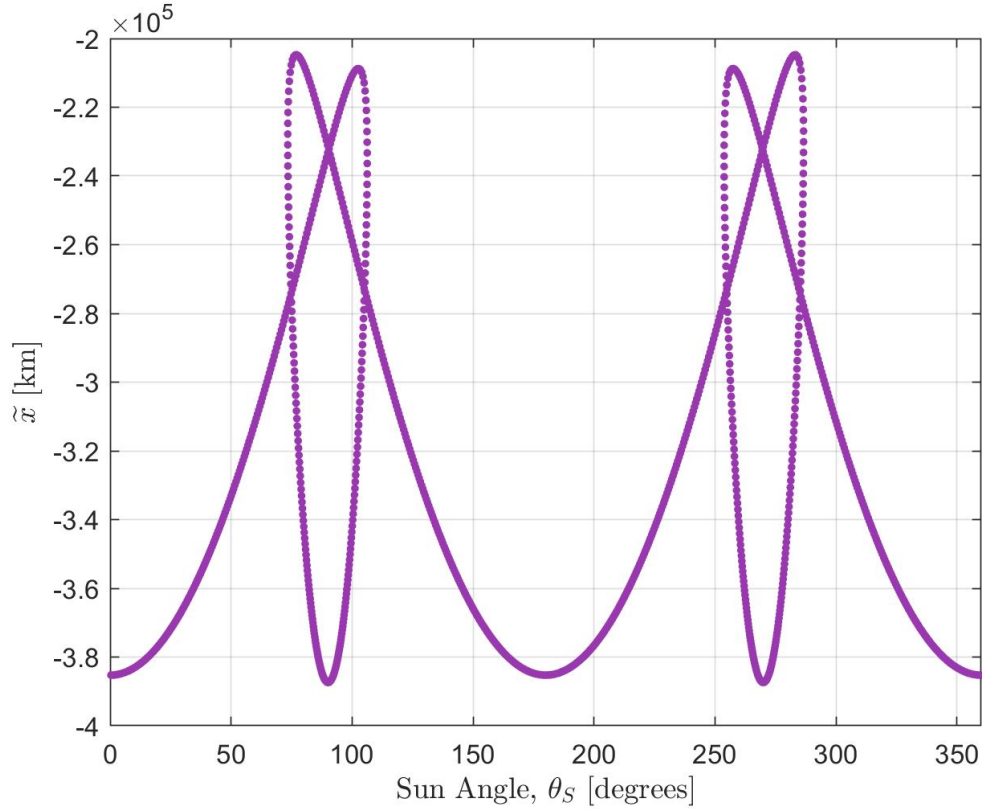
Figure 2.20. Position of $\widetilde{E}_3$ in $\widetilde{x}$ across all Sun angles (θ_S)

Moon Hamiltonian for all five sets of instantaneous equilibrium solutions where $0 \leq \theta_S < 360$ degrees is plotted in Figure 2.21. Similar to the Jacobi constant, the sets of instantaneous equilibrium solutions increase in energy value from $\widetilde{E}_1$ to $\widetilde{E}_5$. As the sets of solutions vary in position space, the instantaneous value of the corresponding Earth-Moon Hamiltonian varies as a function of Sun angle. For some values of the Earth-Moon Hamiltonian, for example $H_{EM} = 1694.972$, both $\widetilde{E}_1$ and $\widetilde{E}_2$ include solutions. Thus, both the energy level for P_3 and the relative orientation of the primary bodies are relevant for to consider when assessing available transfer designs. Instantaneous equilibrium solutions and their variation in terms of the Earth-Moon Hamiltonian values across each set offers insight into the available dynamical structures within the BCR4BP.
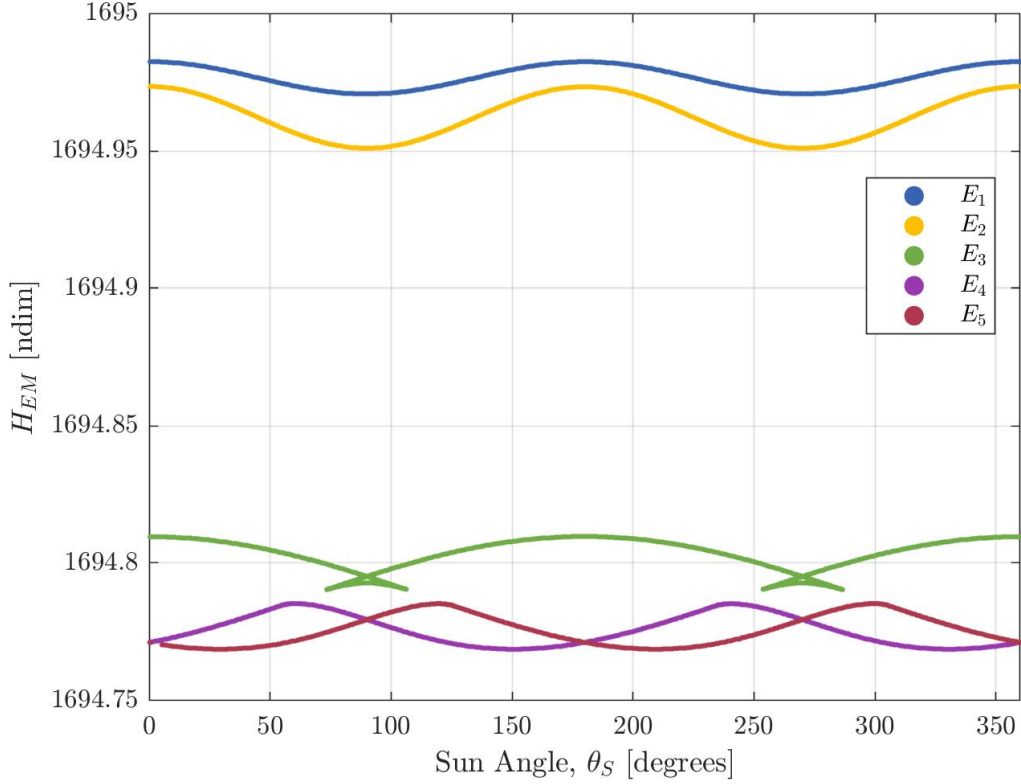
Figure 2.21. Earth-Moon nondimensional Hamiltonian values across each set of instantaneous equilibrium solutions as a function of Sun angle(θ_S)

Instantaneous Zero Velocity Surfaces

Zero velocity surfaces in the BCR4BP rely on the Hamiltonian properties across the path for P_3 and the relative orientation of the primary bodies. For the Earth-Moon formulation of the BCR4BP, the Earth-Moon Hamiltonian expressed in Equation (2.56), relies on the velocity of the body and the pseudo-potential function ($\widetilde{\Upsilon}$). Given an instantanoues value of H_{EM}, Equation (2.24) is rearranged to the following,

$$\widetilde{V}^2 = -H_{EM} + 2\widetilde{\Upsilon} \tag{2.57}$$

where $\widetilde{V}$ is the velocity magnitude for P_3 in the Earth-Moon BCR4BP. Similar to the formulation for the zero velocity surfaces in the CR3BP, the velocity of P_3 must be a real number.

Therefore, for a given Earth-Moon Hamiltonian value and Sun angle, some sets of positions are inaccessible to the spacecraft. In the CR3BP, the zero velocity surfaces offer insight into the accessible regions for a given energy value. A challenge associated with the BCR4BP is that Hamiltonian values vary along a trajectory and the pseudo-potential functions are explicit functions of time. Thus, the zero velocity surfaces evolve as P_3 traverses a ballistic path. For example, Figures 2.22 through 2.24 reflect the same value of Earth-Moon Hamiltonian, but for differing Sun angles. Access to the lunar vicinity relies on both the orientation of the Sun and the energy of P_3 relative to the Earth-Moon frame. The zero velocity curves allow P_3 to transit though the region near the Moon in Figure 2.22, where both the portals near $\widetilde{E}_1$ and $\widetilde{E}_2$ are open. Whereas in Figure 2.24, both portals are closed for the same energy value. The accessible regions in the BCR4BP are bounded by the instantaneous equilibrium solutions but remain functions of time via Sun angle. The energy and orientation of the primaries associated with the instantaneous equilibrium solutions enable low energy transfers with access to regions of space throughout the Earth-Moon system.
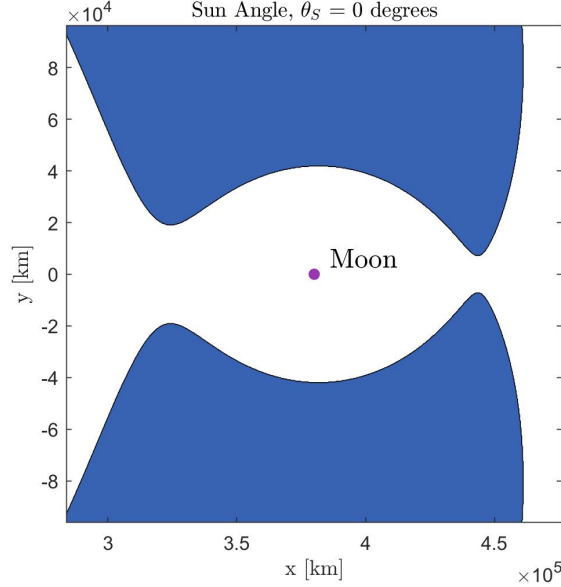
Figure 2.22. Zero velocity curves in the BCR4BP with an Earth-Moon Hamiltonian of $H_{EM} = 1694.9726$ and a Sun angle of $\theta_S = 0$ degrees
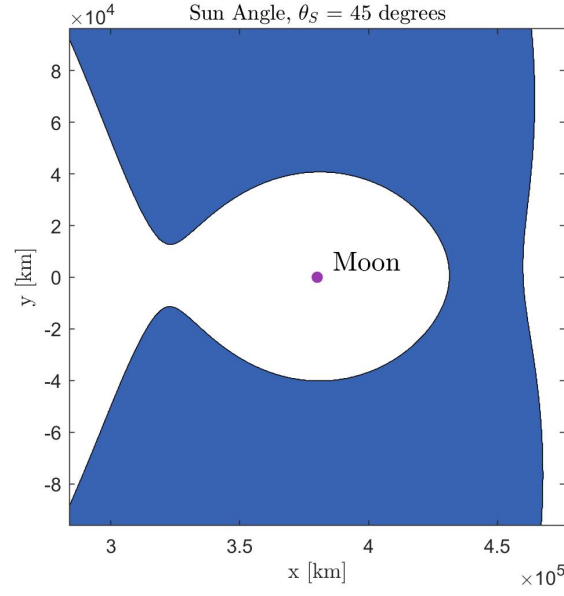
Figure 2.23. Zero velocity curves in the BCR4BP with an Earth-Moon Hamiltonian of $H_{EM} = 1694.9726$ and a Sun angle of $\theta_S = 45$ degrees
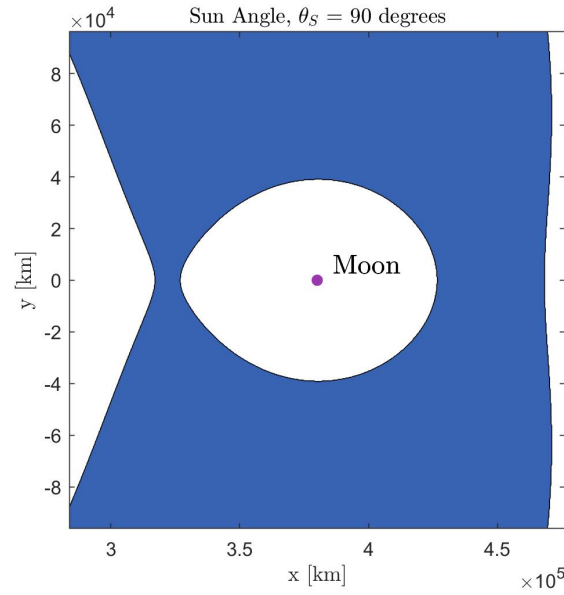
Figure 2.24. Zero velocity curves in the BCR4BP with an Earth-Moon Hamiltonian of $H_{EM} = 1694.9726$ and a Sun angle of $\theta_S = 90$ degrees

2.3.3 Sun-B_1 Rotating Coordinate Frame

Characterizes the motion of P_3 relative to a fixed orientation of the Sun is enabled by the use of the Sun-B_1 rotating coordinate frame. Construction of the rotating coordinate frame relies on the definition of the P_4-B_1 system, where the Sun is P_4 and the Earth-Moon barycenter is B_1 for this application. To specify the rotating coordinate frame, underlined quantities are related to the Sun-B_1 rotating frame. The motion of the primary bodies in the Sun-B_1 rotating frame is illustrated in Figure 2.25. The Earth and Moon, i.e., P_1 and P_2, traverse the concentric circles about B_1 counterclockwise. The angle θ_{EM} orients the Earth-Moon system in the Sun-B_1 frame.
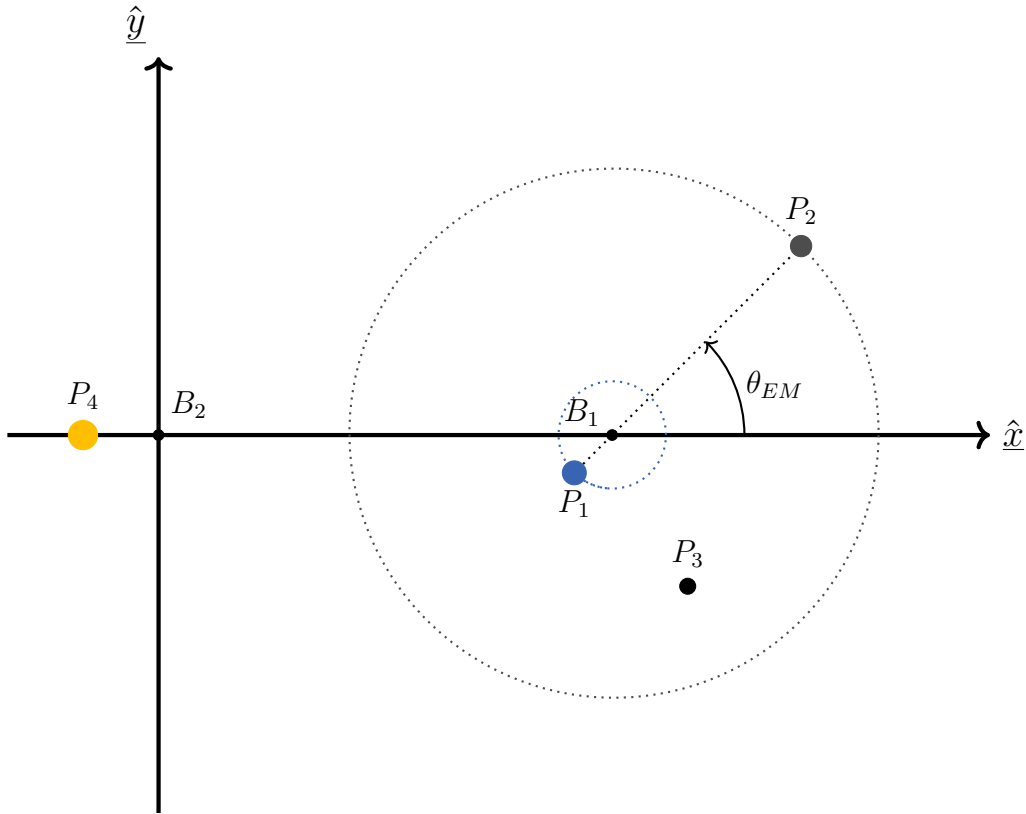
Figure 2.25. The P_4-B_1 rotating coordinate frame

Derivation of the Equations of Motion

The equations of motion in the Sun-B_1 system represent a model for the motion of P_3 relative to the orientation of the Sun. The Sun-B_1 rotating coordinate frame relies on the P_4-B_1 system, where the Sun is P_4 and the Earth-Moon barycenter is B_1. The equations of motion are nondimensionalized in the BCR4BP to generalize the results and to mitigate numerical errors. The characteristic quantities in the Sun-B_1 system are defined as

$$\underline{l^\star} := |\vec{R}_{4B_1}| \approx 1.4960\text{e}8 \text{ km} \tag{2.58}$$

$$\underline{m^\star} := M_1 + M_2 + M_4 \approx 1.9886\text{e}30 \text{ kg} \tag{2.59}$$

$$\underline{\tau^\star} := \sqrt{\frac{l^{\star 3}}{G\underline{m^\star}}} \approx 5.0226\text{e}6 \text{ s} \tag{2.60}$$

where $\underline{l^\star}$ is the distance from the Sun to the Earth-Moon barycenter B_1, $\underline{m^\star}$ is the total mass of the Earth-Moon-Sun system, and $\underline{\tau^\star}$ is the characteristic time for the Sun-B_1 system. Consistent with the characteristic quantities in the Earth-Moon rotating coordinate frame as defined in Equations (2.38), (2.39), and (2.40), the quantities $\underline{l^\star}$, $\underline{m^\star}$ and $\underline{\tau^\star}$ are re-evaluated for the Sun-B_1 system. The characteristic quantities are employed to nondimensionalize position vectors, mass, and time as follows,

$$\underline{\vec{r}} = \frac{\vec{R}_3}{\underline{l^\star}}$$

$$\vec{r}_{13} = \frac{\vec{R}_{13}}{\underline{l^\star}}$$

$$\vec{r}_{23} = \frac{\vec{R}_{23}}{\underline{l^\star}}$$

$$\underline{\mu} = \frac{M_1 + M_2}{\underline{m^\star}} = 1 - \frac{M_4}{\underline{m^\star}}$$

$$\underline{t} = \frac{\tau}{\underline{\tau^\star}}$$

The nondimensional position vectors $\vec{\underline{r}}$, $\vec{\underline{r}}_{13}$, $\vec{\underline{r}}_{23}$, and $\vec{\underline{r}}_{43}$ describe the position of P_3 from B_2, the Earth, the Moon, and the Sun, respectively. The value $\underline{\mu}$ is the mass parameter of the Sun-B_1 system, and $\underline{t}$ is the nondimensional time. The vector differential equation governing the motion of P_3 as viewed by an inertial observer is expressed in Equation (2.36). To nondimensionalize the equation of motion, the mass parameters of the two primary systems ($\underline{\mu}$, $\widetilde{\mu}$), and the characteristic quantities for the P_4-B_1 system are introduced. The resultant nondimensional vector differential equation is expressed as,

$$\frac{\tau^{\star 2}}{\underline{l}^{\star}}{}^{I}\vec{R}_{B_2 3}'' = \left[-G\frac{M_1}{R_{13}^3}\vec{R}_{13} - G\frac{M_2}{R_{23}^3}\vec{R}_{23} - G\frac{M_4}{R_{43}^3}\vec{R}_{43}\right]\frac{\tau^{\star 2}}{\underline{l}^{\star}}$$

$$^{I}\ddot{\vec{\underline{r}}}_{B_2 3} = \left[-G\frac{M_1}{R_{13}^3}\vec{R}_{13} - G\frac{M_2}{R_{23}^3}\vec{R}_{23} - G\frac{M_4}{R_{43}^3}\vec{R}_{43}\right]\frac{\underline{l}^{\star 3}}{G\underline{m}^{\star}\,\underline{l}^{\star}}$$

$$^{I}\ddot{\vec{\underline{r}}}_{B_2 3} = \left[-\frac{M_1}{\underline{m}^{\star}\,\vec{\underline{r}}_{13}^{3}}\vec{\underline{r}}_{13} - \frac{M_2}{\underline{m}^{\star}\,\vec{\underline{r}}_{23}^{3}}\vec{\underline{r}}_{23} - \frac{M_4}{\underline{m}^{\star}\,\vec{\underline{r}}_{43}^{3}}\vec{\underline{r}}_{43}\right]$$

$$^{I}\ddot{\vec{\underline{r}}}_{B_2 3} = -\frac{(1-\widetilde{\mu})\underline{\mu}}{\underline{r}_{13}^3}\vec{\underline{r}}_{13} - \frac{\widetilde{\mu}\underline{\mu}}{\underline{r}_{23}^3}\vec{\underline{r}}_{23} - \frac{1-\underline{\mu}}{\underline{r}_{43}^3}\vec{\underline{r}}_{43} \tag{2.61}$$

The acceleration of P_3 relative to the system barycenter B_2 is $^{I}\ddot{\vec{\underline{r}}}_{B_2 3}$. Note that the direction of the acceleration vectors produced in Equation (2.61) and Equation (2.43) are equivalent, with the magnitude varying due to the different characteristic quantities. The mean motion of the P_4-B_1 system ($\underline{n}_{SB_1}$) is defined to be one as the system is nondimensionalized relative to the P_4 and B_1.

The Sun-B_1 rotating reference frame locates B_2 as the origin, where the system rotates with the motion of Sun and B_1. The frame is orthonormal, and defined with the $+\underline{\hat{x}}$-axis directed towards B_1, and the $+\underline{\hat{z}}$-axis is defined along the orbital angular momentum vector for the Sun-B_1 system. The position of P_3 in the Sun-B_1 rotating coordinate frame is written as $[\underline{x},\ \underline{y},\ \underline{z}]$, and for convenience, vectors from the origin to body i are denoted as $\vec{\underline{r}}_i$. The $\underline{\hat{x}}\underline{\hat{y}}$-projection of the Sun-$B_1$ rotating coordinate frame is illustrated in Figure 2.25. As B_2 is an inertially fixed point in the system, the equations of motion are derived following the procedure in the CR3BP. The position of the Sun and B_1 in rotating coordinate frame are

$\vec{\underline{r}}_4 = -\underline{\mu}\hat{\underline{x}}$ and $\vec{\underline{r}}_{B_1} = (1 - \underline{\mu})\hat{\underline{x}}$, respectively. The instantaneous positions of the Earth and Moon, i.e., P_1 and P_2, in the Sun-B_1 rotating coordinate frame are

$$
\begin{aligned}
\vec{\underline{r}}_1 &= (1 - \underline{\mu} - \frac{1}{a_S}\widetilde{\mu}\cos{(\theta_{EM})})\hat{\underline{x}} - \frac{1}{a_S}\widetilde{\mu}\sin{(\theta_{EM})}\hat{\underline{y}} = \underline{x}_E\hat{\underline{x}} + \underline{y}_E\hat{\underline{y}} \\
\vec{\underline{r}}_2 &= (1 - \underline{\mu} + \frac{1}{a_S}(1 - \widetilde{\mu})\cos{(\theta_{EM})})\hat{\underline{x}} + \frac{1}{a_S}(1 - \widetilde{\mu})\sin{(\theta_{EM})}\hat{\underline{y}} = \underline{x}_M\hat{\underline{x}} + \underline{y}_M\hat{\underline{y}}
\end{aligned}
\tag{2.62}
$$

where θ_{EM} is the Earth-Moon angle, measured counterclockwise from the $+\hat{\underline{x}}$-axis to $\vec{\underline{r}}_{B_12}$. The Earth-Moon angle describes the orientation of the Earth and Moon in the Sun-B_1, system as depicted in Figure 2.25. Recall the constant a_S is the scalar distance from the Sun to B_1 and is nondimensionalized relative to the Earth-Moon system ($a_S \approx 388.8204$ ndim). The quantities $\underline{x}_E$, $\underline{y}_E$, $\underline{x}_M$, and $\underline{y}_M$ are defined as the scalar components of position for the Earth and Moon in the rotating frame. With the basic kinematic equation (Equation (2.19)), and the angular velocity of the system equal to the nondimensional rate of the Sun-B_1 system ($^I\vec{\omega}^R = \underline{n}_{SB_1}\hat{\underline{z}} = 1\hat{\underline{z}}$). Given the inertial acceleration of P_3 (Equation (2.61)), and the motion of the Earth and Moon in the Sun-B_1 rotating coordinate frame (Equation (2.62)), the scalar differential equations of motion for P_3 are derived as,

$$
\begin{aligned}
\ddot{\underline{x}} &= 2\dot{\underline{y}} + \underline{x} - \frac{(1 - \mu)(x + \mu)}{r_{43}^3} - \frac{\mu(1 - \widetilde{\mu})(x - x_E)}{r_{13}^3} - \frac{\mu\widetilde{\mu}(x - x_M)}{r_{23}^3} \\
\ddot{\underline{y}} &= -2\dot{\underline{x}} + \underline{y} - \frac{(1 - \mu)y}{r_{43}^3} - \frac{\mu(1 - \widetilde{\mu})(\underline{y} - \underline{y}_E)}{r_{13}^3} - \frac{\mu\widetilde{\mu}(\underline{y} - \underline{y}_M)}{r_{23}^3} \\
\ddot{\underline{z}} &= -\frac{(1 - \mu)z}{r_{43}^3} - \frac{\mu(1 - \widetilde{\mu})z}{r_{13}^3} - \frac{\mu\widetilde{\mu}z}{r_{23}^3}
\end{aligned}
\tag{2.63}
$$

where $\underline{\mu}$ is the mass parameter of the Sun-B_1 system, and $\widetilde{\mu}$ is the mass parameter of the Earth-Moon system. Equation (2.63) defines the scalar components of acceleration for P_3 as viewed in the Sun-B_1 rotating coordinate frame. A pseudo-potential function ($\underline{\Upsilon}$) simplifies the acceleration expressions to,

$$
\underline{\Upsilon} = \frac{1}{2}(\underline{x}^2 + \underline{y}^2) + \frac{1 - \underline{\mu}}{\underline{r}_{43}} + \frac{\underline{\mu}(1 - \widetilde{\mu})}{\underline{r}_{13}} + \frac{\underline{\mu}\widetilde{\mu}}{\underline{r}_{23}}
\tag{2.64}
$$

$$\underline{\ddot{x}} = 2\underline{\dot{y}} + \underline{\Upsilon}_{\underline{x}}$$

$$\underline{\ddot{y}} = -2\underline{\dot{x}} + \underline{\Upsilon}_{\underline{y}} \qquad (2.65)$$

$$\underline{\ddot{z}} = \underline{\Upsilon}_{\underline{z}}$$

where $\underline{\Upsilon}_{\underline{x}}$ is the partial derivative of the pseudo-potential function with respect to $\underline{x}$. As the pseudo-potential function relies on the orientation of the Earth and Moon, the model is time dependent. However, since the Earth and Moon traverse in circular orbits within the Sun-B_1 orbital plane, the equations of motion are periodic in the rotating coordinate frame. The use of the Sun-B_1 rotating frame is advantageous in understanding and analyzing dynamical structures with respect to a fixed location of the Sun.

Hamiltonian

The Sun-B_1 Hamiltonian expresses an 'energy-like' quantity relative to the Sun-B_1 system in the BCR4BP. Similar to the Earth-Moon Hamiltonian, the Sun-B_1 Hamiltonian is written as,

$$H_{SB_1} = -(\underline{\dot{x}}^2 + \underline{\dot{y}}^2 + \underline{\dot{z}}^2) + 2\underline{\Upsilon} \qquad (2.66)$$

where $(\underline{\dot{x}}, \underline{\dot{y}}, \underline{\dot{z}})$ are the velocity components of P_3 in the Sun-B_1 rotating frame, and $\underline{\Upsilon}$ is the pseudo-potential function expressed in Equation (2.64). As the pseudo-potential function $\underline{\Upsilon}$ relies on the orientation of the Earth and Moon, which are time-dependent in the Sun-B_1 rotating coordinate frame, the H_{SB_1} varies along a transfer. The variation in energy is due to the additional forces in the equations as compared to the CR3BP, where B_1 is not treated as a fixed mass, but rather two orbiting masses, i.e., the Earth and Moon. In contrast to the Earth-Moon Hamiltonian, as P_3 approaches either the Earth or Moon, the Sun-B_1 Hamiltonian experiences larger variations in energy. Recall the sample transfer in Figure 2.15 and Figure 3.17. The Sun-B_1 Hamiltonian for this transfer is displayed in Figure 2.26. The behavior of the Sun-B_1 Hamiltonian is explored further throughout this investigation.

71
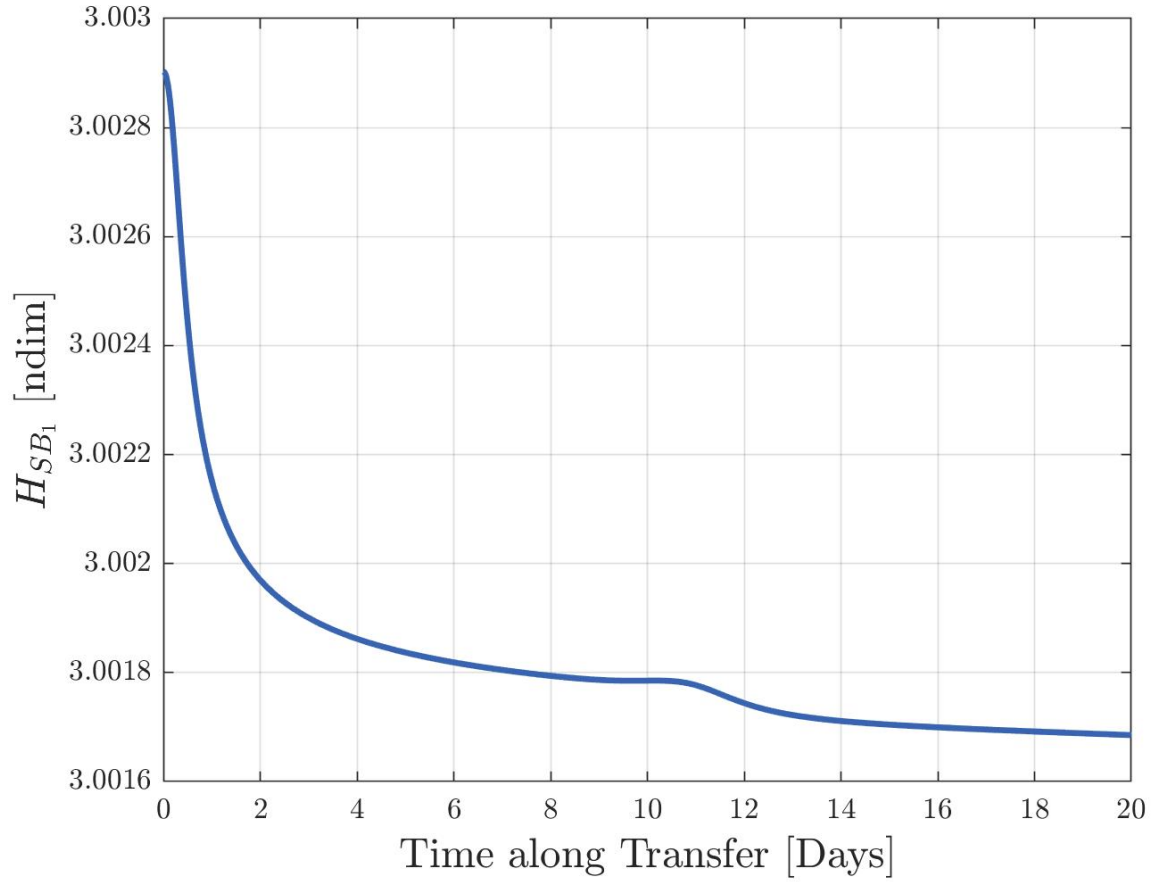
Figure 2.26. The Sun-B_1 Hamiltonian along the example transfer plotted in Figure 3.17

Instantaneous Equilibrium Solutions

Similar to the view of the BCR4BP in the Earth-Moon rotating coordinate frame, instantaneous equilibrium solutions exist in the Sun-B_1 BCR4BP. The solutions rely on the orientation of the Earth and Moon, i.e., the Earth-Moon angle. An instantaneous equilibrium solution in the Sun-B_1 rotating frame at a specific Earth-Moon angle θ_{EM} is labelled as $\underline{E}_i(\theta_{EM})$. The Lagrange point locations from the Sun-B_1 CR3BP are applied to seed the process to determine the sets of solutions. For $\underline{E}_3$, $\underline{E}_4$ and $\underline{E}_5$, the sets vary by less than five kilometers from the positions of the corresponding Lagrange points in the CR3BP. Figure 2.27 and Figure 2.28 include the instantaneous equilibrium solutions $\underline{E}_1$ and $\underline{E}_2$, respectively. The origin in each figure is the total system barycenter B_2.
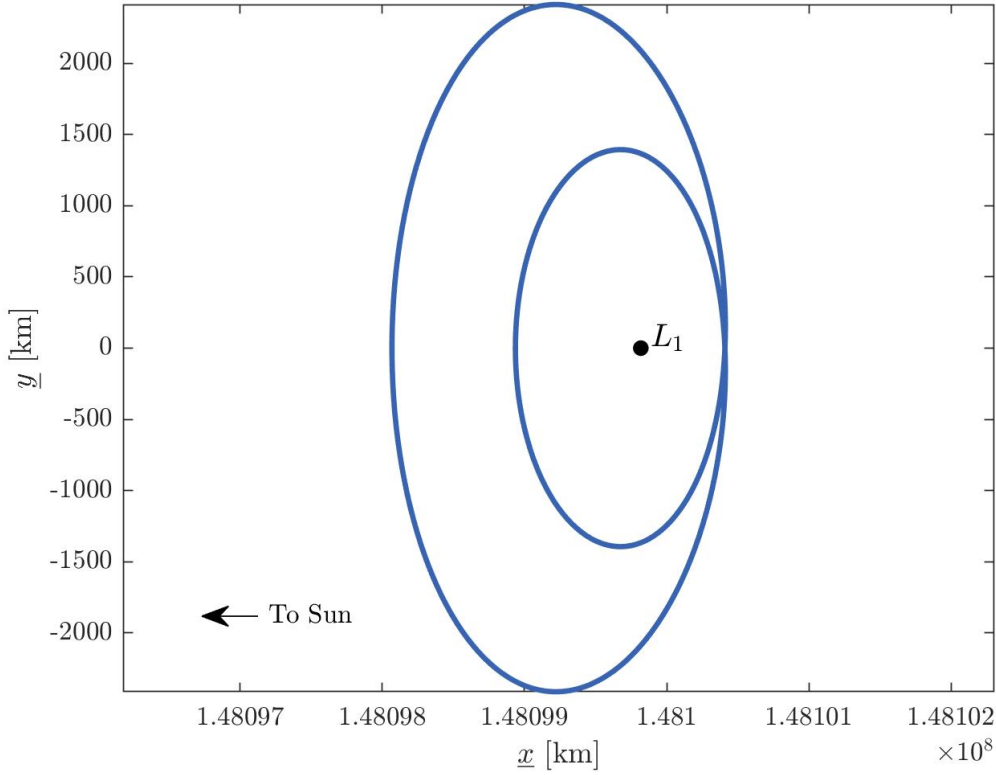
Figure 2.27. Set of instantaneous equilibrium solutions in the BCR4BP, in the vicinity of the Sun-B_1 Lagrange points L_1

2.3.4 Symmetry

Symmetry in the four-body problem is more complex than in the three-body problem, yet offers numerical advantages. The time-dependency in the BCR4BP influences the conditions for symmetric motion. At least one primary body is moving in either the Earth-Moon, or Sun-B_1 rotating frames, thus, symmetry is epoch dependant. For a mirrored image transfer, the time dependent primary body(or bodies) path must also be mirror imaged. As the orientation of the primary bodies is strictly a function of θ_S or θ_{EM}, the reflection occurs
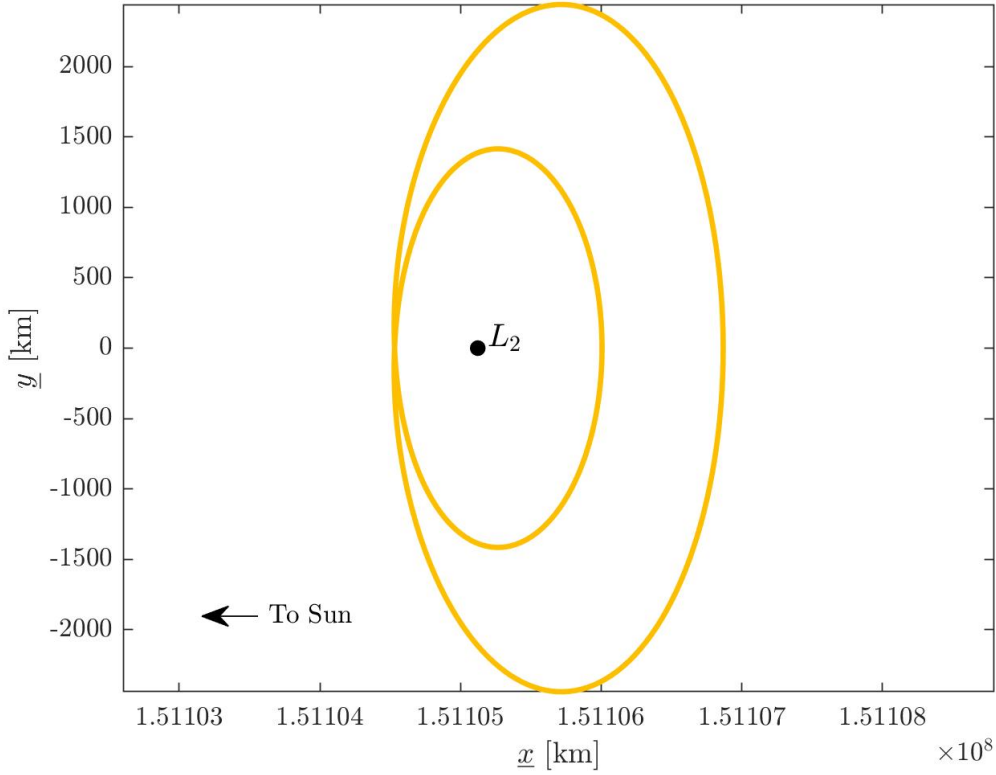
Figure 2.28. Set of instantaneous equilibrium solutions in the BCR4BP, in the vicinity of the Sun-B_1 Lagrange points L_2

at the negative angle, i.e., $-\theta_S$ or $-\theta_{EM}$. The appended transformation matrix for both reference frames in the BCR4BP is

$$
K(-t) = \begin{bmatrix}
1 & 0 & 0 & 0 & 0 & 0 & 0 \\
0 & -1 & 0 & 0 & 0 & 0 & 0 \\
0 & 0 & 1 & 0 & 0 & 0 & 0 \\
0 & 0 & 0 & -1 & 0 & 0 & 0 \\
0 & 0 & 0 & 0 & 1 & 0 & 0 \\
0 & 0 & 0 & 0 & 0 & -1 & 0 \\
0 & 0 & 0 & 0 & 0 & 0 & -1
\end{bmatrix}
\tag{2.67}
$$

For the Earth-Moon rotating frame, the transformation matrix produces a symmetric transfer across the $\hat{\tilde{x}}\hat{\tilde{z}}$-plane when propagated backwards in time. For the Sun-B_1 rotating frame, the

74

symmetry is across the $\underline{\hat{x}}\underline{\hat{z}}$-plane. Similar to the CR3BP, the existence of symmetry reduces length of any simulation, an advantage in any numerical corrections process. Symmetry also suggests dynamical structures that might emerge in a design process. The epoch dependency of the BCR4BP increases the complexity of the patterns. The Mirror Theorem is applied in this investigation to seek dynamical structures that are symmetric across the $\hat{\tilde{x}}\hat{\tilde{z}}$-plane, as one example.

3. DYNAMICAL SYSTEMS THEORY

Dynamical systems theory offers techniques in analyzing nonlinear systems. As the CR3BP and BCR4BP rely on coupled, second-order, nonlinear differential equations, effective solution designs are nontrivial to construct. In the simplest form, linear variational equations approximate motion in the vicinity of fixed states. Extending to continuous transfers, the state transition matrix considers the downstream implication of an initial perturbation to a transfer arc. Differential corrections employ state transition matrices to construct desired transfer designs, periodic solutions, and analyze their respective stability characteristics. The application of Poincaré sections acts as both a visualization tool and aids in the classification of dynamical behavior. Assessment of the Hamiltonian properties in the BCR4BP highlight an explicit relationship between the natural progression in energy and perturbing effects. Incorporating methods from dynamical systems theory is a critical component to this investigation.

3.1 Linear Variational Equations

Linear variational equations offer insight into the stability characteristics of the equilibrium solutions [24]. To incorporate variational equations, a matrix representation of the dynamical system must be introduced. The state vectors of the dynamical models are

$$
\bar{x} = \begin{bmatrix} x \\ y \\ z \\ \dot{x} \\ \dot{y} \\ \dot{z} \end{bmatrix} \qquad
\bar{\bar{x}} = \begin{bmatrix} \widetilde{x} \\ \widetilde{y} \\ \widetilde{z} \\ \dot{\widetilde{x}} \\ \dot{\widetilde{y}} \\ \dot{\widetilde{z}} \\ \theta_S \end{bmatrix} \qquad
\underline{\bar{x}} = \begin{bmatrix} \underline{x} \\ \underline{y} \\ \underline{z} \\ \underline{\dot{x}} \\ \underline{\dot{y}} \\ \underline{\dot{z}} \\ \theta_{EM} \end{bmatrix}
\tag{3.1}
$$

where the vectors associated with the BCR4BP ($\bar{\bar{x}}$ and $\bar{x}$) have an additional seventh state associated with the orientation of the primary bodies, i.e., θ_S and θ_{EM}. The vector components of the first-order differential equations are,

$$
\bar{f}(\bar{x}) = \begin{bmatrix} \dot{x} \\ \dot{y} \\ \dot{z} \\ 2\dot{y} + \Omega_x \\ -2\dot{x} + \Omega_y \\ \Omega_z \end{bmatrix}
\tag{3.2}
$$

where acceleration quantities are formulated in Equation (2.22). Define $\bar{x}_{L_i}$ to be the state vector for the Lagrange point L_i. Thus, the state vector for P_3 in close proximity to L_i is

$$
\bar{x} = \bar{x}_{L_i} + \delta\bar{x}
\tag{3.3}
$$

where $\delta\bar{x}$ is the displacement vector from L_i to P_3. Combining Equation (3.2) and Equation (3.3), the motion of P_3 relative to the Lagrange point L_i is

$$
\bar{f}(\bar{x}) = \bar{f}(\bar{x}_{L_i} + \delta\bar{x}) = \dot{\bar{x}}_{L_i} + \delta\dot{\bar{x}}
\tag{3.4}
$$

The term $\delta\dot{\bar{x}}$ represents the variational equations of P_3 about a fixed point. As $\delta\bar{x}$ is a perturbation vector and not an explicit state in the dynamical model, a Taylor Series expansion is necessary to describe $\delta\dot{\bar{x}}$. The first-order Taylor Series expansion of Equation (3.4) is,

$$
\dot{\bar{x}}_{L_i} + \delta\dot{\bar{x}} \approx \bar{f}(\bar{x}_{L_i}) + \left.\frac{\partial \bar{f}}{\partial \bar{x}}\right|_{\bar{x}_{L_i}} \delta\bar{x} + H.O.T.
\tag{3.5}
$$

where *H.O.T.* stands for higher order terms. By definition the equations of motion for the Lagrange points are equal to zero, i.e. $\bar{f}(\bar{x}_{L_i}) = \dot{\bar{x}}_{L_i} = 0$. Thus, Equation (3.5) is reduced by removing the higher order terms,

$$\delta\dot{\bar{x}} \approx \left.\frac{\partial\bar{f}}{\partial\bar{x}}\right|_{\bar{x}_{L_i}} \delta\bar{x} \tag{3.6}$$

The matrix $\frac{\partial\bar{f}}{\partial\bar{x}}$ is equal to the derivative of the equations of motion with respect to the components of the state vector, i.e. the Jacobian matrix. Written out, the matrix is constructed as

$$\frac{\partial\bar{f}}{\partial\bar{x}} = \mathbf{A}(t) = \begin{bmatrix} \frac{\partial\dot{x}}{\partial x} & \frac{\partial\dot{x}}{\partial y} & \frac{\partial\dot{x}}{\partial z} & \frac{\partial\dot{x}}{\partial\dot{x}} & \frac{\partial\dot{x}}{\partial\dot{y}} & \frac{\partial\dot{x}}{\partial\dot{z}} \\ \frac{\partial\dot{y}}{\partial x} & \frac{\partial\dot{y}}{\partial y} & \frac{\partial\dot{y}}{\partial z} & \frac{\partial\dot{y}}{\partial\dot{x}} & \frac{\partial\dot{y}}{\partial\dot{y}} & \frac{\partial\dot{y}}{\partial\dot{z}} \\ \frac{\partial\dot{z}}{\partial x} & \frac{\partial\dot{z}}{\partial y} & \frac{\partial\dot{z}}{\partial z} & \frac{\partial\dot{z}}{\partial\dot{x}} & \frac{\partial\dot{z}}{\partial\dot{y}} & \frac{\partial\dot{z}}{\partial\dot{z}} \\ \frac{\partial\ddot{x}}{\partial x} & \frac{\partial\ddot{x}}{\partial y} & \frac{\partial\ddot{x}}{\partial z} & \frac{\partial\ddot{x}}{\partial\dot{x}} & \frac{\partial\ddot{x}}{\partial\dot{y}} & \frac{\partial\ddot{x}}{\partial\dot{z}} \\ \frac{\partial\ddot{y}}{\partial x} & \frac{\partial\ddot{y}}{\partial y} & \frac{\partial\ddot{y}}{\partial z} & \frac{\partial\ddot{y}}{\partial\dot{x}} & \frac{\partial\ddot{y}}{\partial\dot{y}} & \frac{\partial\ddot{y}}{\partial\dot{z}} \\ \frac{\partial\ddot{z}}{\partial x} & \frac{\partial\ddot{z}}{\partial y} & \frac{\partial\ddot{z}}{\partial z} & \frac{\partial\ddot{z}}{\partial\dot{x}} & \frac{\partial\ddot{z}}{\partial\dot{y}} & \frac{\partial\ddot{z}}{\partial\dot{z}} \end{bmatrix} \tag{3.7}$$

where many of the quantities are reduced to zero, as there is no dependence between some combination of states. The matrix is rewritten in terms of the pseudo-potential function formulated in Equation (2.22). Therefore, an updated expression for the linear variational equations is

$$\delta\dot{\bar{x}} = \mathbf{A}(t)\delta\bar{x} = \begin{bmatrix} 0 & 0 & 0 & 1 & 0 & 0 \\ 0 & 0 & 0 & 0 & 1 & 0 \\ 0 & 0 & 0 & 0 & 0 & 1 \\ \Omega_{xx} & \Omega_{xy} & \Omega_{xz} & 0 & 2 & 0 \\ \Omega_{yx} & \Omega_{yy} & \Omega_{yz} & -2 & 0 & 0 \\ \Omega_{zx} & \Omega_{zy} & \Omega_{zz} & 0 & 0 & 0 \end{bmatrix} \begin{bmatrix} \delta x \\ \delta y \\ \delta z \\ \delta\dot{x} \\ \delta\dot{y} \\ \delta\dot{z} \end{bmatrix} \tag{3.8}$$

Recall the subscripts Ω_{ij} refers to the partial derivative of the pseudo-potential function wit respect to i and j, e.g., $\Omega_{xx} = \frac{\partial^2\Omega}{\partial x^2}$. The same procedure is followed for the BCR4P. One

difference between the BCR4BP and the CR3BP is the dependency on the relative orientation of the primary bodies. Therefore, the linear variational equations for the BCR4BP is

$$\delta\dot{\bar{x}} = \widetilde{\mathbf{A}}(t)\delta\bar{x} = \begin{bmatrix} 0 & 0 & 0 & 1 & 0 & 0 & 0 \\ 0 & 0 & 0 & 0 & 1 & 0 & 0 \\ 0 & 0 & 0 & 0 & 0 & 1 & 0 \\ \widetilde{\Upsilon}_{\widetilde{x}\widetilde{x}} & \widetilde{\Upsilon}_{\widetilde{x}\widetilde{y}} & \widetilde{\Upsilon}_{\widetilde{x}\widetilde{z}} & 0 & 2 & 0 & \widetilde{\Upsilon}_{\widetilde{x}\theta_S} \\ \widetilde{\Upsilon}_{\widetilde{y}\widetilde{x}} & \widetilde{\Upsilon}_{\widetilde{y}\widetilde{y}} & \widetilde{\Upsilon}_{\widetilde{y}\widetilde{z}} & -2 & 0 & 0 & \widetilde{\Upsilon}_{\widetilde{y}\theta_S} \\ \widetilde{\Upsilon}_{\widetilde{z}\widetilde{x}} & \widetilde{\Upsilon}_{\widetilde{z}\widetilde{y}} & \widetilde{\Upsilon}_{\widetilde{z}\widetilde{z}} & 0 & 0 & 0 & \widetilde{\Upsilon}_{\widetilde{z}\theta_S} \\ 0 & 0 & 0 & 0 & 0 & 0 & 0 \end{bmatrix} \begin{bmatrix} \delta\widetilde{x} \\ \delta\widetilde{y} \\ \delta\widetilde{z} \\ \delta\dot{\widetilde{x}} \\ \delta\dot{\widetilde{y}} \\ \delta\dot{\widetilde{z}} \\ \delta\theta_S \end{bmatrix} \tag{3.9}$$

The seventh row in Equation (3.9) equals zero as the Sun angle is independent of the position and velocity of P_3. However, the acceleration of the spacecraft relies on the Sun angle. The dependency on epoch contributes to the values in the seventh column of $\widetilde{\mathbf{A}}(t)$. An equivalent formulation exists for the Sun-B_1 BCR4BP, where the Sun angle is replaced by the Earth-Moon angle and the pseudo-potential function corresponds to the equations of motion written relative to the Sun-B_1 rotating coordinate frame. The linear variational equations approximate motion in the vicinity of fixed points and offer a foundation for other methods used in dynamical systems theory.

3.2 State Transition Matrix

The state-transition matrix (STM) predicts a final perturbed state due to some initial deviation from the transfer. The STM is a linear map from the initial perturbation vector to the final resultant vector,

$$\delta\bar{x}(t) = \mathbf{\Phi}(t, t_0)\,\delta\bar{x}(t_0) \tag{3.10}$$

79

where $\mathbf{\Phi}(t, t_0)$ is the STM from some initial time t_0 to the final time t. In the CR3BP, the elements of the STM are,

$$\mathbf{\Phi}(t, t_0) = \begin{bmatrix} \frac{\partial x}{\partial x_0} & \frac{\partial x}{\partial y_0} & \frac{\partial x}{\partial z_0} & \frac{\partial x}{\partial \dot{x}_0} & \frac{\partial x}{\partial \dot{y}_0} & \frac{\partial x}{\partial \dot{z}_0} \\ \frac{\partial y}{\partial x_0} & \frac{\partial y}{\partial y_0} & \frac{\partial y}{\partial z_0} & \frac{\partial y}{\partial \dot{x}_0} & \frac{\partial y}{\partial \dot{y}_0} & \frac{\partial y}{\partial \dot{z}_0} \\ \frac{\partial z}{\partial x_0} & \frac{\partial z}{\partial y_0} & \frac{\partial z}{\partial z_0} & \frac{\partial z}{\partial \dot{x}_0} & \frac{\partial z}{\partial \dot{y}_0} & \frac{\partial z}{\partial \dot{z}_0} \\ \frac{\partial \dot{x}}{\partial x_0} & \frac{\partial \dot{x}}{\partial y_0} & \frac{\partial \dot{x}}{\partial z_0} & \frac{\partial \dot{x}}{\partial \dot{x}_0} & \frac{\partial \dot{x}}{\partial \dot{y}_0} & \frac{\partial \dot{x}}{\partial \dot{z}_0} \\ \frac{\partial \dot{y}}{\partial x_0} & \frac{\partial \dot{y}}{\partial y_0} & \frac{\partial \dot{y}}{\partial z_0} & \frac{\partial \dot{y}}{\partial \dot{x}_0} & \frac{\partial \dot{y}}{\partial \dot{y}_0} & \frac{\partial \dot{y}}{\partial \dot{z}_0} \\ \frac{\partial \dot{z}}{\partial x_0} & \frac{\partial \dot{z}}{\partial y_0} & \frac{\partial \dot{z}}{\partial z_0} & \frac{\partial \dot{z}}{\partial \dot{x}_0} & \frac{\partial \dot{z}}{\partial \dot{y}_0} & \frac{\partial \dot{z}}{\partial \dot{z}_0} \end{bmatrix} \tag{3.11}$$

Each column of the STM describes the influence one component of the initial state vector has on the final state after propagating for time t. For example, the first column predicts the final perturbation due to some initial change in x, i.e., ∂x_0. Additionally, each row of the STM reflects the deviation on a final state component due to the initial perturbation vector. For example, the second row describes the variation in the final y component due to a perturbation at the initial state. The STM for the BCR4BP is a 7x7 square matrix, where the additional row and column originate from the orienting angles for the respective rotating coordinate frame, i.e., the Sun angle or the Earth-Moon angle. The elements of the STM for an given arc offers insight into the sensitivity and local dynamical structures.

Properties of the STM aid in the construction of the matrices. The first property of the STM describes the matrix at some initial time t_0. Consider Equation (3.10) when $t_0 = t$, the initial and final perturbations are equal as the state is not propagated, i.e., $\delta \bar{x}(t_0) = \delta \bar{x}(t)$. Thus, Equation (3.10) is simplified to,

$$\delta \bar{x}(t_0) = \mathbf{\Phi}(t_0, t_0)\, \delta \bar{x}(t_0)$$
$$\mathbf{\Phi}(t_0, t_0) = \mathbf{I} \tag{3.12}$$

where $\mathbf{I}$ is the identity matrix with dimension equal to the STM. The second property reflects the combination of the STM. Analyze two segments of a trajectory, where the first STM describes an arc propagated from time t_0 to t_1 ($\mathbf{\Phi}(t_1, t_0)$), and the second matrix reflects the

same arc continued from time t_1 to t_2 ($\mathbf{\Phi}(t_2, t_1)$). To map an initial perturbation at time t_0 to the final perturbation at t_2, Equation (3.10) is written as,

$$\delta \bar{x}(t_2) = \mathbf{\Phi}(t_2, t_0) \, \delta \bar{x}(t_0) \tag{3.13}$$

Although, the quantity $\mathbf{\Phi}(t_2, t_0)$ is not explicitly available, employing the STMs associated with the two segment arcs yield an equivalent solution,

$$\delta \bar{x}(t_1) = \mathbf{\Phi}(t_1, t_0) \, \delta \bar{x}(t_0)$$
$$\delta \bar{x}(t_2) = \mathbf{\Phi}(t_2, t_1) \, \delta \bar{x}(t_1)$$
$$\delta \bar{x}(t_2) = \mathbf{\Phi}(t_2, t_1) \, \mathbf{\Phi}(t_1, t_0) \, \delta \bar{x}(t_0) \tag{3.14}$$

Comparing the matrices in Equation (3.13) to Equation (3.14) offers the second property of the STM,

$$\mathbf{\Phi}(t_2, t_0) = \mathbf{\Phi}(t_2, t_1) \, \mathbf{\Phi}(t_1, t_0) \tag{3.15}$$

Equation (3.15) reveals the method of combining sensitivity matrices along a transfer. The combination of STMs is repeated for longer trajectories with a multitude of segments. The third property relates the STM to the inverse STM. Rearranging Equation (3.10) produces,

$$\delta \bar{x}(t) = \mathbf{\Phi}(t, t_0) \, \delta \bar{x}(t_0)$$
$$\mathbf{\Phi}^{-1}(t, t_0) \, \delta \bar{x}(t) = \mathbf{\Phi}^{-1}(t, t_0) \, \mathbf{\Phi}(t, t_0) \, \delta \bar{x}(t_0)$$
$$\delta \bar{x}(t_0) = \mathbf{\Phi}^{-1}(t, t_0) \, \delta \bar{x}(t) \tag{3.16}$$

Equation (3.16) is equivalent to the linear mapping of the STM in reverse time from t to t_0, the third property is revealed as,

$$\mathbf{\Phi}^{-1}(t, t_0) = \mathbf{\Phi}(t_0, t) \tag{3.17}$$

Equation (3.17) equates the inverse of the STM for a given trajectory to the STM constructed by following the same arc propagating the model in reverse time.

Properties of the STM in combination with numerical processes aid in the construction of the matrix. The derivative of Equation (3.10) with respect to the final time (t), the following equation is produced

$$\delta \dot{\bar{x}}(t) = \dot{\boldsymbol{\Phi}}(t, t_0)\, \delta \bar{x}(t_0)$$

where the initial perturbation $\delta \dot{\bar{x}}(t_0)$ is independent of the propagation time. Substituting $\delta \dot{\bar{x}}(t)$ with the linear variational equations denoted in Equation (3.8) results in,

$$\mathbf{A}(t)\delta \bar{x}(t) = \dot{\boldsymbol{\Phi}}(t, t_0)\, \delta \bar{x}(t_0)$$

Replace $\delta \bar{x}(t)$ with the general form of the STM, i.e., Equation (3.10),

$$\mathbf{A}(t)\boldsymbol{\Phi}(t, t_0)\delta \bar{x}(t_0) = \dot{\boldsymbol{\Phi}}(t, t_0)\, \delta \bar{x}(t_0)$$
$$\dot{\boldsymbol{\Phi}}(t, t_0) = \mathbf{A}(t)\boldsymbol{\Phi}(t, t_0) \tag{3.18}$$

Equation (3.18) is a linear differential equation that produces the time rate of change in the components of the STM. The STM is constructed by employing Equation (3.18) through numerical integration. Although the STM is built numerically, the formulation relies on the first-order, linear variational equations. Thus, the STM is a first-order approximation to the nonlinear dynamics. Construction of the STM in the BCR4BP follows the same formulation. For dynamical models where no closed-form solutions exist, i.e., the CR3BP and the BCR4BP, the STM acts as an effective tool for evaluating the governing motion.

3.3 Differential Corrections

Developing sufficient transfer designs in the multi-body regime is convoluted. To overcome this challenge, differential correction techniques are applied to aid in the design of a desired trajectory. The numerical approach employed in this investigation is a multi-

dimensional Newton-Raphson scheme. A Newton-Raphson method is a common algorithm used in assessing local solutions in models controlled by a set of nonlinear differential equations [25]. Let $\bar{X}$ be a vector comprised of n free variables called the design vector, i.e.,

$$\bar{X} = \begin{bmatrix} X_1 \\ X_2 \\ \vdots \\ X_n \end{bmatrix} \tag{3.19}$$

and $\bar{F}$ be a vector of m constraints denoted the constraint vector,

$$\bar{F}(\bar{X}) = \begin{bmatrix} F_1(\bar{X}) \\ F_2(\bar{X}) \\ \vdots \\ F_m(\bar{X}) \end{bmatrix} \tag{3.20}$$

The objective of the Newton-Raphson method is to produce a design vector $(\bar{X}^*)$ such that the constraint vector becomes a zero vector, i.e, $\bar{F}(\bar{X}^*) = \bar{0}$. Numerically solving for a solution that perfectly meets each constraint is nontrivial. Thus, to alleviate the numerical challenges, a solution is obtained to meet the following criteria,

$$||\bar{F}(\bar{X}^*)|| < k \tag{3.21}$$

where the term k refers to some set tolerance. The purpose of Equation (3.21) is to guarantee that the Euclidean norm of the constraint vector is below the desired tolerance. Denote the initial design vector as $\bar{X}_0$. To determine a feasible solution to Equation (3.21), the first-order Taylor series expansion of $\bar{F}(\bar{X}^*)$ relative to $\bar{X}_0$ is assessed as,

$$\bar{F}(\bar{X}^*) \approx \bar{F}(\bar{X}_0) + D\bar{F}(\bar{X}_0)(\bar{X}^* - \bar{X}_0) \tag{3.22}$$

where $D\bar{F}(\bar{X}_0)$ is an m x n matrix comprised of the partial derivatives of the constraint vector with respect to each free variable. The $D\bar{F}(\bar{X})$ matrix, labelled the Jacobian matrix, evaluated at $\bar{X}_0$ is written as

$$D\bar{F}(\bar{X}_0) = \frac{\partial \bar{F}}{\partial \bar{X}} = \begin{bmatrix} \frac{\partial F_1}{\partial X_1} & \frac{\partial F_1}{\partial X_2} & \cdots & \frac{\partial F_1}{\partial X_n} \\ \frac{\partial F_2}{\partial X_1} & \frac{\partial F_2}{\partial X_2} & \cdots & \frac{\partial F_2}{\partial X_n} \\ \vdots & \vdots & \ddots & \vdots \\ \frac{\partial F_m}{\partial X_1} & \frac{\partial F_m}{\partial X_2} & \cdots & \frac{\partial F_m}{\partial X_n} \end{bmatrix} \tag{3.23}$$

Rewriting Equation (3.22) such that the desired constraint vector is a zero vector with length m, produces

$$\bar{0} = \bar{F}(\bar{X}_0) + D\bar{F}(\bar{X}_0)(\bar{X}^* - \bar{X}_0) \tag{3.24}$$

The goal of the Newton-Raphson method is to determine $\bar{X}^*$. However, the construction of Equation (3.24) is limited due to the linear approximation of the nonlinear dynamics. Depending on the sufficiency of the initial guess, multiple iterations are necessary to achieve a solution that fulfills the constraints. Therefore, Equation (3.24) is revised such that $\bar{X}^j$ is the current design vector and $\bar{X}^{j+1}$ is the desired update,

$$\bar{0} = \bar{F}(\bar{X}^j) + D\bar{F}(\bar{X}^j)(\bar{X}^{j+1} - \bar{X}^j) \tag{3.25}$$

Recasting Equation (3.25) to solve for $\bar{X}^{j+1}$ relies on the size of the matrix $D\bar{F}(\bar{X}^j)$. Three possibilities exist, $n = m$, $n > m$, and $n < m$. If the Jacobian is square ($n = m$) and non-singular, there are an equal number of free variables and constraints. The update equation for $\bar{X}^{j+1}$ becomes,

$$\bar{X}^{j+1} = \bar{X}^j - (D\bar{F}(\bar{X}^j))^{-1}\bar{F}(\bar{X}^j) \tag{3.26}$$

If there are more free variables than constraints ($n > m$), then the system of equations is underdetermined. Given that a solution exists, an underdetermined system produces an

infinite number of solutions [26]. There are many techniques to solving an underdetermined system. Each method will impact the resultant solution of the targeter. Therefore, the method chosen for solving an underdetermined system relies on the intended results. In this investigation, a minimum-norm approach is considered. The minimum-norm solution provides the closest feasible solution to the initial guess. The update equation to determine the minimum-norm solution is

$$\bar{X}^{j+1} = \bar{X}^j - D\bar{F}(\bar{X}^j)^T \left[D\bar{F}(\bar{X}^j)D\bar{F}(\bar{X}^j)^T \right]^{-1} \bar{F}(\bar{X}^j) \tag{3.27}$$

If there are more constraints than free variables ($n < m$), then $D\bar{F}(\bar{X}^j)$ is overdetermined. If each constraint is linearly independent, then there is no solution to the overdetermined system. Due to the nature of this investigation, overdetermined systems are not employed.

3.3.1 Single Shooting Method

The single shooting method is the simplest implementation of the Newton-Raphson scheme. The design vector of the method is composed of a subset of one initial state vector; hence the name Single Shooting. The constraint vector relies on the desired outcome of the transfer, including arrival position or velocity states, an apse condition, and energy properties. An example in transfer design is to achieve a desired position by implementing an impulsive maneuver at some fixed location. Consider a spacecraft in the BCR4BP that has the following initial state

$$\bar{\bar{x}}_0 = \begin{bmatrix} \tilde{x}_0 & \tilde{y}_0 & \tilde{z}_0 & \dot{\tilde{x}}_0 & \dot{\tilde{y}}_0 & \dot{\tilde{z}}_0 & \theta_{S0} \end{bmatrix}$$

The state $\bar{\bar{x}}_0$ is propagated forward for time T resulting in the following state

$$\bar{\bar{x}}_f = \begin{bmatrix} \tilde{x}_f & \tilde{y}_f & \tilde{z}_f & \dot{\tilde{x}}_f & \dot{\tilde{y}}_f & \dot{\tilde{z}}_f & \theta_{Sf} \end{bmatrix}$$

By allowing an impulsive maneuver at the initial state, the components of velocity act as the design variable vector,i.e., $\bar{X} = \begin{bmatrix} \dot{\tilde{x}}_0 & \dot{\tilde{y}}_0 & \dot{\tilde{z}}_0 \end{bmatrix}$. Let the desired position of the spacecraft at the final state be $\begin{bmatrix} \tilde{x}_d & \tilde{y}_d & \tilde{z}_d \end{bmatrix}$. Therefore, the constraint vector is

$$\bar{F}(\bar{X}) = \begin{bmatrix} \tilde{x}_f - \tilde{x}_d & \tilde{y}_f - \tilde{y}_d & \tilde{z}_f - \tilde{z}_d \end{bmatrix} \tag{3.28}$$

where a solution is found once $||\bar{F}(\bar{X})||$ is near zero, below a set tolerance k. For this example, the trajectory is set to be epoch dependent, keeping the propagation time (T) and initial Sun angle (θ_{S0}) fixed. Given the free variables and constraints, the Jacobian matrix necessary for the Newton-Raphson method emerges as,

$$DF(\bar{X}) = \begin{bmatrix} \dfrac{\partial(\tilde{x}_f-\tilde{x}_d)}{\partial\dot{\tilde{x}}_0} & \dfrac{\partial(\tilde{x}_f-\tilde{x}_d)}{\partial\dot{\tilde{y}}_0} & \dfrac{\partial(\tilde{x}_f-\tilde{x}_d)}{\partial\dot{\tilde{z}}_0} \\ \dfrac{\partial(\tilde{y}_f-\tilde{y}_d)}{\partial\dot{\tilde{x}}_0} & \dfrac{\partial(\tilde{y}_f-\tilde{y}_d)}{\partial\dot{\tilde{y}}_0} & \dfrac{\partial(\tilde{y}_f-\tilde{y}_d)}{\partial\dot{\tilde{z}}_0} \\ \dfrac{\partial(\tilde{z}_f-\tilde{z}_d)}{\partial\dot{\tilde{x}}_0} & \dfrac{\partial(\tilde{z}_f-\tilde{z}_d)}{\partial\dot{\tilde{y}}_0} & \dfrac{\partial(\tilde{z}_f-\tilde{z}_d)}{\partial\dot{\tilde{z}}_0} \end{bmatrix} \tag{3.29}$$

Since the desired target position of the spacecraft is independent of the design vectors, Equation (3.29) is reduced to

$$D\bar{F}(\bar{X}) = \begin{bmatrix} \tilde{\Phi}_{14} & \tilde{\Phi}_{15} & \tilde{\Phi}_{16} \\ \tilde{\Phi}_{24} & \tilde{\Phi}_{25} & \tilde{\Phi}_{26} \\ \tilde{\Phi}_{34} & \tilde{\Phi}_{35} & \tilde{\Phi}_{36} \end{bmatrix} \tag{3.30}$$

where $\tilde{\mathbf{\Phi}}(t + T, t)$ is the state transition matrix constructed along the propagated arc in the Earth-Moon rotating frame from time t to $t + T$ and $\tilde{\Phi}_{ij}$ is the element in row i and column j of the STM. For this scenario, the number of free variables matches the number of constraints, i.e., the Jacobian is non-singular. Therefore, Equation (3.26) is employed iteratively to determine a solution that meets the constraints. A sample single shooting scenario is illustrated in Figure 3.1. The magenta point is the initial state of the transfer, $\bar{\tilde{x}}_0 = [.5 \ .1 \ 0 \ 0 \ .55 \ 0 \ 0]$ nondimensional units. The initial state propagated for five days results in the red point. The target position is denoted by the black dot, $[-0.1492 \ -0.3233 \ 0]$ nondimensional units.
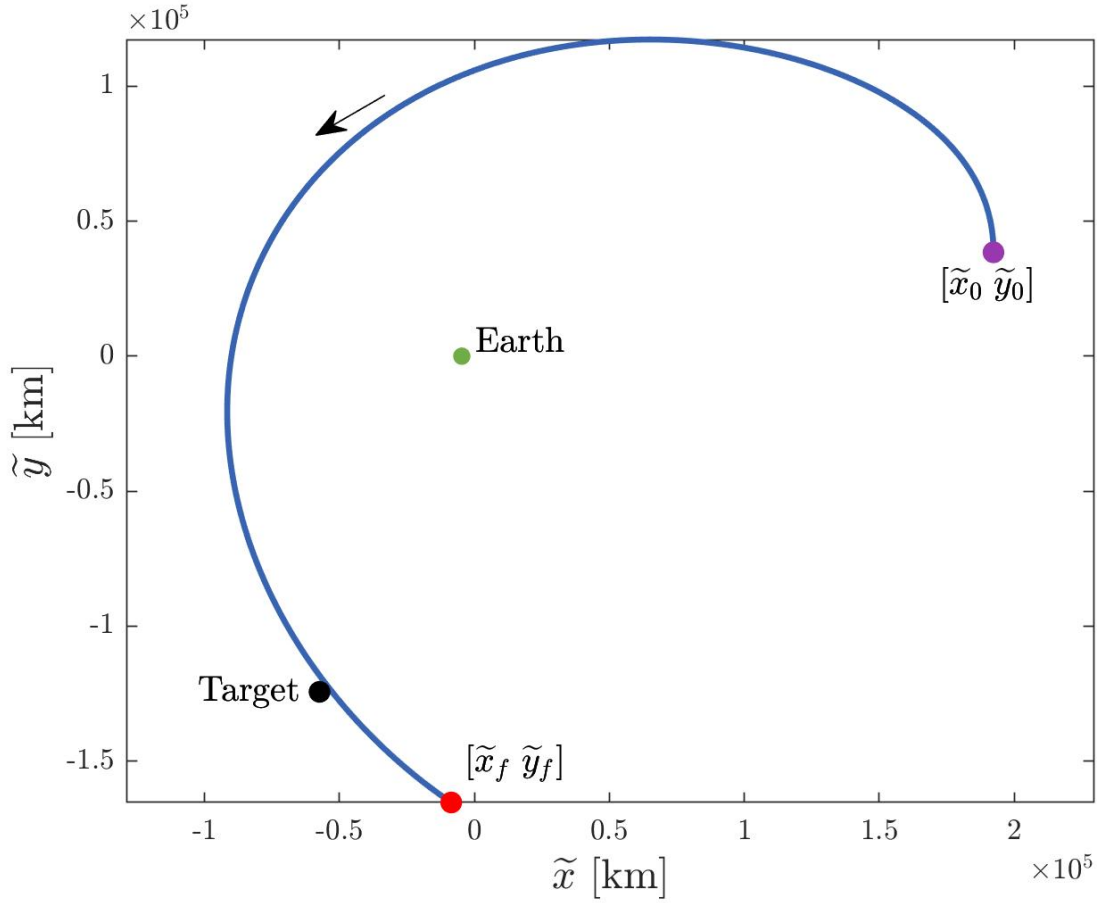
Figure 3.1. Planar transfer propagated for five days, with an initial Sun angle of zero degrees

The constraint vector from Equation (3.28), the free variable vector composed of the initial velocity, and the Jacobian matrix from Equation (3.30) are implemented into Equation (3.26) to construct a unique solution. Recall that the time of flight and the initial Sun angle are fixed in this scenario. An iterative Newton-Raphson method is applied to determine the initial state that produces the desired transfer. A solution to the single shooting method is illustrated in Figure 3.2. The resultant transfer is the blue arc, and the initial guess is the yellow dashed line. The black, red, and magenta dots are equivalent to the points in Figure 3.1. As the initial components of position were not free variables, the magenta point does not change in position space. The solution is $\bar{\bar{x}} = [.5 \ .1 \ 0 \ .1 \ .6 \ 0 \ 0]$ in nondimensional units.

For a spacecraft at $\bar{\bar{x}}_0$, an impulsive maneuver of $\Delta V = 114.5$ meters per second is necessary to change its path from the yellow dotted line to the blue curve.
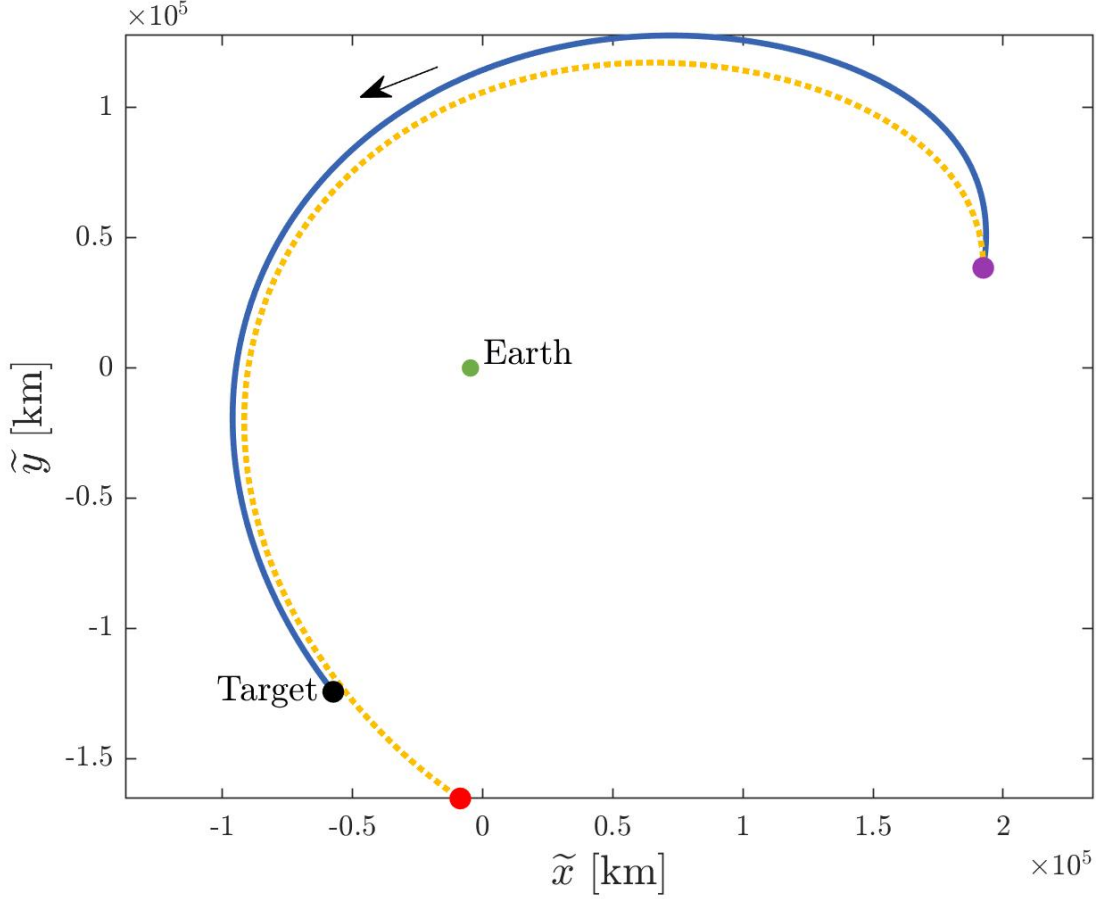
Figure 3.2. Resultant transfer from the single shooting algorithm (blue) with the initial guess to the targeter (yellow)

There are an abundance of techniques to implementing single shooting algorithms. The example portrayed in Figure 3.2 is one type of single shooting algorithm. The process of selecting the free variables and constraints offer numerous targeting problem. For instance, if the previous scenario is extended to allow the time of flight to vary, then the Jacobian is no longer square, and an infinite number of solutions exist. Likewise, instead of including the time of flight, allowing the initial Sun angle to change provides insight into the impact of solar perturbations on this transfer. The application of Newton-Raphson methods through single shooting is an effective tools in trajectory design.

3.3.2 Multiple Shooting Method

Multiple shooting algorithms are an approach to addressing the nonlinear challenges in dynamically sensitive regions. The Newton-Raphson approach relies on a linear approximation of the nonlinear dynamics. As the propagation time for a single arc increases, or the arc passes near a primary body, the linear approximation becomes less effective. Multiple shooting algorithms discretize a transfer arc into multiple segments, each with a set of free variables and constraints. Discretizing the baseline path aids in complications due to sensitive dynamical regions and long transfer times. A disadvantage to multiple shooting is the complexity in building the algorithm and increased computational resources. A schematic for the multiple shooting approach for three segments is illustrated in Figure 3.3. Each segment is defined by the initial state $\bar{x}_{i,0}$ and propagation time t_i, where i is the segment number. Each arc in Figure 3.3 has a final state denoted as $\bar{x}_{i,f}$. The desired final state of the entire transfer is illustrated as $\bar{x}_d$.
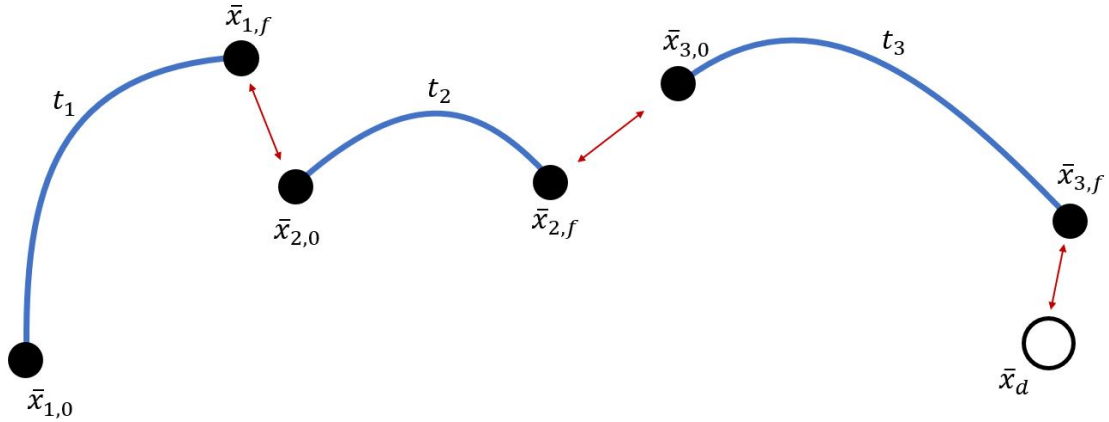
Figure 3.3. Schematic of a discretized transfer prior to differential corrections, an example initial guess for multiple shooting

A majority of multiple shooting algorithms include continuity constraints. Indicated in Figure 3.3 by the red arrow between $\bar{x}_{1,f}$ and $\bar{x}_{2,0}$, a continuity constraint suggests that the final state of one segment equals the initial state of the proceeding segment. If a continuity constraint is met, then a spacecraft follows a ballistic path from one arc to the next. From

89

the schematic in Figure 3.3, two continuity constraints exist. Convergence in the multiple shooting algorithm produces the schematic illustrated in Figure 3.4, where the continuity and targeting constraints are met, i.e., $\bar{x}_{1,f} = \bar{x}_{2,0}$, $\bar{x}_{2,f} = \bar{x}_{3,0}$, and $\bar{x}_{3,f} = \bar{x}_d$.
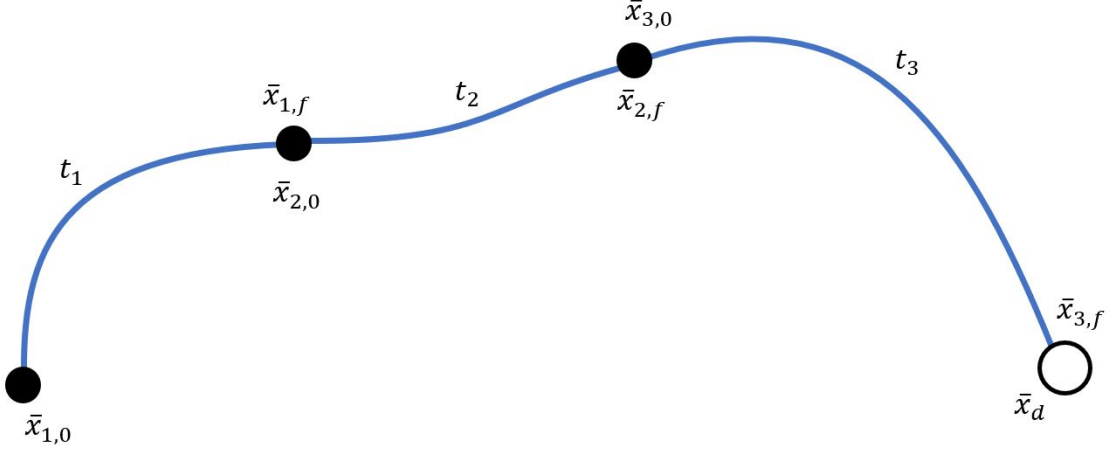
Figure 3.4. Schematic of a discretized transfer after differential corrections, a result of multiple shooting

To construct a multiple shooting algorithm, consider an arc discretized into Q segments. Assume segments one through $Q-1$ has a continuity constraint. Segment Q targets a desired state $\bar{x}_d$. A schematic for of segments for the case where $Q = 3$ is portrayed in Figure 3.3. The design variable vector is composed of the initial states of each segment,

$$\bar{X} = \begin{bmatrix} \bar{x}_{1,0} & \bar{x}_{2,0} & \bar{x}_{3,0} & \cdots & \bar{x}_{Q-1,0} & \bar{x}_{Q,0} \end{bmatrix} \tag{3.31}$$

and the constraint vector is

$$\bar{F} = \begin{bmatrix} \bar{x}_{1,f} - \bar{x}_{2,0} & \bar{x}_{2,f} - \bar{x}_{3,0} & \cdots & \bar{x}_{Q-1,f} - \bar{x}_{Q,0} & \bar{x}_{Q,f} - \bar{x}_d \end{bmatrix} \tag{3.32}$$

As six components are necessary to define a state in the CR3BP, there are $6Q$ free variables and constraints in this multiple shooting formulation. Thus, the Jacobian is a $6Q$x$6Q$ matrix written as,

$$D\bar{F}(\bar{X}) = \begin{bmatrix} \mathbf{\Phi}_1 & -\mathbf{I} & \mathbf{0} & \cdots & \mathbf{0} & \mathbf{0} \\ \mathbf{0} & \mathbf{\Phi}_2 & -\mathbf{I} & \cdots & \mathbf{0} & \mathbf{0} \\ \vdots & \vdots & \ddots & \ddots & \vdots & \vdots \\ \mathbf{0} & \mathbf{0} & \mathbf{0} & \cdots & \mathbf{\Phi}_{Q-1} & -\mathbf{I} \\ \mathbf{0} & \mathbf{0} & \mathbf{0} & \cdots & \mathbf{0} & \mathbf{\Phi}_Q \end{bmatrix} \tag{3.33}$$

where $\mathbf{\Phi}_i$ is the state transition matrix of segment i, $\mathbf{I}$ is a six-dimensional identity matrix, and $\mathbf{0}$ is a 6x6 zero matrix. Since the matrix $D\bar{F}(\bar{X})$ is non-singular the update equation as formulated in Equation (3.26) is applied. The size of the Jacobian matrix grows by six rows and columns for each segment added. Therefore, the computational load for a multiple shooting algorithm increases for each discretized segment. Although many of the entries are zero, computing the inverse of a large matrix is computationally expensive. Therefore, arbitrarily choosing a large number of segments comes with numerical consequences.

Multiple shooting is applied extensively throughout this investigation. Similar to the single shooting method, the scenario devised is one application of multiple shooting. Selecting the appropriate constraints and free variables directly impacts the desired result of the targeter. Additional constraints include periapse, periodicity, radius, time of flight, epoch, energy, and velocity direction constraints. Incorporating desired constraints aids in development of trajectory design.

3.4 Continuation Methods

It is insightful to analyze a larger design space when assessing the efficiency of a solution. A range of solutions offers comparison metrics, that are employed to determine relative performance. A set of solutions that vary across some parameter is denoted as a family. In this investigation, there are families of transfers, periodic orbits, and instantaneous equilibrium points. Families are constructed by applying a continuation scheme to a solution. Two con-

91

tinuation methods considered are applied in this analysis. Natural Parameter continuation varies a physical quantity of the solution (that is not a design variable), and recomputes a new solution. The second approach is Pseudo-Arclength continuation, that steps along a non-physical property of the design vector.

3.4.1 Natural Parameter Continuation

Constructing a family by stepping along a physical parameter of the solution is labelled Natural Parameter continuation. Physical parameters represent perceptible components of a transfer, including position or velocity components, primary angles (Sun angle or Earth-Moon angle), energy quantities, time of flight, and maneuver magnitude. Natural Parameter continuation begins with a converged solution to a Newton-Raphson targeting algorithm. A natural parameter of the solution is augmented, and the differential corrections process is recomputed until convergence. The iterative process resumes until the targeting algorithm no longer converges, or a terminal condition is met. Note the continuation parameter must not be a design variable of the corrections algorithm, otherwise the targeter could reconverge on the initial solution.

Recall the sample scenario constructed for the single shooting method in Figure 3.2. The time of flight remained fixed at five days, resulting in solution that require an impulsive maneuver of $\Delta V = 114.5$ m/sec to fulfill the constraints. Consider that the time of flight is allowed to vary, such that a minimum maneuver magnitude is desired. Natural parameter continuation is applied to the solution illustrated in Figure 3.2, where the time of flight is varied. As the final position constraints are no longer fulfilled, the single shooting method is reapplied to determine an updated solution. A family of transfers that arrive at the desired position is illustrated in Figure 3.5. Each transfer remains in the $\tilde{x}\tilde{y}$-plane, and the colors correspond to the maneuver cost necessary to impart from the initial state.
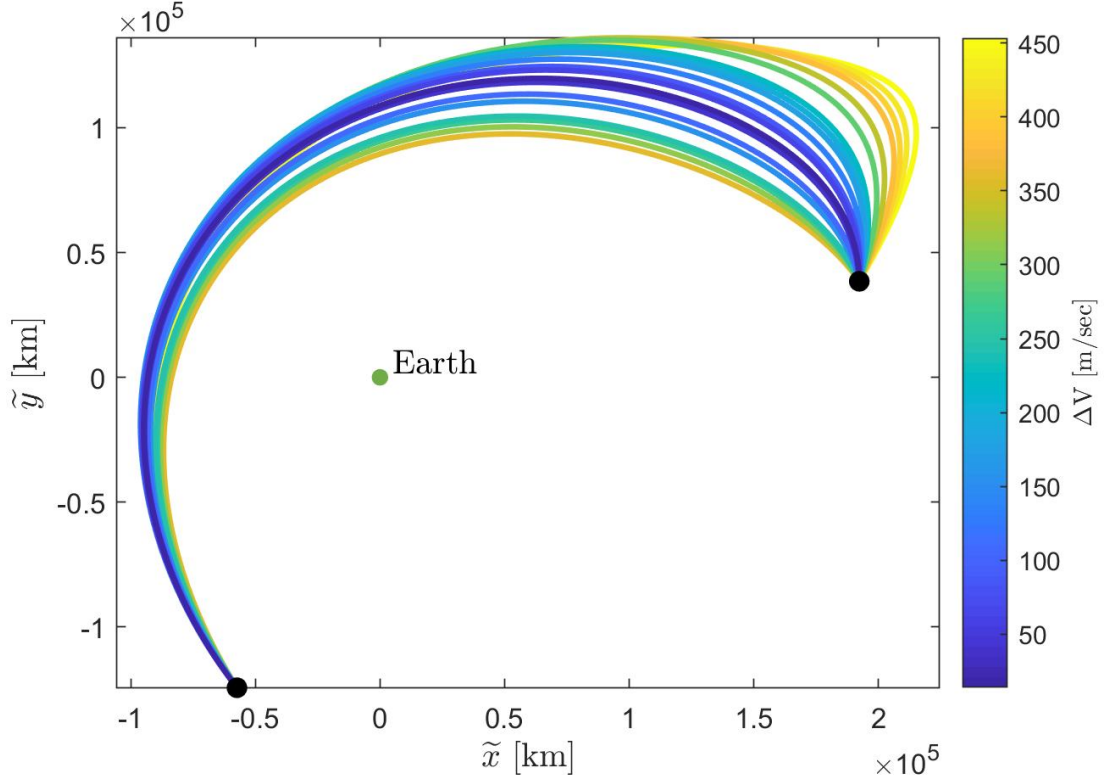
Figure 3.5. Family of planar transfers with the same initial and final position

The variation in time of flight along the family and the influence on the maneuver cost are depicted in Figure 3.5. Recall the single shooter scenario, the transfer had a flight duration of five days, and requires an impulsive maneuver of $\Delta V = 114.5$ meters per second. The curve illustrated on Figure 3.6 demonstrates that lower maneuver cost solutions exist, if the time of flight is free to change.
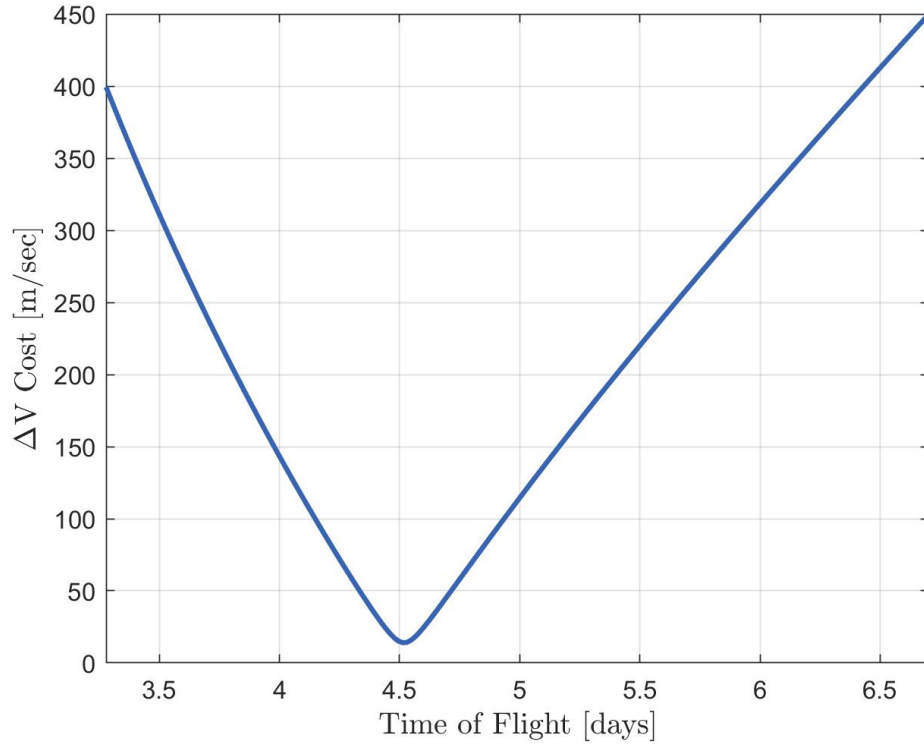
Figure 3.6. Evolution of time of flight and maneuver cost for the family of transfers depicted in Figure 3.5

Natural parameter continuation is limited by the natural progression of the family. An assumption that is made when pursing natural parameter continuation is that a solution exists with the specified initial guess provided. In general, there is no a priori knowledge of the solution-space. Therefore, is it not guaranteed that a given natural parameter will result in a member of the family. The disadvantage to continuing along a natural parameter is the uncertainty of solutions, since it is not guaranteed that a solution will exist for a arbitrary parameter. However, the main advantage to continuing through a natural parameter is the intuition provided by the physical quantity. As a family progresses as a function of a physical quantity, there is a clear understanding how the members of the family relate to each other.

3.4.2 Pseudo-arclength Continuation

Families of solutions are constructed along a non-physical parameter through pseudo-arclength continuation [27]. Natural parameter continuation is aided by knowledge of the family. However, in the case where the solution space is unfamiliar, it is not ensured that another solution exists with the anticipated initial condition. Pseudo-arclength continuation requires no prior insight into the solution space. Consider a differential corrections problem where the free variable vector has length n and the constraint vector has length m, as described in Equation (3.19) and Equation (3.20), respectively. To continue along a family, the differential correction scheme is composed such that there is one more free variable than constraint, i.e., $n - m = 1$. Recall that such a corrector would be underdetermined, and thus, an infinite number of solutions fulfill the constraint vector. The Jacobian by definition has a nullity of one, where the nullspace vector has dimension of $n \times 1$, and is tangent to the solution space of the family.

A non-physical stepping parameter is applied to the nullspace vector to target unique solutions amongst the family. The process first requires an initial solution to the constraint vector, $\bar{X}_i$. Let $\Delta \bar{X}_i = \text{Null}(D\bar{F}_i)$ where $D\bar{F}_i$ is the Jacobian of the initial solution. The initial condition for the next step in the continuation scheme is $\bar{X}_{i+1} = \bar{X}_i + s\Delta\bar{X}_i$, where s is an arbitrary scalar step along the nullspace vector. As the Jacobian is underdetermined, it is not guaranteed that a new solution is produced, as the targeter may reconverge on the first solution. Therefore, an additional constraint is introduced to ensure the new solution is unique, i.e., further along the solution space.

$$F_n = (\bar{X}_{i+1} - \bar{X}_i)\Delta\bar{X}_i - s \tag{3.34}$$

The constraint guarantees that the previous solution $\bar{X}_i$ and new solution $\bar{X}_{i+1}$ are of length s apart along the null vector of the Jacobian. The partial derivative of Equation (3.34) with respect to the free variable vector is the nullspace vector. The psuedo-arclength constraint

is appended to the constraint vector of the differential corrector. The result is a vector with length $m + 1$, which equals n.

$$\bar{F} = \begin{bmatrix} F_1(\bar{X}_{i+1}) \\ F_2(\bar{X}_{i+1}) \\ \vdots \\ F_m(\bar{X}_{i+1}) \\ (\bar{X}_{i+1} - \bar{X}_i)\Delta\bar{X}_i - s \end{bmatrix} \tag{3.35}$$

The Jacobian is constructed as the partial of the constraint vector relative to the free variable vector $\bar{X}_{i+1}$, resulting in a square matrix. An iterative update formulated in Equation (3.26) is applied to fulfill the constraint vector. Once the constraints are met, the initial free variable vector $(\bar{X}_i)$ is updated to the new solution, and the corrections process is repeated.

Pseudo-arclength continuation aids in the construction of dynamical structures. There is not always a physical parameter that will grow monotonically with a family. Therefore, an advantage to pseudo-arclength is that the initial guess steps along a vector to tangent to the solution-space, rather than a single parameter. A disadvantage to pseudo-arclength continuation is the lack of significance of a step size or direction, as the solution space is generally a higher dimensional vector. It is simpler to comprehend natural parameter continuation, as each member of the family evolves strictly a function of one component. The continuation scheme employed is reliant on the intended results, and the complexity of the problem.

3.5 Periodic Solutions

Periodic orbits offer insight into repeatable structures and flow throughout a dynamical model. A periodic orbit is a trajectory that repeats back to the initial state at a later time. There are multiple approaches to constructing periodic orbits. These techniques include linear stability analysis around an equilibrium solution, leveraging symmetry of a dynamical model, and enforcing continuity constraints between the initial and final states. Each technique is frequently aided by the others, where the selected approach is governed by

the characteristics of the intended result. The numerical process of constructing a periodic orbit relies on differential correction schemes. By definition, periodic orbits in the BCR4BP are similar to those in the CR3BP, yet due to slight differences in the model, result in more complex behavior.

The Mirror Theorem provides a framework to compute symmetric periodic orbits. The transformation matrix from Equation (2.35) maps a state in the CR3BP to its symmetric counterpart across the $\hat{x}\hat{z}$-plane, where the transfer in reverse time matches the state propagated forward in time. For a state to be equivalent to its symmetric counterpart, $\bar{x}J(-t) = \bar{x}$, i.e., $y = \dot{x} = \dot{z} = 0$. The physical interpretation is denoted as a perpendicular crossing, where P_3 lies on the $\hat{x}\hat{z}$-plane, and the velocity vector is along the $\hat{y}$ direction. If along a transfer, two states occur that fulfill the perpendicular crossing condition, then that trajectory is part of a periodic orbit [21]. The time between the two perpendicular crossings is half the period of the entire periodic orbit. To construct a perpendicular crossing targeter, a single shooting algorithm is adapted to where the free variable and constraint vectors are

$$
\bar{X} = \begin{bmatrix} x_0 \\ z_0 \\ \dot{y}_0 \\ t \end{bmatrix} \qquad\qquad \bar{F} = \begin{bmatrix} y_f \\ \dot{x}_f \\ \dot{z}_f \end{bmatrix} \tag{3.36}
$$

and $y_0 = \dot{x}_0 = \dot{z}_0 = 0$ must also be fulfilled. The Jacobian is underdetermined, thus, an infinite number of solutions are available. One example of a symmetric periodic orbit is a L_1 Lyapunov. An L_1 Lyapunov orbit is illustrated in Figure 3.7. The Jacobi constant value of this orbit is 3.0656, and the orbit has a period of 14.8 days. The spacecraft traverses the orbit clockwise, as denoted by the arrows. The dashed line along the $\hat{x}$-axis represents the line of symmetry. The two instances where the periodic orbit crosses the $\hat{x}$-axis fulfill the perpendicular crossing constraints from Equation (3.36). The orbit in Figure 3.7 is called a L_1 Lyapunov orbit, because the initial conditions of this orbit family originate from a Lyapunov stability analysis of the L_1 equilibrium point. Hence, the orbit is centered around L_1, rather than the Earth or Moon.
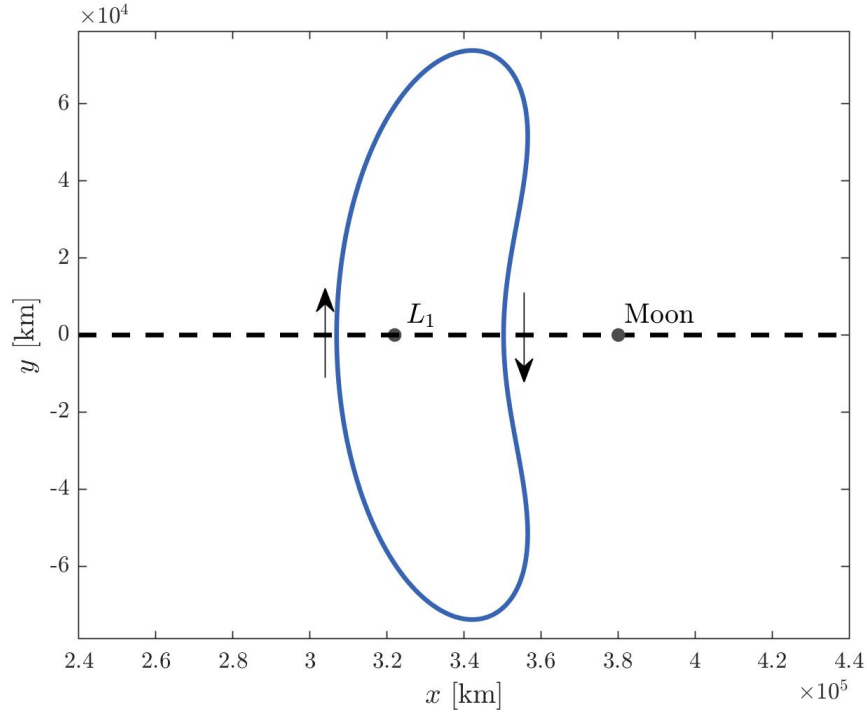
Figure 3.7. L_1 Lyapunov Orbit in the Earth-Moon CR3BP, with period of 14.8 days

As the perpendicular crossing targeter is underdetermined, a family of periodic orbits is constructed. A subset of the L_1 Lyapunov orbit family in the Earth-Moon CR3BP is illustrated in Figure 3.8. The color scale represents the Jacobi constant for each member of the family; yellow corresponds to a higher Jacobi constant, or a lower energy. The L_1 Lyapunov orbit family is just one example of a family that exists in the CR3BP. There is extensive analysis in the field of multi-body dynamics into types of periodic orbits, their accessibility throughout space, and mission applications. Periodic orbit families offer expanded sets of solutions with similar dynamical properties.
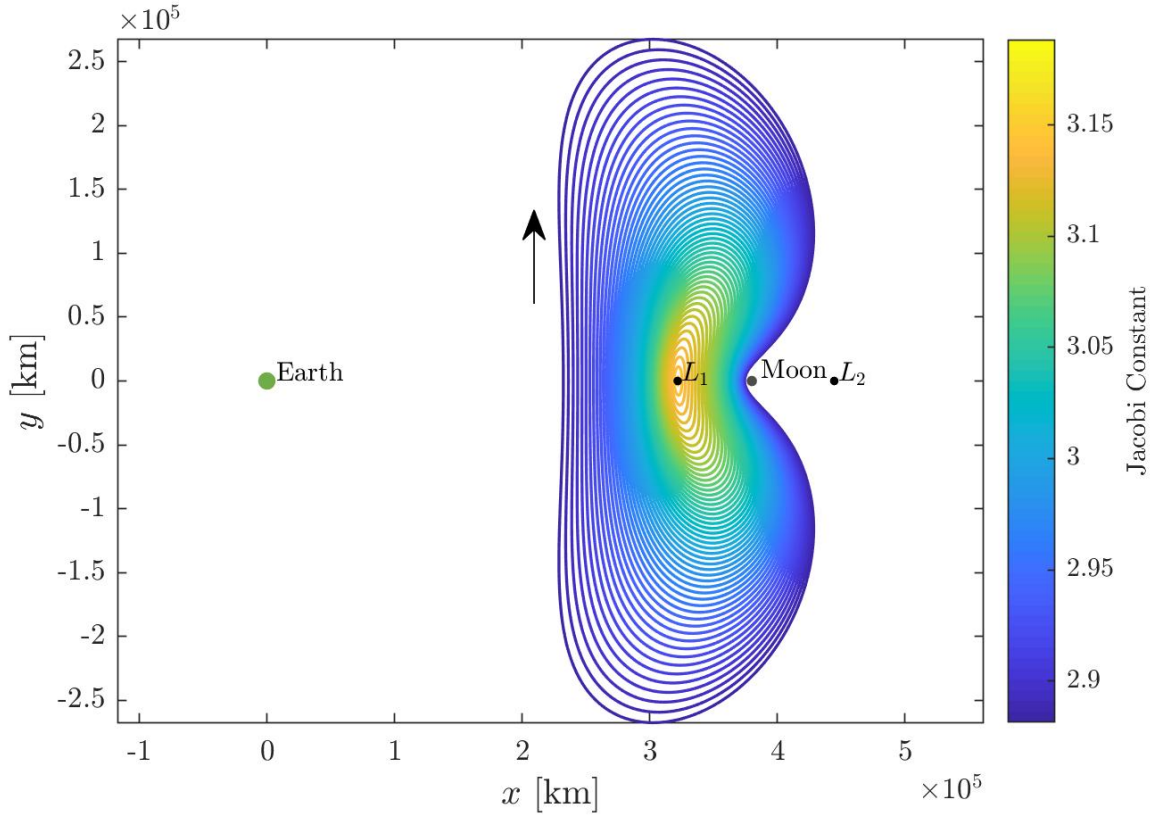
Figure 3.8. Family of L_1 Lyapunov orbits in the Earth-Moon CR3BP, where the color scale corresponds to the Jacobi constant of each member

Periodic orbits in the BCR4BP rely on a resonance with the synodic period. As a periodic orbit requires all states to return back to the initial condition, the orientation angles θ_S and θ_{EM} evolve linearly with time. Therefore, the period of a periodic orbit in the BCR4BP must be an integer multiple of the synodic period. Unlike the CR3BP where there are periodic orbit families with evolving periods, the BCR4BP has unique point solutions. There are multiple approaches to constructing periodic orbits in the BCR4BP: natural parameter continuation, periodicity from a CR3BP orbit, perpendicular crossing targeter. Each technique is more complex than the approaches in the CR3BP, as the additional restriction on period limits the available solutions. Natural parameter continuation leverages an initial condition from the CR3BP, and gradually steps in Sun mass or distance between the Earth and Moon, until the

full BCR4BP is met [15], [28]. The perpendicular crossing targeter for the BCR4BP requires the perpendicular crossings to occur when the Sun angle or Earth-Moon angle are equal to an integer multiple of π, as $\theta_S = -\theta_S$ must be fulfilled. To obtain an initial condition from the CR3BP, consider the L_1 Lyapunov orbit family in the CR3BP displayed in Figure 3.8. To assess which orbit members have resonance with the synodic period T_{syn}, properties of each orbit are plotted as a continuous curve in Figure 3.9. The blue curve depicts the evolution in period and Jacobi constant along the L_1 Lyapunov family. The synodic resonance ratio is the period of an orbit divided by the synodic period, i.e., $\frac{T}{T_{syn}}$. The black dots are $A : B$ resonance ratios between the period of the orbit and the synodic period, where A is the number of revolutions of the orbit for B synodic periods. For example, the CR3BP orbit with a 4:3 resonance would complete four revolutions of the Lyapunov orbit in the amount of time it takes the Sun to traverse around the Earth-Moon rotating frame three times ($3T_{syn}$). Likewise, the CR3BP orbit with a 1:1 resonance has the same orbital period as the synodic resonance.
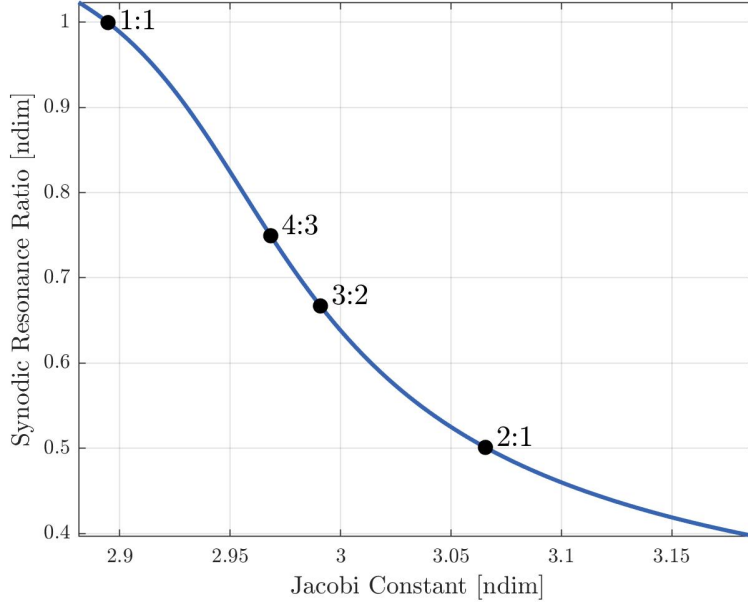
Figure 3.9. Evolution of the Jacobi constant and period for the L_1 Lyapunov orbit family in the Earth-Moon CR3BP; black dots represent where the period is an integer ratio of the synodic period

A periodic orbit in the BCR4BP is constructed using the perpendicular crossing technique. To display the method, the 2:1 synodic resonant L_1 Lyapunov in the CR3BP is selected as the initial condition. The first step obtains one of the two perpendicular crossing states from the corresponding orbit in the CR3BP. For this scenario, the initial condition in the CR3BP is $\bar{x} = \begin{bmatrix} 0.9104 & 0 & 0 & 0 & -0.4677 & 0 \end{bmatrix}$ (nondimensional units) and the period of the orbit is 14.797 days $(\frac{1}{2}T_{syn})$. A Sun angle of either zero or π is appended to construct a complete state in the BCR4BP. A single shooting, differential corrector is formulated as

$$\bar{\bar{X}} = \begin{bmatrix} \tilde{x}_0 \\ \tilde{z}_0 \\ \dot{\tilde{y}}_0 \end{bmatrix} \qquad \bar{\bar{F}} = \begin{bmatrix} \tilde{y}_f \\ \dot{\tilde{x}}_f \\ \dot{\tilde{z}}_f \end{bmatrix} \qquad (3.37)$$

A key difference between Equation (3.36) and Equation (3.37) is the control of the propagation time. As the BCR4BP requires both perpendicular crossings to occur at a specific Sun angle, the period of the orbit is restrained. Where before in the CR3BP the problem was underdetermined and a family of solutions existed, the BCR4BP has a unique solution to the targeter. However, multiple solutions in the BCR4BP are obtained through proper selection of the initial conditions. In this case, after the targeting scheme is applied, the states $\bar{\bar{x}}_L = \begin{bmatrix} 0.7961 & 0 & 0 & 0 & 0.3778 & 0 & 0 \end{bmatrix}$ and $\bar{\bar{x}}_R = \begin{bmatrix} 0.9072 & 0 & 0 & 0 & -0.4479 & 0 & 0 \end{bmatrix}$ in nondimensional units are revealed. The states represent two separate 2:1 synodic resonant L_1 Lyapunov orbits in the BCR4BP. Where the subscripts L and R correspond to having either a left or right perpendicular crossing when the Sun angle is zero. The two 2:1 synodic resonant L_1 Lyapunov orbits in the Earth-Moon rotating frame are illustrated in Figure 3.10. The blue curve portrays $\bar{\bar{x}}_L$, and the yellow curve represents $\bar{\bar{x}}_R$. Both orbits follow similar motion to the initial guess from the CR3BP, with slight deviations due to the influence of the Sun. The orbits visually appear periodic after one revolution (14.797 days), however, they are not. As these are 2:1 synodic resonant orbits, the orbits are only periodic after two revolutions, i.e., one synodic period.
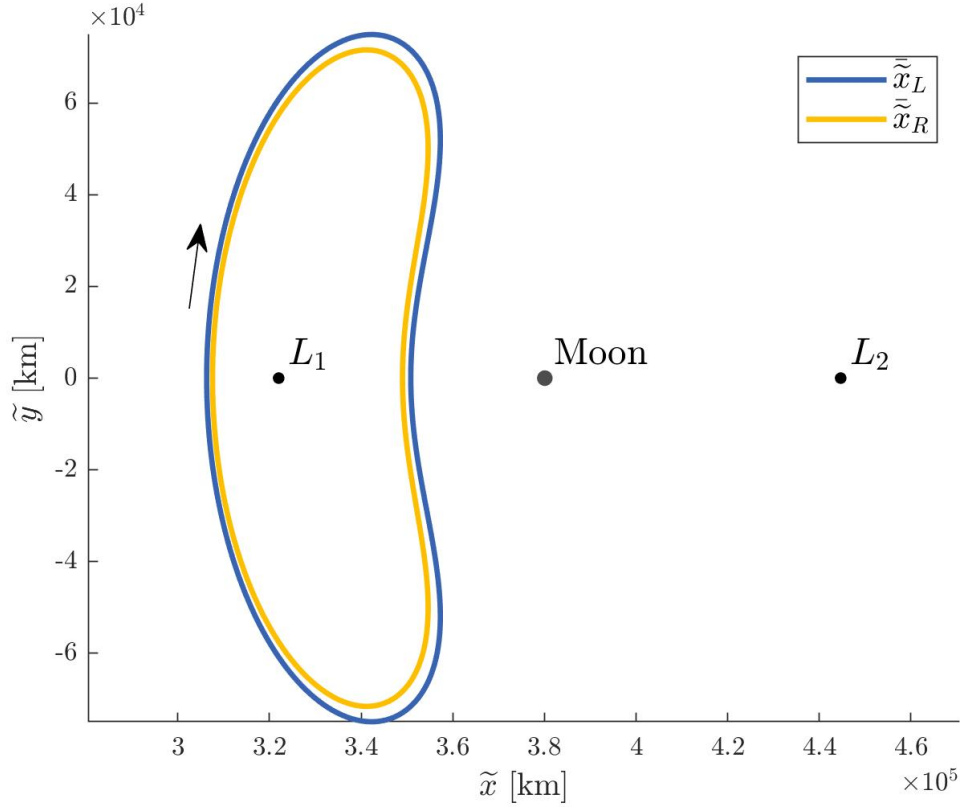
Figure 3.10. Two 2:1 synodic resonant L_1 Lyapunov orbits in the Earth-Moon rotating frame of the BCR4BP

Periodic orbits in the BCR4BP are periodic in both the Earth-Moon and Sun-B_1 rotating frames. As the two rotating frames are time-dependent on the synodic period, the system repeats at the same interval (orientation of the primary bodies). Thus, a closed curve in one rotating frame is also closed in the other. This is not true if an orbit is transitioned to the the initial reference frame, as the initial frame also relies on the sidereal period of the system. Therefore, plotting motion in two references frames provides insight into differences between dynamical structures. For example, the two 2:1 L_1 Lyapunov orbits in Figure 3.10 illustrates the motion that emulates the solution from the CR3BP, but is unclear how the orientation of the Sun influences the patterns. By displaying the same periodic orbits in the Sun-B_1 rotating coordinate frame, where the location of the Sun is fixed, the impact of the Sun is clearly visualized. The two 2:1 synodic resonant L_1 Lyapunov orbits plotted in the Sun-B_1 rotating reference frame is illustrated in Figure 3.11. The dashed black circle

is the Moon's orbit, and the black circle is the Earth's orbit, both about the Earth-Moon barycenter B_1. The Sun is to the left in this frame. In the Sun-B_1 rotating frame, the solar influence becomes more apparent as the periodic solutions appear to be offset by one another by a fourth of the synodic period (7.38 days).
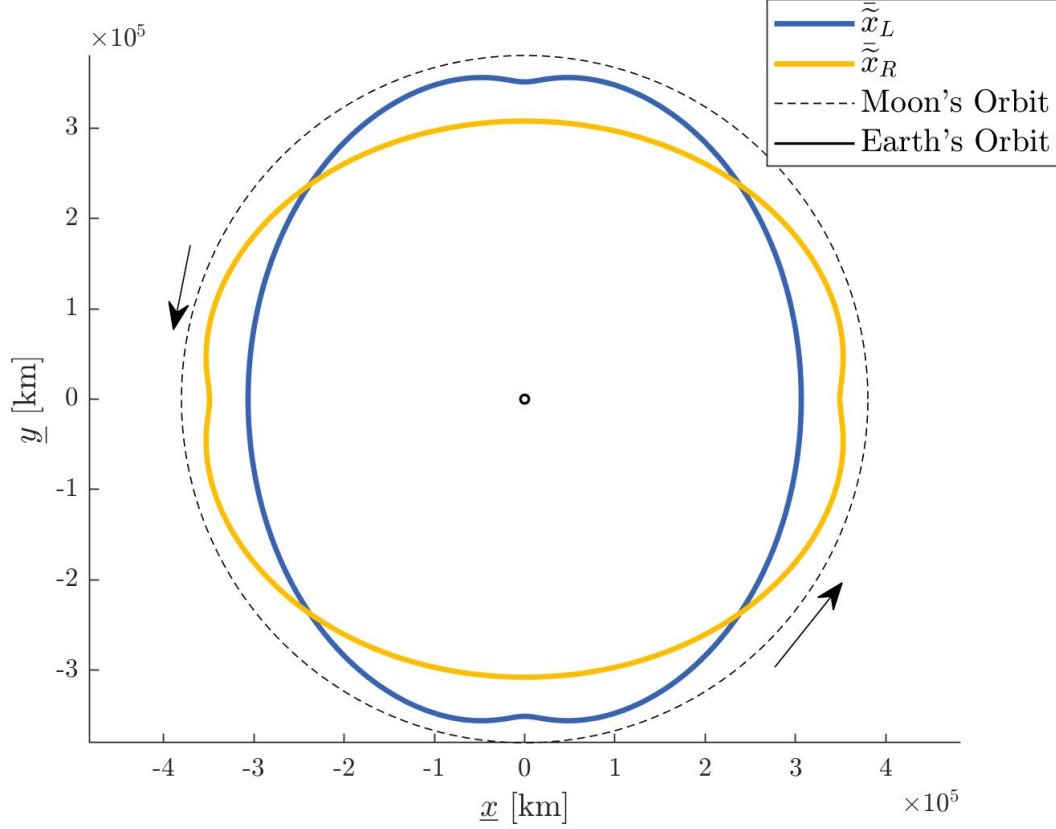
Figure 3.11. Two Earth-Moon 2:1 synodic resonant L_1 Lyapunov orbits in the Sun-B_1 rotating frame, centered at B_1 with the Sun to the left

The Hamiltonian evolves as a spacecraft traverses along a periodic orbit. Much like an arbitrary trajectory, the Hamiltonian values vary as P_3 moves through the BCR4BP. However, as the trajectory must return back to the initial state, the Hamiltonian is periodic. Unlike the CR3BP, the energy of the spacecraft varies at different locations on the periodic solution. The Hamiltonian values for the same two L_1 Lyapunov orbits as a function of Sun angle is portrayed in Figure 3.12. The Earth-Moon Hamiltonian H_{EM} is represented in Figure 3.12a, and Figure 3.12b demonstrates the Sun-B_1 Hamiltonian H_{SB_1}. The blue and

yellow curves represent $\bar{\bar{x}}_L$ and $\bar{\bar{x}}_R$, respectively. Each Sun angle represents a unique state along the orbits. The curves in Figure 3.12a demonstrate that the blue orbit has a lower Earth-Moon Hamiltonian throughout all time. Whereas Figure 3.12b reveals the Sun-B_1 Hamiltonian between the two orbits is nearly equivalent, but offset by 90 degrees.
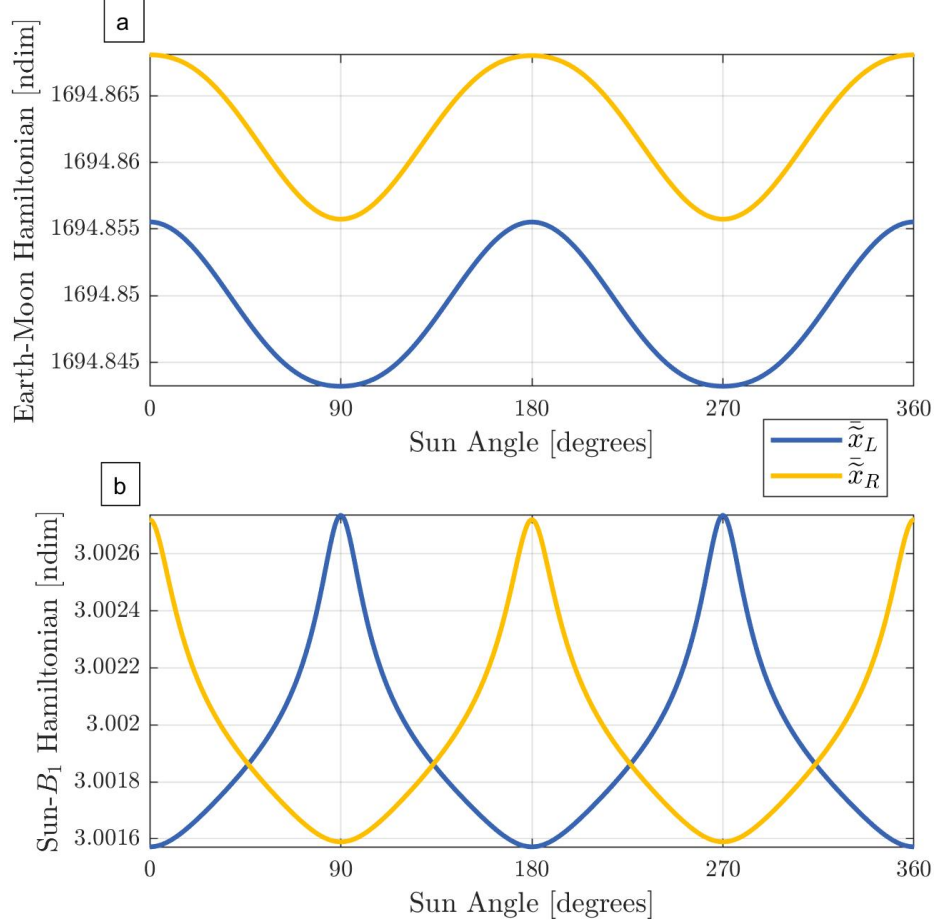
Figure 3.12. Evolution in the Earth-Moon (a) and Sun-B_1 (b) Hamiltonian for the L_1 Lyapunov orbits illustrated in Figure 3.10

Periodic orbits provide favorable, repeatable motion which is advantageous in dynamical systems theory. Periodic solutions in the multi-body regime offer solutions that would otherwise be impossible in the two-body problem. Periodic orbits offer starting locations, desired destinations, and intermediate arcs in the CR3BP and the BCR4BP. Families of periodic orbits present insight into the dynamical structures that govern motion in the CR3BP. Point

solution orbits near the Earth and Moon in the BCR4BP extend the repeatable motion into a more complex environment, under the perturbing influence of the Sun. Through Lyapunov stability analysis, further insight is gained from dynamical structures in the multi-body regime.

3.6 Poincaré Maps

Poincaré maps are effective tools that lower the dimensionality of dynamical structures. A Poincaré map is defined as a hyperplane, or smooth surface denoted as Σ. The hyperplane is chosen to fulfill a desired criteria, including but not limited to a $\hat{x}\hat{z}$-plane crossing when $y = 0$, an apse condition about a primary, or a specified orientation of the primaries [29]. For the instant where a transfer passes through the hyperplane, that state is projected onto the Poincaré map. In the CR3BP, it is advantageous to fix the Jacobi constant for a Poincaré map, as the integral of motion also lowers the dimensionality of the state. For example, a planar trajectory in the CR3BP can be fully described by a Poincaré map for a fixed Jacobi constant, as the four dimensional state is reduced to two dimensions, which is trivial to visualize. Trajectories passing through a Poincaré map is illustrated in Figure 3.13. The arc in green starts on the map at $x(t_0)$, and propagates forward until intersecting the map again at $x(T + t_0)$. One trajectory can be represented on the hyperplane multiple times, as displayed by the two green points. The transfer in black intersects the hyperplane at x^*. As the state at x^* evolves with time, it returns back to the same state, making it a periodic orbit. Periodic solutions are fixed points on Poincaré maps, which aids in the analysis of stability characteristics for these orbits.

Periapse Poincaré maps are employed in this investigation to aid in visualization for motion throughout the BCR4BP. The time-dependency and lack of an integral of the motion increases the complexity of the BCR4BP. Therefore, by incorporating Poincaré maps into the analysis, specified conditions are compared across a range of trajectories. For Poincaré maps that rely on a physical property of a rotating frame, such as an $\hat{\hat{x}}\hat{\hat{z}}$-plane crossing), the condition is less intuitive in the Sun-B_1 rotating frame. Therefore, an apse condition is advantageous for the BCR4BP as the condition is perceptive in both rotating frames. For
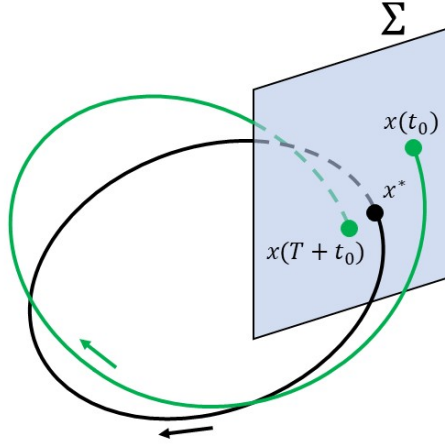
Figure 3.13. Illustration of a Poincaré map, adapted from Perko [29]

the construction of ballistic lunar transfer, periapse conditions about the Earth and Moon produce effective departure and arrival locations.

3.7 Invariant Manifolds

Invariant manifold theory leverages stability properties to reveal underlying dynamical structures within a model. Insight into flow throughout the model is obtained by performing stability analyses about fixed points. In this investigation, equilibrium and periodic solutions are fixed points in the continuous and discrete time systems, respectively. To assess stability in the vicinity of these solutions, a Lyapunov stability analysis is performed. Lyapunov stability leverages linear characteristics of the solution to predict local motion. These characteristics rely on the eigenstructure of the Jacobian matrix [30].

3.7.1 Equilibrium Solution Manifolds

Manifolds off equilibrium points demonstrate local flow. Consider the Lagrange points for the Earth-Moon system, written in Table 2.1. Understanding motion toward and away from the Lagrange points is nontrivial. As the model progresses through time, the equilib-

106

rium solution remains fixed. A stability analysis is performed to uncover properties of the solutions. As each of the five points have a unique position, they each have a unique set of linear variational equations $\mathbf{A}(t)$, written out in Equation 3.8. For the Lagrange points, $\mathbf{A}(t)$ is a constant Jacobian matrix describing motion in the CR3BP. Assume some small perturbation $\delta\bar{x}$ from the fixed point, the time response produces

$$\delta\bar{x}(t) = e^{\mathbf{A}(t-t_0)}\delta\bar{x}(t_0) \tag{3.38}$$

The eigenstructure of the Jacobian is necessary, $\mathbf{A}(t-t_0)\mathbf{S} = \mathbf{\Lambda S}$, where $\mathbf{S}$ is a the eigenvector matrix, and $\mathbf{\Lambda}$ is a diagonal matrix composed of eigenvalues. An eigenvalue (λ) in the first row of $\mathbf{\Lambda}$ relates to the eigenvector $(\bar{\nu})$ in the first column of $\mathbf{S}$. The spectral decomposition of the matrix exponential produces

$$e^{\mathbf{A}(t-t_0)} = \sum_{i=1}^{j} e^{\lambda_i}\bar{\nu}_i\bar{w}_i^T \tag{3.39}$$

where $\bar{w}_i$ is the left eigenvector associated with i^{th} eigenvalue, and j is the size of the Jacobian, which is six for the CR3BP and seven for the BCR4BP. Combing Equation (3.38) and Equation (3.39) results in

$$\delta\bar{x}(t) = \sum_{i=1}^{j} e^{\lambda_i(t-t_0)}\bar{\nu}_i\bar{w}_i^T\delta\bar{x}(t_0) \tag{3.40}$$

Although Equation (3.40) appears complex, the term $\bar{w}_i^T\delta\bar{x}(t_0)$ is a scalar. Selection in the initial perturbation produces an isolated stability response. Consider $\bar{x}(t_0)$ as an eigenvector of $\mathbf{A}(t)$, $\bar{\nu}_k$. As the linear variational equations are linearly independent, for all left eigenvectors $\bar{w}_i$ for $i \neq k$, the product with the right eigenvector is zero, i.e., $\bar{w}_i^T\delta\bar{\nu}_k = 0$. However, for the case when $i = k$, the product of the left and right eigenvalues produces one, i.e., $\bar{w}_i^T\delta\bar{\nu}_k = 1$. Therefore, for the case when $\delta\bar{x}(t_0)$ is an eigenvector of the matrix $e^{\mathbf{A}(t-t_0)}$, the isolated response is

$$\delta\bar{x}(t) = e^{\lambda_k(t-t_0)}\bar{\nu}_k \tag{3.41}$$

Equation (3.41) demonstrates the significance of the eigenstructure on dynamic responses, and the case for Lyapunov stability in a continuous time system. Recall the initial perturbation is originating from a fixed point. The direction of flow is governed by the eigenvector, and the deviation magnitude depends on the eigenvalue. If the real component of an eigenvalue is less than zero, i.e., $\text{Re}[\lambda_k] < 0$, then $e^{\lambda_k(t)}$ approaches zero as time progresses. Describing motion that approaches the Lagrange point, this motion is called asymptotically stable. Conversely, if the real component of an eigenvalue is positive, i.e., $\text{Re}[\lambda_k] > 0$, then $e^{\lambda_k(t)}$ grows exponentially through time. The continuous expansion departs from the Lagrange point, and is referred to as unstable. If the eigenvalue is complex, $\text{Im}[\lambda_k] \neq 0$, the perturbation produces oscillatory motion, denoted as a center subspace. The eigenstructure is separated into three subsets, the stable, unstable, and center subspace, also written as E^S, E^U, and E^C. Table 3.1 contains the six eigenvalues for each Lagrange point in the Earth-Moon CR3BP. The three collinear points have a one-dimensional stable subspace, a one-dimensional unstable subspace, and a four-dimensional center subspace. Whereas the equilateral Lagrange points have a six-dimensional center subspace. For a fixed point to be Lyapunov stable, a small perturbation to the solution must remain near the equilibrium point for all time [24]. Therefore, equilateral points in the Earth-Moon system are Lyapunov stable, as they do not possess an unstable subspace. The collinear points in the Earth-Moon system are unstable, as they have an unstable subspace.

Table 3.1. Eigenvalues of the Earth-Moon Lagrange Points

L_1	$\pm\ 2.9321$	$\pm\ 2.3344i$	$\pm\ 2.2688i$
L_2	$\pm\ 2.1587$	$\pm\ 1.8626i$	$\pm\ 1.7861i$
L_3	$\pm\ 0.1779$	$\pm\ 1.0053i$	$\pm\ 1.0104i$
L_4 and L_5	$\pm\ 0.9545i$	$\pm\ 0.2982i$	$\pm\ 1.0000i$

Invariant manifolds describe the natural flow of motion in the vicinity of fixed points. As the eigenvalues segregate the stability characteristics into distinct subsets, the eigenvectors provide physical directions to illustrate the dynamics. One limitation of the eigenstructure is the dependency on a linear approximation. However, eigenvectors aid in the construction of invariant manifolds. Stable manifolds are structures that dictate the flow that leads

towards a fixed point. Conversely, unstable manifolds convey motion that departs from a fixed point. Center manifolds describe oscillatory motion that remains bounded about the initial condition. Center manifolds off of equilibrium points result in periodic motion [31]. The dimensionality of the manifold is equivalent to the dimension of the subspace. For example, the L_1 Lagrange point has a one-dimensional stable manifold, a one-dimensional unstable manifold, and a four-dimensional center manifold. A stable manifold is denoted as W^{S^+}. The letter of the superscript symbolizes the corresponding subspace, and the sign dignifies the initial $\hat{x}$ step from the fixed point. The stable and unstable manifolds about the L_1 Lagrange point in the Earth-Moon CR3BP are illustrated in Figure 3.14. The blue curves are arcs approximating the stable manifold, leading toward the equilibrium solution, while the red arcs resemble the unstable manifold, departing from the fixed point. The dotted black lines are the stable and unstable subspaces. As the manifolds and subspaces are higher dimensional structures, Figure 3.14 is a projection onto the $\hat{x}\hat{y}$-plane. The initial conditions for the manifolds are constructed by taking a scaled step off of the fixed point along the associated eigenvector. The step size for Figure 3.14 is normalized to be 40 km off of the equilibrium point. Trajectories along the unstable manifold are propagated forward in time, whereas arcs along a stable manifold are propagated in reverse time.
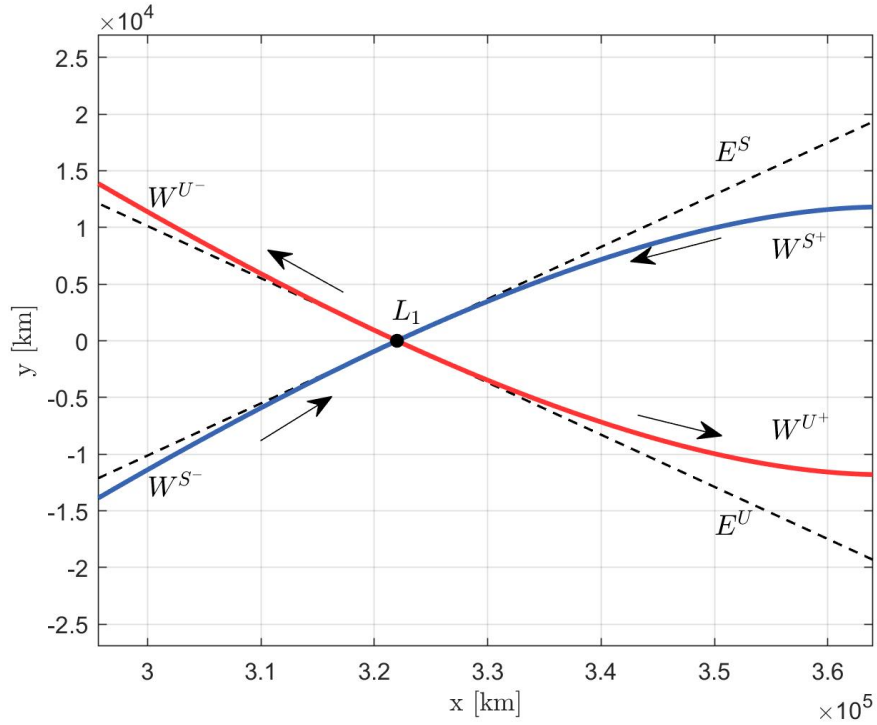
Figure 3.14. Stable and unstable manifolds about the L_1 Lagrange point in the Earth-Moon CR3BP

Trajectories of off instantaneous equilibrium solutions possess some characteristics of invariant manifold. Recall in Section 2.3.2, true equilibrium solutions do not exist in the BCR4BP. However, for a fixed orientation of the primary bodies, instantaneous equilibrium solutions occur. Invariant manifolds only exist off of these solutions for a fixed orientation of the Earth, Moon, and Sun. To leverage flow toward and away the instantaneous equilibrium points, the state themselves are propagated forward and backward in time, producing a transfer in the BCR4BP. These trajectories are not manifolds. Transfers through instantaneous equilibrium points offer low-energy transfer which naturally traverse through small portals in the zero velocity curves.

3.7.2 Periodic Orbit Manifolds

Stability of a periodic solution offers insight into the local dynamical structures. A periodic orbit is a fixed point on a Poincaré map, as illustrated by Figure 3.13. Stability

about the fixed point is performed in a similar approach to the equilibrium points. However, the main difference is the hyperplane maps the motion to a discrete time system [32]. Rather than using the linear variational equations, the stability analysis originates from the STM for one full period of the orbit $\boldsymbol{\Phi}(T+t_0, t_0)$, also called the monodromy matrix. By applying a perturbation $\delta\bar{x}(t_0)$ to a state along the periodic orbit, the resultant deviation after one period is

$$\delta\bar{x}(T + t_0) = \boldsymbol{\Phi}(T + t_0, t_0)\delta\bar{x}(t_0) \tag{3.42}$$

The difference between Equation (3.38) and Equation (3.42) is the monodromy matrix is applied directly to the perturbation. Thus, the eigenstructure of the monodromy matrix describes the stability of the periodic orbit in a discrete time system. The monodromy matrix in an time-independent system is symplectic [32]. The eigenvalues of a symplectic matrix come in reciprocal pairs. For the CR3BP, two of these eigenvalues are equal to one and designate the periodicity of the orbit and the existence of periodic orbit families [33]. To emphasize the value of the two unitary eigenvalues, in a discrete time system, an eigenvalue equal to one would represent deviation from the initial state, such that after one period the state returns back to the initial deviation. The two possibilities for unit eigenvalues include an eigenvector that points along the current periodic solution, and an eigenvector that points toward a new periodic orbit, i.e., along the family of periodic solutions. In the BCR4BP, only one eigenvalue of the STM equals one. The unitary eigenvalue is associated with the progression of the primary bodies, i.e., evolution of time throughout the system. Therefore, the unit eigenvalue in the BCR4BP corresponds to an eigenvector that points along the periodic orbit. The existence of continuous periodic orbit families in the BCR4BP is currently unknown, as the discrete time eigenstructure does not signify their existence.

Stability properties of the monodromy matrix describe behavior near a periodic orbit. In a discrete time system, stability is assessed relative to the unit circle in a complex plane. An eigenvalue that lies within the unit circle, $|\lambda| < 1$ is a part of the stable subspace. Similar to the stability for a Lagrange point, a stable subspace describes motion that flows into the periodic orbit. Conversely, an eigenvalue that exists outside of the unit circle, $|\lambda| > 1$ is part

of the unstable subspace. The unstable subspace represents motion that departs from the orbit. Lastly, eigenvalues that lie on the unit circle, $|\lambda| = 1$ are a part of the center subspace. A center subspace produces oscillatory motion which stay in the vicinity of the periodic orbit. As the monodromy matrix has eigenvalues of reciprocal pairs, a stable subspace has to be accompanied by an unstable subspace. Therefore, there are no asymptotically stable periodic orbits in the CR3BP or the BCR4BP. For families of periodic orbits, the stability characteristics evolve across members of the family [34]. A change in stability is called a bifurcation, and can lead to additional families of periodic orbits [35].

Manifolds structures off of periodic solutions enable transfers that naturally enter or depart the orbit. A trajectory that lies on a manifold is constructed by taking a scaled step off of the periodic orbit, in the direction of eigenvector. Similar to the manifolds off the Lagrange points, an unstable eigenvector will produce a trajectory that is nearly on the unstable manifold. For multiple segments along the manifold, the periodic orbit is discretized. The eigenvalues are independent of the starting location on the periodic orbit, however the eigenvectors are not. Therefore, the associated eigenvector is updated for each discretized point along the periodic orbit. The stable and unstable manifold structures off of an L_1 Lyapunov orbit are illustrated in Figure 3.15. The black curve is the baseline periodic orbit. The eigenvalues for this orbit associated with the stable and unstable motion are $\lambda_{S,U} = [\frac{1}{2467}, 2467]$. The blue arcs are along the stable manifold, and demonstrate flow into the Lyapunov orbit. The red trajectories lie on the unstable manifold, and indicate departing motion from the orbit. The initial conditions are constructed by taking a 100 km step off of the orbit along the corresponding eigenvector.
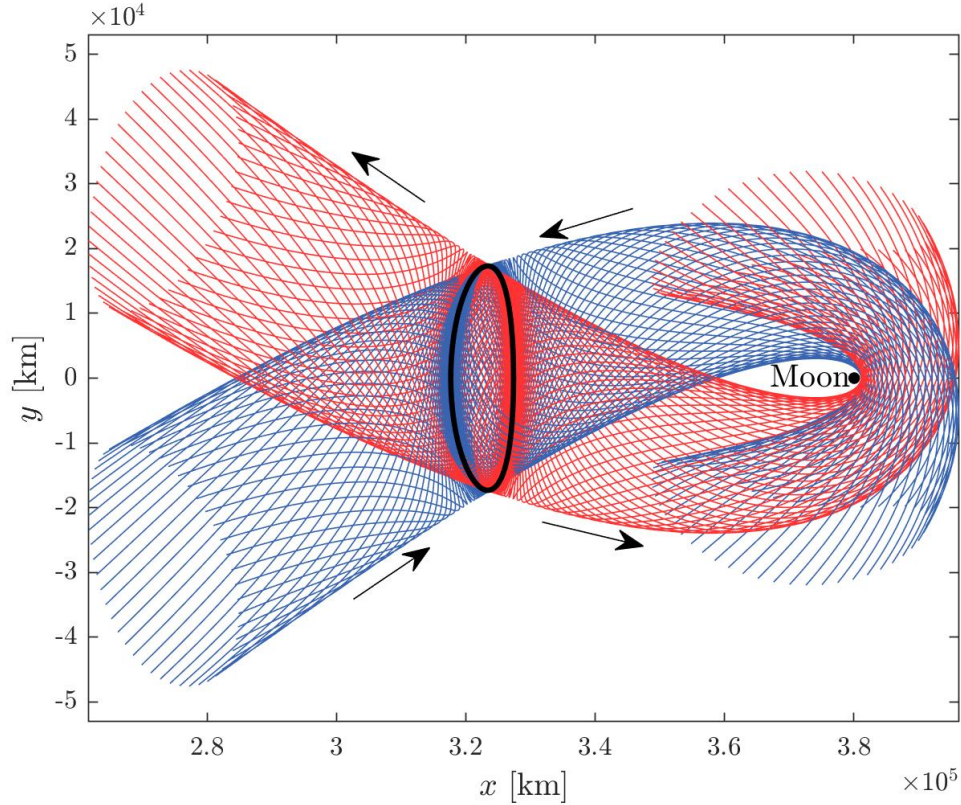
Figure 3.15. Arcs along the stable and unstable manifolds of a L_1 Lyapunov Orbit in the Earth-Moon system, $JC = 3.1792$

3.8 Evolution of the Hamiltonian

An integral characteristic of the BCR4BP is the natural variation in energy along a transfer. Identifying the source of that energy change and quantifying the deviation in energy offers insight into the gravity models. As an integral of the motion, the Jacobi Constants aids in the classification of dynamical structures. In the BCR4BP, the Hamiltonian values vary along a ballistic arc. The lack of an integral of the motion in the BCR4BP is a disadvantage to the model. However, analyzing the change in energy possesses vast insight into the available structures for transfer design. The natural energy change that occurs within the BCR4BP is advantageous. Leveraging the rate of change in either Hamiltonian value allows for low-energy transfer solutions that would otherwise be infeasible in the CR3BP[36]. Revealing patterns in the Hamiltonian aids in the classification of transfers and their efficacy.

3.8.1 Earth-Moon Hamiltonian

To understand the variation in the Earth-Moon Hamiltonian, the nondimensional time derivative of Equation (2.56) is taken, first by following the chain rule,

$$\dot{H}_{EM} = \frac{dH_{EM}}{d\theta_S} \frac{d\theta_S}{dt} \tag{3.43}$$

where $\frac{dH_{EM}}{d\theta_S}$ is the derivative of the Earth-Moon Hamiltonian with respect to the Sun angle. As the Earth-Moon Hamiltonian relies on the velocity of P_3 and the pseudo-potential function, the $\frac{dH_{EM}}{d\theta_S}$ is reduced to,

$$\frac{dH_{EM}}{d\theta_S} = 2\frac{d\widetilde{\Upsilon}}{d\theta_S}$$

where $\frac{d\widetilde{\Upsilon}}{d\theta_S}$ is the derivative of the Earth-Moon pseudo-potential relative to the Sun angle. By expanding the pseudo-potential function, $\frac{dH_{EM}}{d\theta_S}$ becomes,

$$\frac{dH_{EM}}{d\theta_S} = 2\frac{d}{d\theta_S}\left[\frac{1}{2}(\tilde{x}^2 + \tilde{y}^2) + \frac{1-\tilde{\mu}}{\tilde{r}_{13}} + \frac{\tilde{\mu}}{\tilde{r}_{23}} + \frac{\widetilde{m}_S}{\tilde{r}_{43}} - \frac{\widetilde{m}_S}{a_S^2}(\tilde{x}\cos(\theta_S) + \tilde{y}\sin(\theta_S))\right]$$

$$\frac{dH_{EM}}{d\theta_S} = 2\frac{d}{d\theta_S}\left[\frac{\widetilde{m}_S}{\tilde{r}_{43}} - \frac{\widetilde{m}_S}{a_S^2}(\tilde{x}\cos(\theta_S) + \tilde{y}\sin(\theta_S))\right]$$

$$\frac{dH_{EM}}{d\theta_S} = 2\widetilde{m}_S\left[\frac{-\tilde{x}a_S\sin(\theta_S) + \tilde{y}a_S\cos(\theta_S)}{\tilde{r}_{43}^3} - \frac{1}{a_S^2}(-\tilde{x}\sin(\theta_S) + \tilde{y}\cos(\theta_S))\right]$$

$$\frac{dH_{EM}}{d\theta_S} = 2\widetilde{m}_S a_S\left(-\tilde{x}\sin(\theta_S) + \tilde{y}\cos(\theta_S)\right)\left(\frac{1}{\tilde{r}_{43}^3} - \frac{1}{a_S^3}\right) \tag{3.44}$$

Equation (3.44) describes the evolution in energy for P_3 as the Sun moves through time, i.e., θ_S varies. As $\frac{d\theta_S}{dt}$ equals the mean motion of the Sun in the Earth-Moon rotating frame ($\dot{\theta}_S$), written in Equation (2.53). The time rate of change in the Earth-Moon Hamiltonian is constructed by combining Equation (3.43) and Equation (3.44) with $\dot{\theta}_S$, written as,

$$\dot{H}_{EM} = 2\dot{\theta}_S\widetilde{m}_S a_S\left(-\tilde{x}\sin(\theta_S) + \tilde{y}\cos(\theta_S)\right)\left(\frac{1}{\tilde{r}_{43}^3} - \frac{1}{a_S^3}\right) \tag{3.45}$$

Equation (3.45) is dependent on the position of the spacecraft relative to the Sun and the Earth-Moon barycenter; thus, $\dot{H}_{EM}$ is strictly a function of the spacecraft position in the Sun-B_1 rotating frame. A heat map is plotted in Figure 3.16, illustrating the evolution of the Earth-Moon Hamiltonian in the Earth-Moon-Sun BCR4BP as a function of position in the Sun-B_1 rotating frame. The variation in the Earth-Moon Hamiltonian is independent of both P_3 and the relative orientation of the Earth and Moon. The regions are separated by the $\underline{x}$-axis and the curve $\tilde{r}_{43} = a_S$. In close proximity to the Earth-Moon system, the regions of space are approximated by four distinct quadrants in the Sun-B_1 rotating frame, centered at B_1. Davis et al. investigated the tidal impacts on a spacecraft within the vicinity of P_2, observing the impact perturbations from a third body has on orbital elements over time[37]. Within the CR3BP, the tidal influence caused by P_1 impacts the periapse and eccentricity of an orbit in close proximity to P_2. For this analysis, the evolution of the Earth-Moon Hamiltonian value is related to those four quadrants. Transfers that traverse through quadrants I and III experience a decrease in the Earth-Moon Hamiltonian, which corresponds to a increase in the energy of P_3 relative to the Earth-Moon system. Similarly, transfers that traverse through quadrants II and IV experience an increase in the Earth-Moon Hamiltonian, or a decrease in energy. The light magenta and cyan colors in Figure 3.16 denote larger magnitudes of $\dot{H}_{EM}$, which occur further away from the Earth-Moon system. The yellow circle indicates the orbit of the Moon.
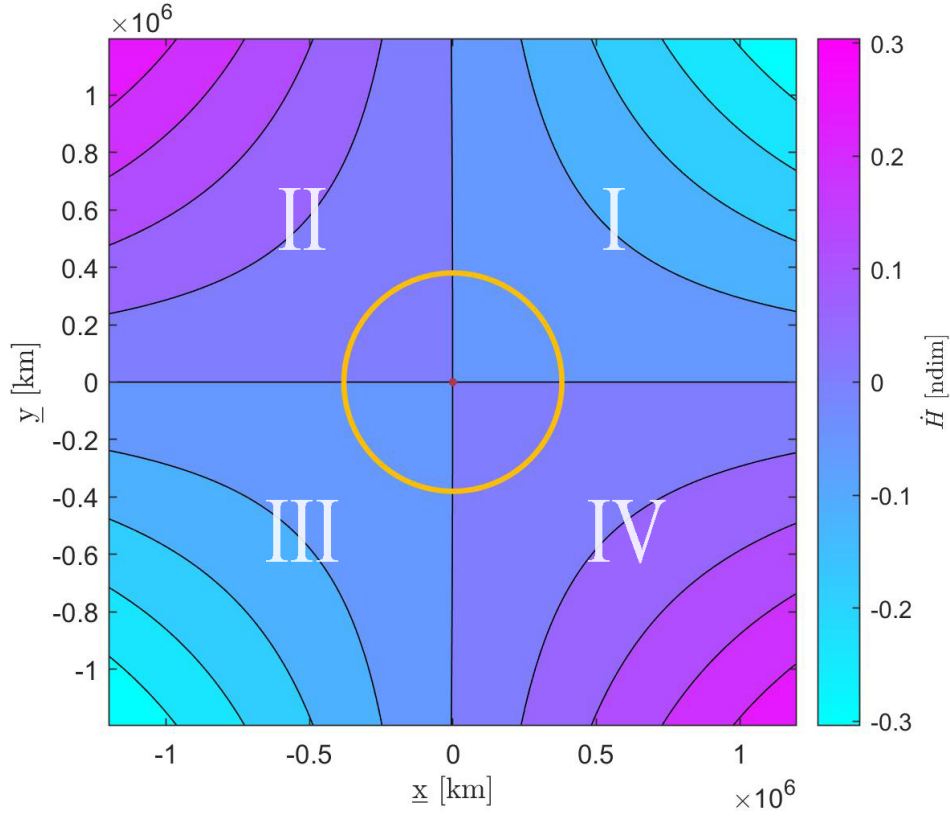
Figure 3.16. Contour plot illustrating the value of $\dot{H}_{EM}$ at various locations throughout the Sun-B_1 rotating reference frame centered at B_1 with the Sun to the left (yellow circle represents the Moon's orbit)

Consider the sample trajectory illustrated in Figure 2.15. Transforming the trajectory into the Sun-B_1 rotating coordinate frame produces Figure 3.17. The origin of Figure 3.17 is centered at the Earth-Moon barycenter B_1, the yellow circle represents the orbit of the Moon which traverses counter-clockwise in this reference frame, and the horizontal and vertical lines correspond to the energy quadrant boundaries as denoted in Figure 3.16. The colored points along the transfer are locations where P_3 traverses from one quadrant to the next, i.e. where $\dot{H}_{EM}$ equals zero. The same Hamiltonian plot as Figure 2.16 is illustrated in Figure 3.18 with additional colored points, that correspond to the locations along the trajectory in Figure 3.17. Each colored point in Figure 3.18 is a local extrema in the Earth-Moon Hamiltonian. The impact of solar perturbations on P_3 is more apparent by visualizing the transfer in the Sun-B_1 rotating frame alongside the Earth-Moon Hamiltonian.

116
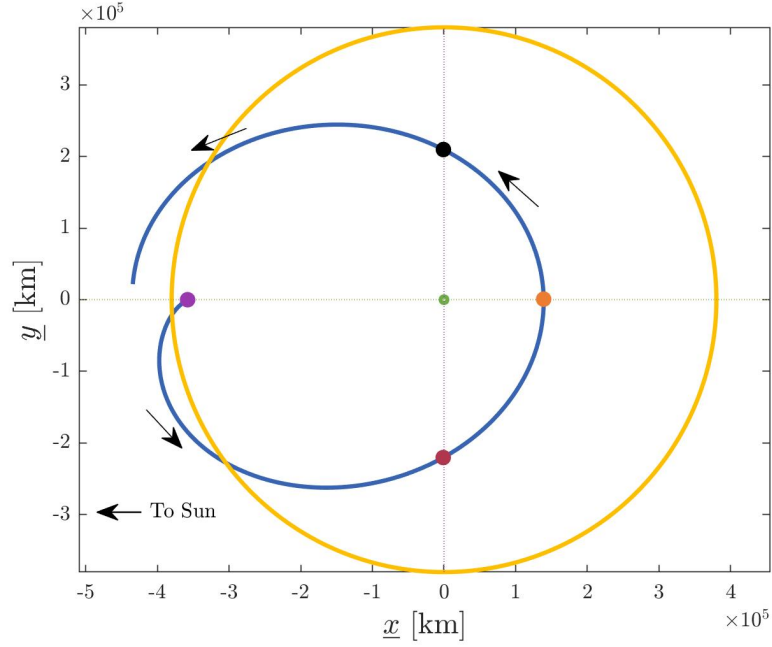
Figure 3.17. Example trajectory from Figure 2.15 illustrated in the Sun-B_1 Rotating Coordinate Frame, where colored points represent crossing between energy quadrants
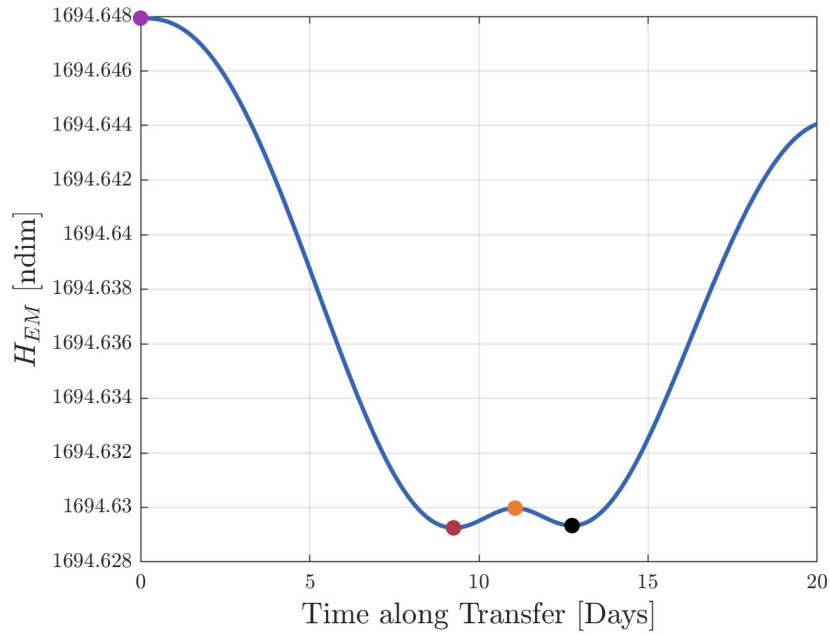
Figure 3.18. The Earth-Moon Hamiltonian along an example transfer, where the colored points correlated to the same locations as illustrated in Figure 3.17

The Earth-Moon Hamiltonian provides insight into the evolution of energy along a transfer. Solar perturbative effects impact the energy progression of P_3 along an arc. The Earth-Moon Hamiltonian, much like the Jacobi Constant, has many insightful properties that are leveraged for spacecraft trajectory design. Understanding the variation in energy provides additional techniques to construct cost effective transfers. One of the advantages to the BCR4BP is the ability to incorporate perturbations into spacecraft trajectory design. As low-energy transfers rely on solar perturbations to achieve reduced maneuver costs, knowledge concerning the variation in energy of P_3 is desired.

3.8.2 Sun-B_1 Hamiltonian

Variations in the Sun-B_1 Hamiltonian are unclear by initial visual inspection. To understand the fluctuations in energy, the time derivative of Equation (2.66) (H_{SB_1}) is taken as,

$$\dot{H}_{SB_1} = \frac{dH_{SB_1}}{d\theta_{EM}}\frac{d\theta_{EM}}{dt} \tag{3.46}$$

where $\frac{dH_{SB_1}}{d\theta_{EM}}$ is the derivative of the Sun-B_1 Hamiltonian with respect to the Earth-Moon angle. Similar to the Earth-Moon Hamiltonian, the Sun-B_1 Hamiltonian relies on the velocity of P_3 and the respective pseudo-potential function (Υ), $\frac{dH_{SB_1}}{d\theta_{EM}}$ is reduced to,

$$\frac{dH_{SB_1}}{d\theta_{EM}} = 2\frac{d\Upsilon}{d\theta_{EM}}$$

where $\frac{d\Upsilon}{d\theta_{EM}}$ is the derivative of the Sun-B_1 pseudo-potential function with respect to the Earth-Moon angle. Using the definitions of $\underline{r}_{13}$ and $\underline{r}_{23}$ written in Equation (2.62), the following steps simplify the variation in Hamiltonian,

$$\frac{dH_{SB_1}}{d\theta_{EM}} = 2\frac{d}{d\theta_{EM}}\left[\frac{1}{2}(\underline{x}^2 + \underline{y}^2) + \frac{1-\mu}{\underline{r}_{43}} + \frac{\underline{\mu}(1-\widetilde{\mu})}{\underline{r}_{13}} + \frac{\underline{\mu}\widetilde{\mu}}{\underline{r}_{23}}\right]$$

$$\frac{dH_{SB_1}}{d\theta_{EM}} = 2\underline{\mu}\frac{d}{d\theta_{EM}}\left[\frac{1-\widetilde{\mu}}{\underline{r}_{13}} + \frac{\widetilde{\mu}}{\underline{r}_{23}}\right]$$

$$\frac{dH_{SB_1}}{d\theta_{EM}} = \frac{2\underline{\mu}(1-\widetilde{\mu})\widetilde{\mu}}{a_S}\left[\frac{(-1+\mu+\underline{x})\sin\theta_{EM} - \underline{y}\cos\theta_{EM}}{\underline{r}_{13}^3} + \frac{(1-\mu-\underline{x})\sin\theta_{EM} + \underline{y}\cos\theta_{EM}}{\underline{r}_{23}^3}\right]$$

$$\frac{dH_{SB_1}}{d\theta_{EM}} = \frac{2\underline{\mu}(1-\widetilde{\mu})\widetilde{\mu}}{a_S}\left((1-\underline{\mu}-\underline{x})\sin\theta_{EM} + \underline{y}\cos\theta_{EM}\right)\left(\frac{1}{\underline{r}_{23}^3} - \frac{1}{\underline{r}_{13}^3}\right) \tag{3.47}$$

Equation (3.47) describes the derivative of the Sun-B_1 Hamiltonian relative to the Earth-Moon angle θ_{EM}. Combining Equation (3.46) and Equation (3.47) with the Earth-Moon mean motion in the Sun-B_1 rotating frame ($\dot{\theta}_{EM}$), $\dot{H}_{SB_1}$ is constructed as,

$$\dot{H}_{SB_1} = \frac{2\underline{\mu}(1-\widetilde{\mu})\widetilde{\mu}\dot{\theta}_{EM}}{a_S}\left((1-\underline{\mu}-\underline{x})\sin\theta_{EM} + \underline{y}\cos\theta_{EM}\right)\left(\frac{1}{\underline{r}_{23}^3} - \frac{1}{\underline{r}_{13}^3}\right) \tag{3.48}$$

Equation (3.48) is dependent on the position of the spacecraft relative to the Earth and Moon; thus, $\dot{H}_{SB_1}$ is a function of the spacecraft position in the Earth-Moon rotating frame. Take a model where the Earth and Moon are simplified to a single point mass at the location of B_1, the problem then becomes equivalent to the Sun-B_1 CR3BP, where the Sun-B_1 Hamiltonian becomes an integral of the motion, i.e., the Jacobi Constant. Thus, the motion of the Earth-Moon system acts as the perturbative force in the formulation relative to the Sun-B_1 rotating coordinate frame. A contour plot in Figure 3.19 depicts the variations of $\dot{H}_{SB_1}$ as P_3 passes through the various quadrants in the Earth-Moon rotating frame. As $\dot{H}_{EM}$ and $\dot{H}_{SB_1}$ are formulated in two different frames, their nondimensional energy rate of change are not related to one another; thus, a direct comparison between the values portrayed in Figure 3.16 and Figure 3.19 is not useful. The quadrants reflecting the rates of change of the Hamiltonian, i.e., $\dot{H}_{SB_1}$, in Figure 3.19 are not as uniform as they appear in the figure. Regions with the largest magnitudes of $\dot{H}_{SB_1}$ in Figure 3.19 occur near the Earth and Moon. The quadrants are separated by the $\widetilde{x}\widetilde{z}$-plane and the plane that lies equidistant from the Earth and Moon, i.e. $\widetilde{x} = 0.5 - \widetilde{\mu}$. For regions off of the $\widetilde{x}$-axis, i.e., $|\widetilde{y}| > 0$, the magnitude of $\dot{H}_{SB_1}$ increases as the distance to either of the primaries decreases. For locations along the $\widetilde{x}$-axis or equidistant from either the Earth and Moon, the magnitude of $\dot{H}_{SB_1}$ is zero. These two boundaries are displayed in Figure 3.19, where the blue and purple regions depict a decrease or increase in the the Sun-B_1 Hamiltonian, respectively. Recall that a decrease in the Hamiltonian value correlates to an increase in the spacecraft energy.
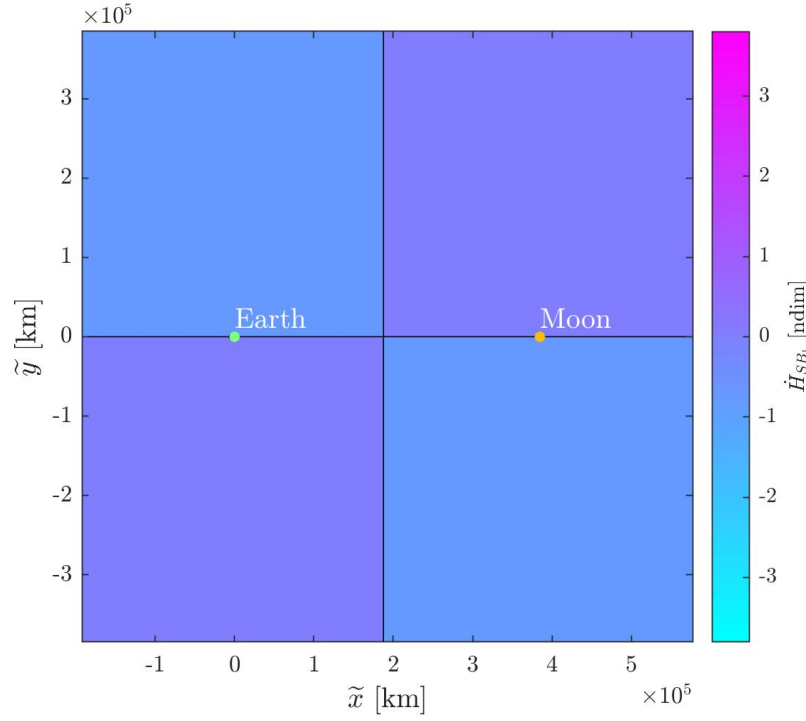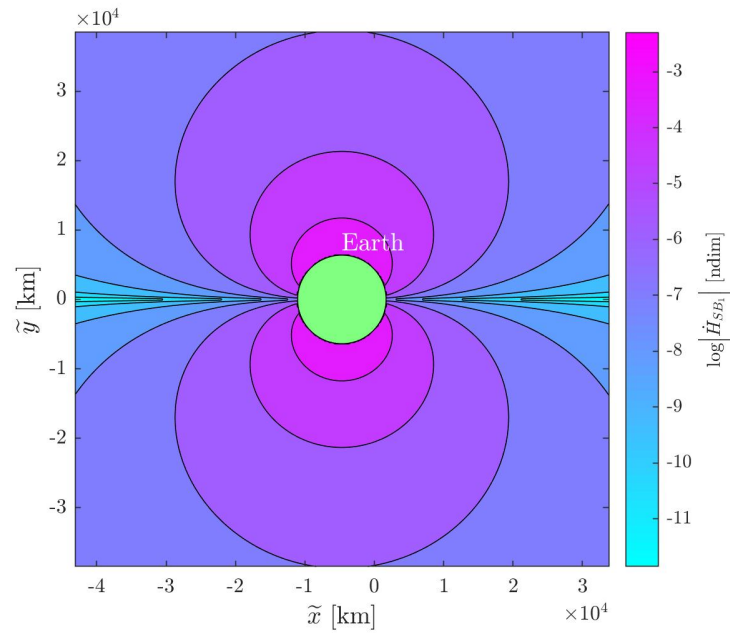
Figure 3.19. Contour plot illustrating the value of $\dot{H}_{SB_1}$ at various locations throughout the Earth-Moon rotating reference frame centered at B_1

The variation in magnitude of $\dot{H}_{SB_1}$ is incomprehensible within Figure 3.19; thus, the contour plot Figure 3.20 illustrates the natural logarithm of the absolute value of the Sun-B_1 Hamiltonian $(\log\left|\dot{H}_{SB_1}\right|)$. As P_3 approaches either the Earth or Moon off the $\widetilde{x}$-axis, the magnitude of $\dot{H}_{SB_1}$ grows cubically. Similarly, as P_3 gets further from Earth-Moon system, the energy variations decrease. The natural logarithm of the energy variations in close proximity to the Earth and Moon are depicted in Figures 3.21 and 3.22. In Figure 3.21, the Earth is plotted to scale as the green circle. In Figure 3.22, the Moon is plotted to scale as the yellow circle, and experiences higher variations in the Sun-B_1 Hamiltonian. Note the sign of $\dot{H}_{SB_1}$ from Figure 3.19 when applied to the magnitude plots. For example, transfers that pass below the Moon in Figure 3.22 experience a large decrease in the Sun-B_1 Hamiltonian.

120
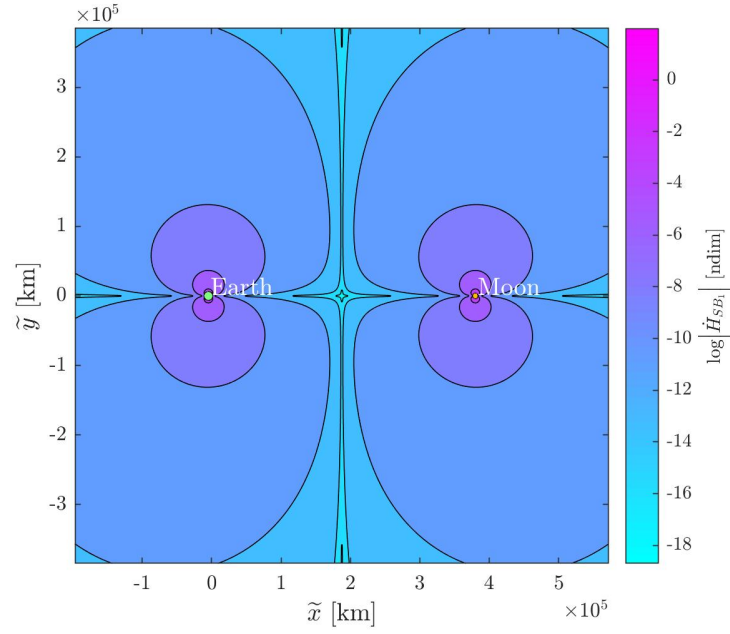
Figure 3.20. Contour plot illustrating the natural log of the magnitude of the Sun-B_1 Hamiltonian ($\log|\dot{H}_{SB_1}|$) in the Earth-Moon rotating reference frame centered at B_1


Figure 3.21. Contour plot illustrating the natural log of the magnitude of the Sun-B_1 Hamiltonian ($\log|\dot{H}_{SB_1}|$) in close proximity to the Earth in the Earth-Moon rotating reference frame
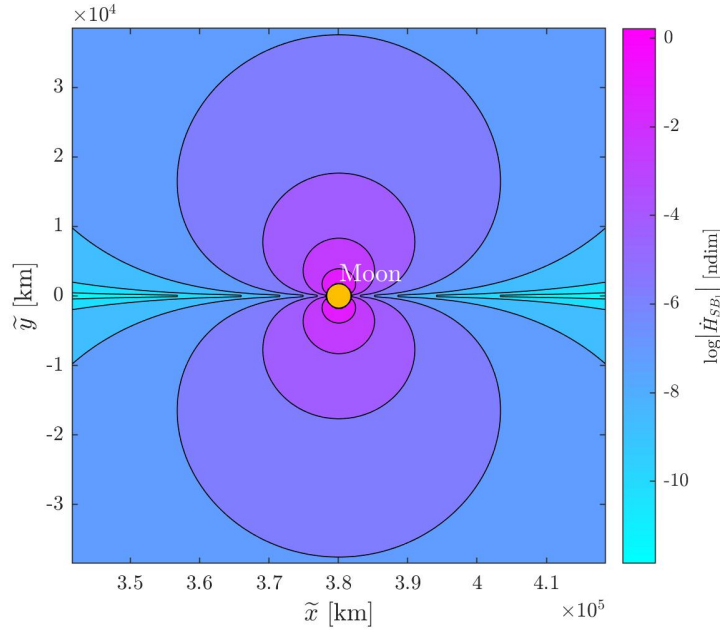
Figure 3.22. Contour plot illustrating the natural log of the magnitude of the Sun-B_1 Hamiltonian $(\log|\dot{H}_{SB_1}|)$ in close proximity to the Moon in the Earth-Moon rotating reference frame

Recall the sample transfer Figure 2.15. The Sun-B_1 Hamiltonian along the transfer is illustrated in Figure 2.26. As the evolution of energy relies on the position of P_3 in the Earth-Moon rotating frame, colored markers are added to distinguish where the spacecraft transitions between regions. The trajectory in the Earth-Moon rotating coordinate frame is illustrated in Figure 3.23, where the colored points are locations along the transfer where $\dot{H}_{SB_1} = 0$. Traversing between the quadrants dictates locations where P_3 transitions from an increase in energy to a decrease in energy, or vice versa. The Sun-B_1 Hamiltonian along the transfer is depicted in Figure 3.24 with the same colored points, corresponding to the timing of the events. From Figure 3.24, H_{SB_1} decreases rapidly at the beginning of the transfer which lies shortly after the purple dot. Comparing to the trajectory in Figure 3.23, slightly after the purple point the spacecraft is in close proximity to the Moon. The close approach to the Moon produces a large variation in the Sun-B_1 Hamiltonian, or a high magnitude of $\dot{H}_{SB_1}$.
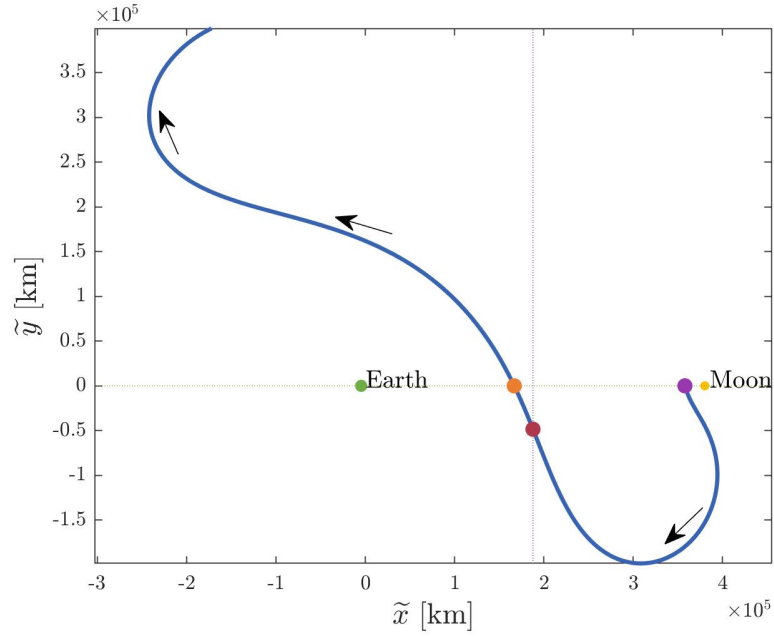
Figure 3.23. Example trajectory from Figure 2.15 where colored points represent crossing between Sun-B_1 Hamiltonian regions
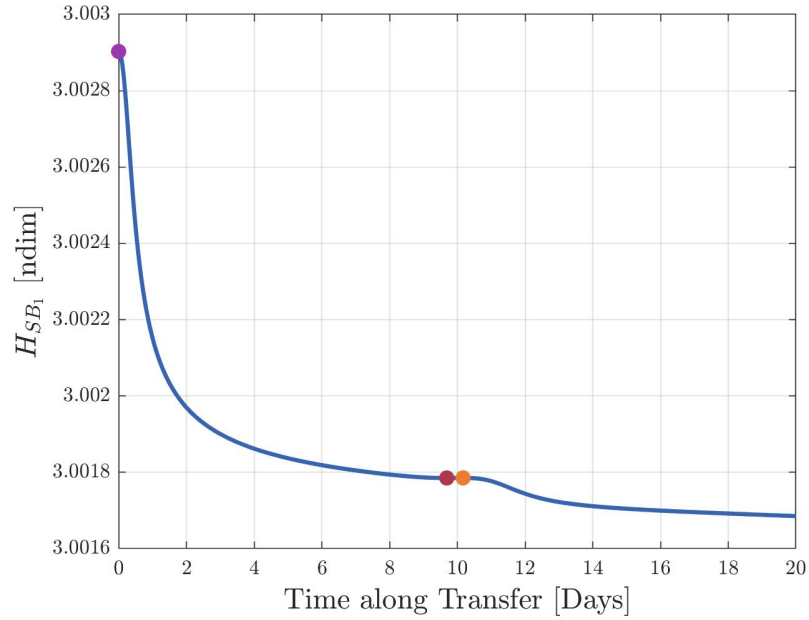
Figure 3.24. The Sun-B_1 Hamiltonian along the transfer in Figure 3.23 with colored points marking the transition between Sun-B_1 Hamiltonian regions

The Sun-B_1 Hamiltonian describes the variation in energy along a transfer. The Earth and Moon act as perturbing bodies off of B_1, impacting the energy progression of P_3 along an arc. The Sun-B_1 Hamiltonian, much like the Earth-Moon Hamiltonian and the Jacobi Constant, is employed for spacecraft trajectory design. Leveraging the natural structures that govern the energy of P_3 aids in the construction of cost effective transfers.
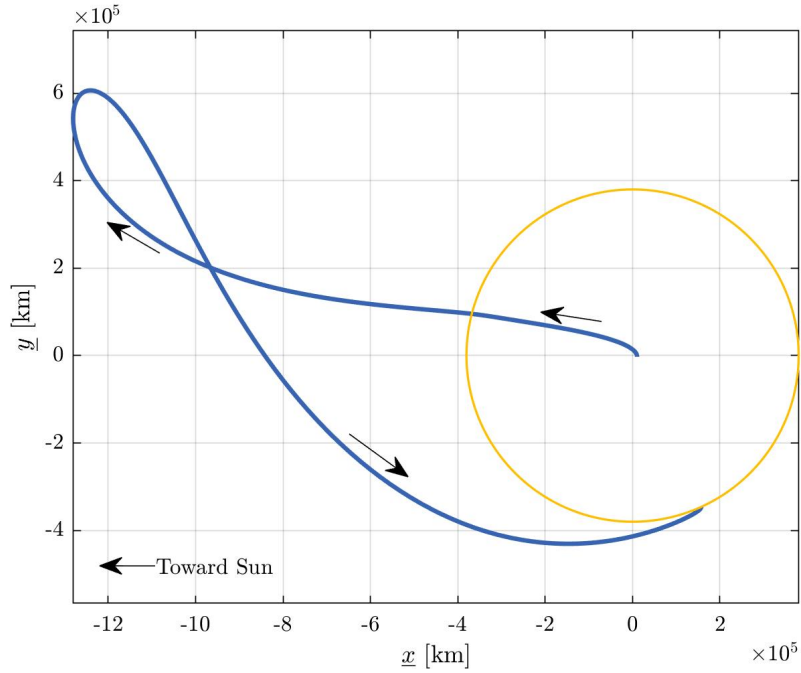
4. CONSTRUCTING BALLISTIC LUNAR TRANSFERS

Ballistic lunar transfers leverage the gravitational influence of the Earth, Moon, and Sun to reduce the propellant cost necessary to reach the Moon. Developing such transfers requires the use of multiple gravity models. Ballistic lunar transfers consist of distinct phases. The initial state of the trajectory is the trans-lunar injection maneuver (TLI). The location of the TLI relies on the parking orbit about the Earth. In this investigation, the parking orbit is assumed to be circular with an altitude of 150 km above Earth. Post-TLI includes the cruise phase. In spaceflight application, the cruise phase consists of multiple trajectory correction maneuvers to maintain the desired path. This investigation assumes there are no tracking or navigation errors involved. Therefore, the spacecraft follows ballistic motion. The cruise phase also may include unpowered flyby(s), either about the Moon or Earth. A flyby, though complex and epoch-dependent, reduces the propellant cost of TLI. The final phase is the arrival into the desired orbit near the Moon. The final orbit relies on the goal of the mission and includes conic or multi-body orbit. For most cases, a lunar orbit insertion maneuver (LOI) is necessary to enter the intended orbit. The largest cost-savings between direct transfers and ballistic lunar transfers occur at the LOI. As depicted in Section 3.8, solar perturbations in the BCR4BP provide a natural energy variation. Therefore, with precise understanding and control of the governing dynamics, low-cost transfers are constructed.

4.1 Definition of Ballistic Lunar Transfers

Ballistic lunar transfers are defined to provide a feasible pathway to the Moon. The primary goal of a ballistic lunar transfer is to reduce the energy of the spacecraft upon arrival at the Moon, such that the insertion propellant costs are reduced. The source of energy reduction originates from the gradual impact of solar perturbations on the spacecraft. To exploit the gravitational influence of the Sun, it is essential that the trajectory deviates from the Earth-Moon barycenter, B_1. By traversing beyond the distance of the Moon, the influence of the Sun presents a larger role in the structure of the transfer. Initially, a ballistic lunar transfer originates near the Earth, at a state associated with a launch state or post-TLI. The original states have relatively high energy, as the ZVCs must not inhibit

the motion to the exterior of the Earth-Moon system. As the transfer departs further from B_1, the Sun's impact on the energy of the spacecraft becomes more apparent. An explicit function for the change in energy is written in Equation (3.45). To produce a transfer that reduces the energy prior to arrival into cislunar space, motion through quadrants II and IV of Figure 3.16 in the Sun-B_1 rotating frame is desired. A sample trajectory is illustrated in Figure 4.1 for reference. The blue curve represents the ballistic lunar transfer, and the Moon follows the yellow circle counterclockwise. The origin of the plot is the Earth-Moon barycenter B_1. The evolution of the Earth-Moon Hamiltonian for this transfer is depicted in Figure 4.2. The sample trajectory leverages the perturbations in quadrant II to increase the Earth-Moon Hamiltonian. The oscillatory behavior of the Earth-Moon Hamiltonian near the end of the transfer relates to the capture dynamics near the Moon. Variations in the Earth-Moon Hamiltonian are reduced as the spacecraft gets closer to B_1.

Figure 4.1. A ballistic lunar transfer in the BCR4BP, illustrated in the Sun-B_1 rotating coordinate frame, centered about B_1

126
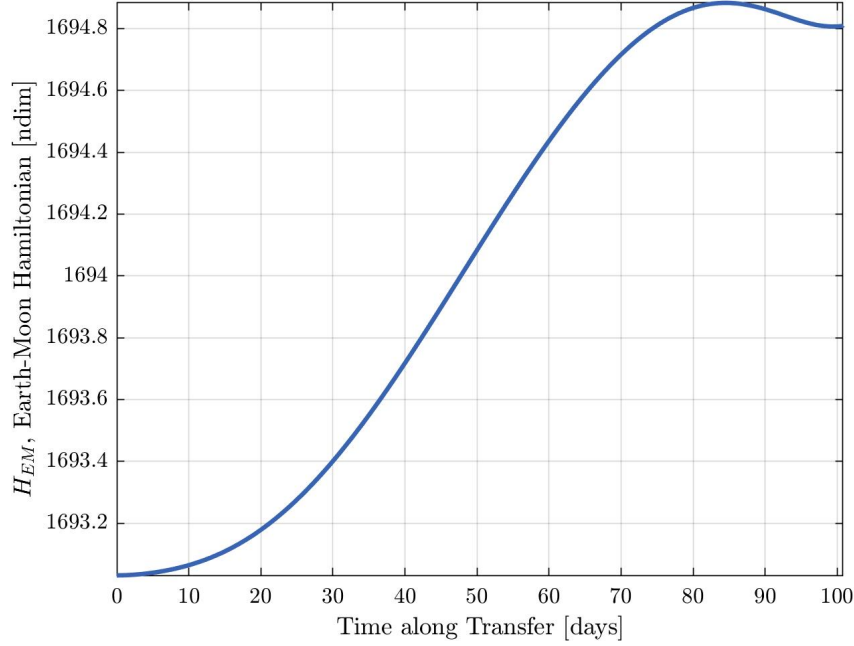
Figure 4.2. Variation in Earth-Moon Hamiltonian along the transfer plotted in Figure 4.1

Since the energy is decreasing far from the Earth and Moon, the ZVCs will begin to close. Therefore, there is an upper-bound to the incoming Hamiltonian value upon arrival at the Moon. This upper-bound depends on the energy necessary to traverse through the $\widetilde{E}_2$ portal. The desired Earth-Moon Hamiltonian upon arrival at the Moon depends on the desired final orbit. In general, a ballistic lunar transfer is a trajectory that naturally reduces its energy through solar perturbations by traveling beyond the orbit of the Moon.

## 4.2 Ballistic Lunar Transfers in the CR3BP

Analysis of ballistic lunar transfers within the CR3BP provides a discrete approach to assessing dynamical structures. The Earth-Moon and Sun-Earth CR3BP systems can be examined independently to characterize phases of the transfer. The Earth-Moon CR3BP is an appropriate model for preliminary design to represent motion arriving in the lunar vicinity. Solutions from the Earth-Moon CR3BP offer effective initial conditions for exploring solutions in the BCR4BP [16]. The Sun-Earth CR3BP models the influence of solar

perturbations on the spacecraft as it departs the Earth-Moon region. Although the Sun-Earth CR3BP does not include the gravitational influence of the Moon, broader knowledge about the dynamics of the system aids in the construction of ballistic lunar transfers in the BCR4BP. The Sun-Earth CR3BP is employed to construct families of ballistic lunar transfer geometries and to characterize their energy, time of flight, and arrival location.

Periapse Poincaré maps aid in characterizing structures within a dynamical system. In this investigation, periapse Poincaré maps are leveraged. Poincaré maps are first introduced in Section 3.6. Periapse Poincaré maps represent discrete points in configuration space where a periapse occurs along a given trajectory. The effectiveness of a Poincaré map relies on the initial conditions used to generate the map. To explore arcs that mimic the motion of ballistic lunar transfers, the initial position states are restrained to the parking orbit or feasible locations of TLI. The parking orbit lies in the ecliptic planar (planar case for Sun-Earth CR3BP), and is circular, having an altitude of 150 km above the Earth. The velocity magnitude post-TLI is determined by the Jacobi constant value for the map

$$V_f = \sqrt{2\Omega - JC_{\mathrm{MAP}}} \tag{4.1}$$

where V_f is the magnitude of the velocity vector after the TLI maneuver, Ω is the pseudo-potential for the state along the parking orbit, and JC_{MAP} is the value of the Jacobi constant for the periapse Poincaré maps. In the CR3BP the dimensionality of the map is reduced by one when all transfers have the same value of the Jacobi constant. Equation (4.1) is a reformatted expression of Equation (2.24). Selecting the direction of the initial velocity vector is nontrivial, in application, a TLI is generally unconstrained in orientation. Rather than inspecting each velocity direction, characteristics of the CR3BP are incorporated into the analysis. An impulsive maneuver is a change in the velocity of the spacecraft. Figure 4.3 illustrates a vector diagram for an impulsive maneuver. The initial and final velocity directions are $\bar{V}_i$ and $\bar{V}_f$, respectively. The change in velocity $\Delta\bar{V}$, designates the maneuver direction and magnitude, i.e., $\Delta\bar{V} = \bar{V}_f - \bar{V}_i$. The quantity β denotes the angle between the two velocity vectors. For a TLI maneuver performed along the parking orbit, the initial velocity vector is available. As Equation (4.1) defines the final velocity magnitude, the only
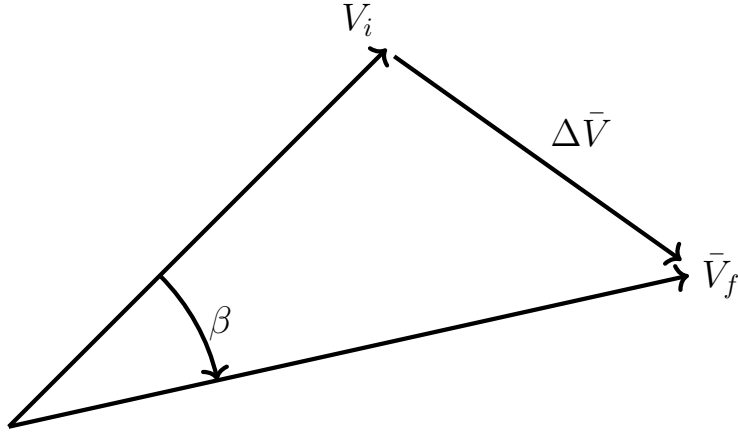
Figure 4.3. Vector diagram for an impulsive maneuver

free variable is the orienting angle β. Given the law of cosines, a relationship between the velocity magnitudes is written as,

$$\Delta V = \sqrt{V_i^2 + V_f^2 - 2V_i V_f \cos(\beta)} \tag{4.2}$$

As the initial and final velocity magnitudes are held constant, Equation (4.2) is minimized when the term $2V_i V_f \cos(\beta)$ is maximized. Cosine is maximized when the angle is zero or any integer multiple of 2π, i.e., $\beta = 0$. Thus, to perform a maneuver such that a desired Jacobi constant value is met, the initial and final velocity vectors must be aligned to minimize the ΔV. The most efficient maneuver to increase the Jacobi constant is to perform the maneuver in the anti-velocity direction. Conversely, a maneuver aligned with the velocity direction is the optimal approach to decreasing the Jacobi constant value. The purpose of investigating velocity direction is to construct initial conditions for a periapse Poincaré map. A periapse Poincaré map is employed explicitly as a result of Equation (4.2). As the Moon is not modeled in the Sun-Earth CR3BP, arrival at the lunar orbit radius with a velocity aligned with the Moon's velocity, i.e., a periapse, indicates comparable dynamical behavior to a coherent ballistic lunar transfer. The initial states are constrained to the parking orbit about the Earth, where a maneuver is performed along the rotating, orbital velocity direction to achieve the desired Jacobi constant value. As the parking orbit is circular, each initial state is a periapse. The trajectories are propagated forward for 365 days in the Sun-Earth

CR3BP to illustrate attainable locations [38]. Consider the periapse map in Figure 4.4 constructed with a Jacobi constant value of $JC = 3.000804$. The origin of Figure 4.4 lies at the Earth, with the Sun to the left. The Moon's orbit is plotted on the map in gold to designate the desired arrival altitude.
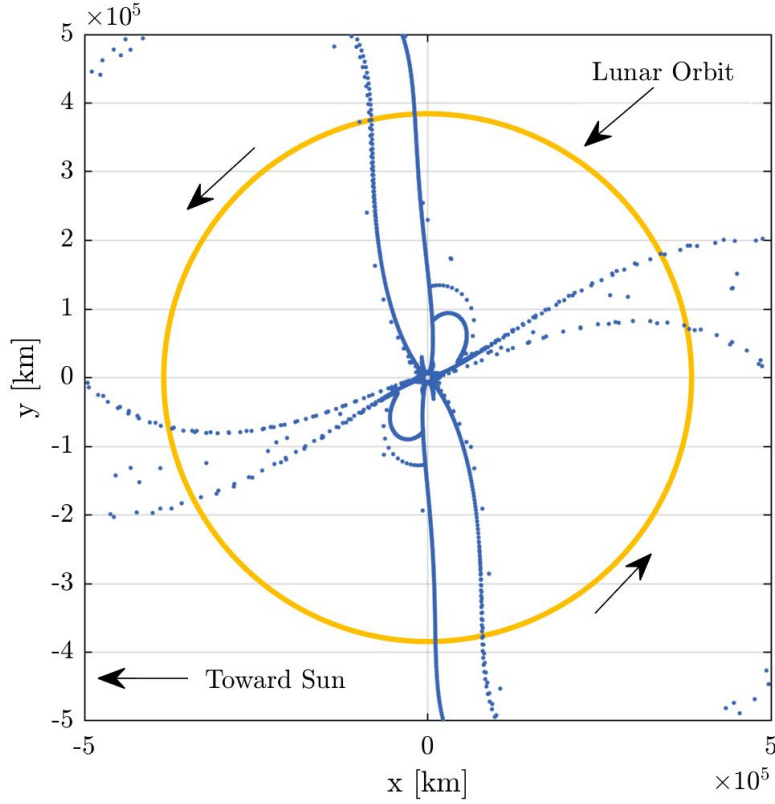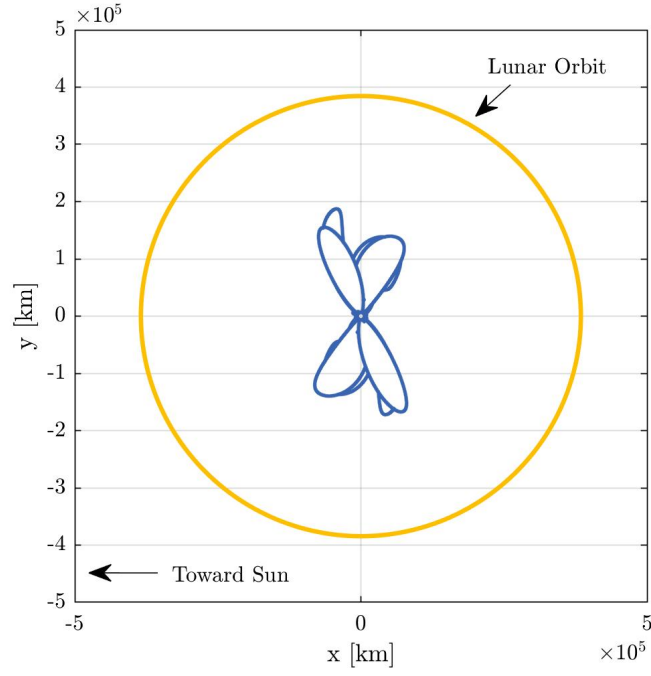

Figure 4.4. Periapse Poincaré map in the Sun-Earth CR3BP, with a Jacobi constant value of $JC = 3.000804$

Each blue dot on Figure 4.4 is a periapse on the trajectories constructed. Points that lie along the gold circle have a periapse at a radius from Earth equal to the lunar orbit radius. A sample transfer selected off of the periapse Poincaré map is illustrated in Figure 4.5. The same map with a purple point denoting the position of a selected transfer is displayed in Figure 4.5a. The trajectory constructed from the purple point illustrated in Figure 4.5b. The transfer departs from the parking orbit about the Earth and arrives at the lunar orbit radius. The transfer depicted is one of an abundance of applicable trajectories. Each intersection of the lunar orbit produces a different geometry in position space.

130
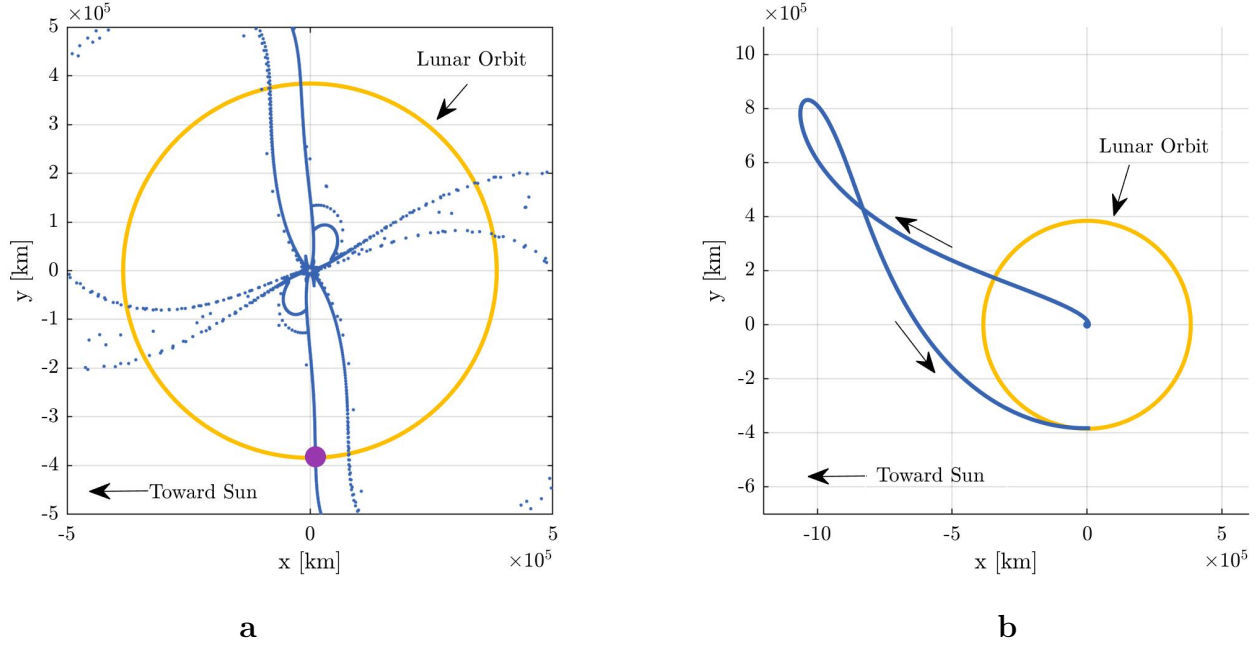
Figure 4.5. Periapse Poincaré map ($JC = 3.000804$) in Sun-Earth CR3BP (a); trajectory associated with purple periapse point in the Sun-Earth Rotating Frame (b)

Classes of transfer solutions rely on the energy of periapse Poincaré maps. The insight obtained by a periapse Poincaré map in the CR3BP correlates to the value of the Jacobi Constant. Figure 4.4 illustrates trajectories that depart from the Earth and arrive at the lunar orbit radius for a described energy. Varying the Jacobi constant value associated with the map outlines the influence energy has on accessible transfer geometries. Using the same initial parking orbit as before, Figure 4.6 depicts a periapse Poincaré map for a Jacobi constant value of $JC = 3.000854$. A lower energy map reveals that none of the periapsides reach the lunar orbit radius for the year time-span. The periapse Poincaré map showcases the energy necessary to achieve a ballistic lunar transfer for transfers that are unaided by an outbound lunar flyby. Lowering the Jacobi constant value to $JC = 3.000829$ produces a map where multiple periapsides attain the lunar orbit radius, illustrated in Figure 4.7. By comparing Figures 4.4 and 4.7, both maps contain points that reach the desired altitude; however, the higher energy map (lower Jacobi constant) has more viable transfer options.

Figure 4.6. Periapse Poincaré map in the Sun-Earth CR3BP, with a Jacobi constant value of $JC = 3.000853$
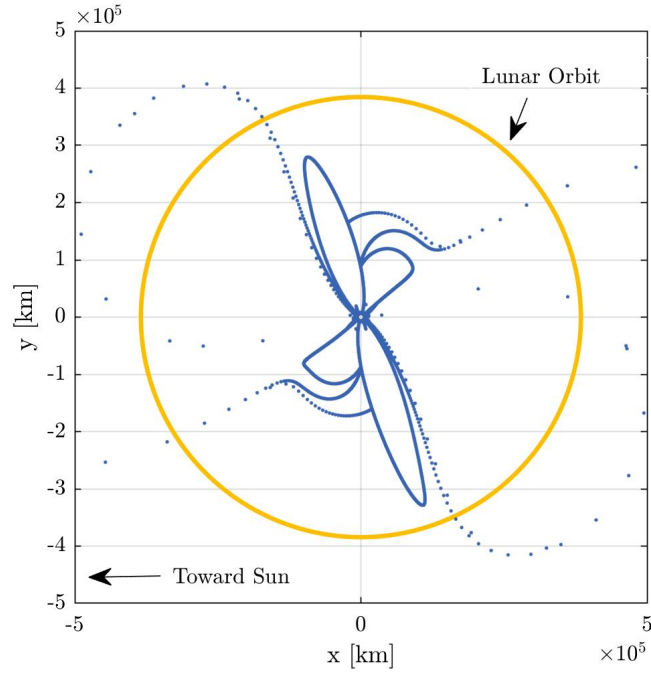
Figure 4.7. Periapse Poincaré map in the Sun-Earth CR3BP, with a Jacobi constant value of $JC = 3.000829$

Sets of transfers solutions offer a metric of comparison to how the trajectories evolve across defining features such as energy and time of flight. To grow a family of ballistic lunar transfers in the Sun-Earth CR3BP, a continuation scheme is employed. In this investigation, the transfer geometries within the Sun-Earth CR3BP are restricted to the ecliptic plane, i.e, the $\hat{x}\hat{y}$-plane. A single shooting algorithm is constructed as

$$\bar{X} = \begin{bmatrix} x_0 \\ y_0 \\ \dot{x}_0 \\ \dot{y}_0 \\ t \end{bmatrix} \qquad \bar{F} = \begin{bmatrix} \sqrt{(x_0 - 1 + \mu)^2 + y_0^2} - \eta_0 \\ (x_0 - 1 + \mu)\dot{x}_0 + y_0\dot{y}_0 \\ \sqrt{(x_f - 1 + \mu)^2 + y_f^2} - \eta_f \\ (x_f - 1 + \mu)\dot{x}_f + y_f\dot{y}_f \end{bmatrix} \qquad (4.3)$$

where the free variable vector is composed of the initial planar states and the propagation time t. The constraint vector is composed of two radius constraints about Earth, and two apse constraints. The scalar quantity η_0 denotes the initial radius constraint about Earth, which restricts the initial position to lie on the base parking orbit. For a 150 km altitude, circular orbit about Earth, η_0 equals $\frac{6378+150}{l^\star} \approx 4.6043e^{-5}$. Likewise, η_f defines the distance from Earth at the end of the transfer upon reaching the lunar orbit radius. For this analysis, the quantity η_f equals $\frac{3.8475e^5}{l^\star} \approx 2.5719e^{-3}$. The second and fourth row of the constraint vector corresponds to initial and final states being an apse about Earth. Note that the apse constraints do not explicitly differentiate between a periapse or apoapse. A pseudo-arclength continuation method is exploited as the targeting scheme devised in Equation (4.3) is underdetermined. The process is seeded with an initial guess selected from the previously constructed periapse Poincaré maps. The transfer from Figure 4.5b is continued to create the family of ballistic lunar transfers depicted in Figure 4.8, denoted as Family 1. Not constrained by energy, Family 1 continues to grow into multiple quadrants about the Sun-Earth CR3BP system. The gray transfers plotted in Figure 4.8 are a subset of the family with a time of flight shorter than 115 days. The transfers begin traveling in the direction of the Sun, towards quadrant II in the Sun-Earth rotating coordinate frame. The origin of the

plot is the Earth, and the black circle represents the lunar orbit. The transfer colored in gold is the lowest energy solution of this family, having a Jacobi constant of $JC = 3.0008265$, and a time of flight of 97.7 days. The green arc has the shortest time of flight, taking 75.9 days, while having a lower Jacobi constant value $JC = 3.0007286$. Figure 4.9 illustrates the
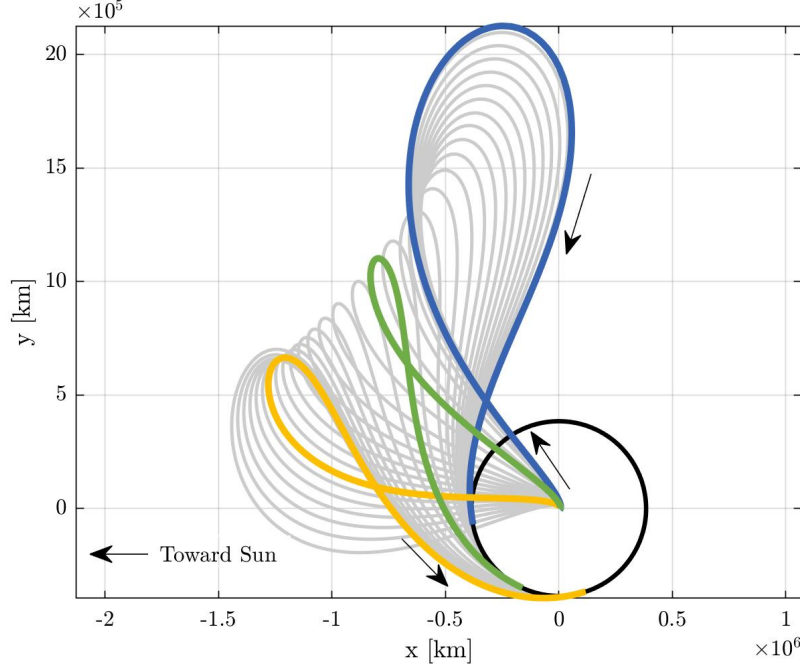
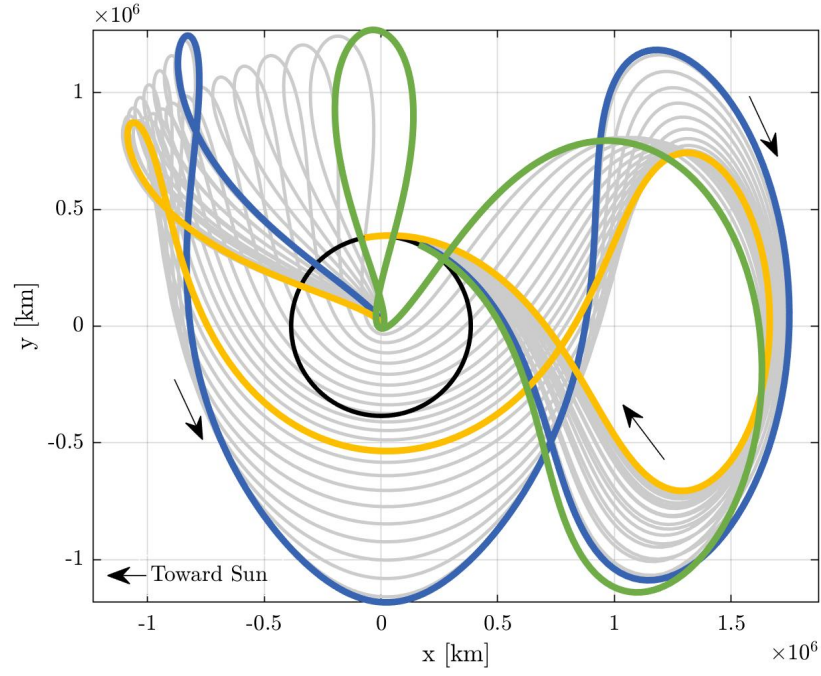**Figure 4.8.** Family 1: Family of ballistic lunar transfers in the Sun-Earth CR3BP

progression of energy and flight duration along the family. The colored points along the back curve indicate the positions associated with the same colored trajectories in Figure 4.8. The family of transfers does not grow monotonically as there are multiple solutions for a given flight duration or value of the Jacobi constant. For the members of Family 1 represented by Figure 4.9, the characteristic energy (C_3) at TLI ranges from -0.7437 km^2/sec^2 to -0.3211 km^2/sec^2, which coincides with previous findings [5], [39].

Multiple families of ballistic lunar transfers are constructed in the Sun-Earth CR3BP by applying initial conditions from a periapse Poincaré map. As demonstrated by Family 1, a continuation schematic is applied to a transfer from a Poincaré map. The result is a family of transfers that depart from the Earth and arrive at the lunar orbit radius. By selecting a different point that reaches the lunar orbit, a new family is built. Figure 4.10
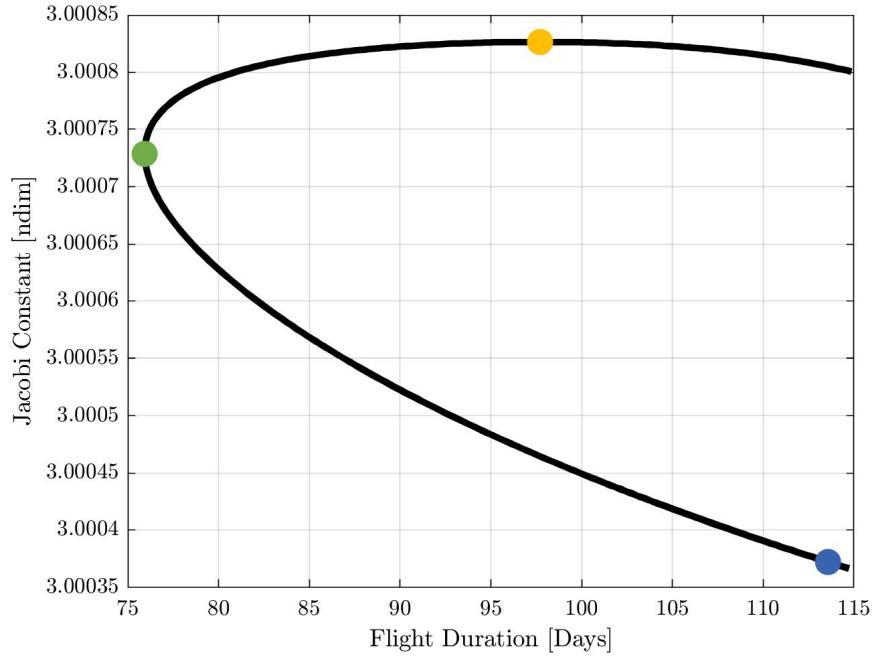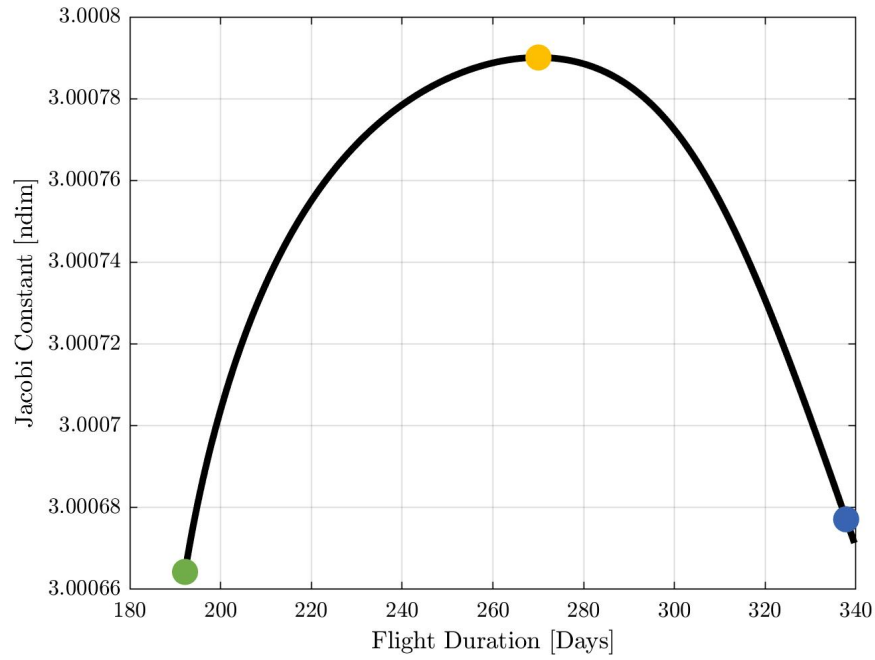
Figure 4.9. Jacobi constant versus flight duration for Family 1 in Figure 4.8

illustrates another family of transfers, denoted as Family 2. Comparable to Figure 4.8, the gray arcs represent a subset of the family with a time of flight less than 340 days. Family 2 has multiple revolutions about the Earth, initially departs the Earth towards the Sun, or in the direction of L_1. The transfers then pass back by the Earth and fly away from the Sun towards L_2. The black circle is the lunar orbit, and the origin of the plot is the location of Earth. The yellow transfer is the lowest energy transfer for Family 2, having a Jacobi constant of $JC = 3.0007902$ and a time of flight of 270 days. The green transfer is the shortest flight duration, taking 193 days with a higher energy of $JC = 3.0006679$.
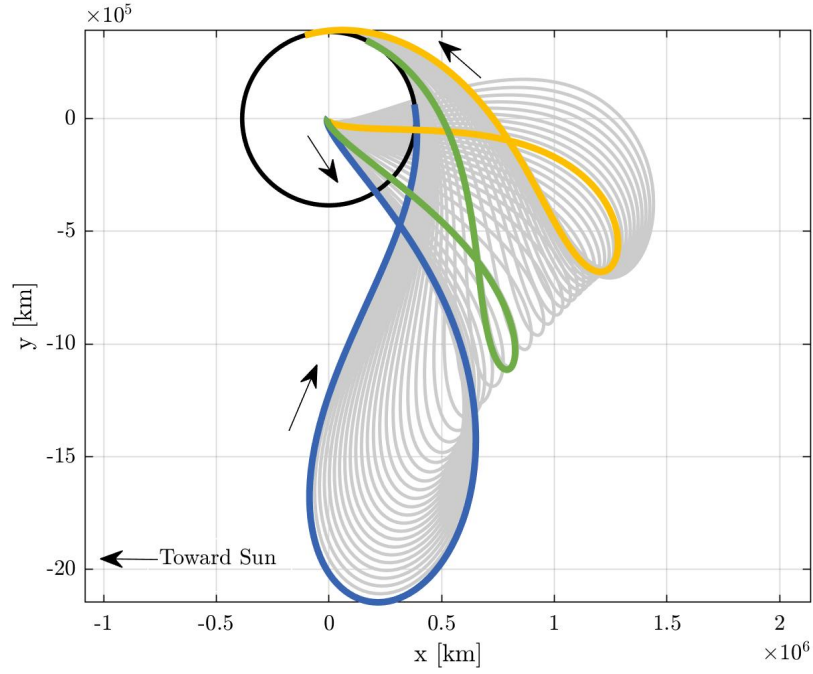
Figure 4.10. Family 2: Family of ballistic lunar transfers in the Sun-Earth CR3BP
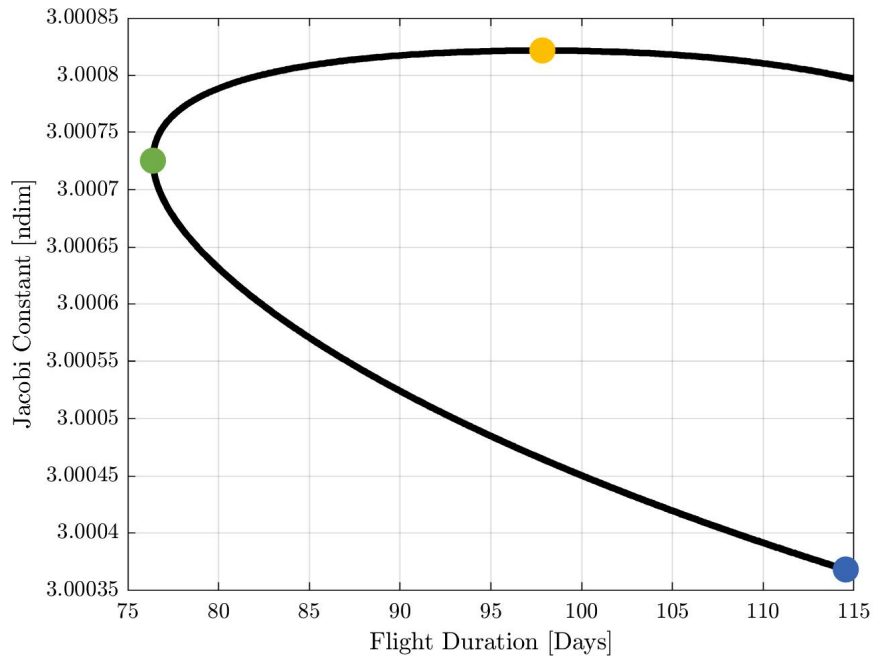

Figure 4.11. Jacobi constant versus flight duration for Family 2 in Figure 4.10

The families of transfers illustrated in both Figure 4.8 and Figure 4.10 depart from Earth in the direction of the Sun, or towards L_1. Section 3.8 details the value of the four quadrants about the Earth. As most easily inspected from Figure 4.8, a majority of the transfers lie within quadrant II. It is predicted that similar geometries exist in quadrant IV, i.e., initial departing the Earth away from the Sun. By selecting another initial condition from the map, Figure 4.12 is crafted. From visual inspection, the family appears to be a rotation of 180 degrees of 4.8 about Earth. The arc in yellow is the lowest energy transfer, having a Jacobi constant value of $JC = 3.0008216$ and a time of flight of 97.8 days. Comparing to Family 1, the lowest energy trajectory has a slightly longer time of flight and higher energy. Likewise, the shortest flight duration arc, as plotted in green, has a time of flight of 76.4 days. Although Family 1 and Family 3 resemble rotations of each other, Family 1 produces a marginal advantage in both time of flight, and energy. Figure 4.13 depicts the characteristics of Family 3, with the colored points correlating to the same colored transfers in the Figure 4.12. As a comparison, Figure 4.14 exhibits the evolution of energy and flight duration for both Families 1 and 3. The blue curve represents Family 1, and the gold line is Family 3. For lower energy solutions (higher values of the Jacobi constant) and shorter times of flight, the difference between the two families is distinguishable.

Figure 4.12. Family 3: Family of ballistic lunar transfers in the Sun-Earth CR3BP, the L_2 counterpart to Family 1
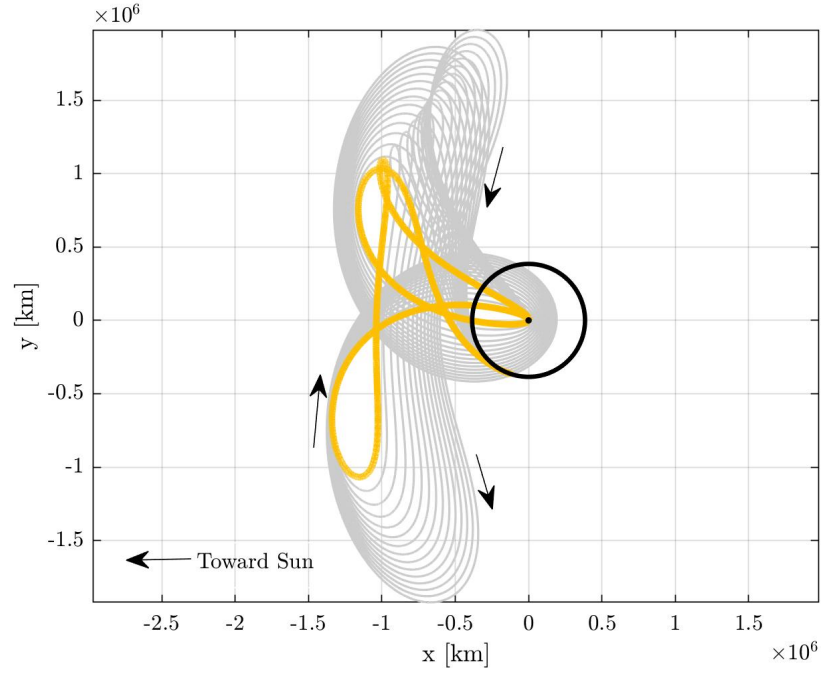

Figure 4.13. Jacobi constant versus flight duration for Family 3 in Figure 4.12
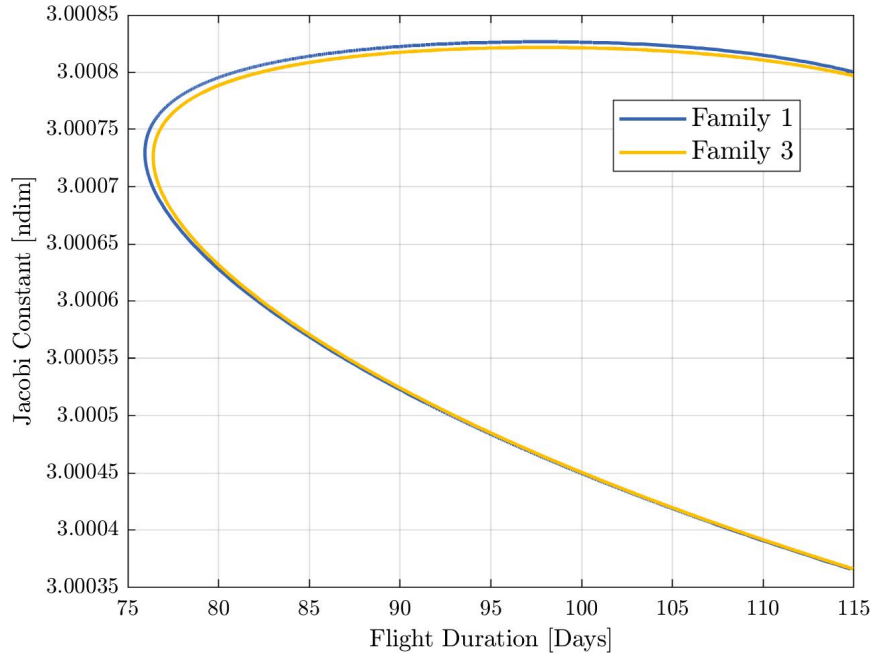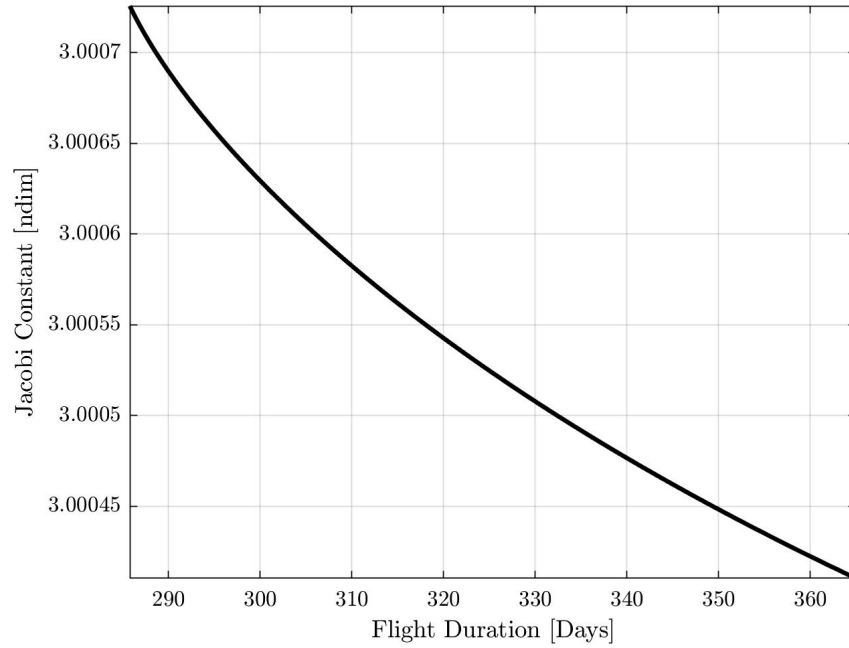
Figure 4.14. Jacobi constant and flight duration comparisons between Family 1 (L_1) and Family 3 (L_2)

The Sun-Earth CR3BP offers a variety of low energy transfer designs to the Moon. The joint influence of the Sun and Earth on the spacecraft produces trajectories that attain a variety of regions about the Earth. Families 1, 2 and 3, are a few of the many possible geometries which reach the lunar orbit radius by incorporating the perturbing effects of the Sun. Figures 4.15-4.24 exemplifies a catalog of transfer geometries and the corresponding properties of the trajectories. The gold arc in each plot illustrates the transfer with the maximum value of the Jacobi constant. The explored families are under the presumption that the flight duration is less than 365 days. Therefore, additional sets of transfers are accessible if longer flight times are attainable. The lowest energy family of transfers is represented in Figure 4.23, having a maximum Jacobi constant value of $JC = 3.0008419$.

Figure 4.15. Family 4: Family of ballistic lunar transfers in the Sun-Earth CR3BP

Figure 4.16. Evolution of Jacobi constant and flight duration along Family 4 of transfers in the Sun-Earth CR3BP

Figure 4.17. Family 5: Family of ballistic lunar transfers in the Sun-Earth CR3BP

Figure 4.18. Evolution of Jacobi constant and flight duration along Family 5 of transfers in the Sun-Earth CR3BP
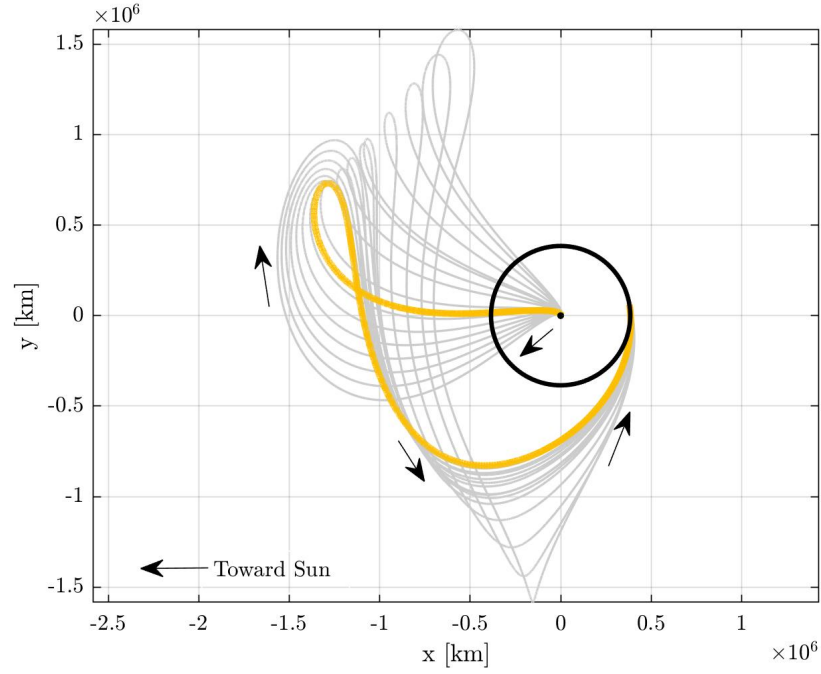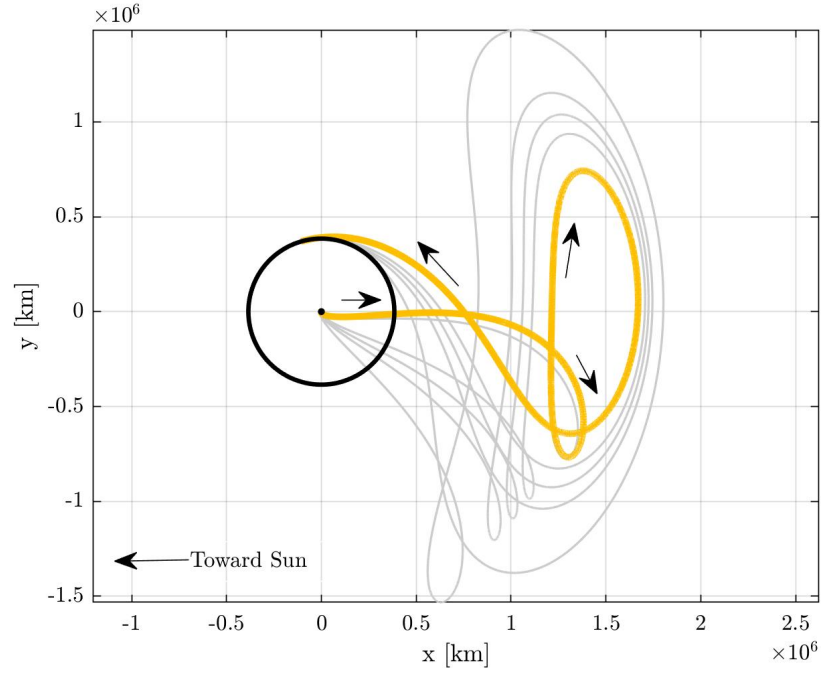
Figure 4.19. Family 6: Family of ballistic lunar transfers in the Sun-Earth CR3BP

Figure 4.20. Evolution of Jacobi constant and flight duration along Family 6 of transfers in the Sun-Earth CR3BP

Figure 4.21. Family 7: Family of ballistic lunar transfers in the Sun-Earth CR3BP
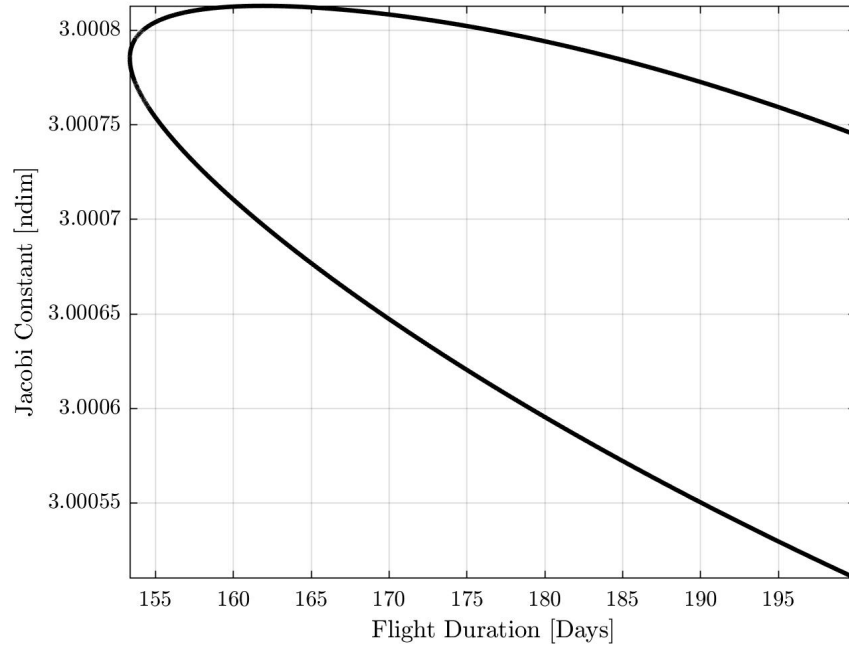

Figure 4.22. Evolution of Jacobi constant and flight duration along Family 7 of transfers in the Sun-Earth CR3BP

Figure 4.23. Family 8: Family of ballistic lunar transfers in the Sun-Earth CR3BP

Figure 4.24. Evolution of Jacobi constant and flight duration along Family 8 of transfers in the Sun-Earth CR3BP
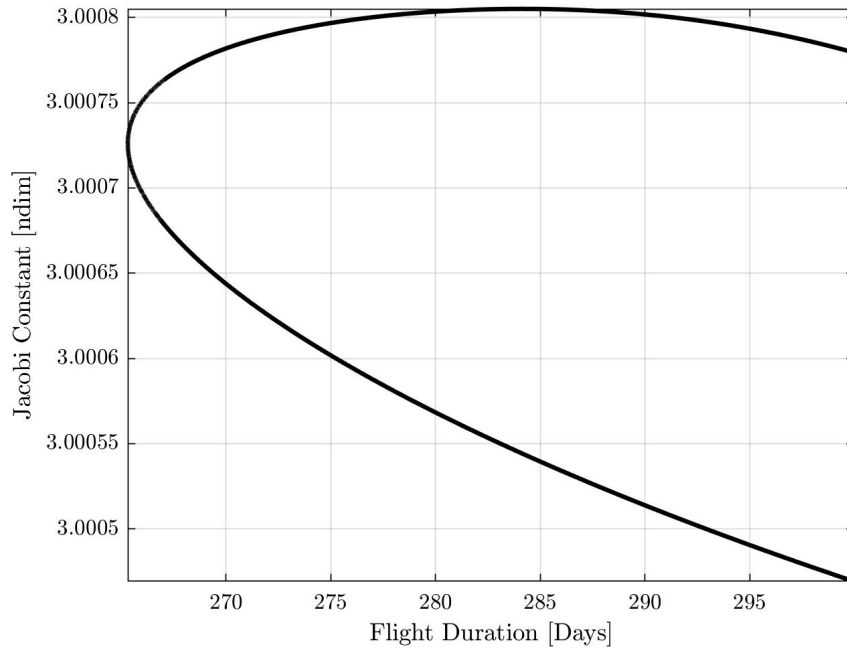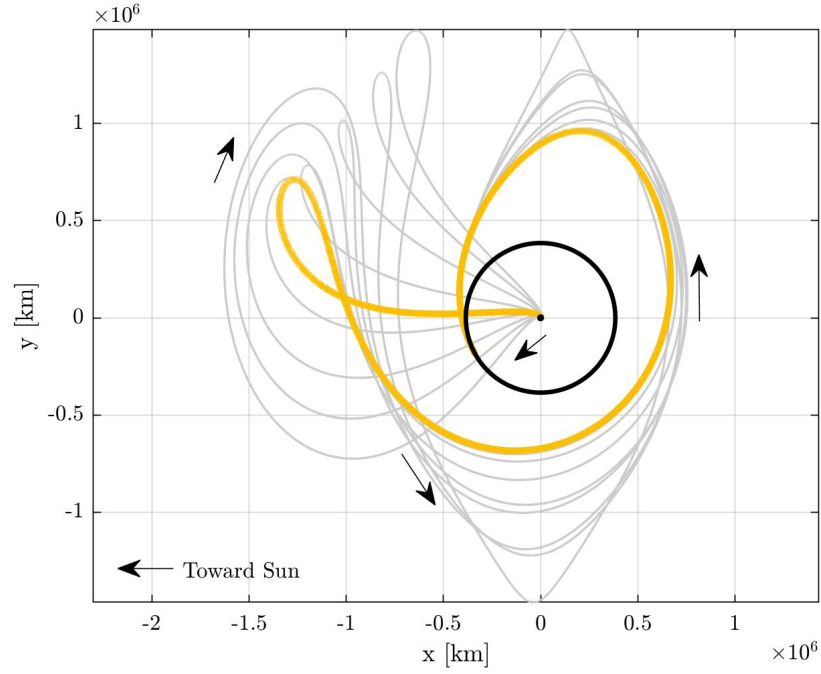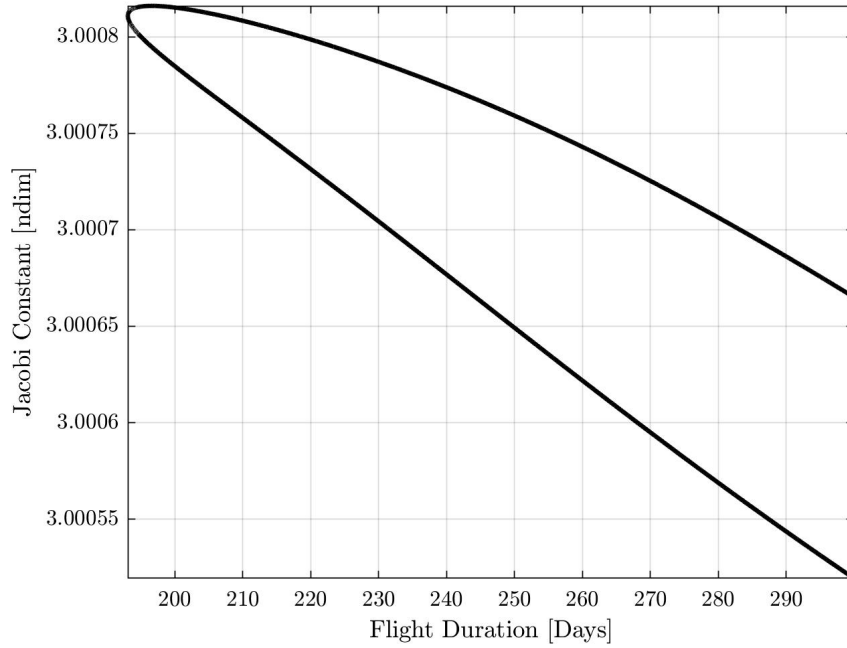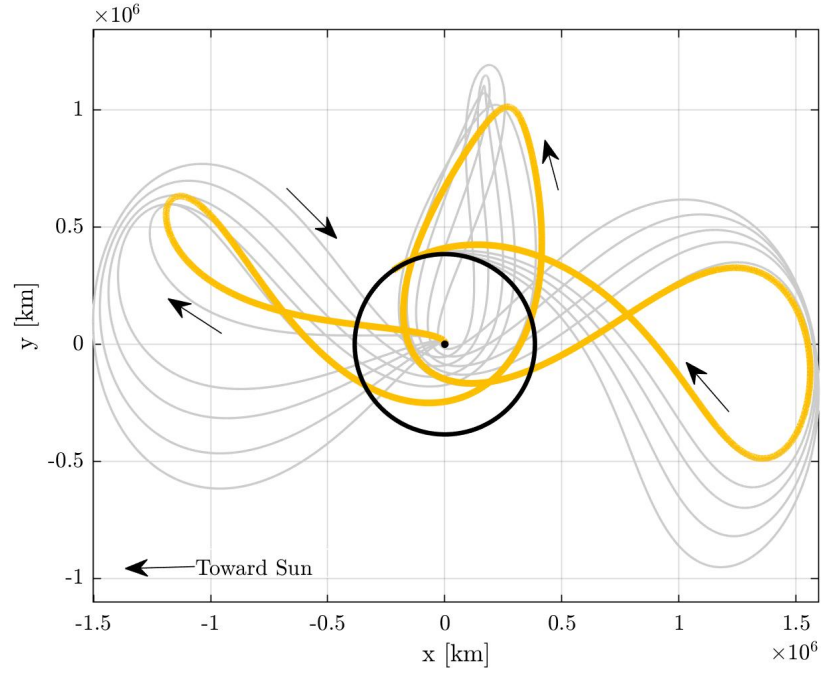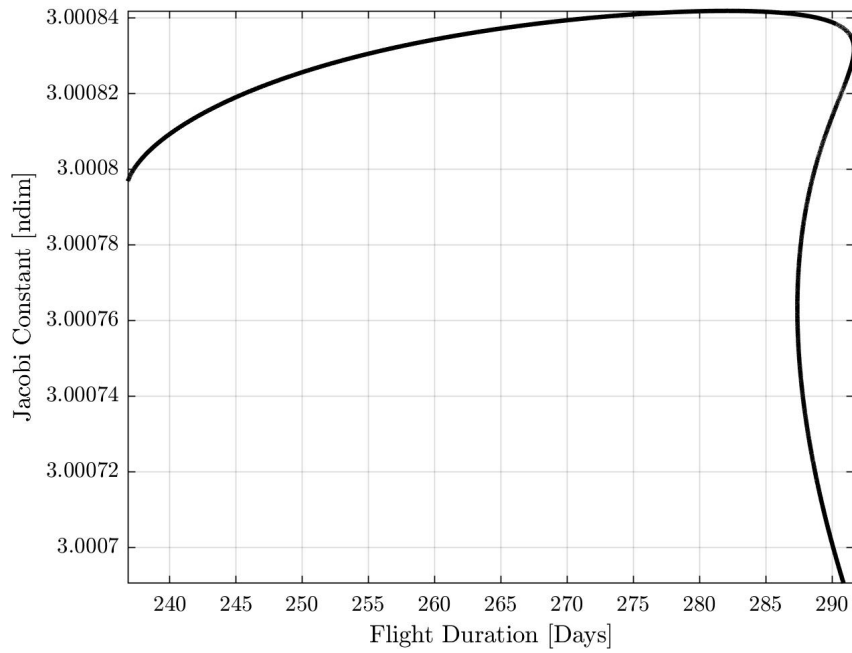
144

Families of transfers in the Sun-Earth CR3BP offer insight into the solar influence on trajectories near the Earth. From the explored families, it is apparent that underlying flow is governing the motion of the transfers. Family 1 offers the shortest time of flight, with some of the lowest energy solutions for the time of flight considered. Whereas Family 8 includes the lowest energy solution, yet requires an additional 200 days to reach the lunar orbit radius. Other families traverse the near the L_1 and L_2 Lagrange points, which could offer scientific advantages depending on the mission. The Sun-Earth CR3BP offers an effective model the analyze the dominant characteristics of these complex transfers.

4.3 Ballistic Lunar Transfers in the BCR4BP

Ballistic lunar transfers are governed by the gravitational influence of the Earth, Moon, and Sun. The BCR4BP offers an effective model to construct such transfers, as simplifications to the complex environment present a time-periodic system. The periodicity of the models offers solutions that recur each synodic month. Trajectories within the four-body model flow back and forth between the dominant influence of the Earth-Moon and Sun-B_1 systems. Likewise, dynamical structures are naturally perturbed by the two systems. Therefore, manifold structures off of periodic solutions are incorporated to construct low-energy solutions. Multiple techniques within dynamical systems theory are applied to produce families of ballistic lunar transfers. The first approach applies solutions from the Sun-Earth CR3BP as an initial guess to produce transfers to conic orbits about the Moon. The second approach incorporates the instantaneous equilibrium points as near-optimal energy transfers through the L_2 portal. The third concept explores transfers into multi-body periodic orbits by employing invariant manifold theory for unstable orbits and varied lunar orbit insertion maneuvers for stable orbits.

4.3.1 Transfers to Conic Orbits

Conic orbits about the Moon offer a multitude of applications ranging from staging orbits to lunar surface observations. For this analysis, the assumption is made that the desired orbit is a 100 km circular orbit, that lies in the orbital plane of the Earth, Moon, and Sun,

i.e.,˜-plane. Likewise, the parking orbit about the Earth is selected as a planar circular orbit with an altitude of 150 km above the Earth. A targeting schematic is necessary to devise the transfers. The strategy to produce ballistic lunar transfers to conic orbits mimics the design used for the Sun-Earth CR3BP. Consider the following targeting algorithm,

$$
\bar{X} = \begin{bmatrix} \tilde{x}_0 \\ \tilde{y}_0 \\ \dot{\tilde{x}}_0 \\ \dot{\tilde{y}}_0 \\ \theta_S \\ t \end{bmatrix}
\qquad
\bar{F} = \begin{bmatrix} \sqrt{(\tilde{x}_0 + \tilde{\mu})^2 + \tilde{y}_0^2} - \eta_0 \\ (\tilde{x}_0 + \tilde{\mu})\dot{\tilde{x}}_0 + \tilde{y}_0\dot{\tilde{y}}_0 \\ \sqrt{(\tilde{x}_f - 1 + \tilde{\mu})^2 + \tilde{y}_f^2} - \eta_f \\ (\tilde{x}_f - 1 + \tilde{\mu})\dot{\tilde{x}}_f + \tilde{y}_0\dot{\tilde{y}}_f \end{bmatrix}
\qquad (4.4)
$$

where the free variable vector $\bar{X}$ is composed of the initial position, velocity, Sun angle, and time of flight for a planar state in the Earth-Moon BCR4BP. The constraint vector $\bar{F}$ is comparable to the constraint vector used in Equation (4.3). The first element of $\bar{F}$ restricts the initial position to lie on the parking orbit, i.e., a distance of $\eta_0 = 6528$ km from the center of Earth. The second element of $\bar{F}$ confines the initial state to be an apse about Earth. The third and fourth constraints are similar to the first two, however, the primary body of focus is the Moon. The third element constrains the final position to be a set distance from the center of the Moon $\eta_f = 1837$ km, and the fourth element requires the final state to be an apse about the Moon. Note that the free variable vector has two more elements than the constraint vector. As a family evolves along one free variable, an additional constraint needs to be included in order to construct a family of unique solutions. In this investigation, four types of families are considered: fixed period, fixed arrival epoch, fixed TLI maneuver magnitude and fixed LOI maneuver magnitude. Selecting which family to consider relies on the intended mission requirements.

Fixed Period Families

Fixed period families assess available transfer geometries for a designated flight duration. To assemble a family of transfers with a consistent time of flight, either an additional con-

146

straint is added to Equation (4.4), or the time t is removed from the free variable vector. Provided a time of flight is desired, an initial guess is selected from a family of transfers in the Sun-Earth CR3BP. A family of ballistic lunar transfers with a flight duration of 73 days is illustrated in Figure 4.25. The plot is in the Sun-B_1 rotating frame, centered about B_1, where the yellow circle represents the Moon's orbit. Each gray arc is a transfer that departs from a 150 km altitude parking orbit about Earth, and 73 days later arrives into a 100 km altitude low lunar orbit (LLO). The colored transfers exhibit the different feasible geometries within this family. The blue trajectory traverses primarily through quadrant II, and has motion similar Family 1 in the Sun-Earth CR3BP, charted in Figure 4.8. The green arc also possesses ballistic lunar transfer geometry, moving through quadrant IV. However, the purple path moves throughout I and has behavior unforeseen for low energy transfers.
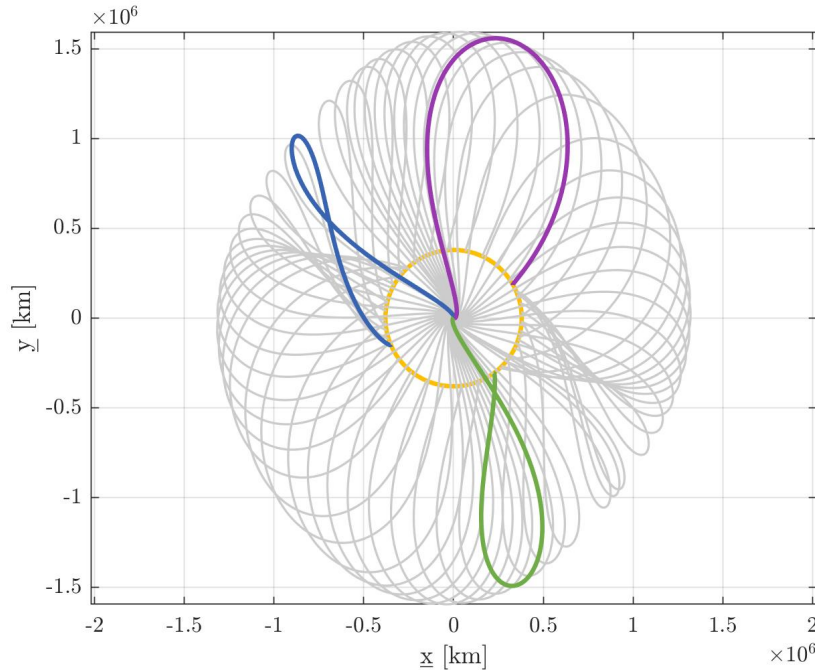
Figure 4.25. Family of ballistic lunar transfers in the BCR4BP with a time of flight of 73 days, depicted in the Sun-B_1 rotating frame

Note the resultant family of ballistic lunar transfers are solutions to the continuation scheme, and do not assess the practicality of the transfers. To further describe the notion of applicability, consider Figure 4.26. The curve expresses the variation in LOI maneuver cost as a

147

function of the initial Sun angle. The family repeats on itself, constructing a closed set of available transfers with a time of flight of 73 days. The colored points on the curve correlate to the colored transfers in Figure 4.25. The blue dot lies on the minimum LOI cost for this family. The other local minimum of the chart is offset by 180 degrees, associated with a transfer that directs away from the Sun. Recall that LOI maneuvers for direct transfers to the Moon cost approximately $\Delta V = 950$ m/s. Therefore, any member of the family that has a higher ΔV than a direct transfer is not leveraging solar perturbations, but rather, is hindered by them. The purple point offers a sample of such transfer. As the solar perturbations dictate, traversing through quadrants I or III far from the Earth-Moon system impedes the desired energy change. Thus, the geometry of the purple transfer in Figure 4.25 is not a practical low energy solution.
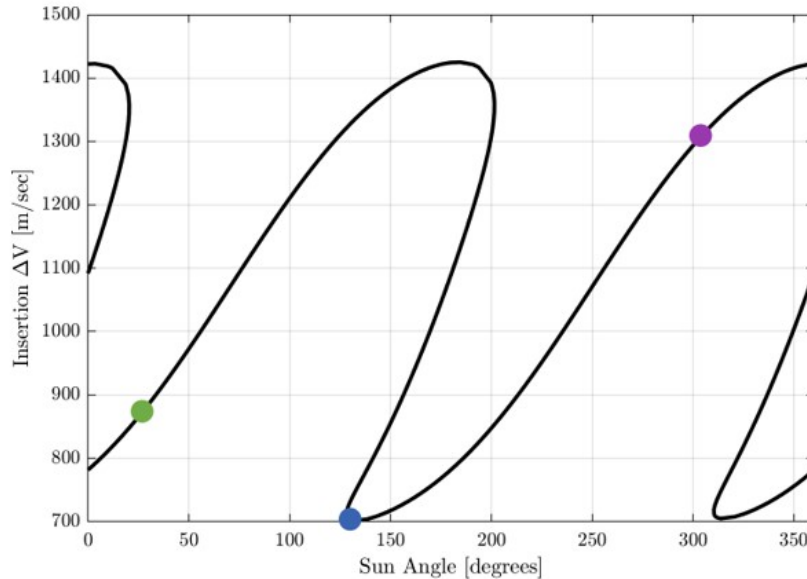
Figure 4.26. Properties of the Family illustrated in Figure 4.25

Various transfer geometries are achievable given a fixed period family. For longer duration ballistic lunar transfers, multiple revolutions about the Earth-Moon system offer extended transfer options. Consider the family of transfers displayed in Figure 4.27. Each transfer has a flight duration of 167 days, and initially departs the Earth away from the Sun. The blue curve designates the solution with the lowest LOI maneuver cost, i.e., $\Delta V = 648$ m/s. A

148

full representation of the TLI and LOI maneuver costs is depicted in Figure 4.28, where the blue dot correlates to the blue transfer. Additional sample transfers from the family with a fixed flight duration of 180 days are represented in Figures 4.29 and 4.30.
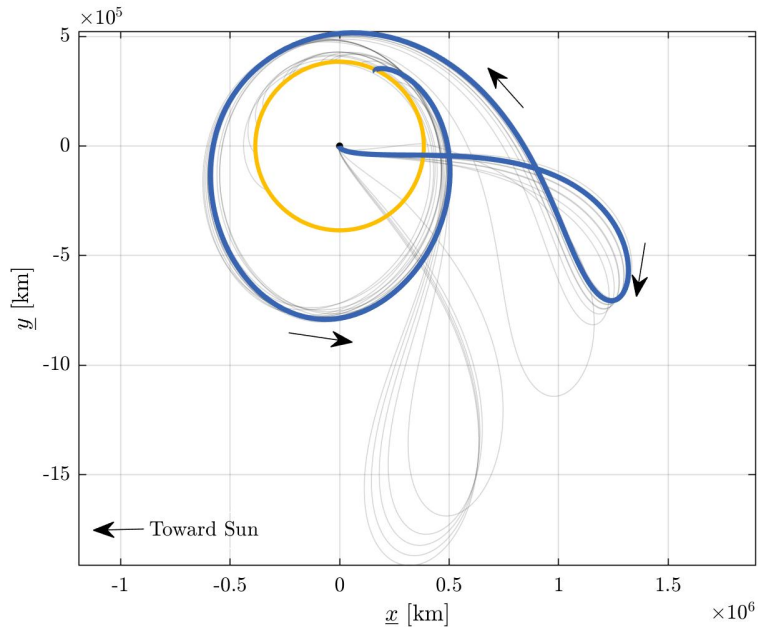
Figure 4.27. Family of ballistic lunar transfers in the BCR4BP with a time of flight of 167 days, depicted in the Sun-B_1 rotating frame
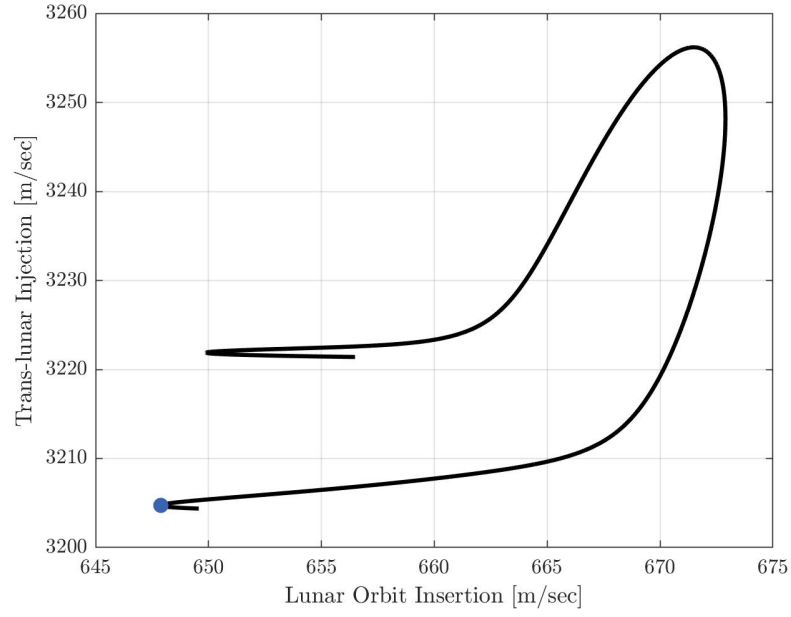
Figure 4.28. Maneuver properties of the fixed transfer duration family illustrated in Figure 4.27
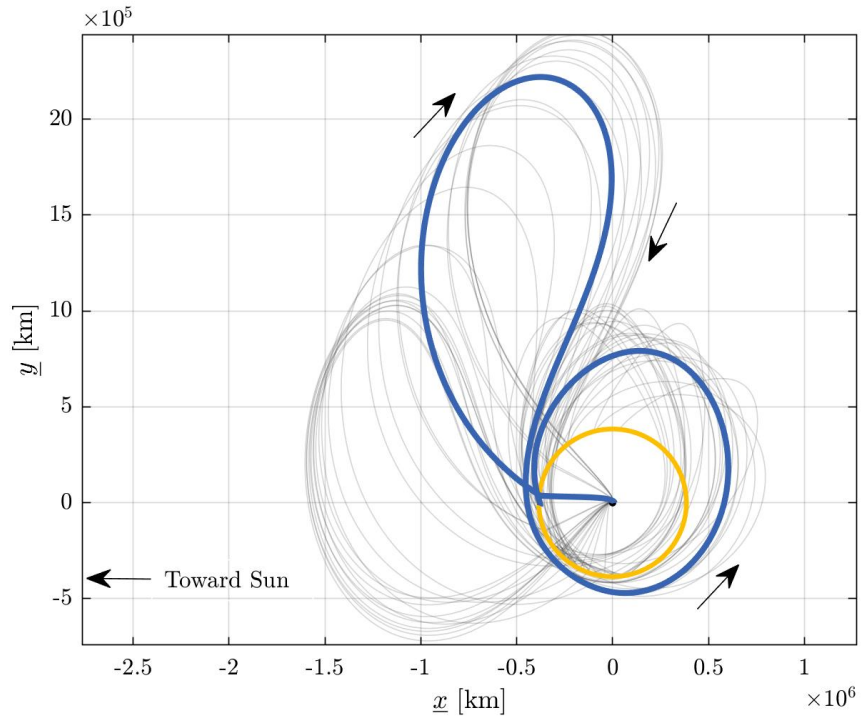
Figure 4.29. Family of ballistic lunar transfers in the BCR4BP with a time of flight of 180 days, depicted in the Sun-B_1 rotating frame

Figure 4.30. Maneuver characteristics of the fixed transfer duration family illustrated in Figure 4.29

Fixed Arrival Epoch Families

It is favorable to compare transfers that reach the Moon at a given epoch. In the BCR4BP, the desired epoch is represented by either the Earth-Moon angle or the Sun angle. By holding the arrival epoch const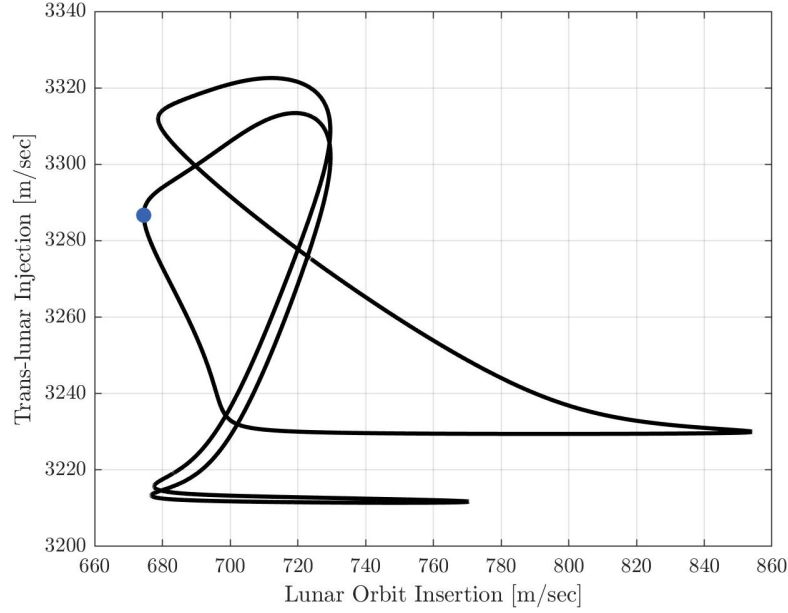ant, an additional entry is appended to the constraint vector in Equation 4.4. Analogous to the fixed period family, a pseudo-arclength continuation scheme is conducted to produce a family of ballistic lunar transfers. The initial guess for the continuation scheme originates from either the transfer in the Sun-Earth CR3BP or a member from other families in the BCR4BP. The family of transfers in Figure 4.31 exhibit the fixed arrival epoch constraint in the Sun-B_1 rotating frame. Each transfer arrives at the desired conic orbit when the Moon is a waxing crescent, i.e., the Sun angle is $\theta_S = -\pi/4$. The yellow circle indicates the Moon's orbit about B_1, and each gray curve is a member of the family. The geometry of the family mimics the structure depicted in Family 1 of the Sun-Earth CR3BP, as illustrated in Figure 4.8.
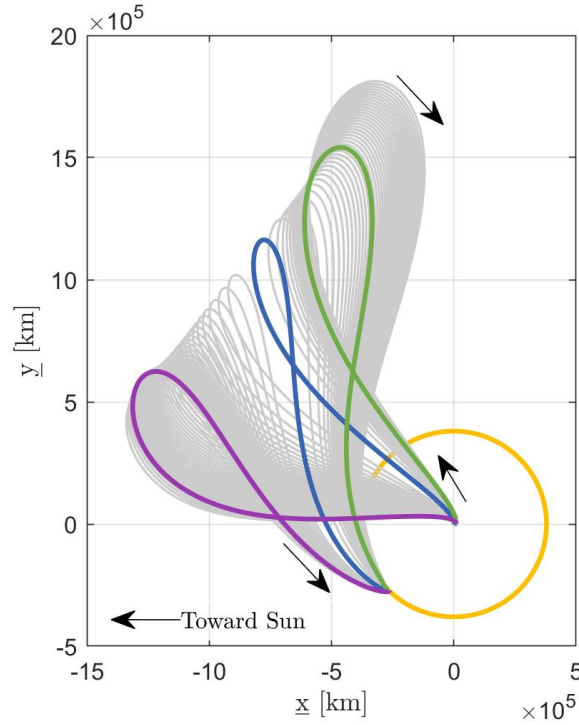
Figure 4.31. Family of ballistic lunar transfers in the BCR4BP that arrives at the Moon with $\theta_S = \text{-}\pi/4$, depicted in the Sun-B_1 rotating frame

As the arrival Sun angle is fixed, the time of flight evolves along the family. Figure 4.32 highlights the variation in the lunar orbit insertion costs as a function of flight duration for the family in Figure 4.31. Each colored point on Figure 4.32 correlates with the colored transfer on Figure 4.31. The blue dot is associated with the lowest insertion maneuver cost along the family.

Continuation along a planar fixed arrival epoch family incorporates outbound lunar fly-bys. Assume a family of transfers initially departs from the Earth in the direction of $\underline{E}_1$, i.e., in the direction of the Sun. The time of flight for a fixed arrival epoch family varies throughout the continuation process, causing the initial Sun angle (epoch) of the trajectory to change. Therefore, the departure arc from Earth in the Earth-Moon rotating frame will revolve about the system. Such motion is depicted by the family of transfers in Figure 4.33. The plot illustrates a family of ballistic lunar transfers in the Earth-Moon rotating frame, that arrive at the Moon at a first-quarter phase, i.e., Sun angle equal to $-\pi$. The green and
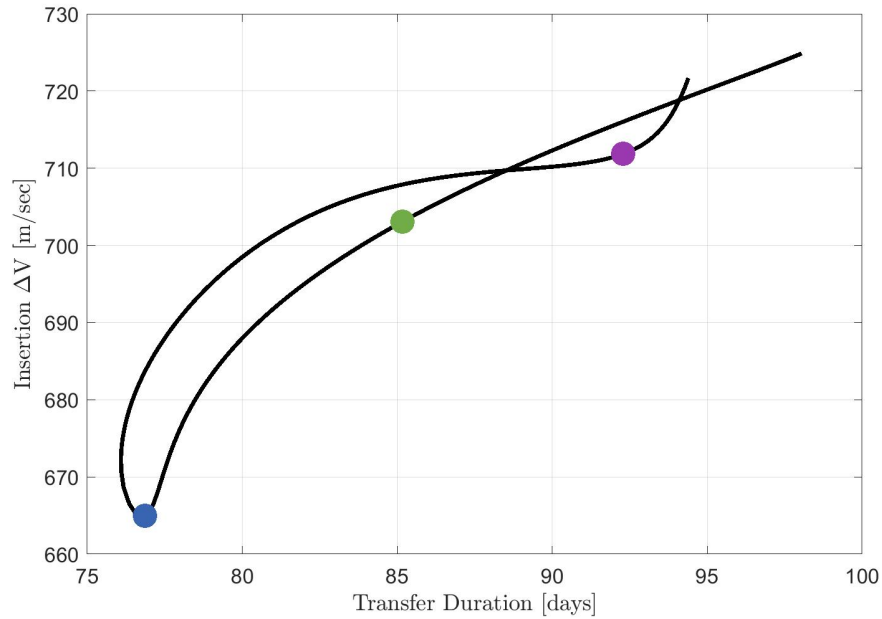
Figure 4.32. Insertion maneuver costs versus flight duration for the fixed epoch family illustrated in Figure 4.31

yellow points represent the location of the Earth and Moon, respectively. The gray transfers appear to initially radiate from the Earth in all directions in the Earth-Moon rotating frame. The blue and purple transfers both represent members of the family, however, the blue transfer departs the Earth away from the Moon, whereas the purple path flies near the Moon. Therefore, members of the family approach the Moon on the outbound leg of the transfer.

Figure 4.33. Family of ballistic lunar transfers in the BCR4BP that arrives at the Moon with $\theta_S = $ -π, depicted in the Earth-Moon rotating frame
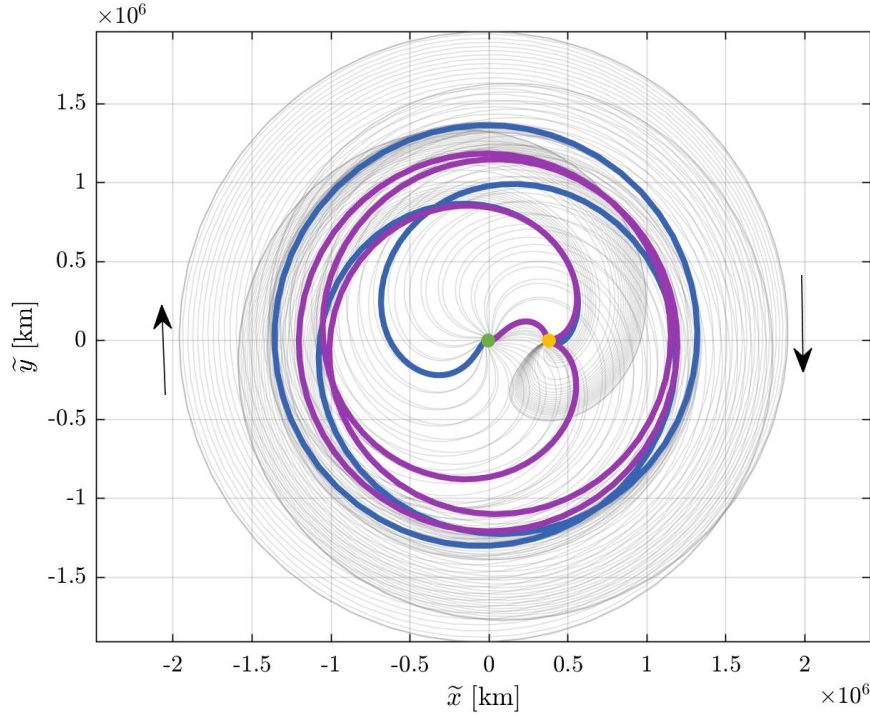
The general motion of ballistic lunar transfers is non-trivial to visualize in the Earth-Moon rotating frame. Thus, Figure 4.34 expresses the same family in the Sun-B_1 rotating frame. The arrival at a first-quarter Moon orientation is apparent in the Sun-B_1 rotating frame. The blue arc is the transfer with the lowest lunar orbit insertion ΔV cost, with a $\Delta V_{LOI} = $ 656 m/sec to circularize into the LLO. The purple trajectory has an outbound lunar flyby, with an altitude above the Moon of 3,873 km. The flyby is noticeable in Figure 4.34 as denoted by the corner near the lunar orbit radius upon departure from Earth. Due to the flyby, the purple arc has the lowest trans-lunar injection cost, $\Delta V_{TLI} = 3{,}142$ m/sec. Figure 4.35 expresses the variation maneuver costs along the family of solutions, where the colored points correlated to the colored transfers in Figure 4.33 and Figure 4.34.
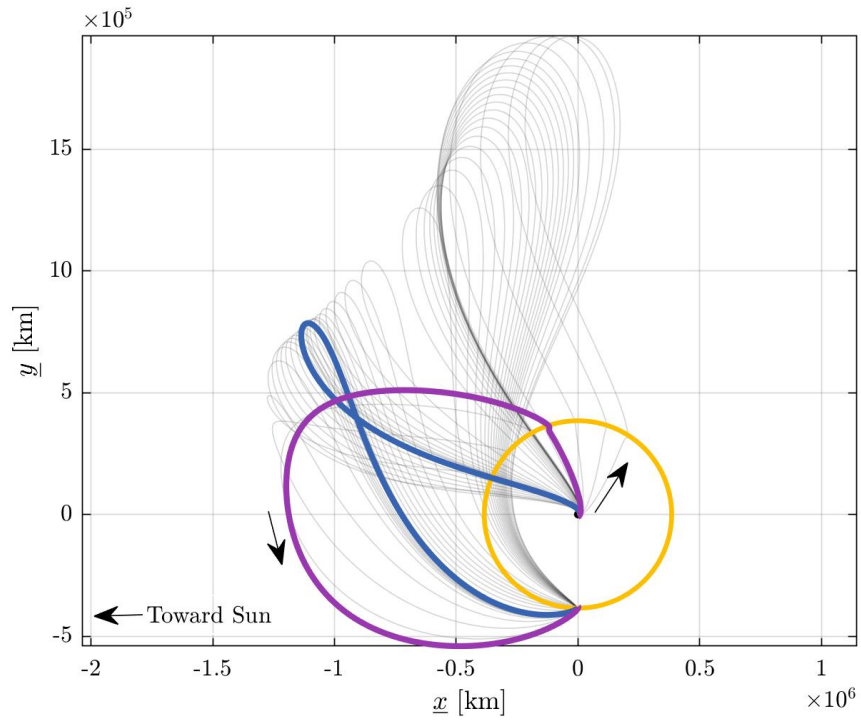
Figure 4.34. Family of ballistic lunar transfers in the BCR4BP that arrives at the Moon with $\theta_S = \text{-}\pi$, depicted in the Sun-B_1 rotating frame

Figure 4.35. Variation in maneuver costs for the family of transfers depicted in Figure 4.33 and Figure 4.34

Figure 4.36 provides a family of ballistic lunar transfers with multiple sets of outbound lunar flybys. The arrival epoch is at a waning crescent phase of the Moon, i.e., the Sun angle is π. The transfer in blue has the minimum trans-lunar injection cost across the family. To
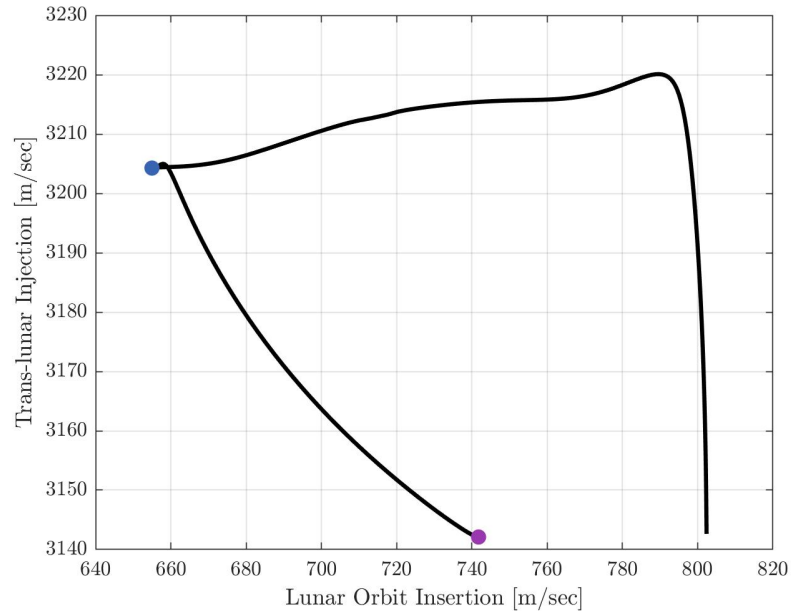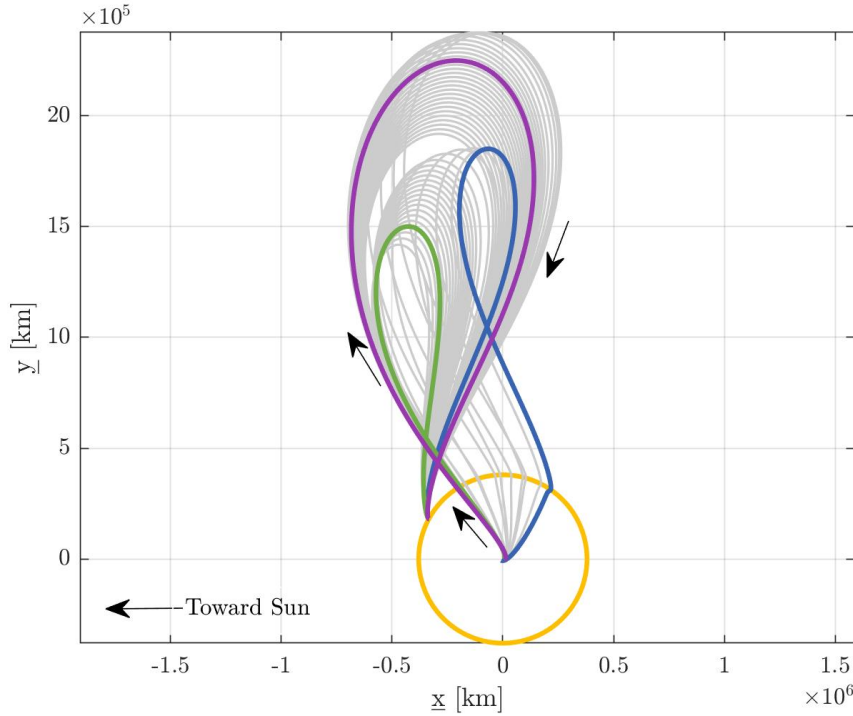

Figure 4.36. Family of ballistic lunar transfers in the BCR4BP that arrives at the Moon with $\theta_S = \pi/4$, depicted in the Sun-B_1 rotating frame

illustrate the occurrence of lunar flybys, Figure 4.37 displays the variation in TLI cost as a function of flight duration along the family. The colored points along the plot correlated to the colored transfers in Figure 4.36. The abrupt dive in TLI maneuver cost occurs at the location where the departure leg of the transfer encounters a lunar flyby. This concurrence repeats roughly every synodic period. As the initial departure from the Earth is defined by the arrival sun angle (remains constant along the family) and the varying time of flight. By leveraging an outbound lunar flyby, the TLI maneuver is reduced by 80 m/sec.
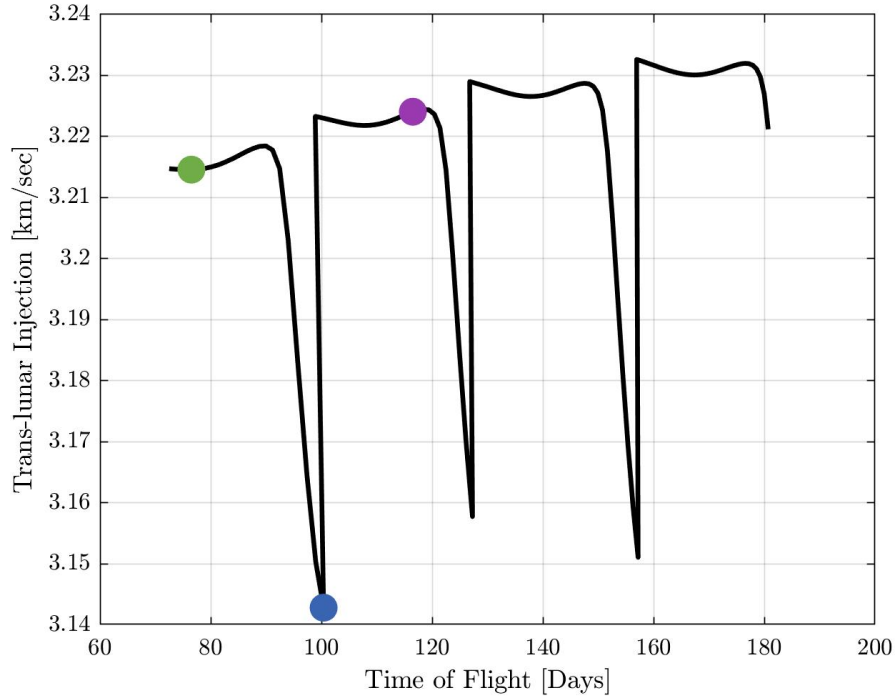
Figure 4.37. Variation in injection maneuver costs as a function of time of flight for the family of transfers depicted in Figure 4.36

Fixed Maneuver Families

Trajectory design considers limitations on launch and maneuver performance for a given spacecraft. Assessing available transfer designs for a given injection or insertion maneuver assists in the exploration of feasible paths to the Moon. To evaluate maneuver conditions, families of fixed maneuvers are employed. Consider a family of transfers that all depart from the parking orbit about the Earth with the same trans-lunar injection maneuver magnitude. To construct such a family, an additional constraint is appended to the constraint vector in Equation (4.4)

$$F_{\text{TLI}} = \sqrt{\dot{x}_0^2 + \dot{y}_0^2 + \dot{z}_0^2} - \Delta V_{\text{TLI}} - V_{\text{LEO}} \qquad (4.5)$$

Equation (4.5) constrains the initial velocity magnitude to be equal to the sum of the TLI maneuver (ΔV_{TLI}) and the orbital velocity of the initial parking orbit V_{LEO}. An initial

condition is selected from a transfer in the Sun-Earth CR3BP, or from a previous set of transfers in the BCR4BP. Figure 4.38 depicts a family of ballistic lunar transfers in the Sun-B_1 rotating frame. Each arc departs from the Earth with a TLI maneuver magnitude of 3,204 m/sec. The blue curve represents the trajectory with the lowest LOI burn, with a magnitude of 654 m/sec. The purple path has a time of flight of 69 days, corresponding to the shortest flight duration along the family. Since each member of the family in Figure
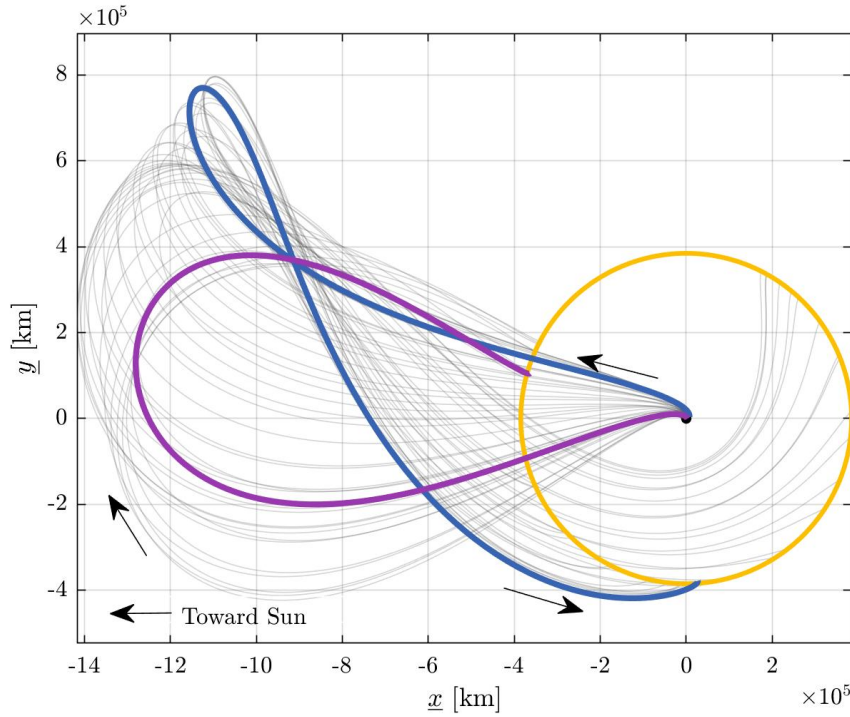
Figure 4.38. Family of ballistic lunar transfers in the BCR4BP that departs the Earth with a TLI maneuver of $\Delta V_{\text{TLI}} = 3,204$ m/sec, depicted in the Sun-B_1 rotating frame

4.38 has the same TLI cost, Figure 4.39 illustrates a trade-space for viable solutions. The curve in Figure 4.39 expresses variation in LOI maneuver costs and flight duration across the family of transfers. Where the colored points correlate to the colored transfers plotted in position space. Although the purple transfer represents the shortest flight duration, the high LOI cost deters from selecting such as solution.
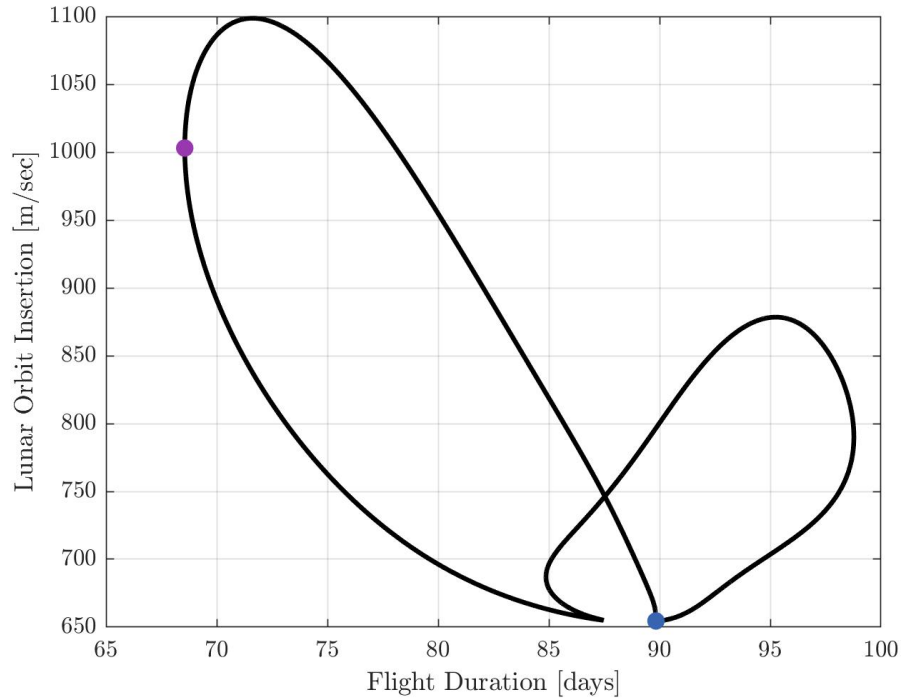
Figure 4.39. Evolution of flight duration and LOI maneuver cost along the family of transfers depicted in Figure 4.38

Selecting a suitable trans-lunar injection maneuver produces a family of transfers that incorporate outbound lunar flybys. Members of the family from Figure 4.36 leverage outbound lunar flybys to reduced the TLI maneuver cost. With proper selection of the TLI maneuver magnitude, the transfer is implicitly constrained to include an outbound lunar flyby. A sample family is illustrated in Figure 4.40. The family includes more transfers, however, for simplicity of visualization, only transfers with an LOI maneuver of less than 850 m/sec are being considered. The lunar flyby altitude varies between 3000 and 7000 km throughout the family. The blue trajectory has the lowest LOI maneuver of 654 m/sec, and the purple curve has the shortest time of flight of 97 days. The variation in flight duration and LOI maneuver cost is illustrated in Figure 4.41.
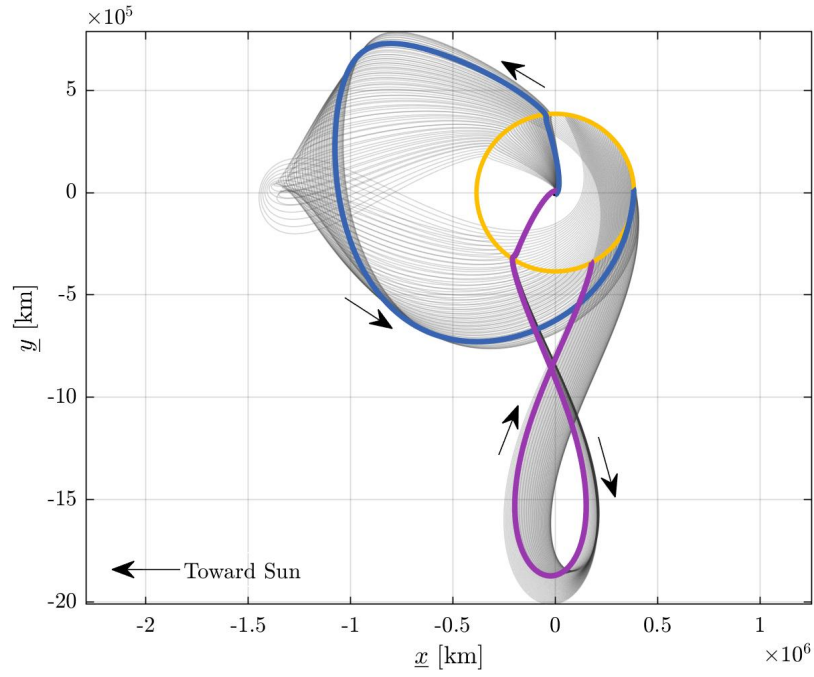
Figure 4.40. Family of ballistic lunar transfers in the BCR4BP that departs the Earth with a TLI maneuver of $\Delta V_{\text{TLI}} = 3{,}146$ m/sec, depicted in the Sun-B_1 rotating frame
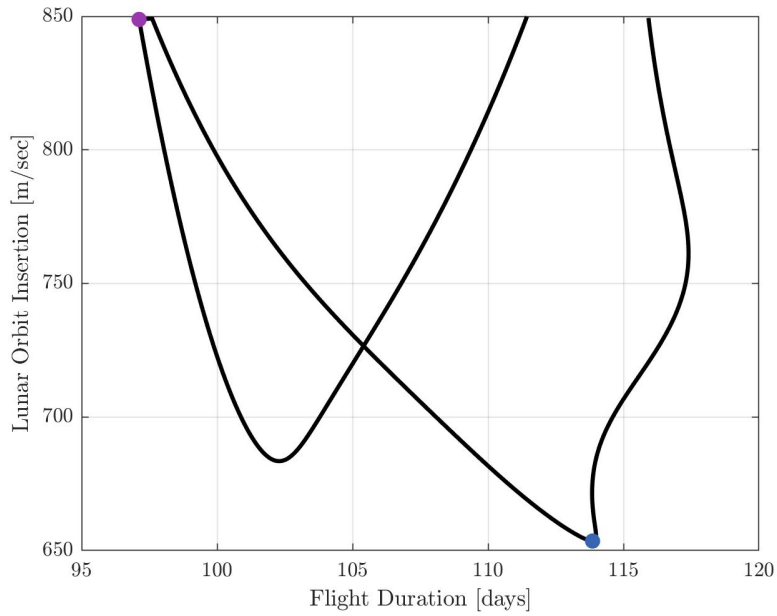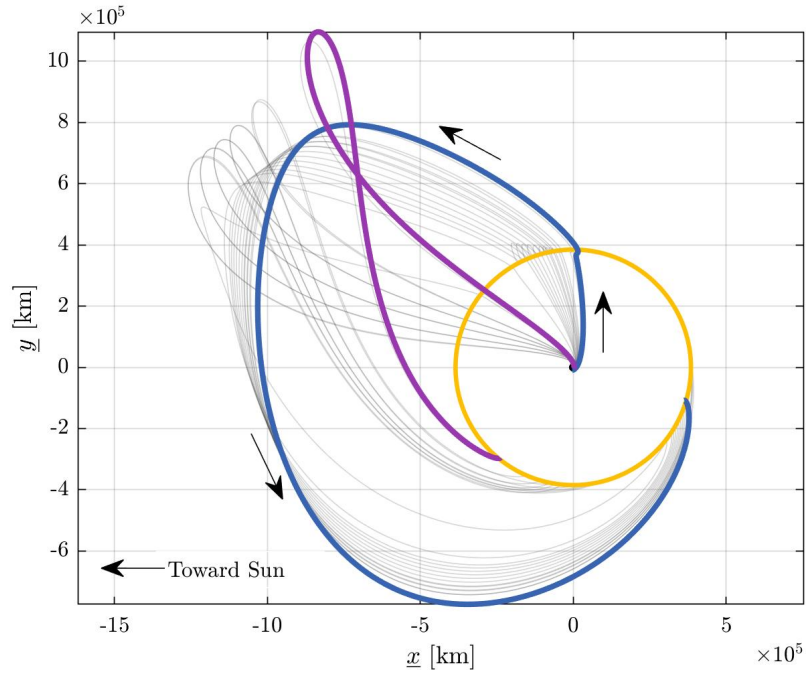

Figure 4.41. Evolution of flight duration and LOI maneuver cost along the family of transfers depicted in Figure 4.40

Families of transfers with a fixed maneuver LOI cost aids in the classification of viable insertions into the lunar vicinity. Ballistic lunar transfers are often selected to reduce the maneuver cost associated with inserting into an orbit about the Moon, thus, fixed maneuver families offer insight into the accessible transfer geometries for certain mission criteria. Consider a set of transfers that depart from the Earth, and arrive into a conic orbit about the Moon, with a constant LOI maneuver cost. To build the solution space, an additional constraint is appended to the constraint vector from Equation (4.4),

$$F_{\mathrm{LOI}} = \sqrt{\dot{\tilde{x}}_f^2 + \dot{\tilde{y}}_f^2 + \dot{\tilde{z}}_f^2} - \Delta V_{\mathrm{LOI}} - V_{\mathrm{LLO}} \qquad (4.6)$$

where ΔV_{LOI} is the desired LOI maneuver cost, and ΔV_{LOI} is the velocity of the conic orbit at the point of insertion. Recall that the constraint vector formulated in Equation (4.4) assumes that the arrival condition at the Moon is an apse. A family of transfers with an LOI maneuver magnitude $\Delta V_{\mathrm{LOI}} = 660$ m/sec is illustrated in Figure 4.42. Each gray arc leaves from a 150 km circular parking orbit about the Earth and inserts onto a 100 km circular LLO. The blue transfer offers the lowest cost TLI maneuver to depart from the Earth with a value of $\Delta V_{\mathrm{TLI}} = 3142$ m/sec. The purple curve has the shortest flight duration, with a total time of flight of 76.9 days. A section of the family leverages outbound lunar flybys to reduce the injection cost, however, maintain the LOI magnitude constraint. The evolution of TLI maneuver cost and flight duration is plotted in Figure 4.43. The colored points represent the same colored transfers in Figure 4.42.

Figure 4.42. Family of ballistic lunar transfers in the BCR4BP that departs the Earth with a TLI maneuver of $\Delta V_{\text{LOI}} = 660$ m/sec, depicted in the Sun-B_1 rotating frame
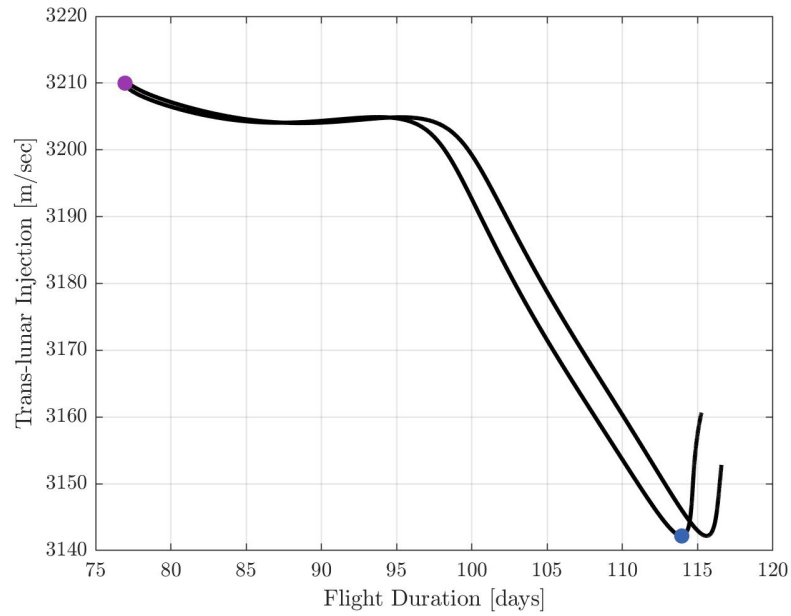
Figure 4.43. Evolution of flight duration and TLI maneuver cost along the family of transfers in Figure 4.40

4.3.2 Theoretical Minimum Lunar Orbit Insertion

One challenge associated with ballistic lunar transfers is assessing the effectiveness of lunar orbit insertion. As described in section 3.8, energy naturally evolves throughout the BCR4BP. Thus, in theory, any natural arc is achievable given enough time and the correct perturbations due to the Sun. However, given a set of assumptions, an approximate theoretical minimum LOI maneuver is determined for conic orbits about the Moon.

The Jacobi constant of the Lagrange points in the CR3BP dictates the energy necessary to transit through a portal. Recall, for Jacobi constant values below the L_2 Lagrange point, motion within the Earth-Moon vicinity remains bounded for all time. The instantaneous equilibrium solutions in the BCR4BP offer similar properties. As a ballistic lunar transfer has to transit through the $\widetilde{E}_2$ portal prior to insertion at the Moon, the Earth-Moon Hamiltonian at that point must be below the maximum Hamiltonian of $\widetilde{E}_2$. The variation in Hamiltonian across the $\widetilde{E}_2$ points is illustrated in Figure 2.21. An assumption is made that near the Moon, the Earth-Moon Hamiltonian remains nearly constant. Therefore, a near-optimal ballistic lunar transfer will arrive at its lunar orbit insertion with an Earth-Moon Hamiltonian equivalent to the maximum Hamiltonian for the set of $\widetilde{E}_2$ points. The maximum Earth-Moon Hamiltonian for the set $\widetilde{E}_2$ is 1694.9734 nondimensional units. For a more conservative estimate, the maximum Hamiltonian for the set of $\widetilde{E}_1$ points is applied, i.e., 1694.9824 nondimensional units.

The theoretical minimum lunar orbit insertion maneuver cost depends on the energy level of the final orbit. Low lunar orbits about the Moon have a higher Earth-Moon Hamiltonian than the sets of instantaneous equilibrium points. Consider a planar circular orbit around the Moon with an altitude of 1000 km. After propagating for an entire synodic period, the variation in the Earth-Moon Hamiltonian is illustrated in Figure 4.44. From section 3.8, the Earth-Moon Hamiltonian evolves as a function of the position in the Sun-B_1 rotating coordinate frame. Thus, a transfer closely bounded by the Moon will exhibit slight variations in the Hamiltonian. Since a ballistic lunar transfer upon arrival at the Moon has much higher energy than the conic orbit, the desired insertion location along the LLO occurs where the Hamiltonian is at a minimum. For the 1000 km circular orbit, the minimum Earth-

Moon Hamiltonian is 1696.4592 nondimensional units. Note that the minimum Earth-Moon Hamiltonian will change as the conic orbit about the Moon is varied.
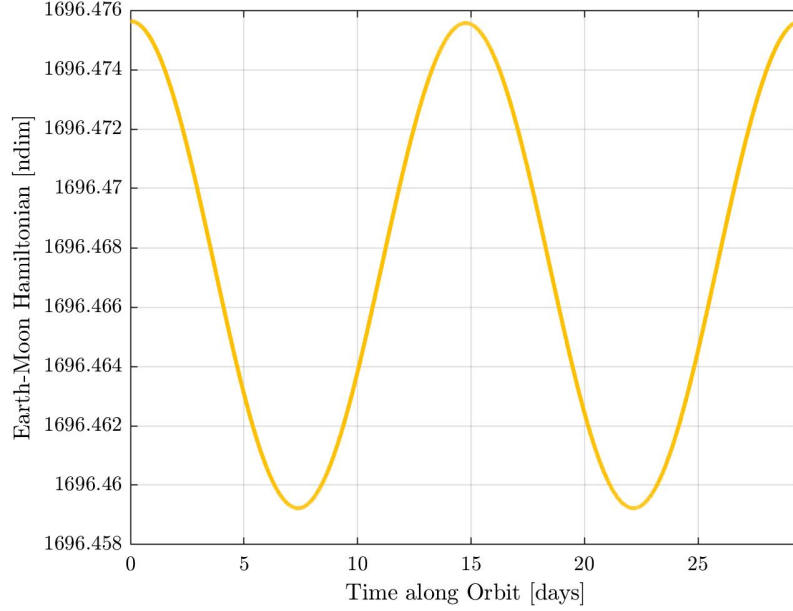
Figure 4.44. Evolution of the Earth-Moon Hamiltonian along a 1000 km circular orbit about the Moon across one synodic period

The difference in energy between an incoming transfer and the desired conic orbit offers a theoretical minimum insertion maneuver cost. Given the assumption that the incoming ballistic lunar transfer is assumed to have an energy equivalent to the maximum $\widetilde{E}_2$ Hamiltonian, i.e., $H_{\mathrm{BLT}} = 1694.9734$ nondimensional units. Likewise, the transfer is arriving into the desired 1000 km altitude circular orbit about the Moon, with a minimum Hamiltonian of $H_{\mathrm{LLO}} = 1696.4592$ nondimensional units. The difference between the two energy values are written in terms of the expression in Equation 2.56,

$$H_{\mathrm{LLO}} - H_{\mathrm{BLT}} = 2\widetilde{\Upsilon}_{\mathrm{LLO}} - 2\widetilde{\Upsilon}_{\mathrm{BLT}} - V_{\mathrm{LLO}}^2 + V_{\mathrm{BLT}}^2 \tag{4.7}$$

where $\widetilde{\Upsilon}_{\mathrm{LLO}}$ and $\widetilde{\Upsilon}_{\mathrm{BLT}}$ are the pseudo-potential values for the LLO and ballistic lunar transfer, respectively. The quantities V_{LLO} and V_{BLT} are the scalar velocity of trajectories in the

164

rotating coordinate frame. As an maneuver is required to occur at specific position and epoch, $\widetilde{\Upsilon}_{\mathrm{LLO}} = \widetilde{\Upsilon}_{\mathrm{BLT}}$, thus, Equation (4.7) is reduced to

$$H_{\mathrm{LLO}} - H_{\mathrm{BLT}} = V_{\mathrm{BLT}}^2 - V_{\mathrm{LLO}}^2 \tag{4.8}$$

As the velocity of a conic orbit is known, Equation (4.8) is rewritten to solve of the velocity of the ballistic lunar transfer upon arrival at the insertion location,

$$V_{\mathrm{BLT}} = \sqrt{V_{\mathrm{LLO}}^2 + H_{\mathrm{LLO}} - H_{\mathrm{BLT}}} \tag{4.9}$$

Recall that the minimum velocity magnitude necessary to perform an energy change is tangential to the current velocity direction, as illustrated in Figure 4.3 and written quantitatively in (4.2). Therefore, an expression for the theoretical minimum insertion maneuver is derived,

$$\Delta V_{\mathrm{MIN}} = V_{\mathrm{BLT}} - V_{\mathrm{LLO}}$$
$$\Delta V_{\mathrm{MIN}} = \sqrt{V_{\mathrm{LLO}}^2 + H_{\mathrm{LLO}} - H_{\mathrm{BLT}}} - V_{\mathrm{LLO}} \tag{4.10}$$

where ΔV_{MIN} is the scalar theoretical maneuver magnitude necessary to insert into the desired conic orbit. Note that the terms $V_{\mathrm{LLO}}^2 + H_{\mathrm{LLO}}$ can be reduced to $\widetilde{\Upsilon}_{\mathrm{LLO}}$. Given the case where a near-optimal ballistic lunar transfer is arriving into a 1000 km circular orbit, Equation (4.10) yields $\Delta V_{\mathrm{MIN}} = 494$ m/sec. A curve of theoretical minimum maneuver magnitudes is produced by varying the altitude of the desired conic orbit, illustrated in Figure 4.45. The blue curve corresponds to an incoming ballistic lunar transfer with an Earth-Moon Hamiltonian equivalent to the maximum Hamiltonian of the set of $\widetilde{E}_1$ points, i.e., H_{BLT} = 1694.9824 nondimensional units. Whereas the yellow arc has an incoming Hamiltonian equivalent to the maximum Hamiltonian for the set of $\widetilde{E}_2$ points, i.e., H_{BLT} = 1694.9734 nondimensional units. The general trend for the two curves is similar, as the altitude of the circular orbit increases, the theoretical minimum LOI cost decreases. The set of $\widetilde{E}_1$ produce lower ΔV_{MIN} values for a given altitude because the energy estimate is more conservative.

Since it is frequently of interest to insert into a conic orbit in close vicinity of the Moon, the set of solutions within 1000 km of the surface is plotted in Figure 4.46.
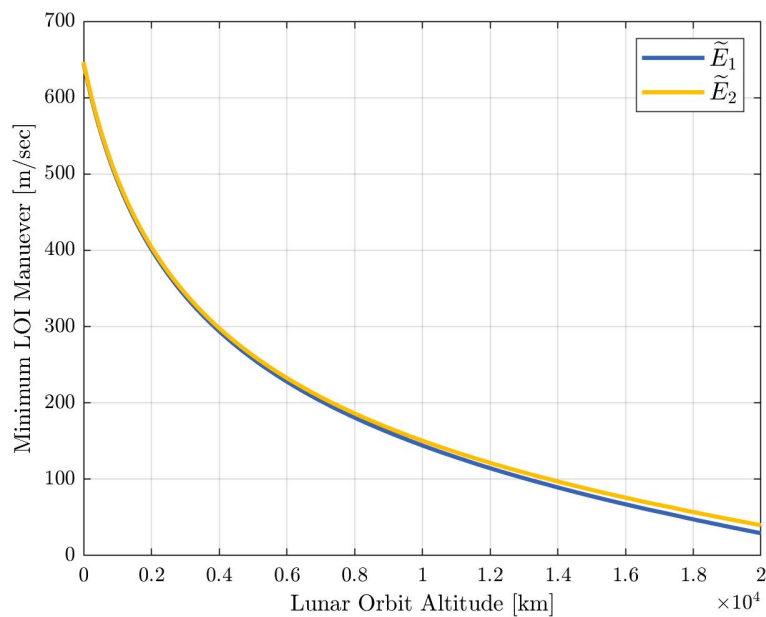

Figure 4.45. Theoretical minimum LOI costs for ballistic lunar transfers with varying lunar orbit altitude
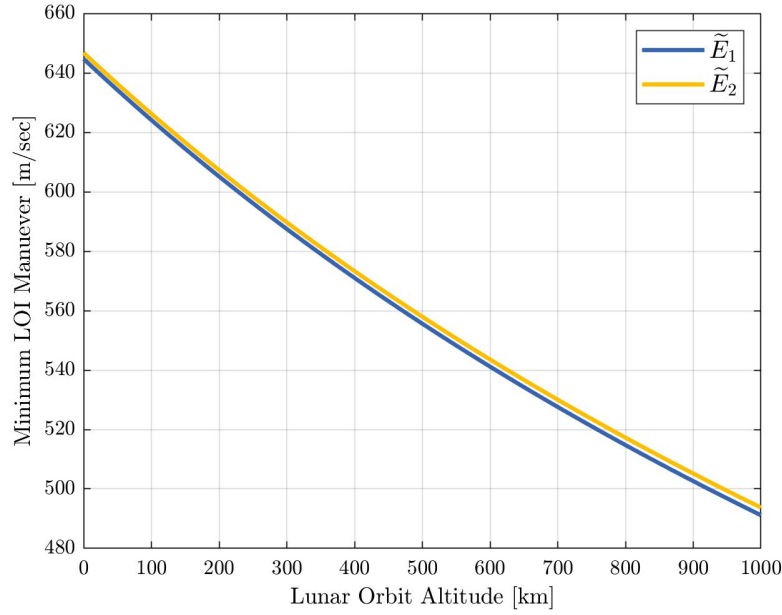
Figure 4.46. Theoretical minimum LOI costs for ballistic lunar transfers with varying lunar orbit altitude less than 1000 km

Instantaneous equilibrium solutions offer low energy transfers that transit through portals in the zero velocity curves. An instantaneous equilibrium point in the BCR4BP is a fixed point for a given orientation of the Earth, Moon, and Sun in a rotating coordinate frame. As the model is propagated forward through time, the point becomes a trajectory. The set $\widetilde{E}_2$ offers solutions that transit though the L_2 portal. To find points that relate to the motion of a ballistic lunar transfer, an instantaneous equilibrium solution propagated forward in time approaches the Moon and departs from the Earth-Moon vicinity propagated in reverse time. To narrow the search even further, the arc must return back to the Earth at the desired parking orbit altitude, for a feasible ballistic lunar transfer. A viable transfer option to a 7500 km altitude circular orbit about the Moon is illustrated in Figure 4.47. The blue arc represents the transfer, and the Moon traverses counterclockwise about the yellow circle. The LOI maneuver cost for this transfer is 207.7 m/sec. The theoretical minimum LOI cost for a 7500 km altitude circular orbit is 196.6 m/sec.

167
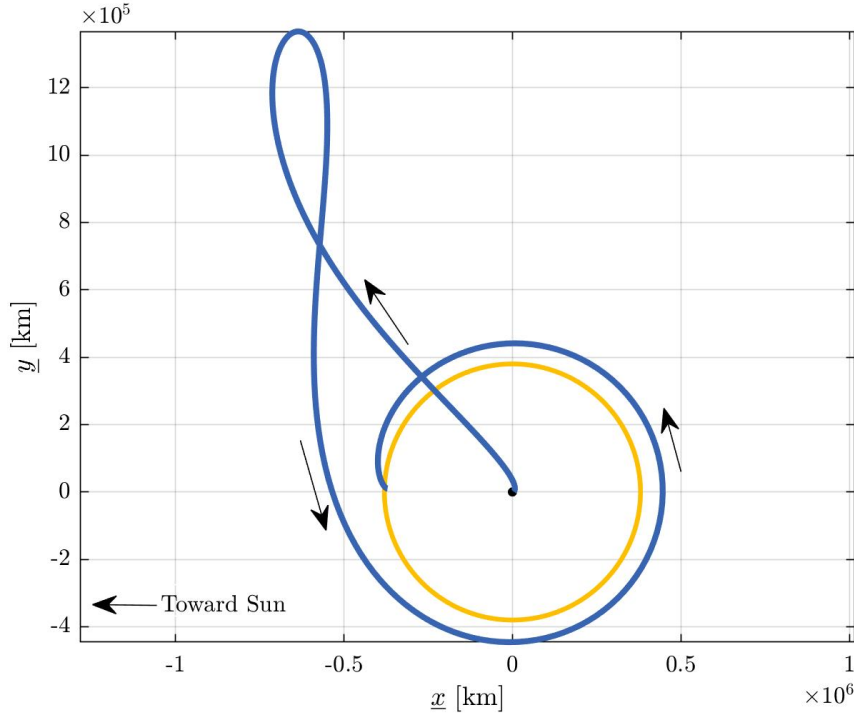
Figure 4.47. A ballistic lunar transfer that includes an instantaneous equilibrium solution along the path, plotted in the Sun-B_1 rotating coordinate frame centered at B_1

The transfer in Figure 4.47 leverages the dynamical structures of a coherent four-body model to insert onto a conic orbit about the Moon at a near theoretical minimum LOI cost. However, the 7500 km altitude circular orbit is only one specific desired orbit. To expand the solution space of this low energy transfer, the trajectory is seeded into a natural parameter continuation scheme. The schematic incrementally decreases the desired altitude of the LOI about the Moon. The resultant family of transfers is illustrated in Figures 4.48 and 4.49. The family of transfers has minor variations in the Sun-B_1 rotating coordinate frame, dissimilar to previous families constructed in the CR3BP and the BCR4BP.
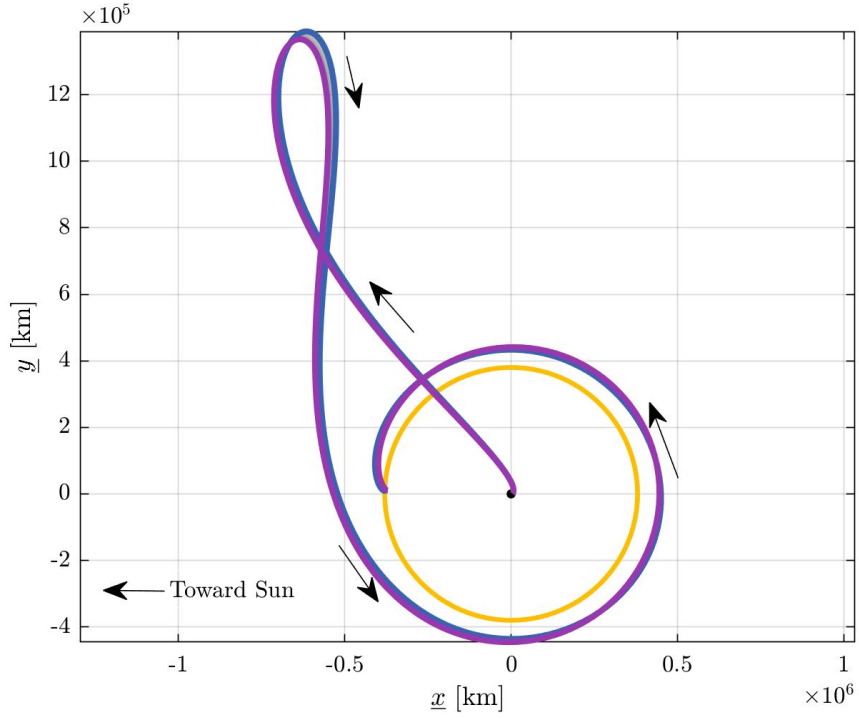
Figure 4.48. Family of ballistic lunar transfers with varying arrival altitude above the Moon, plotted in the Sun-B_1 rotating frame centered about B_1

The transit conditions through the L_2 portal vary as the LOI altitude decreases, as plotted in Figure 4.49. The purple transfer inserts 7500 km above the surface of the Moon, whereas the blue transfer has a 100 km altitude. The size of the Moon is plotted to scale. By visual inspection, as the altitude decreases about the Moon, the family of transfers follows motion similar to the Lyapunov periodic orbits. Although the BCR4BP has limited access to truly periodic motion, the underlying dynamical structures that exist in the CR3BP are still prevalent.
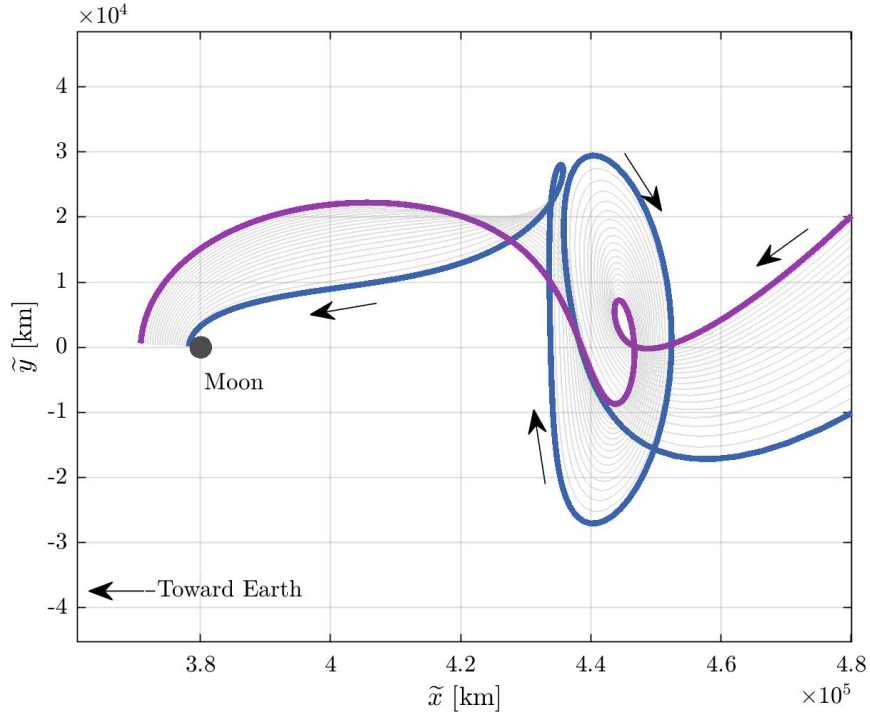
Figure 4.49. Family of ballistic lunar transfers with varying arrival altitude above the Moon, plotted in the Earth-Moon rotating frame focused around the Moon

The LOI maneuver magnitude is assessed for each member of the Family in Figure 4.49, and plotted alongside the minimum theoretical LOI cost in Figure 4.50. The green curve shows the LOI cost for the family as the altitude varies, and closely follows the behavior of the theoretical minimum cases. The transfer associated with the 100 km altitude has an LOI maneuver cost of 632.8 m/sec, with a time of flight of 109.7 days. The theoretical minimum is computed by Equation 4.10 for a 100 km altitude is 626.3 m/sec. In relation to the previous families constructed in the BCR4BP, leveraging the instantaneous equilibrium solutions offers the solution closest the to theoretical minimum. In 1991, Sweetser devised a similar approach using the Jacobi constant of the Lagrange points and predicted the global minimum solution for insertion around the Moon is 622 m/sec [14].
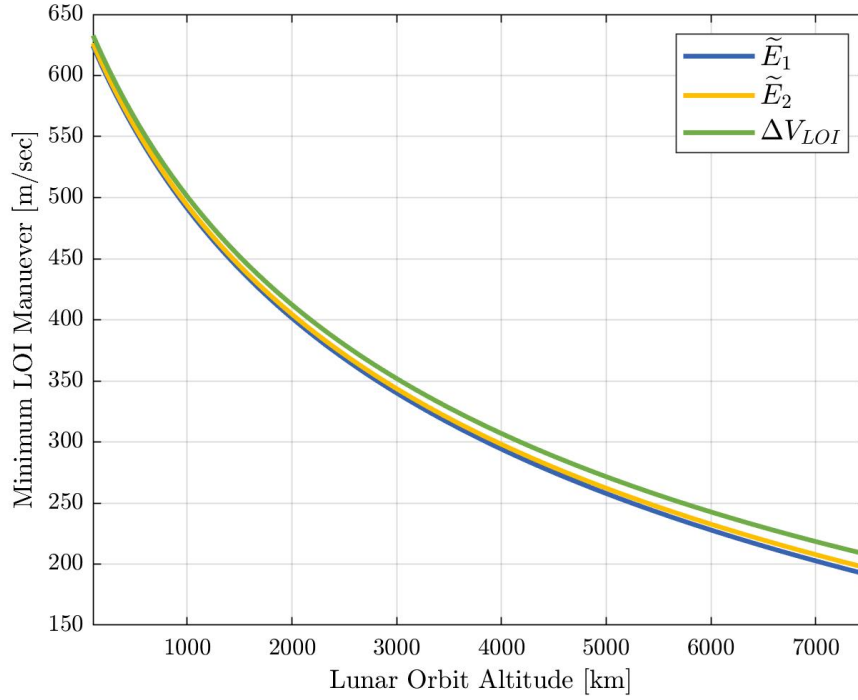
Figure 4.50. Lunar orbit insertion maneuver cost alongside the theoretical minimum maneuver cost for the Family illustrated in Figure 4.49

The theoretical minimum insertion cost offers insight into effective transfer costs. A challenge associated with the four-body model is understanding the limitations of the Sun's impact on a trajectory. By incorporating structures that exist within the Earth-Moon CR3BP, similar behavior is examined within the more complex model. Note that since the BCR4BP is a non-conservative model, there is no true theoretical minimum insertion cost, as the Hamiltonian varies across time. Rather the assumptions made are to simplify the structures to a transfer that is bounded and directly inserts into the desired orbit. Low solutions may exist if more time is spent in the cislunar vicinity, with gradual perturbations from the Sun.

171

4.3.3 Transfers to Unstable Orbits

Unstable periodic orbits in the multi-body regime offer insight into the natural flow throughout the cislunar region. Periodic solutions in the CR3BP and the BCR4BP offer intermediate and destination orbits to explore the lunar vicinity due to their high energy. Arcs along a stable manifold from a periodic orbit approach the orbit as the model evolves forward in time. The manifold structures in the BCR4BP are governed by the dominating effects of both the Earth-Moon and Sun-B_1 systems.

To isolate behavior similar to ballistic lunar transfers, periapse Poincaré maps is employed. Consider the L_2 2:1 synodic resonant Lyapunov orbit in the Earth-Moon system for the BCR4BP, as illustrated by Figure 4.51. The blue arc represents the periodic orbit that has a period of one synodic period, i.e., 29.5 days. The set of instantaneous equilibrium points $\widetilde{E}_2$ are plotted as the black curve within the Lyapunov orbit. The maximum eigenvalue of the monodromy matrix for this orbit is $\lambda \approx 776700$, having a magnitude much greater than one. The Earth-Moon Hamiltonian of the 2:1 synodic resonant Lyapunov orbit is higher than other periodic structures in the BCR4BP. A higher arrival Hamiltonian at the Moon is advantageous to low-energy solutions.
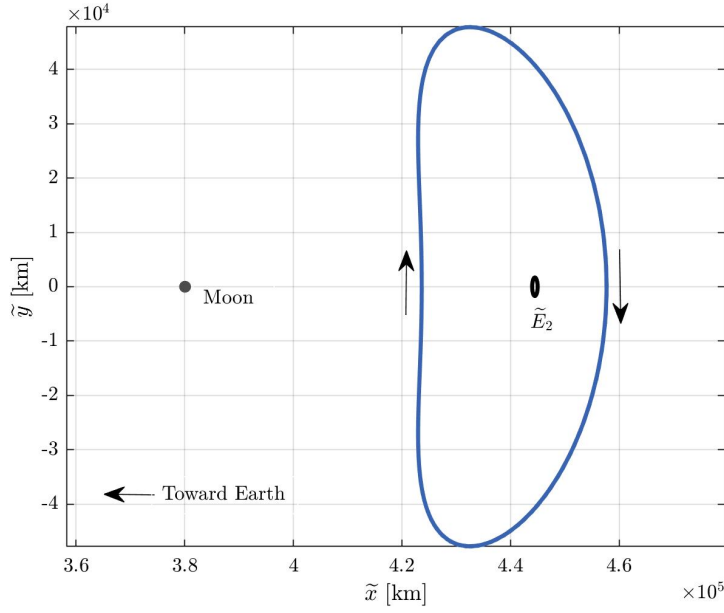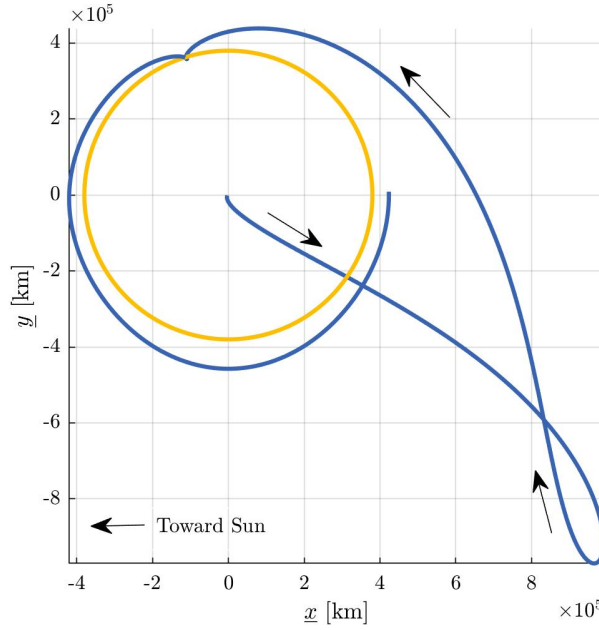
Figure 4.51. L_2 2:1 synodic resonant Lyapunov orbit in the BCR4BP, in the Earth-Moon rotating frame

A periapse Poincaré map is constructed from the L_2 2:1 synodic resonant Lyapunov orbit. By discretizing the orbit by 40,000 points, a position normalized eigenvector is employed to step off the periodic orbit at a distance of 40 km. Since motion arriving into the orbit is desired, only the eigenvector associated with the stable eigenvalue is leveraged. After propagating the initial conditions for 365 days and recording each periapse instance, the map illustrated in Figure 4.52 is created. Each point on the map corresponds to a periapse about the Earth that lies along the manifold structure of the Lyapunov orbit. The color represents the time of flight of the arc from the periapse condition to arrival into the orbit. The green-filled circle is the Earth to scale, and the white circle around the Earth corresponds to a 150 km altitude parking orbit. The map includes the first and second periapsides about the Earth. Coloring the points by flight duration is an option by the user, additional characteristics of the periapse points can be used as a color scale, including the TLI maneuver cost, Earth-Moon Hamiltonian, Sun angle, and periapse number. Additionally, transforming the point to the Sun-B_1 rotating frame to offer insight into the departure conditions relative to the direction of the Sun.

173
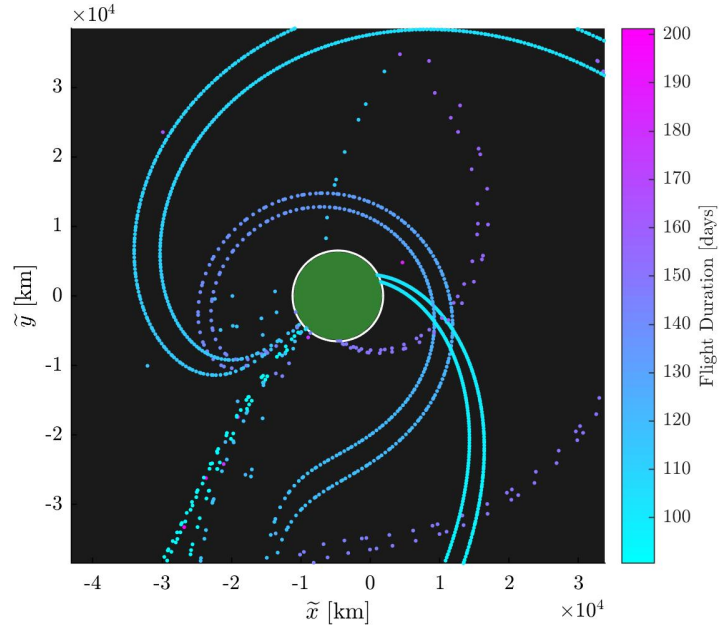
Figure 4.52. Periapse Poincaré map of stable manifold arcs off of the L_2 2:1 resonant Lyapunov orbit in the BCR4BP, in the Earth-Moon rotating frame focused about the Earth

Selecting a periapse that lies near the 150 km parking orbit offers a ballistic lunar transfer to the Lyapunov orbit. A sample transfer is illustrated in Figures 4.53 and 4.54. The blue arcs in both plots represent the trajectory. The entire path is depicted in Figure 4.53, as the curve departs the Earth traveling away from the Sun and toward quadrant IV. The yellow circle represents the lunar orbit. The arrival into the cislunar vicinity is displayed in Figure 4.54, where the Moon is plotted to scale. The arc along the manifold offers a ballistic path onto the Lyapunov orbit due to the unstable nature.

Figure 4.53. Ballistic lunar transfer to the L_2 2:1 synodic resonant Lyapunov orbit, in the Sun-B_1 rotating frame centered at B_1

Additional transfer solutions are available by selecting different points from the periapse Poincaré map. A set of three sample trajectories are illustrated in Figures 4.55, 4.56, and 4.57. These paths do not represent all possible geometries to the L_2 2:1 synodic resonant Lyapunov orbit but offer insight into the structure of the model. Including motion that initially departs the Earth both toward and away from the Sun, i.e., toward quadrants II and IV. Additionally, solutions exist that leverage outbound lunar flybys, and multiple revolutions of the Earth-Moon system to lower TLI costs.
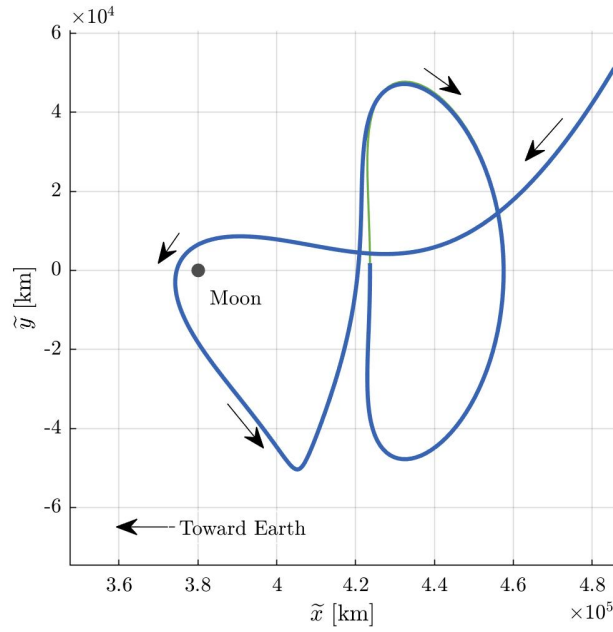
Figure 4.54. Arrival of a ballistic lunar transfer onto a L_2 2:1 resonant Lyapunov orbit, in the Earth-Moon rotating frame focused about the Moon

Figure 4.55. Ballistic lunar transfer to the L_2 2:1 synodic resonant Lyapunov orbit, in the Sun-B_1 rotating frame centered at B_1

Figure 4.56. Ballistic lunar transfer to the L_2 2:1 synodic resonant Lyapunov orbit, in the Sun-B_1 rotating frame centered at B_1
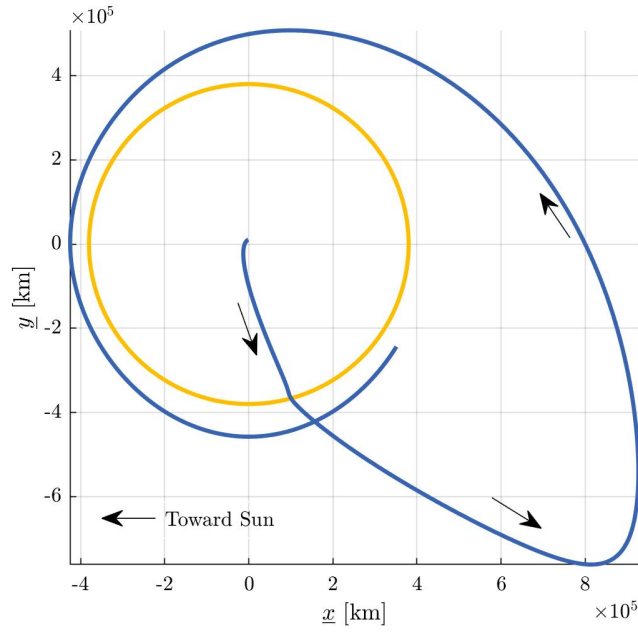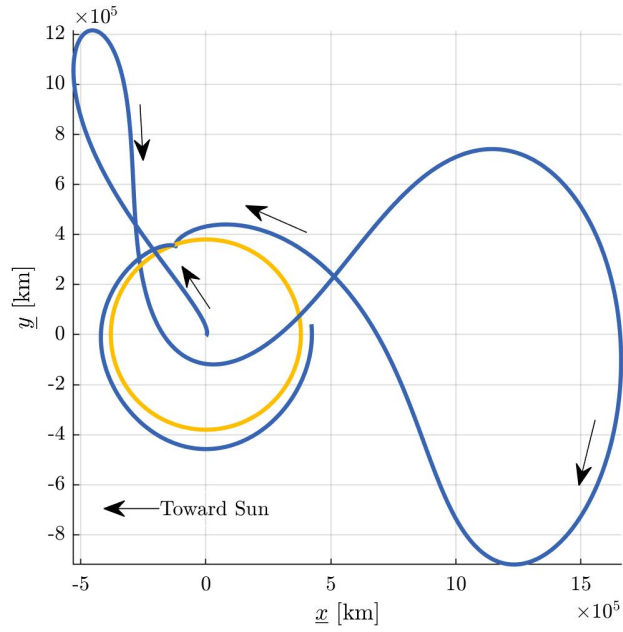

Figure 4.57. Ballistic lunar transfer to the L_2 2:1 synodic resonant Lyapunov orbit, in the Sun-B_1 rotating frame centered at B_1

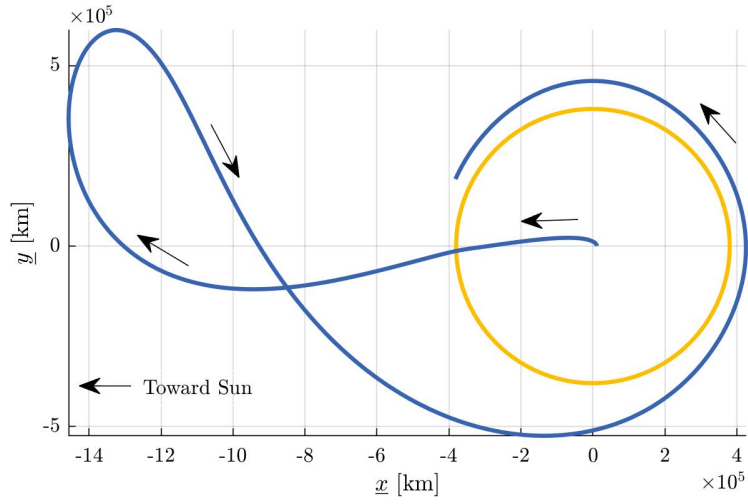Manifold structures from unstable spatial orbits present viable out-of-plane transfer solutions. Spatial periodic orbits offer scientific, communication, and eclipsing advantages. Motion leading to unstable spatial orbits offers insight into the governing dynamics out of the plane. One such periodic orbit is the L_2 2:1 synodic resonant northern Halo, as illustrated in Figure 4.58. To aid in visualization, Figures 4.59 and 4.60 plot the same orbit in the $\hat{\tilde{x}}\hat{\tilde{y}}$ and $\hat{\tilde{x}}\hat{\tilde{z}}$ projections, respectively. In each illustration of the L_2 2:1 synodic resonant northern Halo, the blue curve is the periodic orbit, and the black curve is the set of $\tilde{E}_2$ points. The Moon is plotted to scale. As the motion is symmetric in Figure 4.60, arrows denoting the motion along the arc are not included. The maximum eigenvalue of the monodromy matrix associated with the Halo orbit is $\lambda \approx 819000$, possessing unstable characteristics.
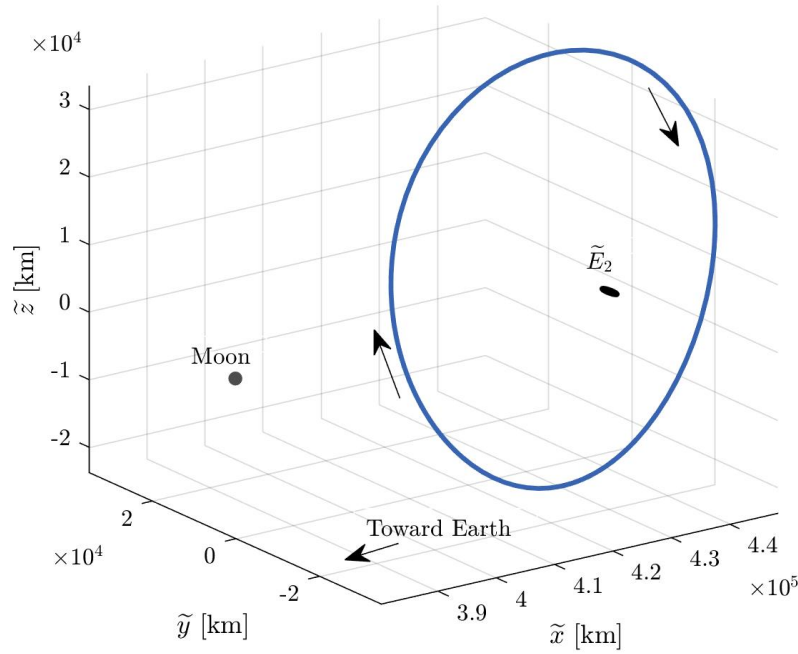
Figure 4.58. Isometric view of the L_2 2:1 synodic resonant northern Halo in the Earth-Moon rotating frame
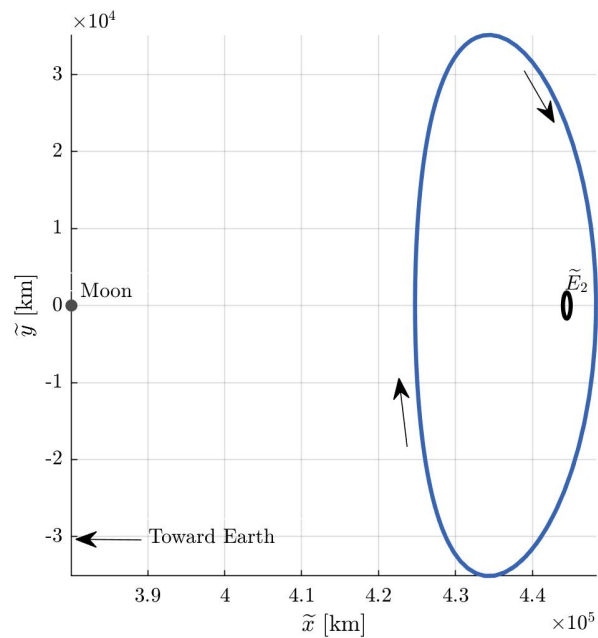
Figure 4.59. $\hat{\widetilde{x}}\hat{\widetilde{y}}$ projection of the L_2 2:1 synodic resonant northern Halo in the Earth-Moon rotating frame
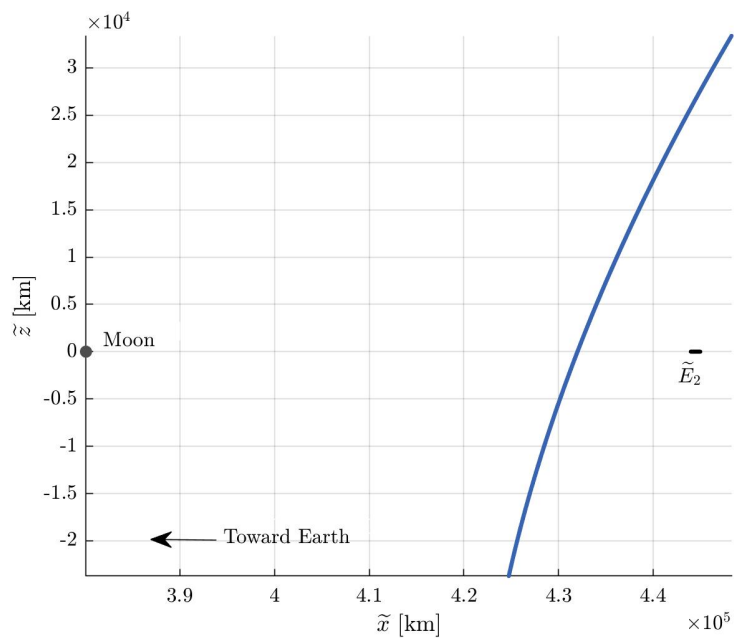
Figure 4.60. $\hat{\widetilde{x}}\hat{\widetilde{z}}$ projection of the L_2 2:1 synodic resonant northern Halo in the Earth-Moon rotating frame

Following the procedure for the planar case, a periapse Poincaré map is constructed from the L_2 2:1 synodic resonant Halo orbit. The orbit is discretized by 30000 points, and at each point, a 40 km step along the eigenvector associated with the stable eigenvalue is performed. By propagating each initial condition for 365 days and recording each periapse. The periapsides in close proximity to the Earth are plotted in Figure 4.61. Like the map for the Lyapunov orbit, points are colored by flight duration, and the green circle represents the Earth to scale. Unlike the planar case, these periapse points are plotted as a projection onto the $\hat{\tilde{x}}\hat{\tilde{y}}$-plane. Therefore, the $\tilde{z}$ component of the periapse needs to be considered when selecting a feasible transfer. A sample transfer to the Halo orbit is illustrated in Figures 4.62 and 4.63. The transfer initially departs the Earth towards quadrant II, i.e., the direction of the Sun, as exhibited in Figure 4.62. Whereas the motion transiting through the L_2 portal into the lunar vicinity is depicted in Figure 4.63.

Figure 4.61. Planar projection of the periapse Poincaré map of stable manifold arcs off of the L_2 2:1 resonant Halo orbit in the BCR4BP, in the Earth-Moon rotating frame focused about the Earth
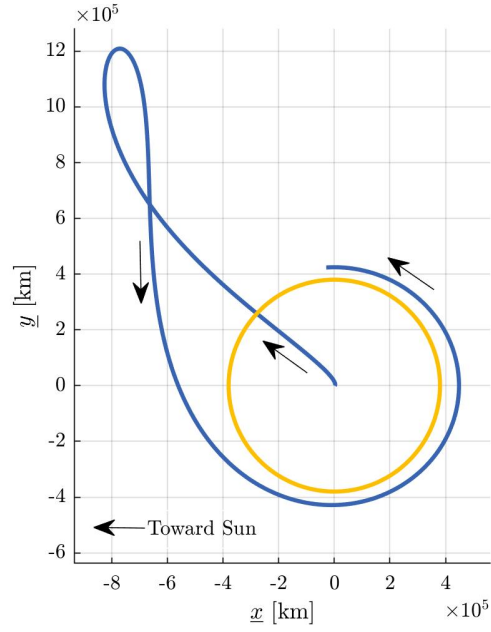
Figure 4.62. Ballistic lunar transfer to the L_2 2:1 synodic resonant Halo orbit, in the Sun-B_1 rotating frame centered at B_1

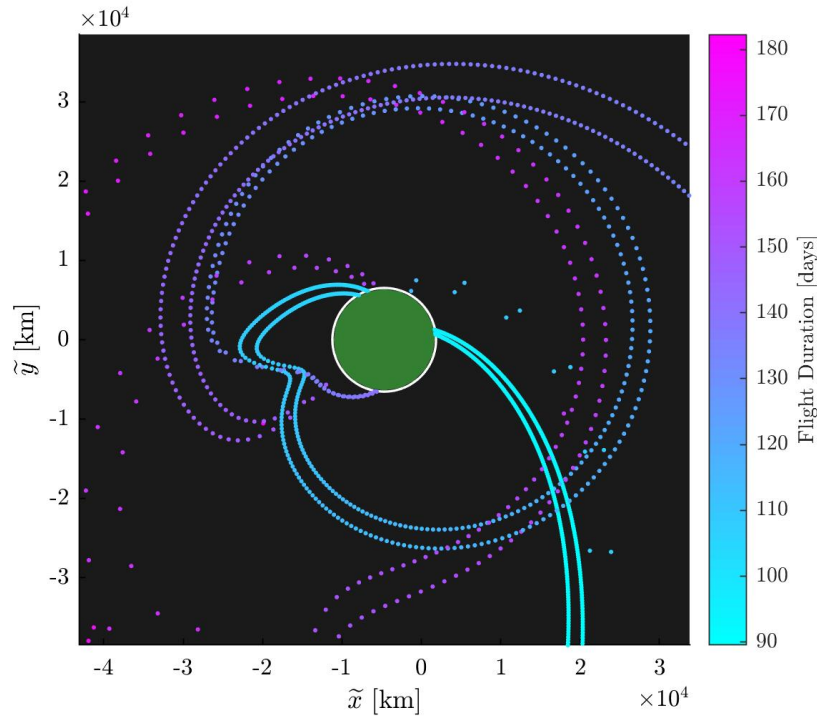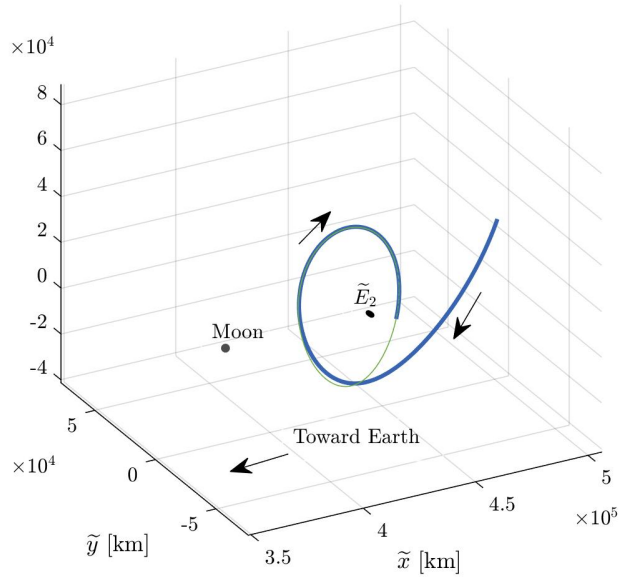**Figure 4.63.** Ballistic lunar transfer to the L_2 2:1 synodic resonant Halo orbit, in the Earth-Moon rotating frame focused near the Moon

Unstable periodic solutions in the BCR4BP offer insight into the natural flow between the two dominating models. Distant from the Earth-Moon system, the manifold structures change in energy in the same manner that ballistic arcs do. The natural change in energy enables the lower maneuver costs associated with inserting about the Moon. For the spatial case, although the planar assumptions involved in formulating the BCR4BP remove out-of-plane perturbations, feasible transfer geometries are accessible. As instability is frequently viewed as an impediment for a solution, unstable periodic solutions present techniques that enable trajectories to embark into the lunar vicinity for minimal deterministic costs.

4.3.4   Transfers to Stable Orbits

Stable periodic orbits in the multi-body regime are advantageous for mission operations as minimal station keeping maneuvers are necessary for a spacecraft to remain in the orbit. Constructing transfers to stable periodic orbits is non-trivial since stable and unstable manifold structures do not exist. For stable periodic solutions with an Earth-Moon Hamiltonian value less than the value required to transit through the L_2 portal, the theoretical insertion maneuver cost is negligible. However, due to the stability of the orbit, a maneuver is performed to insert onto the orbit. Considered the 3:1 synodic resonant distant retrograde orbit (DRO) in the BCR4BP, as illustrated in Figure 4.64. The periodic orbit is depicted as the blue arc and traverses around the Moon in a clockwise direction. The sets of instantaneous equilibrium solutions near the Moon, i.e., $\widetilde{E}_1$ and $\widetilde{E}_2$, are plotted to visualize the scale of the orbit. The period of the orbit is equal to one synodic period, and the maximum eigenvalue of the monodromy associated with the orbit is $\lambda \approx 1.156$. Since the maximum eigenvalue has a magnitude greater than one, in theory, the orbit is unstable. However, compared to the eigenvalues for the Lyapunov and Halo orbits, the rate of departure from the orbit is much slower.
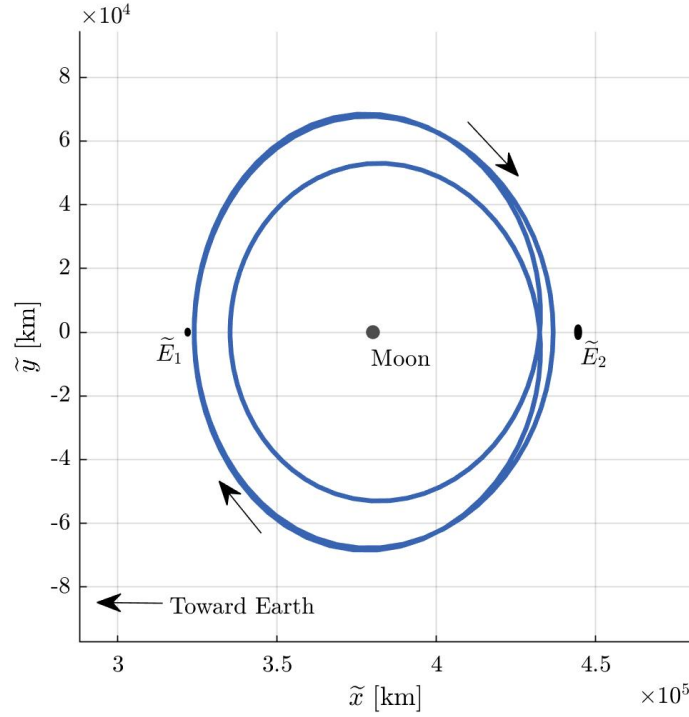
Figure 4.64. The 3:1 synodic resonant DRO in the Earth-Moon rotating frame, focused near the Moon

To account for the reduced divergence rate, a periapse Poincaré map is constructed by performing maneuvers along the orbit. The 3:1 synodic resonant DRO is discretized into 30000 states, and at each instance, a maneuver is performed in the Earth-Moon rotating velocity direction to increase the energy of the transfer. Each initial condition is then propagated in reverse time for 365 days, and each periapse about the Earth is recorded. Selecting a maneuver magnitude is non-trivial, and will influence the structure of the map. Note that the maneuver selected corresponds to LOI costs, and is easily altered for specific mission criteria. The periapse Poincaré map for an LOI maneuver of 50 m/sec is illustrated in Figure 4.65. The color of each point represents the flight duration of the transfer. The filled green circle is the Earth to scale, and the white circle is a planar circular orbit with an altitude of 150 km. The periapse map includes transfers that have up to 5 periapsides prior to reaching the Earth. By comparing the maps of the Halo orbit and the DRO, i.e., Figure 4.61 and Figure 4.65, the structures are less defined for the stable orbit. By increasing the maneuver magnitude to 75 m/sec and 100 m/sec, the periapse Poincaré maps in Figures 4.66 and 4.67

are produced, respectively. The structures within the maps vary as the maneuver magnitude increases, providing a vast range of initial conditions to select from.
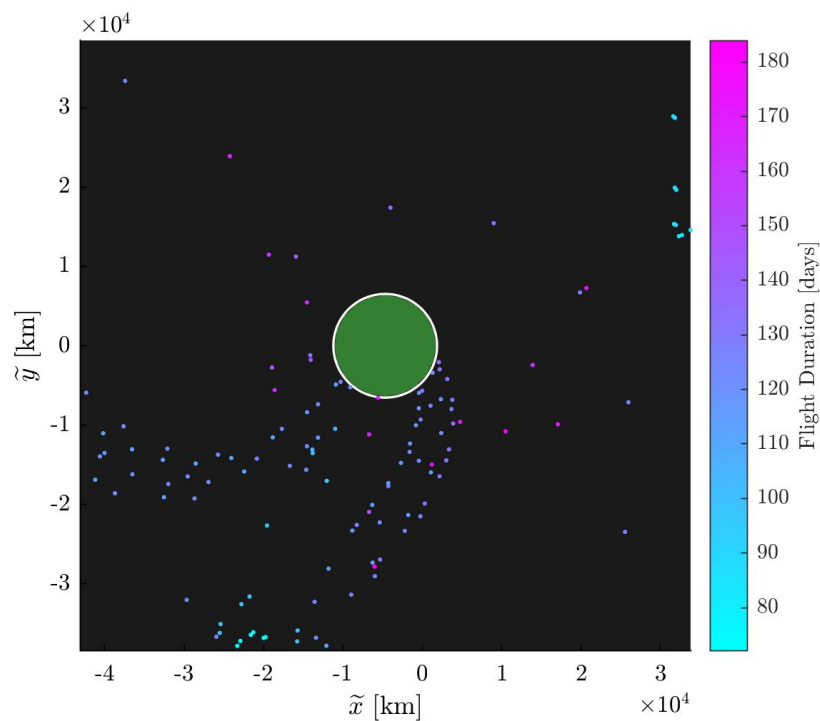
Figure 4.65. Periapse Poincaré map constructed from a 50 m/sec maneuver off the 3:1 synodic resonant DRO, plotted in the Earth-Moon rotating frame
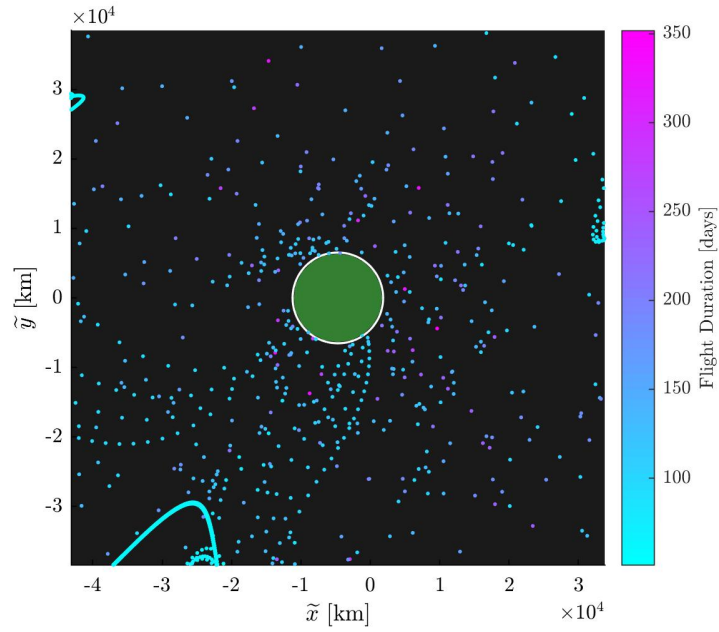
Figure 4.66. Periapse Poincaré map constructed from a 75 m/sec maneuver off the 3:1 synodic resonant DRO, plotted in the Earth-Moon rotating frame
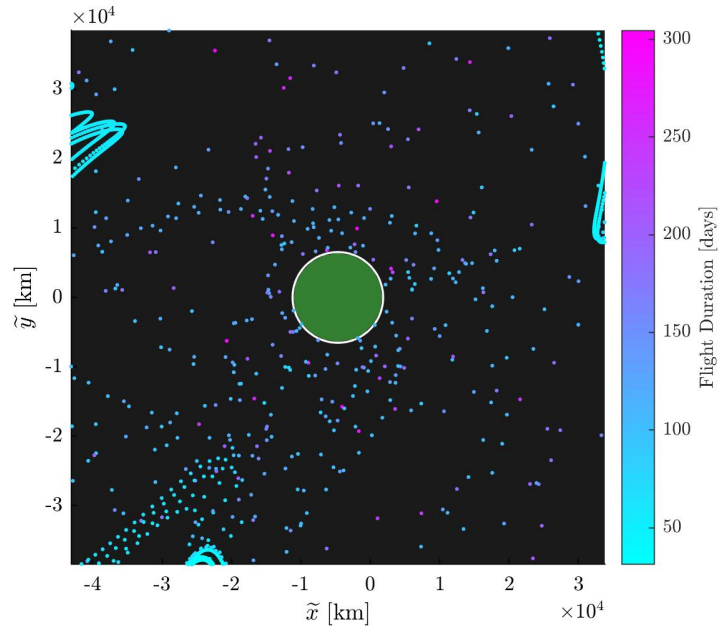
Figure 4.67. Periapse Poincaré map constructed from a 100 m/sec maneuver off the 3:1 synodic resonant DRO, plotted in the Earth-Moon rotating frame

A sample transfer from the 75 m/sec map is illustrated in Figure 4.68. The transfer is plotted in blue, the lunar orbit is yellow, and the green curve is the 3:1 synodic resonant DRO rotated into the Sun-B_1 coordinate frame. The time of flight for the transfer is 100.6 days.
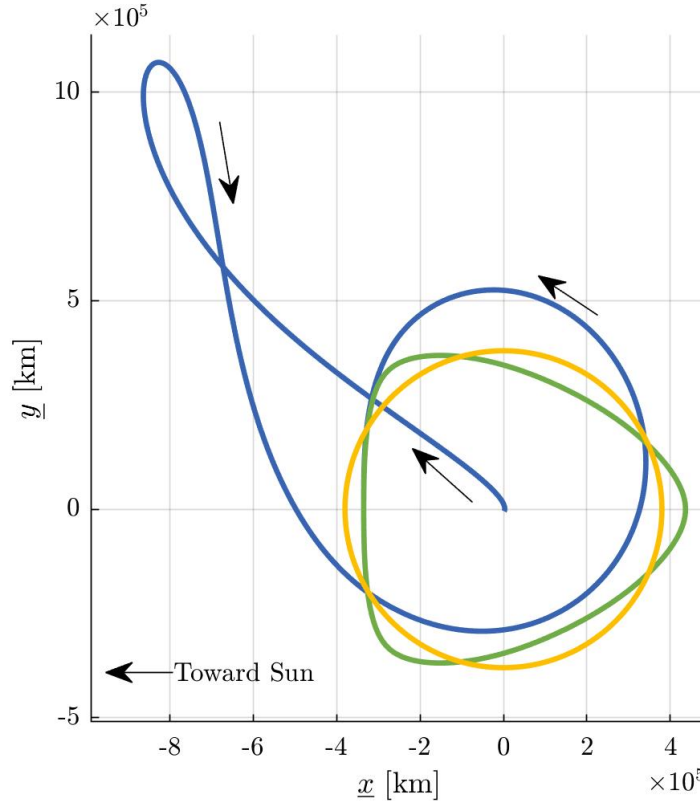
Figure 4.68. A sample ballistic lunar transfer from a 150 km parking orbit at the Earth to a 3:1 synodic resonant DRO, plotted in the Sun-B_1 rotating frame

Various forms of continuation schemes offer a range of family types for transfers to stable periodic orbits. Consider a specific state P along a periodic orbit, denoted as $[\widetilde{x}_P, \widetilde{y}_P, \widetilde{z}_P, \dot{\widetilde{x}}_P, \dot{\widetilde{y}}_P, \dot{\widetilde{z}}_P, \theta_S, P]$.

For a transfer to perform a maneuver onto the periodic orbit, the position and epoch must be equivalent to the desired location. A planar targeting schematic if formulated as

$$\bar{X} = \begin{bmatrix} \widetilde{x}_0 \\ \widetilde{y}_0 \\ \dot{\widetilde{x}}_0 \\ \dot{\widetilde{y}}_0 \\ \theta_{S0} \\ t \\ P \end{bmatrix} \qquad \bar{F} = \begin{bmatrix} \sqrt{(\widetilde{x}_0 + \widetilde{\mu})^2 + \widetilde{y}_0^2} - \eta_0 \\ (\widetilde{x}_0 + \widetilde{\mu})\dot{\widetilde{x}}_0 + \widetilde{y}_0\dot{\widetilde{y}}_0 \\ \widetilde{x}_P - \widetilde{x}_f \\ \widetilde{y}_P - \widetilde{y}_f \\ \theta_{S,P} - \theta_{S,f} \end{bmatrix} \qquad (4.11)$$

where the first two constraints are equivalent to the case formulated for the transfers to conic orbits, described in Equation (4.4). The quantity P in the free variable vector corresponds to the insertion point along the orbit. Similar to the families of transfers to conic orbits, there are two more free variables than constraints. Therefore, to construct a family of transfers, an additional constraint is necessary. The constraint may include any one of the examples discussed in Section 4.3.1. However, additional constraints are available for transfers into periodic orbits. Including a fixed arrival position constraint, and tangential velocity constraints for both the Earth-Moon and Sun-B_1 rotating velocity directions. The fixed arrival position constraint is trivial, as the term P is removed from the free variable vector, i.e., the position and Sun angle quantities in the constraint vector become constant. Applying the sample transfer depicted in Figure 4.68, a family of solutions arriving at that fixed location is constructed and illustrated in Figure 4.69. Each gray arc arrives at the orbit for a Sun angle of $\theta_S = $ -3.3°. The blue arc has the lowest LOI maneuver cost of 75 m/sec, corresponding to the same transfer as the initial guess.
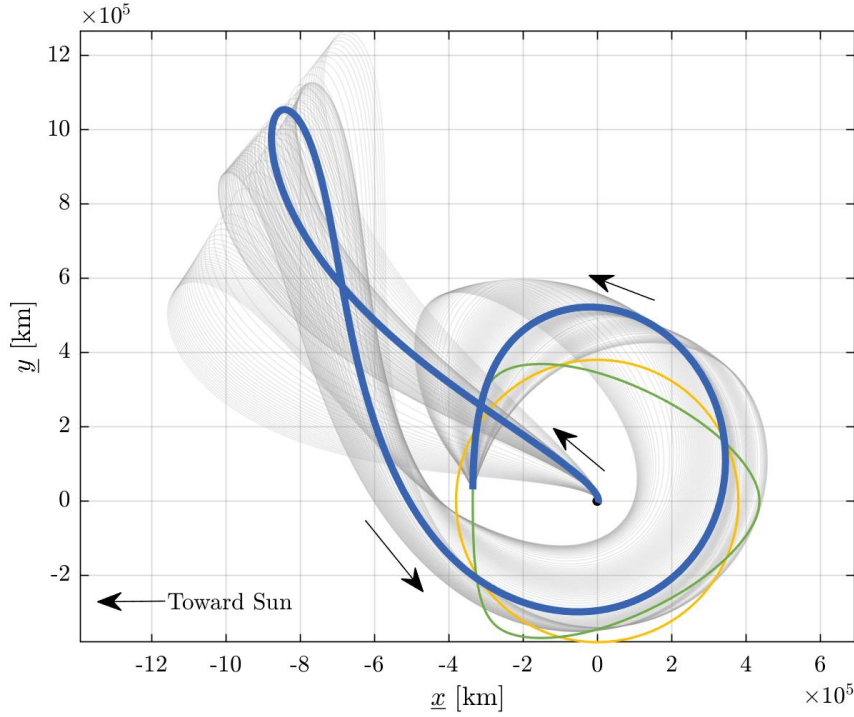
Figure 4.69. Family of transfers to a fixed location along the 3:1 synodic resonant DRO, plotted in the Sun-B_1 rotating frame centered at B_1

A tangential velocity constraint assumes that the incoming velocity of the transfer is tangent to the velocity of the orbit at the insertion location, i.e., the maneuver is in the rotating velocity direction. For a specified change in the Hamiltonian, a maneuver in the velocity direction is the most cost-effective change in energy. However, the energy changes along an arc in the BCR4BP, therefore, it is not true that the optimal maneuver solution will be in the velocity direction. However, a tangential velocity constraint offers insight into the available geometries in the vicinity of an initial guess. Additionally, a tangential maneuver in the Earth-Moon rotating frame is not equivalent to a tangential maneuver in the Sun-B_1 rotating frame. The tangential velocity constraints originate from the dot product between the incoming and orbital velocity vectors, written out as

$$F_{\text{vel,EM}} = \dot{\tilde{x}}_f\dot{\tilde{x}}_P + \dot{\tilde{y}}_f\dot{\tilde{y}}_P + \dot{\tilde{z}}_f\dot{\tilde{z}}_P - \widetilde{V}_f\widetilde{V}_P \tag{4.12}$$

$$F_{\text{vel,}SB_1} = \underline{\dot{x}}_f\underline{\dot{x}}_P + \underline{\dot{y}}_f\underline{\dot{y}}_P + \underline{\dot{z}}_f\underline{\dot{z}}_P - \underline{V}_f\underline{V}_P \tag{4.13}$$

where $F_{\text{vel,EM}}$ is the tangential velocity constraint relative to the Earth-Moon rotating velocity, and $F_{\text{vel,S}B_1}$ is the same constraint for the Sun-B_1 rotating velocity. The quantities $\widetilde{V}$ and $\underline{V}$ are the magnitude of the 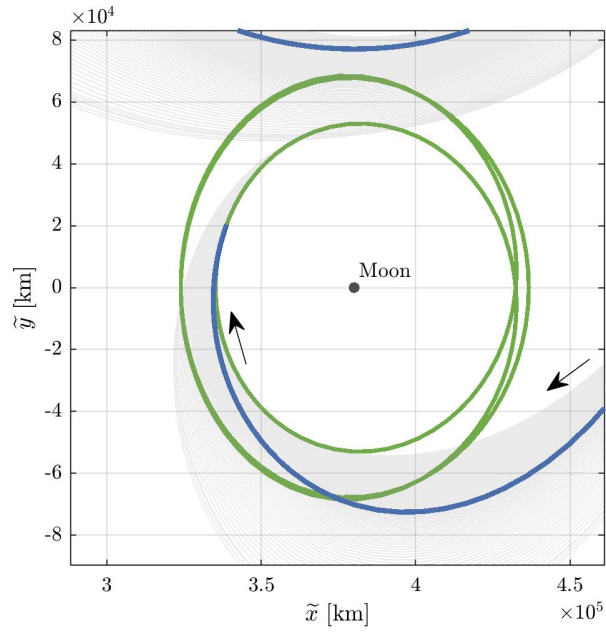rotating velocity vectors in the Earth-Moon and Sun-B_1 rotating frames, respectively. The subscript f corresponds to the final state on the transfer, and P is the state on the periodic orbit. Given the same sample trajectory selected from the periapse Poincaré map, a family of transfers with a tangential arrival Earth-Moon rotating velocity is illustrated in Figures 4.70 and 4.71 The entire transfer geometry in the Sun-B_1 rotating reference frame is depicted in Figure 4.70, and contains a similar structure to the fixed arrival family in Figure 4.69. Each gray arc reaches the 3:1 synodic resonant DRO at a different location along the orbit. The green arcs represents the periodic orbit, and the yellow circle is the orbit of the Moon. The variation in insertion location upon the orbit is more discernible in the Earth-Moon rotating frame, as illustrated in Figure 4.71. The blue transfer is the solution with the lowest LOI cost of 71.7 m/sec. The progression of maneuver cost and time of flight is outlined in Figure 4.72.
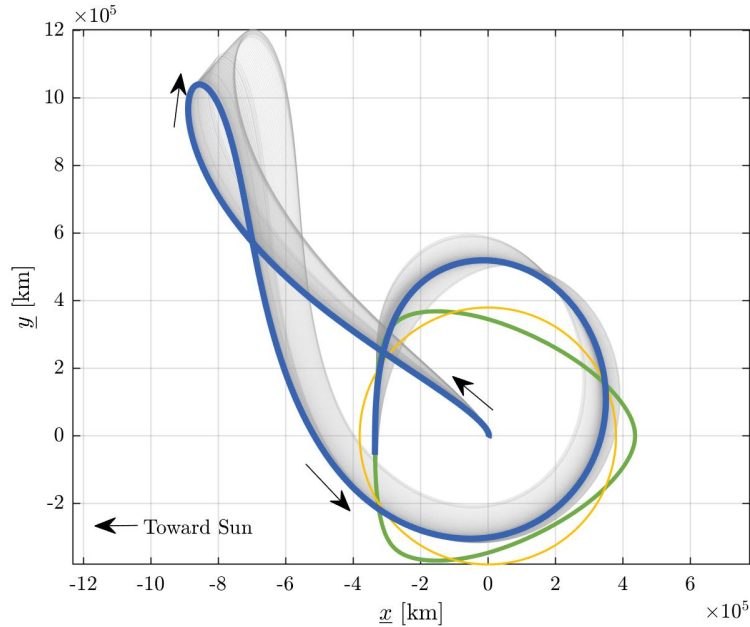
Figure 4.70. Family of transfers that arrive at the 3:1 synodic resonant DRO with a tangential Earth-Moon rotating velocity direction, plotted in the Sun-B_1 rotating frame centered at B_1

Figure 4.71. Family of transfers that arrive at the 3:1 synodic resonant DRO with a tangential Earth-Moon rotating velocity direction, plotted in the Earth-Moon rotating frame focused about the Moon
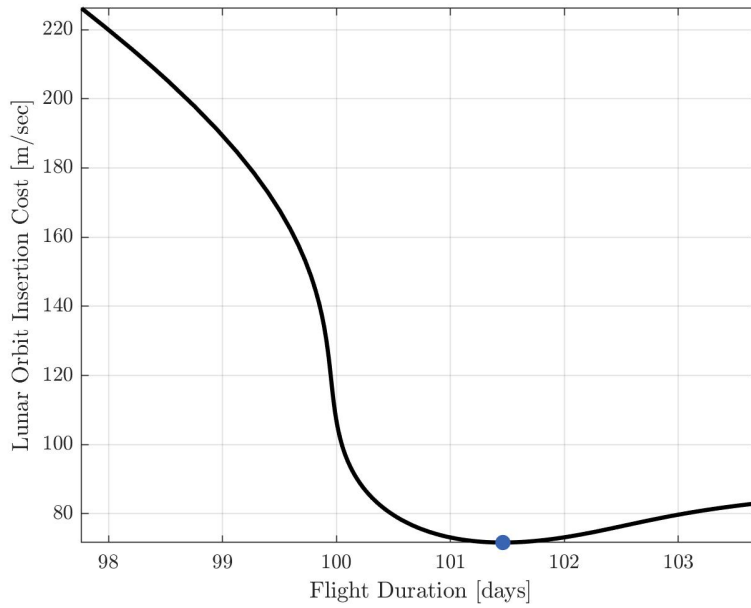
Figure 4.72. Evolution of LOI cost and flight duration along the family of transfers depicted in Figures 4.70 and 4.71

190

Employing the tangential Sun-B_1 velocity constraint in Equation (4.13) to the sample transfer from the map yields the family of transfers illustrated in Figures 4.73 and 4.74. The geometry of the transfers in the Sun-B_1 rotating frame possesses similar behavior to the family from Figure 4.70. The tangential velocity condition is evident in the Earth-Moon rotating frame, from visual inspection, most transfers are not tangent to the 3:1 synodic resonant DRO upon arrival. The blue transfer has an LOI cost of 74.2 m/sec, being the lowest insertion maneuver across the family. The variation in LOI cost and flight duration for the family is plotted in Figure 4.75

Figure 4.73. Family of transfers that arrive at the 3:1 synodic resonant DRO with a tangential Sun-B_1 rotating velocity direction, plotted in the Sun-B_1 rotating frame centered at B_1
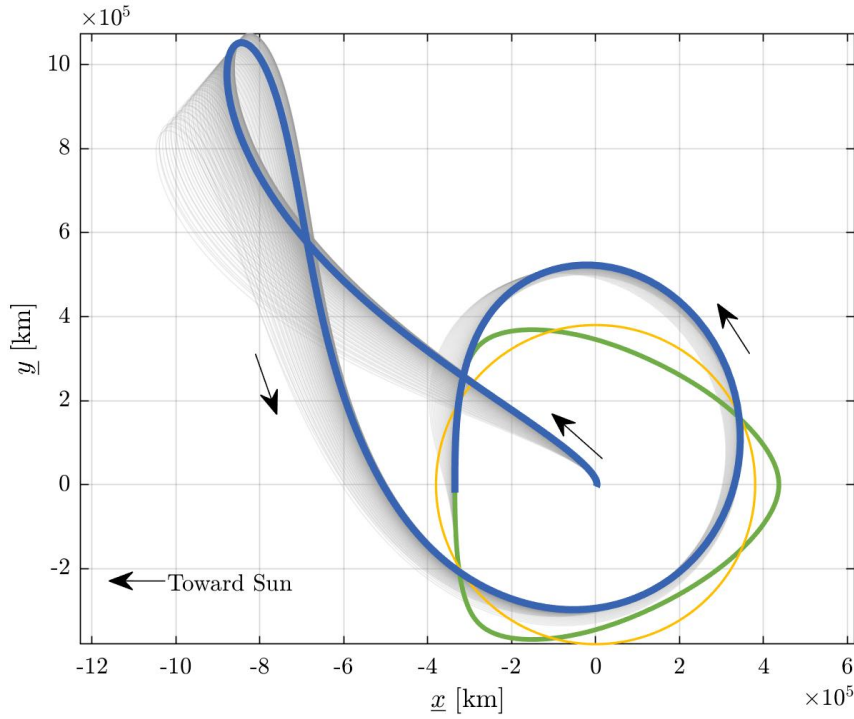
Figure 4.74. Family of transfers that arrive at the 3:1 synodic resonant DRO with a tangential Sun-B_1 rotating velocity direction, plotted in the Earth-Moon rotating frame focused about the Moon
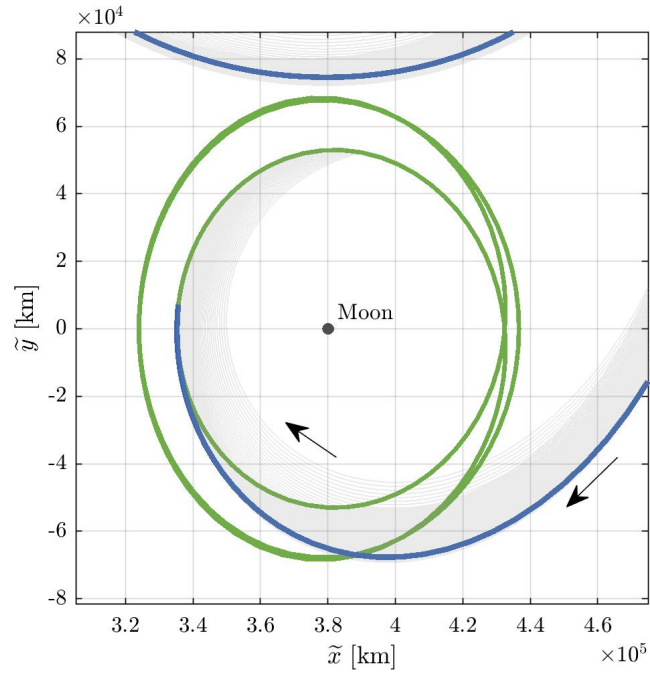

Figure 4.75. Evolution of LOI cost and flight duration along the family of transfers depicted in Figures 4.73 and 4.74
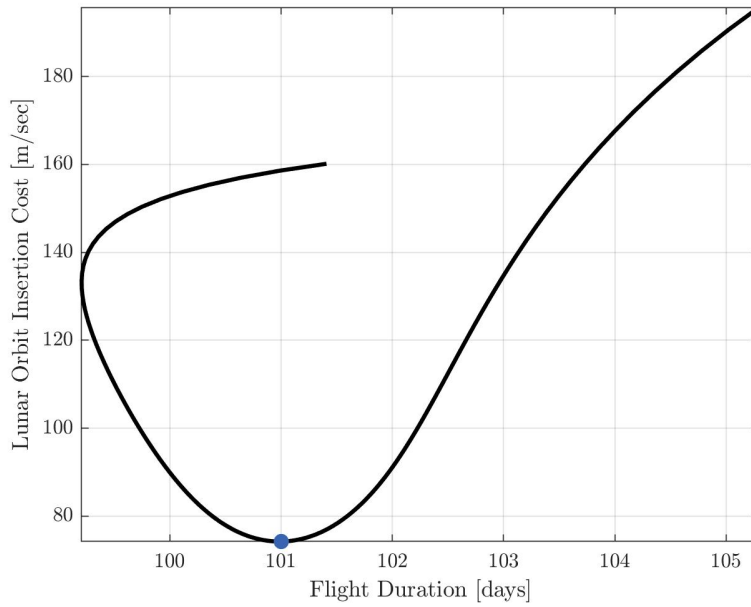
192

Sets of fixed LOI maneuver families characterize local behavior into the stable periodic orbits. Fixed maneuver families to conic orbits illustrate feasible transfer scenarios for a specified mission constraint, i.e., constant TLI or LOI. The same constraint derived in Equation (4.6) is applied upon arrival into stable orbits. Arrival conditions into a stable orbit vary as a function of the maneuver size. A direct comparison between different maneuver magnitude families offers insight into the flow arriving into the orbit. The blue transfer in Figure 4.73 is employed as the initial guess to construct five fixed LOI maneuver families, with insertion costs of 68 m/sec, 70 m/sec, 75 m/sec, 80 m/sec, and 85 m/sec. Observing the difference between the families is non-trivial in position space, as the families overlap in both the Sun-B_1 and Earth-Moon rotating frames. To assess the behavior, the flight duration and arrival epoch into the DRO for each family is illustrated in Figure 4.76. Each curve represents a closed family of planar transfers into the 3:1 synodic resonant DRO. The color in the legend designates the respective LOI maneuver cost for the families. Each arrival Sun angle corresponds to a unique state on the periodic solution. Therefore, each family in Figure 4.76 has two conditions that arrive at the state associated with a Sun angle of -5°, while the 85 m/sec family is the only family with a solution that arrives unto the DRO for a Sun angle of -25°. The larger curve corresponds to a wider range of available solutions. For this sample scenario, as the maneuver magnitude increases, more transfers into the DRO become accessible.
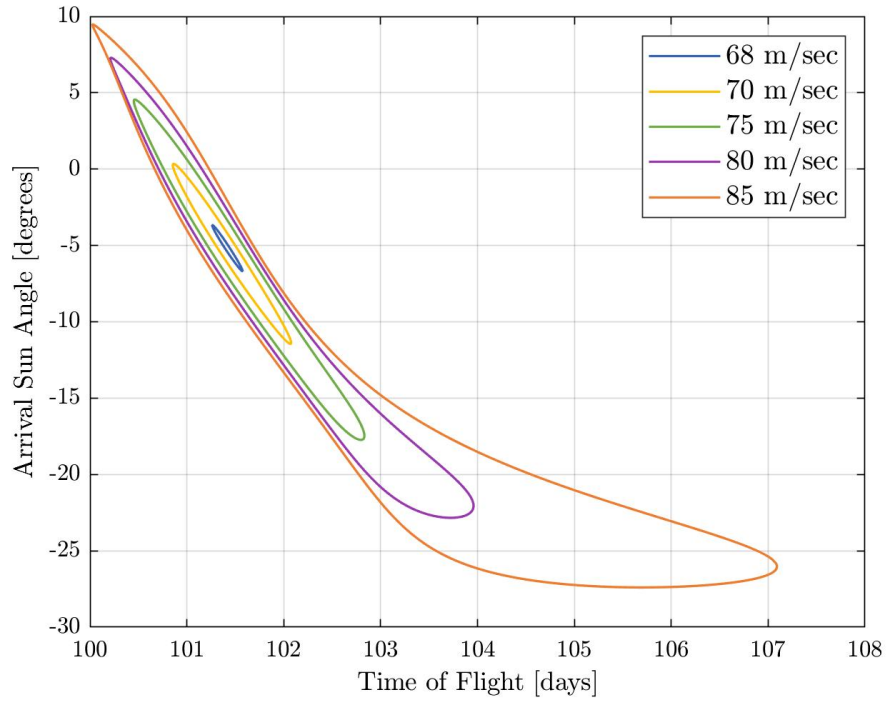
Figure 4.76. Evolution of flight duration and arrival epoch, i.e., Sun angle, for five families of ballistic lunar transfers with varying LOI magnitude

Constructing transfers to stable multi-body orbits is non-trivial. By nature, the motion that traverses into a stable solution is limited. Therefore, an assessment of varying maneuver magnitudes and arrival conditions is necessary. The techniques presented in this section aid in the exploration of viable transfer designs.

194

5. CONCLUDING REMARKS

5.1 Summary

The increasing demand to explore cislunar space necessitates an understanding of low-energy paths to the Moon. Ballistic lunar transfers leverage the gradual influence of the Sun to reduce the propellant cost of lunar orbit insertion. The objective of this investigation is to examine properties of ballistic lunar transfers and introduce techniques that construct families of applicable trajectories. Techniques that explore low-energy transfers in the Earth-Moon-Sun system are presented.

Understanding the natural variation in energy within the BCR4BP offers vast insight into the model. A key component to this investigation is exploring the natural patterns that enable ballistic lunar transfers to reduce LOI costs. Uncovering a quantitative expression for the variation in each Hamiltonian highlights the Earth, Moon, and Sun's impact on the energy of a ballistic arc. The perturbing effects of the Sun, far from the Earth-Moon system, is separated into four distinct regions, i.e., quadrants, that describe the change in the Earth-Moon Hamiltonian. Proper placement of a spacecraft amongst the regions enables low-cost solutions.

Numerical methods are adapted to construct families of ballistic lunar transfers. Families of transfers in the Sun-Earth CR3BP catalog the types of geometries that arrive at the orbit of the Moon tangentially. In the CR3BP, the flight duration and energy of each transfer in the family are considered. Although families in the Sun-Earth system do not include the gravitational influence of the Moon, they are able to depict the governing impact of solar perturbations on a trajectory near the Earth, and offer effective initial conditions when transitioning to a higher fidelity model. The BCR4BP enables end-to-end trajectory design of ballistic lunar transfers by incorporating the Earth, Moon, and Sun into one, coherent model. Due to the additional complexities of the BCR4BP, the solution-space is expanded and a larger range of family types exist. This investigation considered fixed period, fixed arrival epoch, fixed maneuver, and tangential velocity families. Each family type provides different knowledge to desired mission criteria. For example, a fixed maneuver family displays the

range of possible ballistic lunar transfers for a fixed LOI propellant cost. Families of transfers to planar conic orbits, and stable multi-body orbits are constructed.

An understanding of the gravity models facilitates the existence of low-cost ballistic lunar transfers. One challenge associated with low-energy solutions is assessing the optimal costs. Thus, it is advantageous to have a metric to compare the cost of a transfer to. Given the zero velocity surfaces and the natural evolution of energy in the BCR4BP, a theoretical minimum maneuver cost is devised. The theoretical minimum maneuver cost is a quantity that depends on the final orbit about the Moon, and measures the efficiency of a transfer based on its LOI cost. Instantaneous equilibrium solutions in the BCR4BP provide a natural transfer through the portals bounded by the zero velocity surfaces, and thus, provide solutions near the theoretical minimum maneuver. Truly ballistic transfers to cislunar space with no LOI cost are achievable. By leveraging stable manifolds off of unstable periodic orbits, a transfer near Earth follows a ballistic path through the BCR4BP into an unstable orbit. Techniques within dynamical systems theory offer low-cost ballistic lunar transfers.

5.2   Recommendations for Future Work

Ballistic lunar transfers are governed by the complex dynamics of the four-body problem. A majority of this investigation restricted the motion to the planar problem. In practice, the Earth-Moon-Sun system is even more dynamic, and complicated. A direct continuation of this work considers transitioning a transfer from either the CR3BP or BCR4BP to a higher fidelity ephemeris model. Previous authors have shown the capability of transitioning between these models [10] [12]. However, understanding the transformation process is insightful into the higher fidelity system. To analyze the impact of a more complicated model, one area of continued research resides in the Sun out-of-plane BCR4BP. Understanding the impact a spatial primary system has on the motion of a spacecraft is critical to implementing low-energy transfers. Another field of research considers the hidden structures of the BCR4BP. The limited quantity of periodic solutions reduces the natural structures through the system, even though a similar governing flow exists. Assessing the BCR4BP, and the tools within that model, will greatly enhance mission design capabilities. The last recommendation for

future work relates to the application of ballistic lunar transfers. In practice, operating errors and spacecraft constraints will pose more complicated mission architecture. Designing a mission to inhibit the impact of errors and extend the launch window are critical. Further work into assessing the stability of ballistic lunar transfers is desirable.

REFERENCES

[1] R. M. Smith, N. Merancy, and J. Krezel, "Exploration missions 1, 2, and beyond: First steps toward a sustainable human presence at the moon," eng, in *2019 IEEE Aerospace Conference*, vol. 2019-, IEEE, 2019, pp. 1–12, ISBN: 9781538668542.

[2] C. Warner, "NASA Outlines Lunar Surface Sustainability Concept," *web*, Apr. 2020, https://www.nasa.gov/feature/nasa-outlines-lunar-surface-sustainability-concept. [Online]. Available: https://www.nasa.gov/feature/nasa-outlines-lunar-surface-sustainability-concept.

[3] A. A. Siddiqi, *Beyond Earth : a chronicle of deep space exploration, 1958-2016*, Second edition., ser. NASA SP (Series) ; 2018-4041. 2018.

[4] R. Roncoli and K. Fujii, "Mission design overview for the gravity recovery and interior laboratory (grail) mission," eng, in *American Institute of Aeronautics and Astronautics. AIAA Conference Papers*, Reston, 2010.

[5] J. S. Parker, R. L. Anderson, and A. Peterson, "Surveying ballistic transfers to low lunar orbit," eng, vol. 36, no. 5, pp. 1501–1511, 2013, ISSN: 0731-5090.

[6] N. L. Parrish, E. Kayser, S. Udupa, J. S. Parker, B. W. Cheetham, and D. C. Davis, "Ballistic lunar transfers to near rectilinear halo orbit: Operational considerations," in *AIAA Scitech 2020 Forum*.

[7] S. Campagnola, J. Hernando-Ayuso, K. Kakihara, Y. Kawabata, T. Chikazawa, R. Funase, N. Ozaki, N. Baresi, T. Hashimoto, Y. Kawakatsu, T. Ikenaga, K. Oguri, and K. Oshima, "Mission analysis for the em-1 cubesats equuleus and omotenashi," *IEEE Aerospace and Electronic Systems Magazine*, vol. 34, pp. 38–44, Apr. 2019. DOI: 10.1109/MAES.2019.2916291.

[8] R. E. Pritchett, *Strategies for low-thrust transfer design based on direct collocation techniques*, Ph.D. Dissertation, School of Aeronautics and Astronautics, Purdue University, West Lafayette, Indiana, West Lafayette, Indiana, 2020.

[9] J. S. Parker, "Targeting low-energy ballistic lunar transfers," eng, *The Journal of the Astronautical Sciences*, vol. 58, no. 3, pp. 311–334, 2011, ISSN: 0021-9142.

[10] J. S. Parker and G. H. Born, "Modeling a low-energy ballistic lunar transfer using dynamical systems theory," eng, 6, vol. 45, 2008, pp. 1269–1281.

[11] N. L. Parrish, E. Kayser, S. Udupa, J. S. Parker, B. W. Cheetham, and D. C. Davis, "Survey of ballistic lunar transfers to near rectilinear halo orbit," in *AIAA/AAS Astrodynamics Specialist Conference*, 2019.

[12] A. Tselousova, M. Shirobokov, and S. Trofimov, "Geometrical tools for the systematic design of low-energy transfers in the earth-moon-sun system," eng, in *AIAA/AAS Astrodynamics Specialist Conference*, 2020.

[13] K. Oshima, F. Topputo, and T. Yanao, "Low-energy transfers to the moon with long transfer time," eng, *Celestial Mechanics and Dynamical Astronomy*, vol. 131, no. 1, pp. 1–19, 2019.

[14] T. H. Sweetser, "An estimate of the global minimum DV needed for earth-moon transfer," in *Spaceflight Mechanics 1991*, Jan. 1991, pp. 111–120.

[15] K. K. Boudad, *Disposal dynamics from the vicinity of near rectilinear halo orbits in the earth-moon-sun system*, M.S. Thesis, Purdue University, West Lafayette, Indiana, West Lafayette, Indiana, 2018.

[16] K. K. Boudad, K. C. Howell, and D. C. Davis, "Near rectilinear halo orbits in cislunar space within the context of the bicircular four-body problem," in *AIAA/AAS SciTech Forum*, 2019.

[17] I. Newton, *Philosophiae naturalis principia mathematica.* lat;eng, 3d ed. (1726), with variant readings, assembled and edited by Alexandre Koyré and I. Bernard Cohen, with the assistance of Anne Whitman. Cambridge, Mass.: Harvard University Press, 1972, ISBN: 0674664752.

[18] A. E. Roy, *Orbital Motion*, eng, 2nd ed. Bristol: A. Hilger, 1982, ISBN: 0852744625.

[19] L. Euler, "De motu rectilineo trium corporum se mutuo attrahentium," *Novi Commentarii academiae scientiarum Petropolitanae*, vol. 11, pp. 144–151, 1767.

[20] J. L. Lagrange, "Essai sur le probleme' des tois corps," *Prix de l'Acade'mie Royale des Sciences de Paris,*, vol. tome IX, pp. 272–282, 1772.

[21] A. E. Roy and M. W. Ovenden, "On the occurrence of commensurable mean motions in the solar system: The mirror theorem," eng, *Monthly notices of the Royal Astronomical Society*, vol. 115, no. 3, pp. 296–309, 1955, ISSN: 0035-8711.

[22] M. A. Andreu, *The quasi-bicircular problem*, Ph.D. Dissertation, Universitat de Barcelona, West Lafayette, Indiana, 1999.

[23] K. K. Boudad, D. C. Davis, and K. C. Howell, "Disposal trajectories from near rectilinear halo orbits," in *AAS/AIAA Astrodynamics Specialist Conference*, 2018.

[24] V. G. Szebehely, *Theory of Orbits: The Restricted Problem of Three Bodies*, eng. New York: Academic Press, 1967, ISBN: 0-12-395732-X.

[25] C. T. Kelley, *Solving nonlinear equations with Newton's method*, eng, ser. Fundamentals of algorithms. Philadelphia, Pa., 2003, ISBN: 0-89871-546-6.

[26] E. Kreyszig, *Advanced Engineering Mathematics*, eng, 10th edition. 2010.

[27] E. J. Doedel, V. A. Romanov, R. C. Paffenroth, H. B. Keller, D. J. Dichmann, J. Galan-vioque, and A. Vanderbauwhede, "Elemental periodic orbits associated with the libration points in the circular restricted 3-body problem," eng, *International journal of bifurcation and chaos in applied sciences and engineering*, vol. 17, no. 8, pp. 2625–2677, 2007, ISSN: 0218-1274.

[28] K. K. Boudad, D. C. Davis, and K. C. Howell, "Heliocentric access from cislunar space within the context of the bicircular restricted four-body problem," in *AAS/AIAA Astrodynamics Specialist Conference*, 2020.

[29] L. Perko, *Differential equations and dynamical systems*, eng, Third edition., ser. Texts in applied mathematics ; 7. 2001, ISBN: 9781461300038.

[30] T. S. Parker and L. O. Chua, *Practical Numerical Algorithms for Chaotic Systems*, eng. New York: Springer New York, 1989, ISBN: 9781461281214.

[31] J. Guckenheimer, *Nonlinear oscillations, dynamical systems, and bifurcations of vector fields*, eng, ser. Applied mathematical sciences (Springer-Verlag New York Inc.) ; v. 42. New York: Springer-Verlag, 1983, ISBN: 0387908196.

[32] W. S. Koon, M. W. Lo, J. E. Marsden, and S. D. Ross, *Dynamical Systems, The Three Body Problem, and Space Mission Design*, eng. Springer-Verlag, 2006.

[33] *Chaotic worlds : from order to disorder in gravitational N-body dynamical systems*, eng. Dordrecht: Springer, 2006, ISBN: 1402047045.

[34] E. M. Zimovan-Spreen, *Characteristics and design strategies for near rectilinear halo orbits within the earth-moon system*, M.S. Thesis, Purdue University, West Lafayette, Indiana, West Lafayette, Indiana, 2017.

[35] N. Bosanac, *Leveraging natural dynamical structures to explore multibody systems*, Ph.D. Dissertation, School of Aeronautics and Astronautics, Purdue University, West Lafayette, Indiana, West Lafayette, Indiana, 2016.

[36] S. T. Scheuerle, B. P. McCarthy, and K. C. Howell, "Construction of ballistic lunar transfers leveraging dynamical systems techniques," in *AIAA/AAS Astrodynamics Specialist Conference*, 2020.

[37] D. C. Davis, C. Patterson, and K. C. Howell, "Solar gravity perturbations to facilitate long-term orbits: Application to cassini," in *AIAA/AAS Astrodynamics Specialist Conference*, 2007.

[38] D. C. Davis, "Multi-body trajectory design strategies based on periapsis poincare maps," in *PhD Dissertation*, Purdue University, West Lafayette, Indiana, 2011.

[39] P. Antreasian, R. Bhat, S. Broschart, M.-K. Chung, K. Criddle, T. Goodson, S. Hatch, D. Jefferson, E. Lau, S. Mohan, J. Parker, R. Roncoli, M. Ryne, T. Sweetser, T.-H. You, and B. Young, "Navigation of the twin grail spacecraft into science formation at the moon," Oct. 2012.